COMBINING ACOUSTIC EMISSION AND GUIDED ULTRASONIC WAVES FOR GLOBAL PROPERTY PREDICTION AND STRUCTURAL HEALTH MONITORING OF GLASS FIBER COMPOSITES

by

Paul Murdy

A dissertation submitted in partial fulfillment
of the requirements for the degree

of

Doctor of Philosophy

in

Mechanical Engineering

MONTANA STATE UNIVERSITY
Bozeman, Montana

November 2018

©COPYRIGHT

by

Paul Murdy

2018

All Rights Reserved

ACKNOWLEDGEMENTS

First of all, I would like to thank my parents, Susan and Clifford Murdy, for their endless support and advice throughout my life and academic career. Of course, I would not be the person I am today and have achieved my doctorate in mechanical engineering without them. Sometimes I like to think that my achievements and completing my dissertation are more their achievements and a reflection of their characters. I would also like to express my appreciation to the rest of my family and friends, particularly my girlfriend, Arica, for their support during the toughest and most stressful times during my PhD.

With regards to my four and a half years as a graduate student at Montana State University, my endless gratitude goes to my adviser, Dr. David Miller, for triggering and nurturing my interest in composite materials over six years ago. I would like to thank him for teaching me my first composite materials class, taking me on as a PhD student, allowing me to find my own way and providing me with patience and sage advice throughout my degree. I would also like to thank Daniel Samborsky for helping and guiding me through countless hours of testing in the lab, day and night. Great thanks go to my doctoral committee, Dr. Michael Edens, Prof. Douglas Cairns and Prof. Stephen Sofie, for their time, wisdom and patience from when I first proposed my research ideas to when they came into fruition and they accepted and awarded me my degree for them. Finally, I would like to thank everyone else that I have had the pleasure of working with in the Composite Material Technologies group at MSU throughout my time here.

TABLE OF CONTENTS

1. INTRODUCTION 1

2. BACKGROUND 9

Damage in Composites 9
Fatigue Models 15
Structural Health Monitoring 20
Acoustic Emission 23
Damage Classification 26
Global Property Prediction 31
Guided Ultrasonic Waves 33
Combined Monitoring Techniques 37
Statistical Predictive Modeling 40
Multivariate Linear Regression Modeling 41
Principal Component Analysis 47

3. EXPERIMENTAL PROCEDURES 50

Specimen Manufacturing 51
On-Line Damage Monitoring Setup 59
Acoustic Emission 61
Guided Ultrasonic Waves 67
Sensor Attachment 71
Static Testing 74
Benchmark Testing 76
Load-Unload-Reload Testing 78
Fatigue Testing 82
Damage Observation Techniques 88

4. STATIC TESTING RESULTS AND DISCUSSION 90

Benchmark Tests 90
Moduli Measurements 96
Acoustic Emission 99
Load-Unload-Reload Tests 107
Load-Unload-Reload Validation 108
Moduli Degradation 112
Acoustic Emission 114
Guided Ultrasonic Waves 118
Imaging and Microscopy Observations 125

TABLE OF CONTENTS CONTINUED

5. FATIGUE TESTING RESULTS AND DISCUSSION 143

Fatigue Life Results 143
Modulus Degradation 146
Acoustic Emission 151
Guided Ultrasonic Waves 163

6. STATISTICAL PREDICTIVE MODELING PROCEDURES 168

Model Selection 168
Multivariate Linear Regression Modeling 169
Model Validation 171
Variable Reduction 172
Layup Independence 173
Collinearity and Principal Component Analysis 174
Model Summaries 176

7. PREDICTIVE MODELING RESULTS AND DISCUSSION 179

Static Data Modeling 179
Acoustic Emission vs. Guided Ultrasonic Waves 180
Prediction Accuracy 185
Coefficient Comparisons 192
Layup Independent Model 194
Collinearity and Principal Component Analysis 201
Fatigue Data Modeling 213
Prediction Accuracy 214
Coefficient Comparisons 220
Static Testing for Fatigue Prediction 221
Model Improvements 227
Test Setup Changes 227
Additional Variables 230
Other Modeling Techniques 232

8. FUTURE WORK 235

Test Methodologies 235
Acoustic Emission and Guided Ultrasonic Wave Monitoring 238
Modeling Strategies 240

9. FINAL CONCLUSIONS 242

REFERENCES CITED 246

TABLE OF CONTENTS CONTINUED

APPENDICES 257

APPENDIX A: Materials 258
APPENDIX B: Test Coupons 268
APPENDIX C: AE System Information 274
APPENDIX D: Additional Static Test Data 278
APPENDIX E: Additional Fatigue Test Data 298

LIST OF TABLES

Table Page

1. Manufactured laminate numbers, layups, number of coupons cut, thicknesses and volume fractions. 58

2. A comparison of AE system parameters used in this study for the new USB system with the previous Mistras system. 66

3. A summary of the wave velocities used for the AE system for each layup tested, for location monitoring. 67

4. A summary of the layups and coupons tested for acquiring benchmark stress-strain and AE data. 77

5. A summary of the layups and final coupons tested using the increasing LUR procedure, while acquiring AE and GUW data. 82

6. A summary of the layups, maximum stresses and coupons tested during the fatigue phases of testing. 85

7. A comparison of ultimate failure stresses for each layup, with standard deviations. 91

8. A comparison of initial moduli for the five layups tested. 97

9. A comparison of static tensile strengths determined from monotonic and increasing LUR loading for all four layups, with standard deviations. 108

10. A summary of the models constructed using the AE and GUW datasets, acquired during the static tensile LUR tests. 178

11. A summary of the models constructed using the AE and GUW datasets, acquired during the interrupted tension-tension fatigue tests. 178

12. A summary of R^2 values for each extracted variable for each layup when compared with changes in moduli (GUW variables are on top and AE variables are below and separated by the dotted line). 180

LIST OF TABLES CONTINUED

Table Page

13. A summary of fit characteristics and HOCV results for models constructed using only AE data for each of the layups tested in static tension. 181

14. A summary of fit characteristics and HOCV results for models constructed using only GUW data for each of the layups tested in static tension. 182

15. A comparison of variables selected for each respective model and their associated coefficients, β_i (GUW and AE models are split by the double solid line divider). 185

16. A summary of fit characteristics and HOCV results for models constructed when combining the AE and GUW datasets for each of the layups tested in static tension. 186

17. R^2 values for each of the HOCV tests conducted for each layup, where each coupon was removed from the training datasets to validate the models. 187

18. A summary of the variables selected and their respective coefficients for each layup for the combined static models. 193

19. A comparison of R^2 values for each variable with respect to changes in moduli. Variables of interest for the interaction functions are shown in bold. 195

20. A summary of the regression coefficients for each layup independent model. 196

21. A summary of fit characteristics and HOCV results for models constructed when combining the $[0/90]_S$, $[90/0]_S$ and $[0/90/\pm45]_S$ static tension LUR datasets. 196

22. A comparison of VIFs for all the variables for the $[0/90]_S$ dataset, with significant relationships highlighted in yellow (numbers in parentheses relate to the variables in the order presented in previous tables). 203

LIST OF TABLES CONTINUED

Table Page

23. A comparison of VIFs for all the variables for the $[90/0]_S$ dataset, with significant relationships highlighted in yellow (numbers in parentheses relate to the variables in the order presented in previous tables). 203

24. A comparison of VIFs for all the variables for the $[0/90/\pm45]_S$ dataset, with significant relationships highlighted in yellow (numbers in parentheses relate to the variables in the order presented in previous tables). 204

25. A comparison of VIFs for all the variables for the $[90_4]$ dataset, with significant relationships highlighted in yellow (numbers in parentheses relate to the variables in the order presented in previous tables). 204

26. A comparison of linear regression coefficients for each HOCV test for the $[0/90]_S$ model to demonstrate stability. Effects of collinearity of specific variables are highlighted in yellow. 205

27. A summary of the first two principal component loading vectors for each layup dataset. 207

28. A summary of coefficients from the PCRs when all PCs were applied and transformed back to the original data space. Cells highlighted in yellow indicate coefficients affected by collinearity and green indicates coefficients that were not. 212

29. A summary of coefficients from the PCRs transformed back to the original data space for models with reduced PCs, where R^2_{HOCV} was maximized; 7 PCs for $[0/90]_S$, 11 PCs for $[90/0]_S$, 5 PCs for $[0/90/\pm45]_S$, 7 PCs for $[90_4]$. Cells highlighted in yellow indicate coefficients affected by collinearity and green indicates coefficients that were not. 212

30. A summary of R^2 values for each extracted variable for each layup when compared with changes in moduli in fatigue testing (GUW variables are on top and AE variables are below and separated by the dotted line). 214

LIST OF TABLES CONTINUED

Table Page

31. A summary of fit characteristics and HOCV results for models constructed when combining the AE and GUW datasets for each of the layups tested in fatigue. 215

32. A comparison of the regression model coefficients for the fatigue models, with removed variables left blank. 220

LIST OF FIGURES

Figure Page

1. An example of how Boeing utilized composite materials for the construction of their 787 aircraft. 2
2. The rapid increase of wind turbine rotor diameters and projections for the future. 3
3. An example of a significant wind turbine blade failure common in the industry. 3
4. The general approach for designing and testing materials for composite structures. 4
5. Square (left) and hexagonal (right) fiber/matrix representative volume elements (RVEs) with longitudinal strain applied to them to show stress concentrations. 11
6. Diagram displaying a variety of micro-damage modes commonly observed in FRP laminates. 11
7. A GFRP tensile test coupon that displayed significant strain energy release at ultimate failure, due to longitudinal fiber tows failing in a cascading manner. 13
8. An illustration of the three delamination modes typically observed in composite laminates. 14
9. Damage initiation and progression over the life of composite laminates, as presented by Reifsnider. 15
10. An example S-N curve showing differences in fatigue properties for three different matrix materials. 17
11. An example of a CLD for many R values from axial stress fatigue data. 18
12. A diagram showing the primary symmetric (S_0) and antisymmetric (A_0) waves mode shapes for plates. 24
13. Delta-t mapping being used for two-dimensional damage event locating. 25

LIST OF FIGURES CONTINUED

Figure Page

14. Schuster's summary of frequency bins determined by other researchers as well as his own. 27

15. Unsupervised clustering results plotted against peak frequency, showing that the clusters are heavily influenced by signal peak frequencies. 29

16. A diagram showing the effect of in-plane and out-of-plane damage modes on the symmetric and antisymmetric wave modes. 30

17. A plot of AE energy over time for a fatigue test, which indicates significant changes in the laminate's damage state. 32

18. An example of a GUW sensor array setup on a composite aircraft wing-box structure with impact damage. 34

19. A diagram showing how damage within a composite laminate can affect the propagation of GUWs. 34

20. The actuator (top of sample) and sensor (bottom of sample) setup used by Wilson et al. to measure changes in power spectral density through different wave paths. 36

21. A comparison of damage indicators used by Chaki et al. for incremental static tensile loading of GFRP coupons for multiple monitoring techniques, including AE and GUWs. 38

22. A representation of a two predictor linear regression onto a response – a 2D plane across 3D space. 42

23. Plots of possible regression coefficients that are not collinear (left) and highly collinear (right) to show the instability that collinearity can cause. The ellipses are lines of equal RSS. 46

24. Transmitted light and reflected light front and back images of the PPG Devold Biax 810 fabric (left) and the Vectorply E-LT 3800 fabric (right). 53

25. A schematic of the VARIM setup used to manufacture the laminates. 56

LIST OF FIGURES CONTINUED

Figure Page

26. A photo of epoxy being infused into the fabric on the mold, with the red line indicating the flow front. 56

27. A test sample used for a matrix burn-off (left) and the sample once all the epoxy had been burnt off (right). 57

28. A photo as an example of the coupons that were produced with and without end tabs. 59

29. A photo of the test setup for static testing (left) and a schematic of the sensor setup, including dimensions related to the AE setup. 61

30. A Fourier transform of the electromagnetic noise detected by the USB system without sensors attached, show a significant spike at approximately 1.4 MHz 63

31. A comparison of the noise spectrums recorded from each system after the lower sampling rate and 600 kHz LPF had been applied to the new USB system. 64

32. A comparison of the input voltage signal and the voltage signal received by the AE system after a wave has propagated through a test coupon. 68

33. A comparison of frequency content and magnitude of two successive received GUW waveforms, using fast Fourier transforms. 69

34. An example waveform showing how the location monitoring can become inaccurate after the GUWs have been significantly attenuated. 71

35. A photo of the previous hand clamp method used to attach the AE sensors to test coupons. 72

36. A photo of the sensor caps and sleeves used to attach a sensor to a test coupon using rubber bands 74

37. Epsilon 3543 extensometer with a 152 mm gage section used for all static tensile testing. 75

LIST OF FIGURES CONTINUED

Figure Page

38. A plot of GUW energy attenuation against maximum applied load for an incrementally increasing LUR test to compare the effect of applied load on the attenuation of GUWs. 79

39. A strain-time diagram displaying how increasing damage states were introduced to coupons with the acquisition of AE and GUW data indicated. 80

40. First cycle strain against cycles to failure for the Vectorply E-LT 5500 fabric with the Hexion 135/1366 resin system, constructed from previous tests conducted at MSU. 84

41. A photo of the fatigue setup with the AE sensors and Instron extensometer attached. 86

42. An example of a cross-section cast in clear resin and prepared for SEM observations. 89

43. Stress-strain curves for the $[0/90]_S$ coupons tested under monotonic static tensile loading. 93

44. Stress-strain curves for the $[90/0]_S$ coupons tested under monotonic static tensile loading. 93

45. Stress-strain curves for the $[0/90/\pm45]_S$ coupons tested under monotonic static tensile loading. 94

46. Stress-strain curves for the $[90_4]$ coupons tested under monotonic static tensile loading. 94

47. Stress-strain curves for the $[45/-45]_S$ coupons tested under monotonic static tensile loading. 95

48. A stress-strain plot to compare trends between the $[0/90]_S$, $[90/0]_S$ and $[0/90/\pm45]_S$ layups. 95

49. A photo showing the localized failure regions exhibited by the $[45/-45]_S$ coupons. 96

50. A comparison of normalized tangent moduli for a coupon of each layup. 99

LIST OF FIGURES CONTINUED

Figure Page

51. AE accumulated energy plots for the $[0/90]_S$, $[90/0]_S$ and $[0/90/\pm45]_S$ layups with their respective stress-strain curves. 100

52. AE accumulated energy plots for the $[90_4]$ and $[45/-45]_S$ layups with their respective stress-strain curves overlaid. 101

53. A comparison plot of AE accumulated energies for the $[0/90]_S$, $[90/0]_S$, $[0/90/45]_S$ and $[90_4]$ laminates. 102

54. AE event peak frequency against strain for the $[0/90]_S$ (4103_12) layup with the respective stress-strain plot overlaid. 103

55. AE event peak frequency against strain for the $[90/0]_S$ (4110_05) layup with the respective stress-strain plot overlaid. 104

56. AE event peak frequency against strain for the $[0/90/\pm45]_S$ (4120_05) layup with the respective stress-strain plot overlaid. 104

57. AE event peak frequency against strain for the $[90_4]$ (4114_26) layup with the respective stress-strain plot overlaid. 105

58. AE event peak frequency against strain for the $[45/-45]_S$ (4116_06) layup with the respective stress-strain plot overlaid. 105

59. A comparison of stress-strain curves from an increasing LUR test and a monotonic static test for the $[0/90/\pm45]_S$ layup. 109

60. A comparison of stress-strain curves from an increasing LUR test and a monotonic static test for the $[90_4]$ layup. 109

61. A comparison of AE accumulated energies between the monotonic and LUR loading procedures for the $[0/90]_S$ and $[90/0]_S$ layups. 111

62. A comparison of AE accumulated energies between the monotonic and LUR loading procedures for the $[0/90/\pm45]_S$ and $[90_4]$ layups. 111

63. A comparison of normalized modulus change averaged over all seven coupon tests for each layup, with standard deviation error bars included. 112

LIST OF FIGURES CONTINUED

Figure Page

64. A comparison of secant and tangent moduli degradations from the increasing LUR and monotonic static tensile testing procedures. 114

65. A scatter plot of modulus degradation against AE cumulative absolute energy for all seven coupons tested from each of the four layups. 115

66. A scatter plot of modulus degradation against AE cumulative counts for all seven coupons tested from each of the four layups. 116

67. A scatter plot of modulus degradation against AE cumulative number of events for all seven coupons tested from each of the four layups. 116

68. Plots showing the voltage signal, short term Fourier transform and fast Fourier transform of a received GUW applied to an undamaged coupon. 119

69. A scatter plot of modulus degradation against GUW normalized amplitude change for all seven coupons tested from each of the four layups. 120

70. A scatter plot of modulus degradation against GUW normalized absolute energy change for all seven coupons tested from each of the four layups. 121

71. A scatter plot of modulus degradation against GUW normalized rise time change for all seven coupons tested from each of the four layups. 121

72. A scatter plot of modulus degradation against GUW normalized centroid frequency change for all seven coupons tested from each of the four layups. 122

73. An SEM image looking through the transverse direction of a $[0/90]_S$ coupon (4107_12), which had been loaded to 0.6% strain, with the faint cracks highlighted in the black boxes. 126

LIST OF FIGURES CONTINUED

Figure Page

74. An SEM image looking through the transverse direction of a $[90/0]_S$ coupon (411_02), which had been loaded to 0.6% strain, with the faint cracks highlighted in the black boxes..... 127

75. An SEM image looking through the transverse direction of a $[0/90/\pm45]_S$ coupon (4121_07), which had been loaded to 0.6% strain, with the faint cracks highlighted in the black boxes..... 128

76. An SEM image looking through the transverse direction of a $[90_4]$ coupon (4113_18), which had been loaded to 0.6% strain, with the faint cracks highlighted in the black boxes. 128

77. An SEM image looking through the transverse direction of a $[45/-45]_S$ coupon (4115_05), which had been loaded to 1.5% strain, with the faint cracks highlighted in the black boxes..... 130

78. Transmitted light photos of coupons from the (a) $[0/90]_S$, (b) $[90/0]_S$, (c) $[0/90/\pm45]_S$ and (d) $[90_4]$ layups which had been loaded up to 2.5% strain. 131

79. An SEM image of a $[0/90]_S$ coupon (4103_12), which had been loaded up to 2.5% strain, looking in the longitudinal direction. 133

80. An SEM image of a $[0/90]_S$ coupon (4103_12), which had been loaded up to 2.5% strain, looking in the transverse direction..... 134

81. An SEM image of a $[90/0]_S$ coupon (4110_06), which had been loaded up to 2.5% strain, looking in the transverse direction..... 135

82. An SEM image displaying a closer look at the delaminations and other damage modes in a $[0/90/\pm45]_S$ coupon (4120_07), looking in the transverse direction..... 137

83. An SEM image displaying a closer look at the delaminations and other damage modes in a $[0/90/\pm45]_S$ coupon (4120_07), looking in the longitudinal direction. 138

84. An SEM image of a $[90_4]$ coupon (4113_13), which had been loaded up to ultimate failure, looking in the longitudinal direction. 139

LIST OF FIGURES CONTINUED

Figure Page

85. An SEM image of a [90_4] coupon (4113_13), which had been loaded up to ultimate failure, looking in the transverse direction. 140

86. A photo showing coupons from all five layups which had underwent ultimate failure - (a) $[0/90]_S$, (b) $[90/0]_S$, (c) $[0/90/\pm45]_S$, (d) [90_4] and (e) $[45/-45]_S$. 142

87. S-N plot for all fatigue tests that were conducted ($R = 0.1$), excluding premature grip failures and including the static tensile strengths, for all three layups tested. 144

88. Normalized modulus degradation curves for the final five $[0/90]_S$ fatigue test coupons. 147

89. Normalized modulus degradation curves for the final five $[90/0]_S$ fatigue test coupons. 148

90. Normalized modulus degradation curves for the final five $[0/90/\pm45]_S$ fatigue test coupons. 148

91. A comparison of normalized modulus degradation curves for one representative coupon from each of the three layups tested in fatigue. 149

92. AE accumulated absolute energy (aJ) curves for the final five coupons tested for the $[0/90]_S$ layup. 152

93. AE accumulated absolute energy (aJ) curves for the final five coupons tested for the $[90/0]_S$ layup. 153

94. AE accumulated absolute energy (aJ) curves for the final five coupons tested for the $[0/90/\pm45]_S$ layup. 153

95. A comparison of representative AE accumulated energy trends for each of the three layups tested in fatigue. 154

96. A photo showing buckling of tows close to the AE sensors, which had the potential to dislodge them. 155

LIST OF FIGURES CONTINUED

Figure Page

97. A peak frequency plot against life fraction for a $[0/90]_S$ coupon fatigue test (4107_05), with its respective modulus degradation curve overlaid. 159

98. A peak frequency plot against life fraction for a $[90/0]_S$ coupon fatigue test (4110_14), with its respective modulus degradation curve overlaid. 159

99. A peak frequency plot against life fraction for a $[0/90/\pm45]_S$ coupon fatigue test (4121_02), with its respective modulus degradation curve overlaid. 160

100. Changes in moduli plotted against accumulated absolute AE energy for all five coupon tests for each respective layup tested in fatigue. 162

101. Changes in moduli plotted against accumulated number of AE events for all five coupon tests for each respective layup tested in fatigue. 162

102. Changes in moduli in fatigue plotted against GUW normalized absolute energy change for all five coupons tested for the three layups, with linear regression fits included. 164

103. Changes in moduli in fatigue plotted against GUW normalized amplitude change for all five coupons tested for the three layups, with linear regression fits included. 165

104. Changes in moduli in fatigue plotted against GUW normalized counts change for all five coupons tested for the three layups, with linear regression fits included. 165

105. A scatter plot of the HOCV prediction results for the separate AE and GUW models for the $[0/90]_S$ layup. 182

106. A scatter plot of the HOCV prediction results for the separate AE and GUW models for the $[90/0]_S$ layup. 183

107. A scatter plot of the HOCV prediction results for the separate AE and GUW models for the $[0/90/\pm45]_S$ layup. 183

LIST OF FIGURES CONTINUED

Figure Page

108. A scatter plot of the HOCV prediction results for the separate AE and GUW models for the $[90_4]$ layup. 184

109. A scatter plot of the HOCV prediction results for the combined AE and GUW models for the $[0/90]_S$ layup. 187

110. A scatter plot of the HOCV prediction results for the combined AE and GUW models for the $[90/0]_S$ layup. 188

111. A scatter plot of the HOCV prediction results for the combined AE and GUW models for the $[0/90/\pm45]_S$ layup. 188

112. A scatter plot of the HOCV prediction results for the combined AE and GUW models for the $[90_4]$ layup. 189

113. An absolute residual error plot for the $[0/90]_S$ model HOCV results. 190

114. An absolute residual error plot for the $[90/0]_S$ model HOCV results. 191

115. An absolute residual error plot for the $[0/90/\pm45]_S$ model HOCV results. 191

116. An absolute residual error plot for the $[90_4]$ model HOCV results. 192

117. A scatter plot of the HOCV prediction results for the layup independent model with no interaction function applied to the AE data. 197

118. A scatter plot of the HOCV prediction results for the layup independent model with interaction function $f_1(E_L, E_B)$ applied to the AE data. 198

119. A scatter plot of the HOCV prediction results for the layup independent model with interaction function $f_2(E_L, E_B)$ applied to the AE data. 198

120. An absolute residual error plot for the HOCV results of the layup independent model with no interaction parameters. 199

LIST OF FIGURES CONTINUED

Figure Page

121. An absolute residual error plot for the HOCV results of the layup independent model with interaction function $f_1(E_L, E_B)$..... 199

122. An absolute residual error plot for the HOCV results for the layup independent model with interaction function $f_2(E_L, E_B)$. 200

123. A plot of cumulative variance against the number of principal components for each of the four layup datasets. 206

124. A plot showing changes in R^2_{adj}, RMSE and R^2_{HOCV} against the number of principal components used for the $[0/90]_S$ PCR models..... 208

125. A plot showing changes in R^2_{adj}, RMSE and R^2_{HOCV} against the number of principal components used for the $[90/0]_S$ PCR models..... 209

126. A plot showing changes in R^2_{adj}, RMSE and R^2_{HOCV} against the number of principal components used for the $[0/90/\pm45]_S$ PCR models..... 209

127. A plot showing changes in R^2_{adj}, RMSE and R^2_{HOCV} against the number of principal components used for the $[90_4]$ PCR models..... 210

128. A scatter plot of the HOCV prediction results for the combined AE and GUW in fatigue for the $[0/90]_S$ layup..... 216

129. A scatter plot of the HOCV prediction results for the combined AE and GUW in fatigue for the $[90/0]_S$ layup..... 217

130. A scatter plot of the HOCV prediction results for the combined AE and GUW in fatigue for the $[0/90/\pm45]_S$ layup. 217

131. An absolute residual error plot for the HOCV results of the $[0/90]_S$ fatigue model..... 218

132. An absolute residual error plot for the HOCV results of the $[90/0]_S$ fatigue model..... 219

LIST OF FIGURES CONTINUED

Figure Page

133. An absolute residual error plot for the HOCV results of the $[0/90/\pm45]_S$ fatigue model..... 219

134. Measured modulus change against predicted modulus change when the $[0/90]_S$ static model regression coefficients were applied to the $[0/90]_S$ fatigue testing dataset. 222

135. Measured modulus change against predicted modulus change when the $[90/0]_S$ static model regression coefficients were applied to the $[90/0]_S$ fatigue testing dataset. 222

136. Measured modulus change against predicted modulus change when the $[0/90/\pm45]_S$ static model regression coefficients were applied to the $[0/90/\pm45]_S$ fatigue testing dataset. 223

137. Residual errors when the $[0/90]_S$ static model regression coefficients were applied to the $[0/90]_S$ fatigue dataset..... 223

138. Residual errors when the $[90/0]_S$ static model regression coefficients were applied to the $[90/0]_S$ fatigue dataset..... 224

139. Residual errors when the $[0/90/\pm45]_S$ static model regression coefficients were applied to the $[0/90/\pm45]_S$ fatigue dataset. 224

NOMENCLATURE

G_{IC}	Mode I fracture toughness (opening)
G_{IIC}	Mode II fracture toughness (forward shear)
G_{IIIC}	Mode III fracture toughness (inter-laminar torsion)
V_f	Fiber volume fraction
R	Fatigue stress ratio
σ_{min}	Minimum fatigue stress
σ_{max}	Maximum fatigue stress
n	Number of fatigue cycles
N	Number of fatigue cycles to failure
S_0	First symmetric, in-plane wave mode
A_0	First antisymmetric, out-of-plane wave mode
$\hat{Y}$	Response variable vector
β_i	Multivariate linear regression coefficients
X_i	Multivariate linear regression predictor variables
ϵ	Mean zero random error term
F	F-statistic
R^2	Coefficient of determination
R^2_{adj}	Adjusted coefficient of determination for multivariate analyses
m	Number of observations
p	Number of predictors
TSS	Total sum of squares
RSS	Residual sum of squares
VIF	Variance inflation factor
$\underline{W}$	Matrix of principal component analysis loading vectors
$\underline{X}$	An dataset with m observations and p predictors
$\underline{T}$	A $m \times p$ dataset in principal component coordinate space
$\hat{\beta}_{PCA}$	Vector of regression coefficients from a principal component regression
R^2_{HOCV}	Average of R^2 values from hold out cross validation tests
E_L	In-plane longitudinal laminate modulus (GPa)
E_B	Out-of-plane longitudinal laminate bending modulus (GPa)

ABSTRACT

Since the turn of the century, wind turbines have been rapidly growing in size and are projected to continue growing as the technology develops. These increases in size have led to increased failure rates of the glass fiber composite turbine blades. Because of this, it is of utmost importance to understand failure mechanisms in glass fiber composites and investigate new approaches to predicting failures. This has led to advancements in structural health monitoring of large composites structures by applying sophisticated sensing technologies, in attempts to evaluate material damage states and predict structural failures before they occur. This research has taken a novel approach to apply multiple ultrasonic monitoring techniques, in the form of acoustic emission and guided ultrasonic waves, simultaneously to the mechanical testing of glass fiber reinforced composite laminates. Testing of the composite laminates was conducted in the form of increasing load-unload-reload static tension tests and tension-tension fatigue tests, to measure modulus degradation of the laminates while applying the monitoring techniques. Acoustic emission was used to detect damage events that occurred within laminates in real-time and guided ultrasonic waves were applied periodically to the laminates to observe changes in wave propagation and relate back to damage severity within the laminates. Furthermore, the acoustic emission and guided ultrasonic wave datasets were combined and used to train multivariate regression models to predict modulus degradation of the laminates tested, with no prior knowledge of the laminates' loading histories. Overall, the predictive models were able to make good predictions and showed the potential for combining multiple monitoring techniques into singular systems and statistical predictive models. This research has shown that the combination of the two measurement techniques can be implemented for more accurate and reliable monitoring of large composite structures than the techniques used individually, with minimal additional hardware. Ultimately, this research has paved the way for a new form of smart structural health monitoring, with superior predictive capabilities, which will benefit the renewable energy through reducing maintenance and repair costs and mitigating the risk of wind turbine blade failures.

INTRODUCTION

In modern industries, fiber reinforced composites are being utilized more and more for large structures. For example, new commercial aircraft, such as Boeing's 787 and Airbus' A380, are primarily constructed from carbon fiber reinforced polymer laminates (see Figure 1). The construction industry has also taken to applying low-cost glass-fiber composite materials to bridge structures, due to their high specific strength allowing for easier transport and installation. In particular, the renewable energy industry has played a huge role in implementing glass-fiber composites for vital structural components, such as turbine blades, because of their low cost, high specific strength, resistance to environmental effects and the ability to manufacture laminates into complex geometries. The inherent anisotropy of fiber reinforced composite laminae allows composite laminates to be tailored to exhibit desired strengths, stiffnesses and deflections to enhance and optimize structural designs.

The wind energy industry has shown a particular interest in glass fiber reinforced polymers for the construction of wind turbine blades and have made significant efforts to reduce their cost of manufacturing. Over the past several decades, wind turbines have been rapidly increasing in size, with rotor diameters surpassing 125 m on 5 MW turbines, and sizes projected to reach over 250 m in the not so distant future (see Figure 2) [1]. This is based on the philosophy that larger turbines are cheaper overall, because a substantial portion of their costs are related to the number of turbines that need to be installed and maintained i.e. only half as many turbines have to be installed if they produce double the amount of power [2]. Despite this, increased failure rates appear to be

counterbalancing the benefits of large turbines (see Figure 3). This has been a commonly occurring problem. Caithness wind farm in the UK had reported 345 blade failures up until 2016, suggesting that wind turbines could be a huge financial risk for investors [3]. These unexpected premature failures require reactive maintenance, which deviate from typical six month maintenance schedules [4], and significant down time, which can be very costly to the owners and operators. These kind of failures result in operation and maintenance (O&M) costs that are a substantial portion of wind turbine life cycle costs [5]. The UK aims to reduce wind turbine life-cycle costs by at least 30% by the end of 2020 [6].

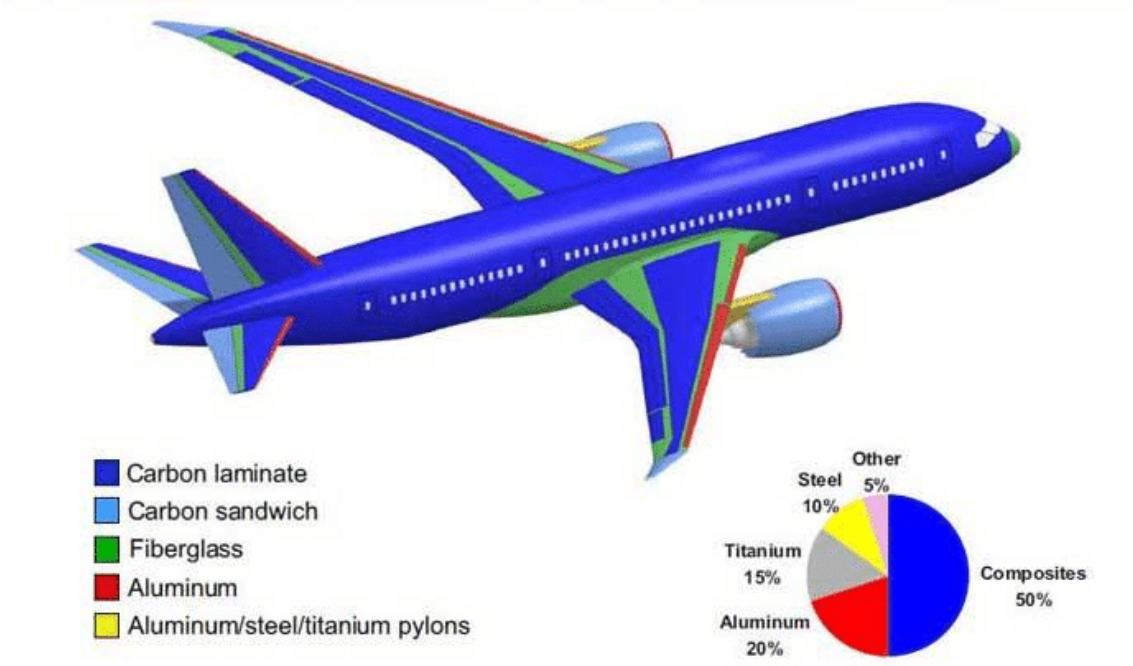


Figure 1: An example of how Boeing utilized composite materials for the construction of their 787 aircraft [7].

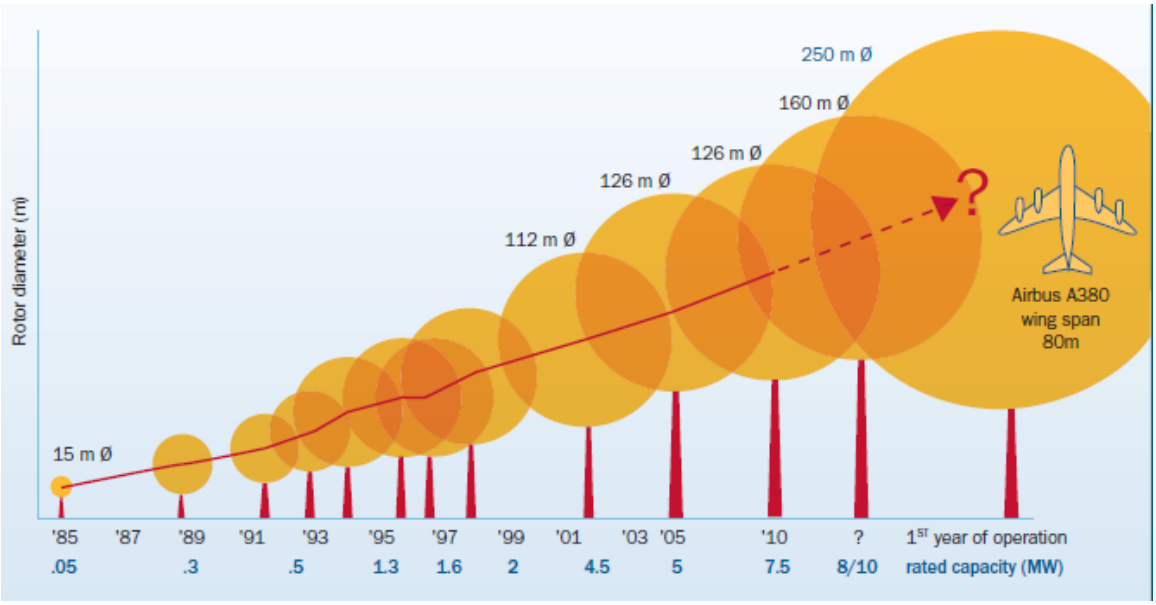


Figure 2: The rapid increase of wind turbine rotor diameters and projections for the future.*



Figure 3: An example of a significant wind turbine blade failure common in the industry.†

* https://gtms1314.wordpress.com/2013/03/18/cost-analysis-of-a-wind-turbine/
† https://basinelectric.wordpress.com/2009/06/04/cause-still-unknown-for-broken-blade-on-wind-turbine/#jp-carousel-1165

There are several key areas that are being continuously investigated to reduce wind turbine O&M costs; material selection and design, manufacturing techniques, the effects and causes of manufacturing flaws and defects, non-destructive inspection (NDI) and structural health monitoring (SHM). All of these areas require significant understanding to allow for efficient designs which are light-weight, but can also withstand long periods of time exposed to harsh environments and loading conditions. Typically, these understandings start with material characterization at small scale coupon levels and the scale is gradually increased as well as structural complexity, with elements, details, sub-components and finally full-scale structures, as displayed in Figure 4. Significant time and costs are also incurred throughout this vital process.

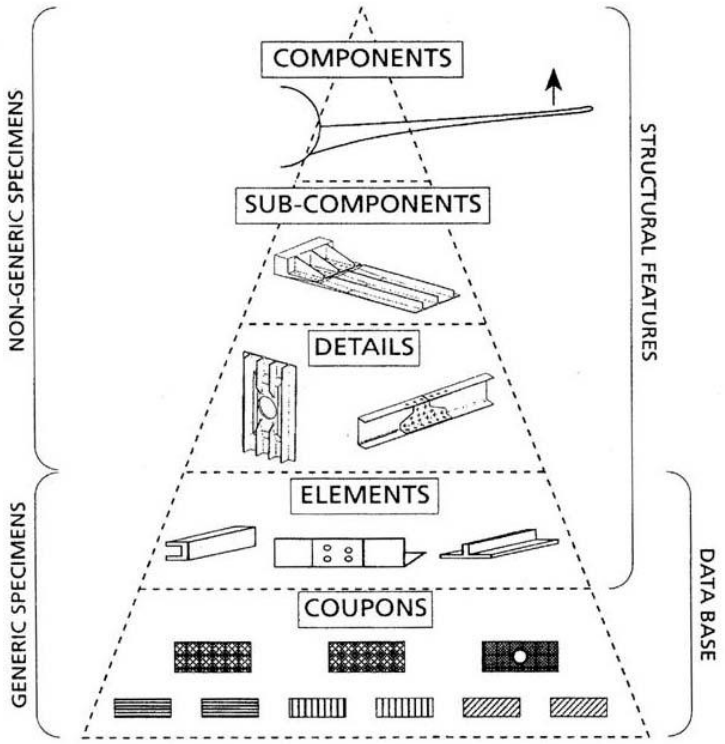


Figure 4: The general approach for designing and testing materials for composite structures [8].

The research presented in this dissertation primarily concentrates on structural health monitoring techniques at the baseline coupon level and aims to make notable steps forward in the vital understanding of suitable and reliable SHM techniques, in the hopes that the knowledge gained can be progressed to larger scales, potentially reduce O&M costs and increase wind turbine reliability. In particular, the research presented herein aims to combine two significant SHM techniques, acoustic emission (AE) and guided ultrasonic waves (GUWs), into a singular, more cost effective and reliable standalone system.

This dissertation presents an in-depth investigation into the many aspects of understanding and techniques required for accurate, reliable and cost effective SHM of large composite structures, beginning with an extensive literature review covering the following things:

- Understanding damage modes and progressions related to composite materials and how they lead up to life-cycle analyses, with regards to fatigue loading scenarios.
- Structural health monitoring and the current methods available and how they are being effectively applied to large composite structures.
- The current state of research with regards to acoustic emission and guided ultrasonic wave techniques and how they can be implemented to detect varying damage types and ultimately overall damage state and life predictions in composite laminates; particularly their current benefits and limitations.

- The statistical modeling approaches that have been taken in current SHM techniques and how they have been applied to AE and GUW research to determine the best techniques to apply to this research to obtain accurate and reliable results.

The extensive background research lead to a variety of experimental testing techniques that have been implemented to produce, measure and evaluate varying damage states and degrading properties, such as residual modulus and remaining fatigue life, in glass fiber composite laminates at the coupon level, whilst applying AE and GUWs simultaneously. Finally, the test data produced from the AE and GUW techniques was combined and used to train statistics-based prediction models to ultimately predict residual moduli and the remaining usable life of laminates. The effectiveness and areas for possible improvements to the models were thoroughly evaluated.

Initially, experiments implemented static tensile testing to develop suitable testing procedures for measuring changing laminate properties and appropriately setting up and applying the two on-line damage monitoring techniques to obtain repeatable and reliable data. These initial testing phases served as a proof of concept for constructing and refining the statistical predictive models, before continuing to tension-tension fatigue testing, due to it being a more complex, costly and time-consuming testing technique. New statistical models were then produced and evaluated to ultimately determine if the techniques developed can be applied effectively to larger composite laminates and structures, as suggested by Figure 4. Finally, this research provides detailed suggestions

of concepts that could be used to apply the techniques developed to larger, more complex laminates, with more complex sensor arrays and more realistic loading scenarios.

To summarize, the overall goals of this research are as follows:

- Understand and evaluate the current state of research with regards to SHM and on-line damage monitoring (particularly AE and GUWs) with composite laminates and structures and their limitations.
- Combine AE and GUWs through static and fatigue test methods to evaluate the health of composite laminates.
- Combine the data of the two techniques for accurate evaluation and prediction of changing laminate properties and health.
- Increase the reliability of on-line damage monitoring techniques with minimal additional complexity and cost.

The broader impacts of the research proposed will be to provide important steps forward in the SHM and reliability of composite structures, particularly wind turbine blades. Accurate SHM is of vital importance to both reducing costs and increasing safety and reliability as the size of wind turbines rapidly increases.

Improvements in AE and GUWs as an in-situ damage monitoring techniques will mainly influence maintenance costs because they have the potential to reduce or even completely eliminate the requirement for regular service intervals. Accurate monitoring could simply sound alarms as and when maintenance or repair is needed. Also, the ability of AE to determine the location of damage events means that areas of significant damage

can be pinpointed for repair, rather than having to conduct costly ultrasounds over entire structures.

More efficient damage monitoring would also lead to advances in the development and design of blades. It would reduce the need to over-engineer them, resulting in lighter and more efficient turbines. Ultimately, improvements in damage monitoring will aid in preventing the catastrophic failure of turbine blades and make wind an even more viable form of renewable energy for the future.

BACKGROUND

As stated previously, a thorough literature review has been conducted to fully understand previous research that has been conducted, its benefits and limitations and to find a novel approach to apply acoustic emission and guided ultrasonic waves to composite laminates for SHM purposes. Initially, it is important to understand how damage presents itself in composite laminates and how this understanding has been applied to real life loading scenarios, such as fatigue, and how it has paved the way for sophisticated SHM techniques. Acoustic emission and guided ultrasonic waves were the two techniques selected for this research and with them comes a whole host of advanced mathematical methods and analysis techniques for a whole variety of research areas, such as damage classification, location, predicting changing laminate properties and various compensation strategies associated with them. Ultimately, this literature review is the cornerstone to why and how this research was conducted, as well as its importance to the renewable energy industry.

Damage in Composites

Understanding how damage manifests itself in composite laminates is of great importance to predicting and monitoring damage to evaluate changing laminate properties and predict ultimate failure. In the context of long fiber reinforced polymer composites (the concentration of this research), laminates are constructed from layers of fibers of varying orientation (plies or laminae) and are constrained by a polymer matrix material. The two constituents (fibers and matrix) typically have noticeably different

properties and failure characteristics. The interactions and load sharing relationships between the constituents then lead to a wide variety of damage mechanisms that can become hard to predict and assess, especially with the inherent anisotropic nature of laminates. For example, the fibers can prevent cracks propagating within the matrix material and also blunt them. This results in the ability of composite laminates to tolerate large amounts of damage, typically in the form of micro-cracks, before ultimate failure.

Thermoset polymers, such as epoxies, are regularly used as a matrix materials in fiber reinforced polymers (FRPs). They are relatively brittle and exhibit lower strains to failure than typical fiber materials, like glass or carbon. These properties result in the most common damage mechanism being matrix cracking, that generally signifies the initiation of damage within laminates. The early onset of matrix cracking can be influenced by many factors, such as load orientation, defects (voids, contaminants or inclusions) and other stress concentrations, such as fibers (see Figure 5), fabric stitching, ply-drops or other already existing damage sites. In a homogenous, brittle, thermoset polymer, a single crack would be able to propagate through the material, resulting in ultimate failure, but, as was stated previously, fibers can act as barriers to crack propagation within the matrix. This means that matrix cracking occurs well before the ultimate failure of FRPs. Figure 6 displays this phenomenon as well as other commonly observed micro-damage types.

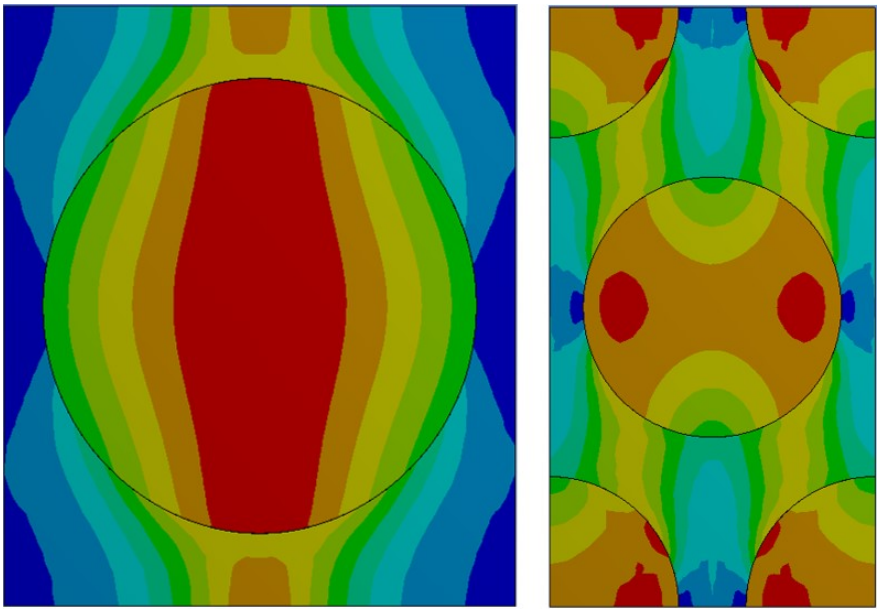


Figure 5: Square (left) and hexagonal (right) fiber/matrix representative volume elements (RVEs) with longitudinal strain applied to them to show stress concentrations.

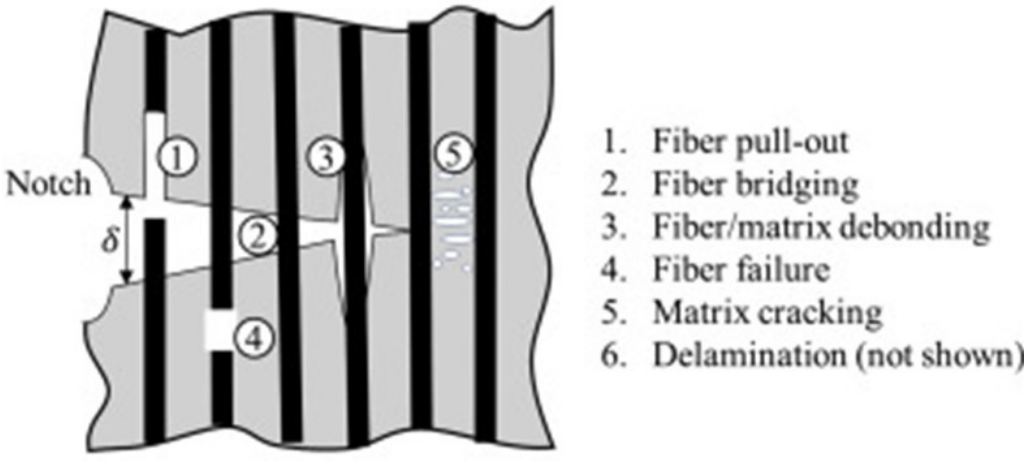


Figure 6: Diagram displaying a variety of micro-damage modes commonly observed in FRP laminates [9].

Figure 6 also shows that fibers naturally only prevent matrix cracks from propagating in one direction. Generally, this leads to matrix cracks following the directions of the fibers, which leads to some of the other damage modes displayed in

Figure 6. Fiber pullout and fiber/matrix debond are types of interface damage originating from the adhesive bond between the fibers and the matrix material. More often than not, the fiber/matrix interface is stronger than the matrix itself, so interface damage usually manifests itself after matrix cracking, or may be caused by the propagation of matrix cracks. Fiber/matrix debonds transpire from stresses normal to the fiber direction, whereas fiber pullouts occur because of shear stresses between the fiber and the matrix. Fiber pullout and fiber/matrix debonding are very similar damage types, which can make it difficult to differentiate between them, especially if they proceed from the propagation of matrix cracks. To identify these types of micro-damage types, high magnification microscopy techniques, such as scanning electron microscopy (SEM) or transmission electron microscopy (TEM), are required to observe them.

Fiber failure is perhaps the most significant type of damage exhibited by composite laminates. Of the two constituent materials, fibers are far stiffer and stronger, meaning they hold the majority of the stresses applied to laminates, particularly if the loading direction is the same as the fiber direction. In a lot of cases, fiber failure can signify the onset of global laminate failure. As fibers begin to break, they transfer stresses to neighboring fibers, which are then brought closer to their ultimate strength, as well as reducing the global laminate stiffness and releasing significant amounts of strain energy, causing more damage, resulting in a “cascading” effect (see Figure 7).

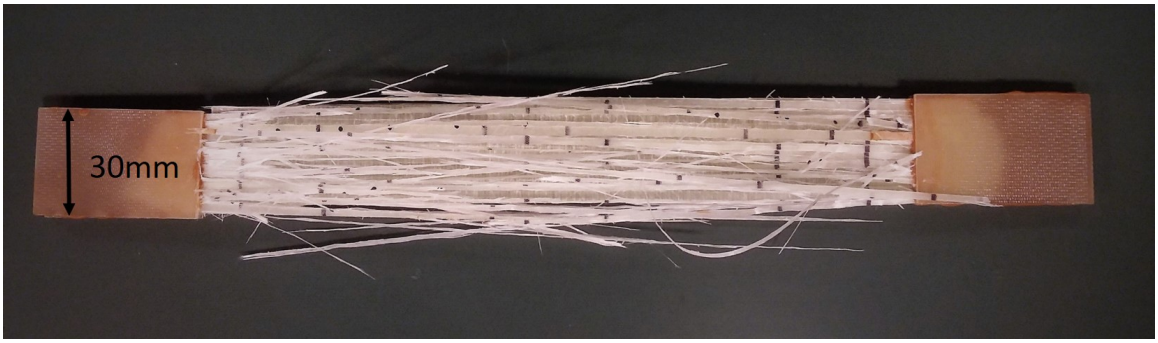


Figure 7: A GFRP tensile test coupon that displayed significant strain energy release at ultimate failure, due to longitudinal fiber tows failing in a cascading manner.

The micro-damage types described above can lead to other macro-damage types, such as delaminations. Delaminations are large-scale debonds between laminate plies, generally caused by inter-laminar shear stresses, under normal loading conditions. They are a result of the propagation of matrix cracking and interface damage along the length and width of laminates. Fiber bridging may also occur between delaminated plies. Delaminations are also a significant indicator for the onset of global failure of laminates. Plies within the laminate are no longer able to transfer and share stresses between each other through inter-laminar shear, so stresses are only applied to the stiffest plies i.e. the ones with fibers oriented in the loading direction. Delamination fracture toughness's are characterized by three modes; mode I (G_{IC}), mode II (G_{IIC}) and mode III (G_{IIIC}). Mode I being the peeling/opening mode, mode II is the forward shear mode and mode III is an inter-laminar torsional mode (see Figure 8). Depending on the stress state of a laminate, delaminations could manifest themselves due to any or a combination of these laminate properties. To determine these laminate properties there are a whole host of mechanical test methods, such as double cantilever beam (DCB), end-notch-flexure (ENF) and overlap shear.

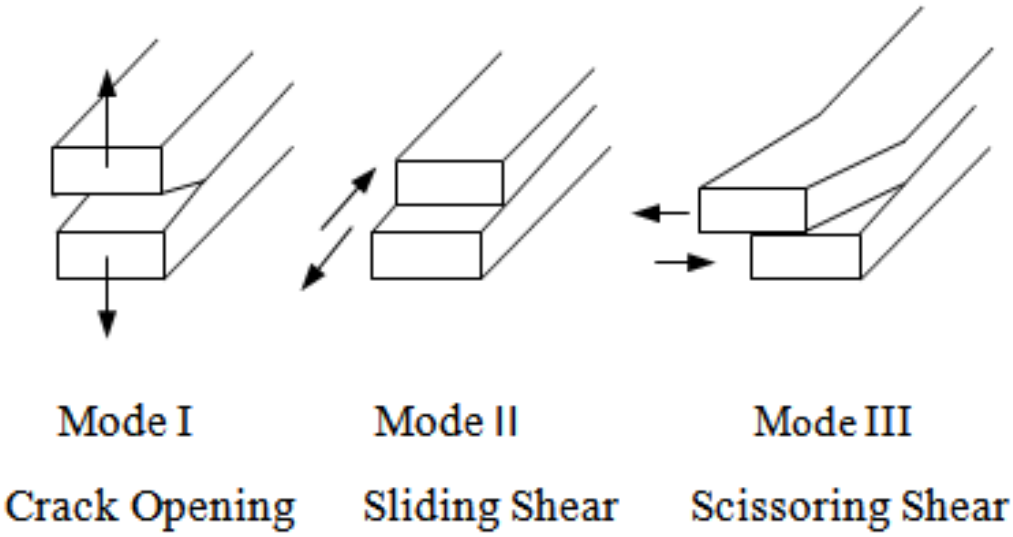


Figure 8: An illustration of the three delamination modes typically observed in composite laminates.[‡]

When considering the damage mechanisms described above separately, they can be relatively simple to understand, but in realistic loading scenarios they can seldom be considered separate, since they interact in very complex ways. The initiation and progression of damage within a laminate affects its global properties and load carrying capacity. The typical progression of damage in composite laminates was well described by Reifsnider [10]. Figure 9 shows how damage initiates and progresses over the life of a laminate. Initiation is signified by matrix cracking which leads to interface failures and the coalescence and propagation of cracks to form delaminations. The delaminations grow and begin to cause localized fiber failures and eventually fracture or global failure of the laminate. This progression and coalescence of damage can be very difficult to predict over the life of laminates, especially in fatigue loading scenarios.

[‡] http://article.sapub.org/10.5923.j.ijme.20140403.06.html

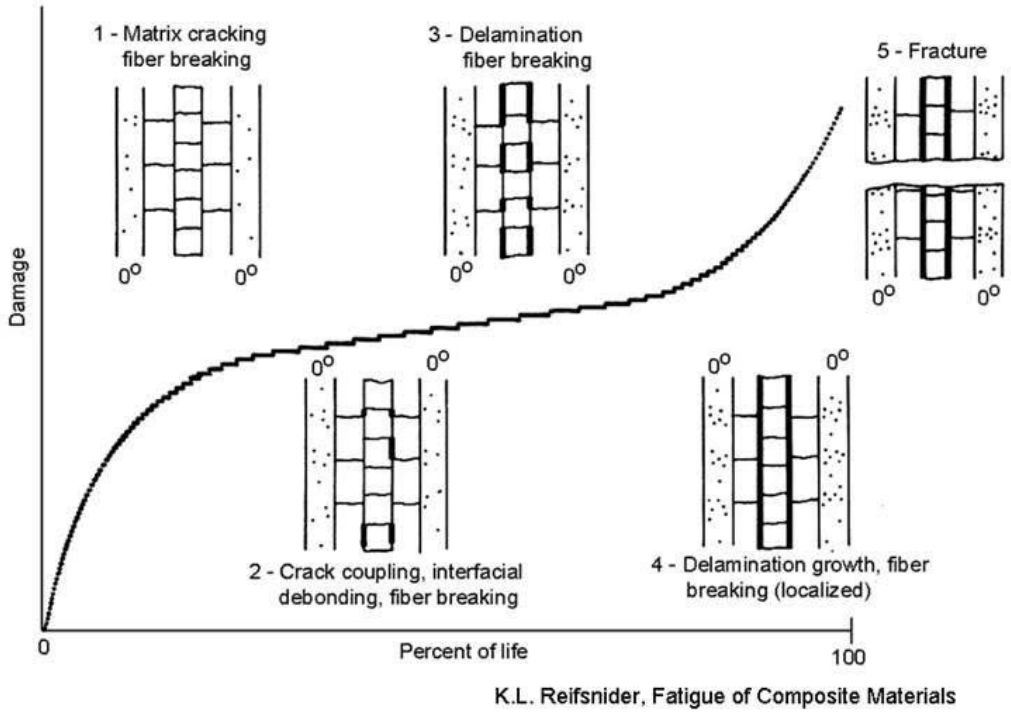


Figure 9: Damage initiation and progression over the life of composite laminates, as presented by Reifsnider.

Fatigue Models

Incorporating laminate fatigue characteristics into structural design can be a very complex task. Fatigue life can be hard to predict for different laminates, as well as the laminate properties that degrade due to fatigue, such as residual modulus and strength. Many laminate and loading parameters can affect the fatigue life, including (but not limited to) fiber type and fabric architecture, matrix type, fiber/matrix interface properties, laminate stacking sequence, manufacturing quality (fiber volume fraction, V_f, defects, porosity etc.), loading spectrum and multiaxial stress states. Because of this, significant amounts of mechanical testing is usually required to determine the fatigue properties of specific laminates.

S-N curves are perhaps the simplest way to display and determine fatigue properties of a given laminate at a given stress ratio (R), where R is the minimum stress (σ_{min}) divided by the maximum stress (σ_{max}). Fatigue test data for given stress ratios are plotted as σ_{max} (or S) against number of cycles to failure (N) on a logarithmic scale (see Figure 10). The experimental data is typically fit in the form of Equation 1, an exponential function, where A is the intercept at one cycle and c is the exponential constant. It should be noted the A often differs from the ultimate strength of a laminate, but there are other equations used to account for this, as well as the inherent statistical scatter observed in fatigue test data. Residual modulus and strength data are plotted in the same manner [11]. The downside to S-N curves is that they are only applicable to the laminate tested and the stress ratio used. Common stress ratios are tension-tension ($R = 0.1$), tension-compression ($R = -1$) and compression-compression ($R = 10$).

$$S = AN^{-\frac{1}{c}} \tag{1}$$

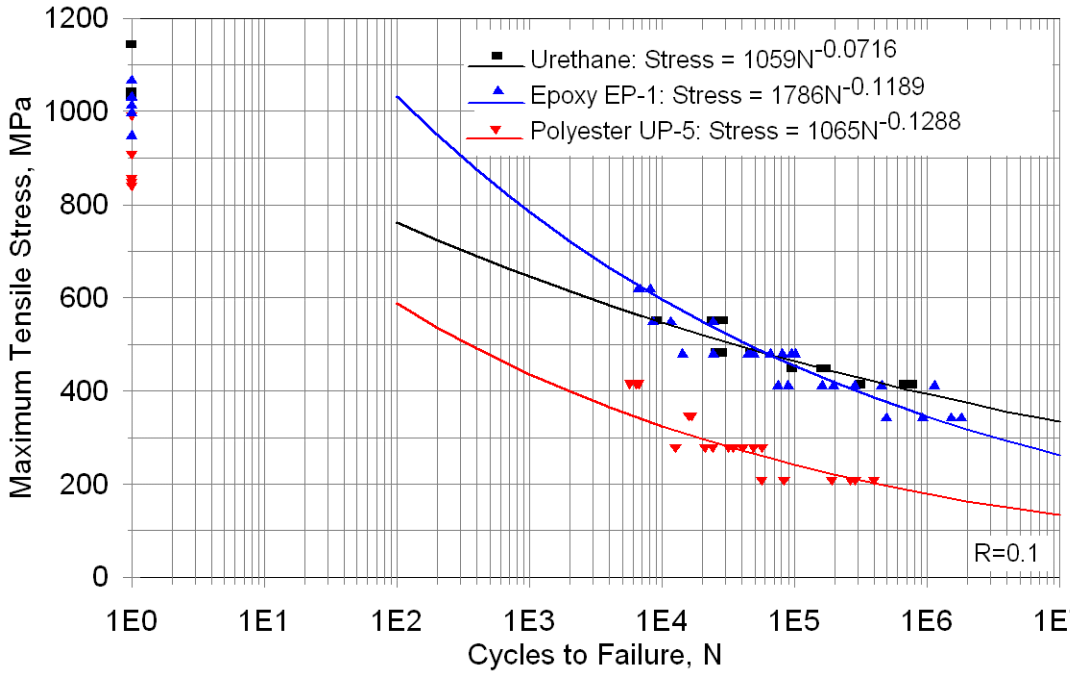


Figure 10: An example S-N curve showing differences in fatigue properties for three different matrix materials [12].

As an extension to S-N curves, constant life diagrams (CLDs) are commonly used to display data from multiple R values (see Figure 11). Alternating stress is plotted against mean stress (σ_{mean}) for all R values and data points for every decade of fatigue life. These plots can be interpolated to determine fatigue lives at different stresses and R values, to a reasonable degree of accuracy, if required. Researchers have also attempted to implement polynomial interpolations between R values to obtain better results, with limited success [13]. CLDs have also been applied to predict the fatigue response of laminates subjected to more complex load spectra, which are generally used to simulate more realistic loading scenarios. Methods such as rainflow counting and Palmgren-Miner's damage summation rule have been applied to CLDs from axial test data with relative success [14].

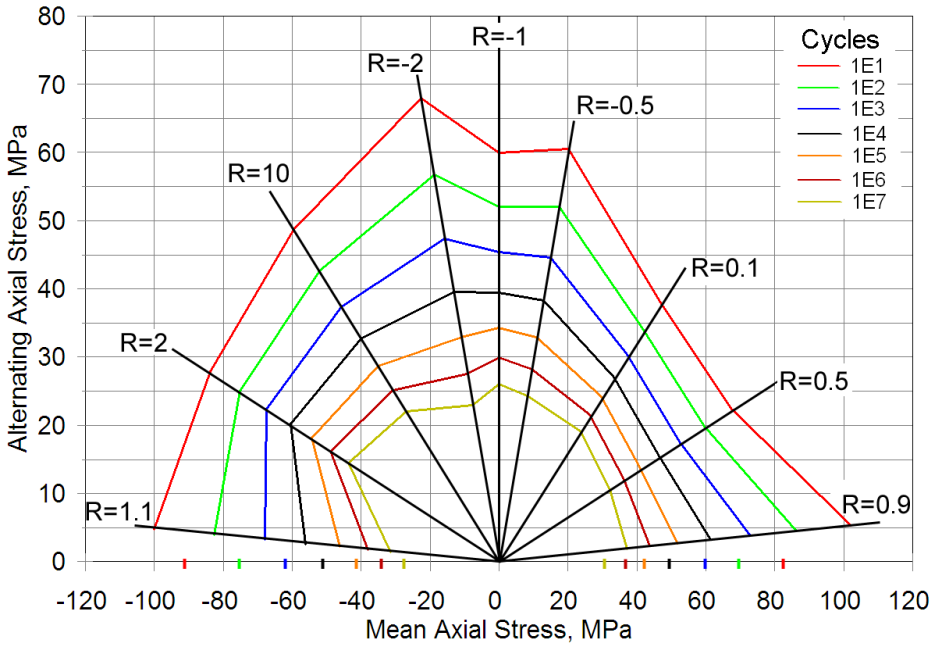


Figure 11: An example of a CLD for many R values from axial stress fatigue data [12].

In the case of isotropic materials, such as metals, fatigue responses to multiaxial stress states can be determined relatively easily through principal stress tensor transformations. With anisotropic laminates, predicting the effect of multiaxial stress states on fatigue responses is much more complex. Initially, to determine multiaxial fatigue responses, a significant amount of test data was required [15]. Since then, other methods have been developed, such as applying composite laminate failure tensors which include *R* values and numbers of cycles, almost like a combination of failure tensors and the Palmgren-Miner rule [16]. Alternatively, Sun et al. applied Puck's criterion in their attempts to predict the effects of multiaxial stress states [17].

The techniques described above have been built upon in attempts to remove the layup dependency. Similar degradation rules have been applied to laminates on a ply-by-ply basis, accounting for the varying stress distributions. Loads are applied on either a

cycle-by-cycle basis or as blocks of cycles. Degradation rules are then applied to the laminate plies, both in the form of moduli degradations and strength degradations. When the applied stress is equal to the residual strength of the laminate, it has reached ultimate failure [18-21]. These methods were further extended to complex geometries through finite element modeling for a notched sample [22-25]. From this, similar tools such as the "Super Mic-Mac" [26] and "MAE" models [27] have also been developed with attempts to reduce testing time through micromechanical assumptions and accelerated test methods. Sihn et al. also incorporated creep behavior into their model for a more universal tool [27]. As a way to make these methods more realistic, Naderi et al. used finite element modeling to add more variability to the material properties [28]. A Gaussian distribution was applied to the strength and stiffness properties element-by-element, so that elements degrade at different rates, similar to initial flaws within a laminate. Computationally, these methods are highly inefficient, so Stens et al. applied classical laminate theory (CLT) with their FEA models to reduce the number of elements that the degradation rules had to be applied to [29]. As well as being computationally inefficient, these modeling approaches require significant amounts of experimental testing to construct them. S-N curves, residual strength curves and residual stiffness curves are required for each ply orientation.

To reduce the reliance on empirical methods and the requirement for large amounts of test data, researchers have tried to evaluate the problems on a more theoretical basis, For example, applying various energy methods through static strength

test data [26, 30]. Alternatively, continuum damage mechanics methods have shown encouraging results, that require far less experimental testing [31].

In summary, there are still no global methods for determining laminate fatigue responses from given constituent properties and layups, which do not require significant amounts of experimental testing and validation. In light of this, researchers have found value in simply tracking the progression of stress-strain histories through methods like observing the migration of hysteresis loops [32] or using embedded sensing methods, such as fiber Bragg gratings, to monitor strain energy release rate throughout the lives of laminates [33] and determine when they might fail. Ultimately, the complexity of determining the fatigue responses of laminates has paved the way for using novel sensing technologies to monitor laminates throughout their life to evaluate their health and predict the probability of failure before it occurs.

Structural Health Monitoring

As has been discussed, degradation of FRP laminates due to fatigue can be very hard to predict, especially when scaled up to full-size structures, such as wind turbine blades. To complicate things, large composite structures also have to endure other unknowns, like manufacturing defects and unexpected loading scenarios. For this reason, structures are inspected at regular intervals to ensure they have not accumulated large amounts of damage and are ultimately healthy enough to continue operating. In this case, non-destructive inspection (NDI) techniques must be applied, in the form of visual observations, ultrasonic inspection or other methods. These methods are often costly due to the skills involved, expensive equipment and downtime from normal operations. Wind

turbines are especially hard to access, because of their size and because they are often located in remote areas, especially off-shore wind turbines.

Structural health monitoring (SHM) refers to the implementation of sensors to a structure to monitor load histories or actively monitor damage as it is occurring in real-time. Ultimately, the methods seek to apply cost-effective ways to transfer from time-based maintenance philosophies to cost-based maintenance philosophies [34]. A variety of sensors may be used to measure the dynamic response of the structure, whether it is on a micro scale or a macro scale. As with all sensing techniques, a wide array of complex signal processing methods and statistical analyses are usually required [34]. Reliability of SHM systems is also of great importance, as false negative alarms could be very costly. Alternatively, over-reliance on them could result in costly unexpected failures.

Currently, the SHM techniques applied to commercial wind turbines are relatively basic. The most common technique is simply monitoring the wind speed, rotor speed and power generation over the life of a turbine [35]. This at least gives a good indication of the loading history that blades have experienced over their lifetime. Most modern SHM techniques are more complex and are still in early phases of research and development and are yet to be deployed to commercial applications.

Fiber Bragg gratings are seeing significant research efforts to monitor complex strain distributions and histories across composite structures. Fiber Bragg gratings consist of optical fibers, which can be embedded in laminates, to detect strain by the changes in wavelength of visible light transmitted through them. In particular, they can be applied to detect natural frequencies and changing mode shapes of large structures to evaluate their

health [36]. An alternative method, developed by NASA, is comparative vacuum monitoring [37]. It implements a series of alternating vacuum and air-filled fine "channels" on the surface of a laminate. When a crack forms across the channels, air can flow between them, which is monitored by flow sensors. This method is capable of detecting crack initiation and growth in real-time.

By far the most researched SHM techniques are ultrasonic methods. This is due to the ability of ultrasonic waves to propagate long distances through structures [38]. Both active and passive approaches are being developed. For example, acoustic emission (AE) is a passive approach, as it detects ultrasonic waves originating from cracks initiating and propagating in real-time. Currently, AE has not been used for commercial wind applications, but several full-scale monitoring tests have been conducted, which were mainly concentrated on detecting the location of damage events [35, 39, 40], despite there being more sophisticated methods for evaluating damage and the health of the structure. This is described in more detail in the proceeding sections.

Guided ultrasonic waves (GUWs) are an example of an active ultrasonic SHM technique. It is a pitch-catch sensing method in which ultrasonic waves are applied to a structure by piezoelectric actuators and detected by other piezoelectric sensors [41]. The propagation of the waves is affected by damage within the structure and can ultimately be used to detect different types of damage and the overall health of the structure. Currently, GUWs are still very much in the research phase of implementation, but have been applied to structures such as aircraft fuselages to evaluate the feasibility of the technique [42]. More details on GUWs are provided in the proceeding sections.

Overall, sophisticated SHM techniques with regards to composite structures are still a long way from being implemented into commercial applications. The reasons why are primarily due to cost and reliability. Currently, the methods described above are too costly and not developed enough to make accurate predictions on the health of large composite structures. There are still many hurdles that need to be overcome before they are economically viable. This is the main driving force for this research.

Acoustic Emission

One of the primary SHM methods that was applied to this research was AE. It is an in-situ damage monitoring technique, which implements arrays of piezoelectric sensors attached to a structure's surfaces to detect stress waves originating from damage events (matrix cracking etc.), as they occur in real time. These stress waves typically consist of multiple wave modes, with the first order extensional (in-plane symmetric, S_0) and first order flexural (out-of-plane antisymmetric, A_0) modes considered to be of most importance (see Figure 12) [43]. Other higher order wave modes, including shear, do exist, but their amplitudes are typically too small to be detected by piezoelectric sensors.

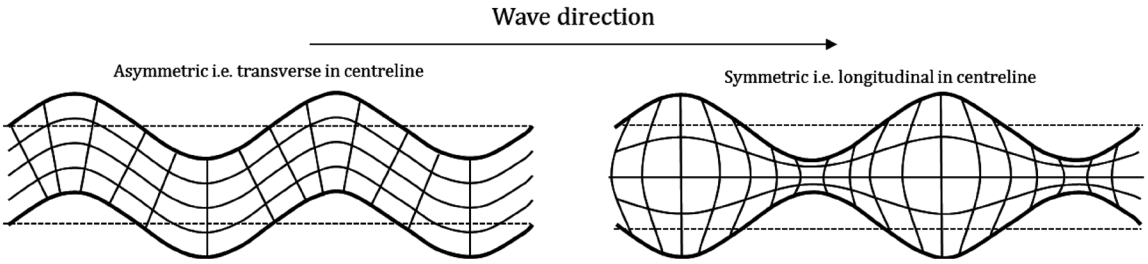


Figure 12: A diagram showing the primary symmetric (S_0) and antisymmetric (A_0) waves mode shapes for plates.[§]

As mentioned previously, AE's primary use, when applied to large composite structures, has been to detect and locate damage events. Location of these damage events can be determined through wave velocities and differences in times of arrivals to each sensor. In-plane elastic wave velocity is directly related to the in-plane stiffnesses of composite laminates (A_{11} and A_{22} terms from CLT) and are non-dispersive. Conversely, out-of-plane wave velocity is related to the out-of-plane stiffness of composite laminates (D_{11} and D_{22} terms from CLT), but they are frequency dispersive, meaning that their velocities are frequency dependent. For this reason, the S_0 wave mode is of most importance to AE monitoring, but separating the two modes can be difficult, although the S_0 mode typically has a much higher velocity than the A_0 mode. Determining the location of origin of damage events in one dimension is simple. The difference in time of arrival between two sensors can be used to linearly locate the damage event, based on the wave velocity between the two sensors. For composite laminates, locating damage events in two dimensions is much more complex, due to the anisotropic nature of composite laminates. With an isotropic plate, only three sensors would be required to locate damage

[§] http://www.mdpi.com/2076-3417/6/1/12/htm

events in two dimensions. The time differences between the three sensors can easily be used to triangulate the location, since the symmetric wave velocities are the same in every direction. This is not the case for composite laminates. Even if a quasi-isotropic layup is used, wave velocities still exhibit a high dependence on their direction of propagation. The most common way to combat this phenomenon is to use a technique called “delta-t mapping” [44]. Delta-t mapping implements pencil lead breaks (PLBs), a common technique used for checking sensor operation, over the surface of the laminate at predetermined points to measure differences in time of arrival between the sensors (see Figure 13). These data points are then used for interpolation when real damage events are being recorded. As one might expect, delta-t mapping is a laborious and inefficient procedure.

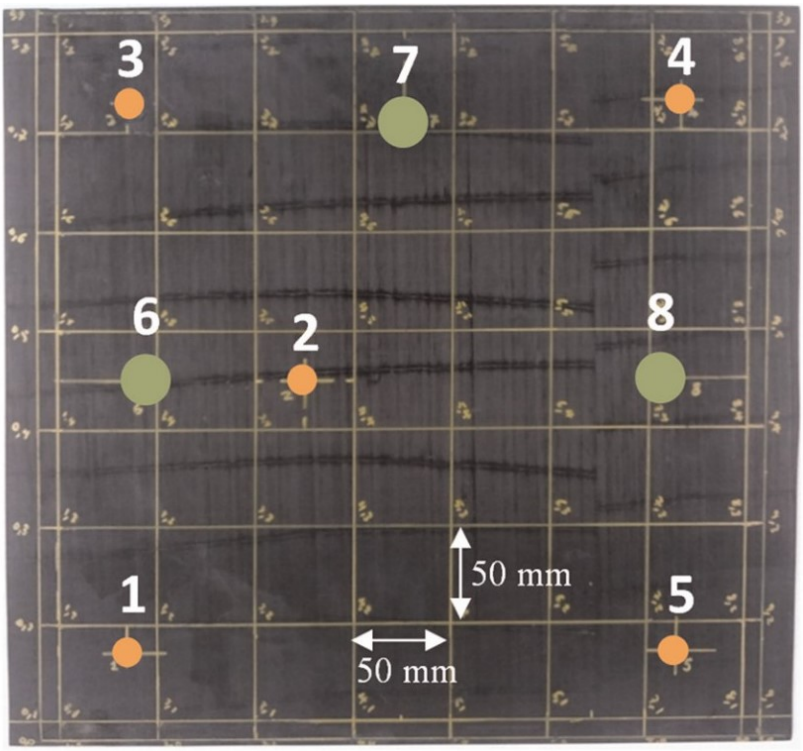


Figure 13: Delta-t mapping being used for two-dimensional damage event locating.

With regards to composite materials research, AE technology has served two main purposes:

1. Damage classification in the material characterization phases of research, to determine the extent of matrix cracking, interface damage and fiber breakage etc.
2. Relating AE data to global laminate properties, such as residual strength/stiffness and remaining fatigue life, for SHM applications.

Damage classification techniques typically concentrate on analyzing waveforms originating from individual damage events, whereas the SHM research concentrates on waveform parameter trends and how they progress throughout the life of laminates, or combinations of the two.

Damage Classification

Damage classification with AE has seen extensive research efforts over the past two decades. Researchers have applied many different testing techniques, statistical analysis methods, finite element modeling and observation techniques with the aim of associating recorded damage events with specific damage modes, such as matrix cracking, interface damage, fiber breakage and delaminations. This research has typically been developed for material characterization purposes. For example, it may be useful to know how much fiber/matrix debonding is occurring within a laminate to test new fiber treatment methods or to assess fiber/matrix adhesion of a new matrix material.

Originally, single parameter methods were frequently used to differentiate between damage modes. Signal parameters, such as ringdown counts (the number of

times a waveform passes a specified threshold) [45-48], amplitude [49, 50], energy [51-53] and peak frequency [54, 55], can be extracted from event waveforms to classify them. Damage classification using single event parameters relies on separating events into "bins" of specific ranges for each given parameter. For example, peak frequency analyses classify damage events depending on what frequency range they fall into; lower frequencies are considered matrix cracking, mid-ranges are interface damage and high frequencies are fiber breakage, which are loosely based on constituent stiffnesses. Of course, these frequency ranges appear to be highly dependent on the constituent materials used and the test methods used to obtain them. Schuster summarized and averaged the frequency bins determined by several researchers to determine his own frequency ranges [56] (see Figure 14). Damage event amplitudes have been used in a similar way. Barre et al. defined low amplitude events as matrix cracking and high amplitude events as fiber breakage [49].

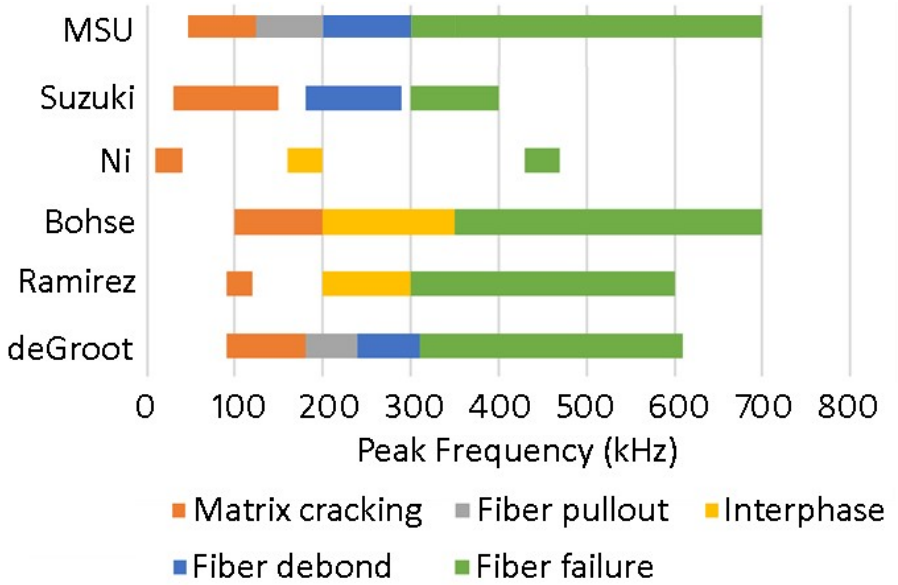


Figure 14: Schuster's summary of frequency bins determined by other researchers as well as his own.

As would be expected, defining damage events is not as simple as using single event parameters. There are many factors that can affect the propagation of ultrasonic waves, making the problem far more complex than defining frequency or amplitude bands. For example, geometry, edge reflections, layup, laminate thickness, constituent properties, sensor placement, sensor response and AE system setup may all affect the measurement of the ultrasonic waves produced by damage events. This makes developing a global method for characterizing damage modes from AE damage events very difficult.

In recent years, this research has progressed to more complex, multi-parameter statistical methods, such as unsupervised clustering techniques (k-means, fuzzy c-means etc.) [44, 57-61] and artificial neural networks [58, 62-65], along with other machine learning methods [35, 66-68]. Essentially, many signal parameters are extracted and plugged into sophisticated, clustering algorithms to determine three or four natural clusters within AE datasets, which are assumed to be damage modes. Interestingly enough, Gutkin et al. plotted their clustering results against peak frequency and found that their results were largely clustered around frequency bands (see Figure 15) [65]. On observation of any peak frequency distribution from a composite AE dataset, this is no surprise. Figure 15 shows that the peak frequencies of event waveforms are already clustered around specific frequencies, before any statistical algorithm has been applied. This is very common when applying AE to mechanical testing of composite laminates. This explains why any statistical clustering methods might automatically weight peak frequency much more heavily than any other signal parameter, especially when other signal parameters exhibit significantly more random noise and variation.

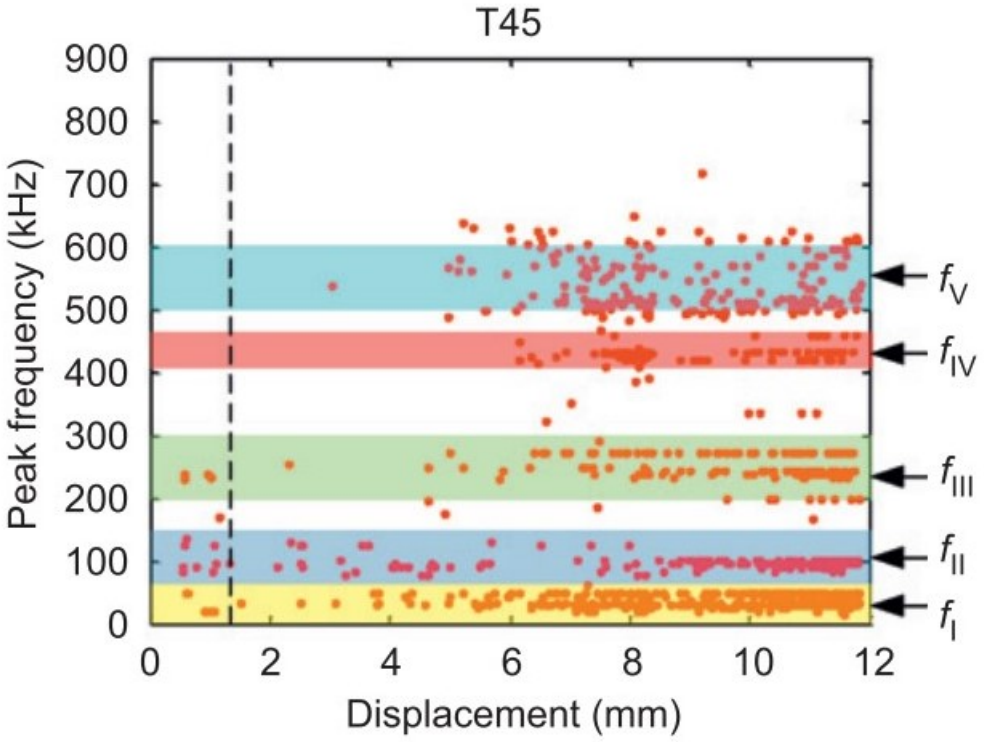


Figure 15: Unsupervised clustering results plotted against peak frequency, showing that the clusters are heavily influenced by signal peak frequencies [65].

Another interesting subset of AE damage classification research are time dependent frequency and modal analyses. Fourier transforms for waveform frequency analysis fall short in this research, since they assume a continuous signal. Typically, AE damage events waveforms are discontinuous. Time dependent frequency analyses are an extension of Fourier transforms to incorporate how the frequency response changes over the time of a signal. For example, wavelet transforms and short-term Fourier transforms are commonly applied to AE waveforms, which can then be implemented into pattern recognition algorithms [59, 69]. Another method, called measured amplitude ratios (MARs), implements these techniques to assess the prominence of the S_0 and A_0 wave modes in the AE signals [43, 58]. The amplitudes of the two modes are compared to

evaluate the modes that events originated from. MARs are based on the philosophy that cracks or delaminations occurring in-plane or closer to the laminate centerline will excite the S_0 more so than the A_0 mode. Alternatively, a more prominent A_0 mode in comparison to the S_0 mode could indicate delaminations or out-of-plane damage modes occurring within the laminate [70] (see Figure 16).

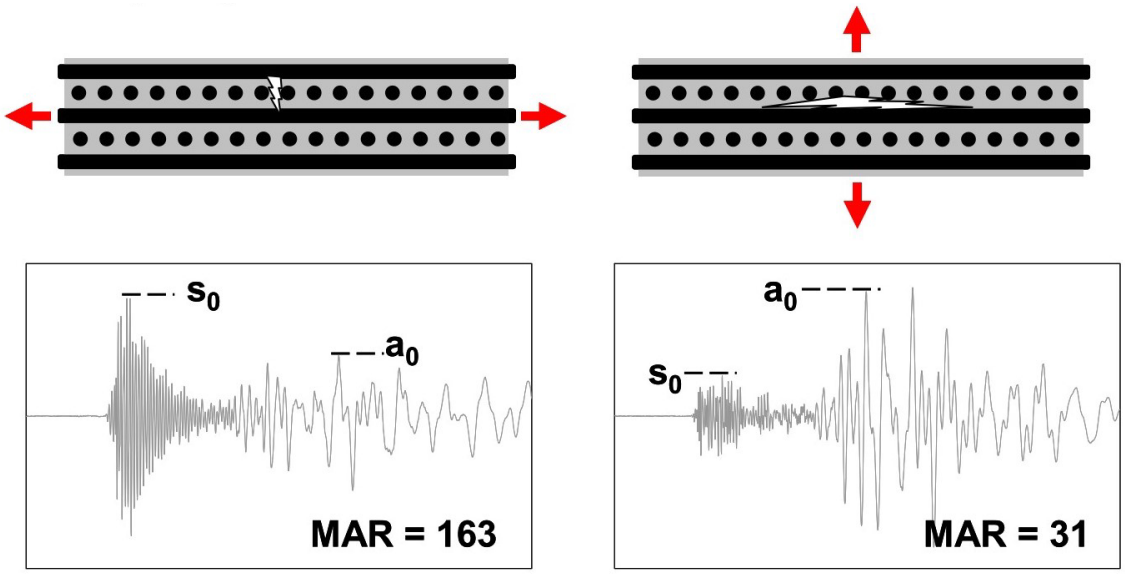


Figure 16:A diagram showing the effect of in-plane and out-of-plane damage modes on the symmetric and antisymmetric wave modes [70].

Unfortunately, it is very taxing to truly verify any of the methods mentioned above. AE event waveforms originate from hundreds to thousands of micro-cracks within the laminates. To effectively verify that a waveform classified as a matrix crack is actually a matrix crack or a waveform classified as a fiber break is actually a fiber break, one would have to search and use microscopy techniques many times over. Scanning electron microscopy (SEM) is commonly used observe damage modes, but it would be highly inefficient to track down every damage mechanism that has occurred.

Despite relative success in this area of AE research, damage classification techniques are seldom applied to predicting changing laminate properties for SHM purposes [35, 71].

Global Property Prediction

Using AE monitoring to make global laminate property predictions is more applicable to SHM. As described in the "Fatigue Models" section, it is important to know how properties such as residual modulus and strength are changing to predict the failure of a laminate before it actually happens. The majority of researchers in this field have applied AE to fatigue testing to track these changes in damage progression and it has proven to be very useful for this. Similar to damage characterization, AE global property prediction methods can be divided into single parameter and multi-parameter techniques.

With regards to making predictions of changing laminate properties, single parameter analysis methods track cumulative signal parameters, such as energy, counts or simply the number of recorded events. A dramatic change in the trends of one of these parameters can indicate a severe change in damage progression, like a laminate is nearing the end of its life or its modulus or strength has dropped dramatically (see Figure 17). For example, cumulative counts have shown to be a reliable signal parameter in fatigue testing to predict remaining fatigue life and residual strength [47, 72]. Cumulative energy has also been used by researchers to predict the remaining fatigue life of composites [51, 53]. Other research has used similar techniques, but only applied AE to static proof load tests after fatigue loading to build empirical models [47, 53], although these techniques are more applicable to pressure vessels in which known stresses are applied to the

structure. Single parameter models have worked well in some cases, but they usually fall short in some way, whether it be certain load ratios, stress levels or laminate stacking sequences. This has led to more sophisticated, multi-parameter statistical modeling techniques.

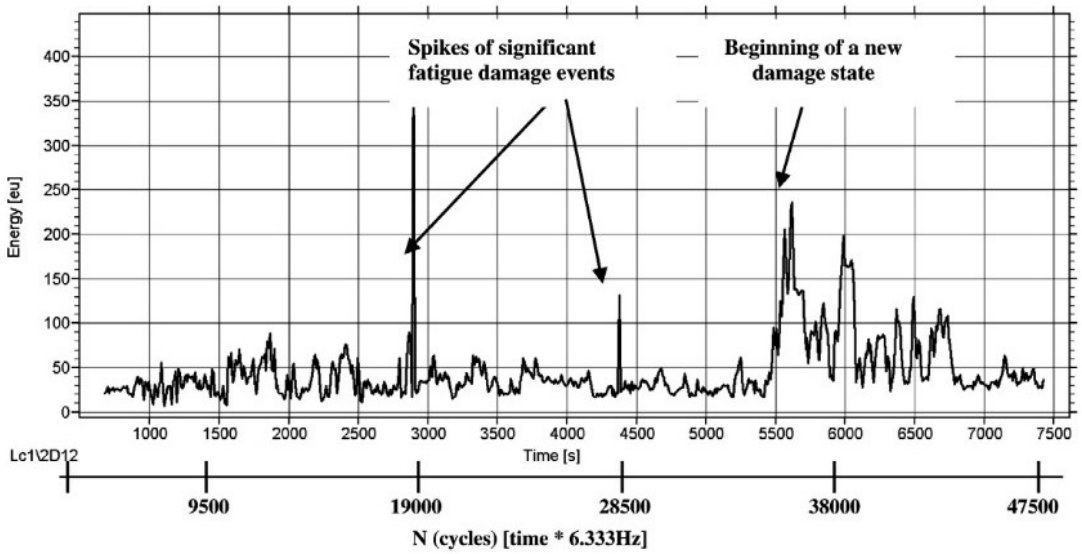


Figure 17: A plot of AE energy over time for a fatigue test, which indicates significant changes in the laminate's damage state [51].

Multi-parameter AE models for global property predictions are very similar to those used for damage classification. Bhat et al. used pattern recognition techniques to apply many variables to their predictions, such as event amplitudes, energies and frequencies, number of events and cumulative event parameters [73]. The pattern recognition technique found three different clusters of events which occurred sequentially throughout the lives of the laminates tested. The third and final cluster signified that the test sample was close to failure. Leone et al. used an artificial neural network approach for predicting residual strength of pre-fatigued laminates, although they only applied AE

during proof loading to failure [63]. This technique has also been applied to predicting strength degradation due to environmental effects, such as water absorption [62], but also relied on proof loading, which is still not particularly applicable to SHM of large composite structures.

Overall, obtaining reliable property degradation predictions with AE is still a difficult task, with most models falling short in some way, especially when thinking ahead to real-life applications.

Guided Ultrasonic Waves

GUWs are a form of non-destructive inspection (NDI), which have seen a lot of research efforts in SHM for all kinds of structures [74], including composite laminates [75]. GUW setups typically consist of arrays of piezoelectric transducers, which act as both actuators and sensors (see Figure 18). When acting as actuators the piezos are used to apply stress waves to be detected by the sensors surrounding it. The propagations of these ultrasonic waves are highly sensitive to defects and cracks (see Figure 19). Ultimately, changes in the propagation of these waves imply changes in the mechanical properties of the material [76]. The Lamb waves can be applied in several forms, such as Dirac delta functions, tone bursts or frequency and amplitude sweeps, to change the resolution of the damage they might detect or the specific wave mode that is excited. Changing the angle of incidence between the actuating sensor and the laminate can also affect the wave mode that is excited within the laminate [75], although this does not seem to be as applicable to in-service, continuous monitoring. Like AE, a variety of signal features are extracted from the received waves, such as amplitudes, time of flight,

frequency content, power spectral densities and phase velocities [77]. To define damage or quantify changes in materials properties, these parameters are commonly compared to those obtained when testing the undamaged structure [34].

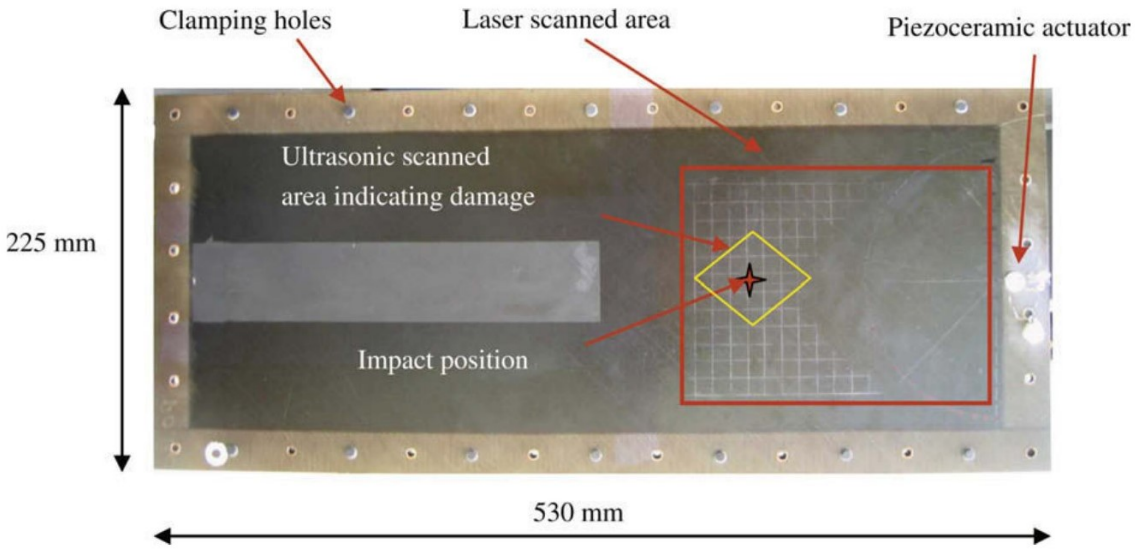


Figure 18: An example of a GUW sensor array setup on a composite aircraft wing-box structure with impact damage [38].

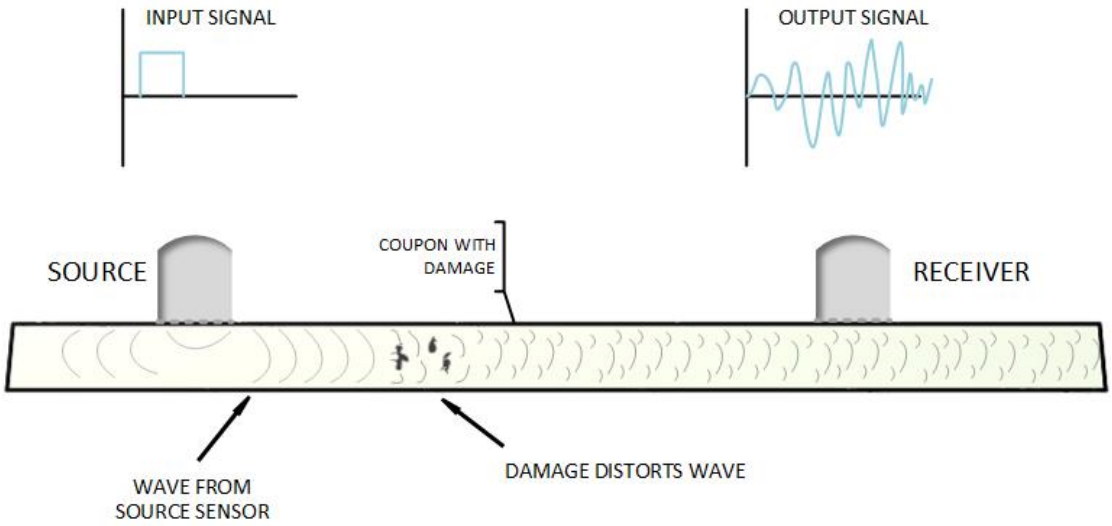


Figure 19: A diagram showing how damage within a composite laminate can affect the propagation of GUWs.

Most commonly, GUWs have been applied to composite structures to locate and determine the severity of barely visible impact damage [41, 42, 78]. Delamination growth has also been effectively quantified by GUWs through DCB tests and on more complex structures, while the results were also verified by finite element simulations [79, 80]. GUWs have also been applied to fatigue testing of composite laminates. Typically, the fatigue tests are interrupted to apply the GUWs before continuing. He et al. measured wave velocity and attenuation of their GUWs throughout the fatigue life of laminates tested in three point bending and found close correlations with residual modulus [81]. Wilson et al. applied arrays of actuators and sensors to laminates (see Figure 20) in tension-tension fatigue [82]. They used changes in power spectral density from different wave paths as their damage index and found that it followed consistent trends with transverse crack density and residual modulus.

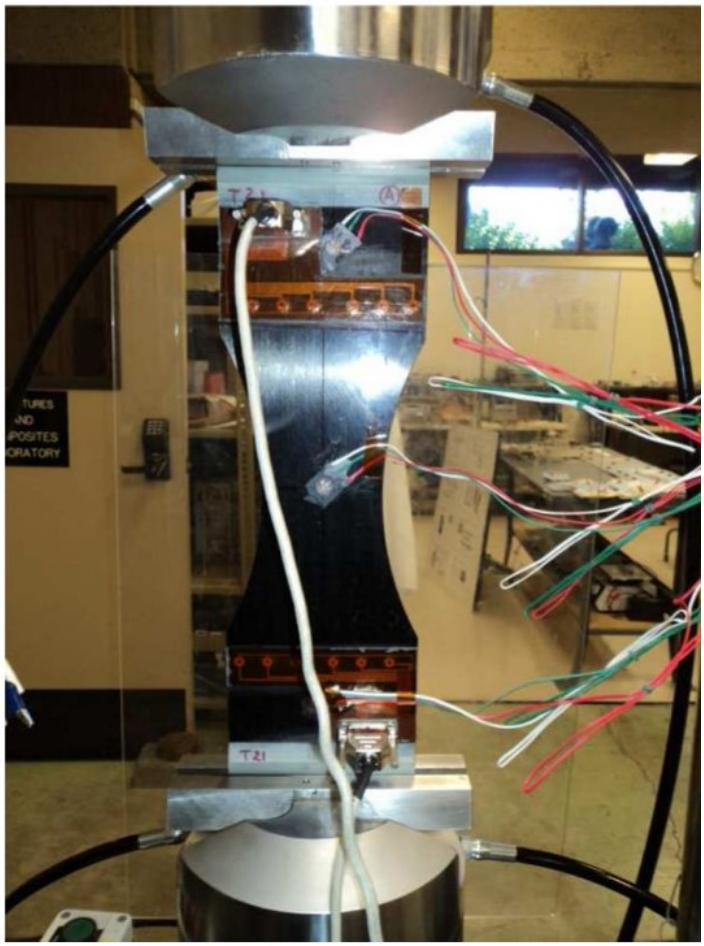


Figure 20: The actuator (top of sample) and sensor (bottom of sample) setup used by Wilson et al. to measure changes in power spectral density through different wave paths [82].

Aside from investigating various types of damage and their severity, other researchers have directed their efforts towards compensation strategies for environmental and load effects on GUWs. Naturally, things like applied load, temperature, humidity and water absorption do affect the propagation of ultrasonic waves. Therefore, compensation strategies are required for in service monitoring. Load compensation strategies are very common, since a structure being monitored might always be under load during its service life [42, 83-86], although the techniques applied tend to lose their validity when damage

is introduced. As laminates are loaded, cracks within them open up and cause the propagating waves to attenuate in a non-linear manner. This phenomenon is much harder to compensate for. Temperature and humidity effects have also been investigated, but of course these effects can also be coupled with loading effects to construct more complex models [85]. These environmental effects on the propagation of ultrasonic waves are now well known, but surprisingly have not been applied to AE research. One would expect that environmental effects, such as load and temperature, would also affect the propagation of waves originating from damage events, but seems to have been overlooked by modern AE research.

As stated above, GUW setups typically consist of large arrays of piezoelectric sensors. With regards to the monitoring of large composite structures, AE uses very similar arrays of sensors to detect and locate damage. This research proposes that it is entirely possible that AE sensor arrays can be used in a similar way to GUW transducers to track changes in ultrasonic wave propagation and ultimately changes in global properties of GFRP laminates.

Combined Monitoring Techniques

Previous research with regards to AE and GUWs has been outlined in detail and it is evident that there are many complex, multivariate statistical analyses that have been associated with these techniques. Interestingly, very few efforts have been made to combine the data from the two techniques. Some researchers have applied multiple in-situ damage monitoring techniques in tandem, but only compared the results. Chaki et al. applied bulk and guided ultrasonic waves, AE and passive and active infrared

thermography simultaneously, during incremental static tensile loading of GFRP laminates [87]. They defined separate damage indicators for each technique. For example, the AE damage indicator was defined as the number of AE events recorded for each load step in comparison to the first load step and used wave velocity from the GUWs. These damage indicators were then compared to each other, as shown in Figure 21. This is a relatively simplistic approach, which only uses single variables from each technique for comparison.

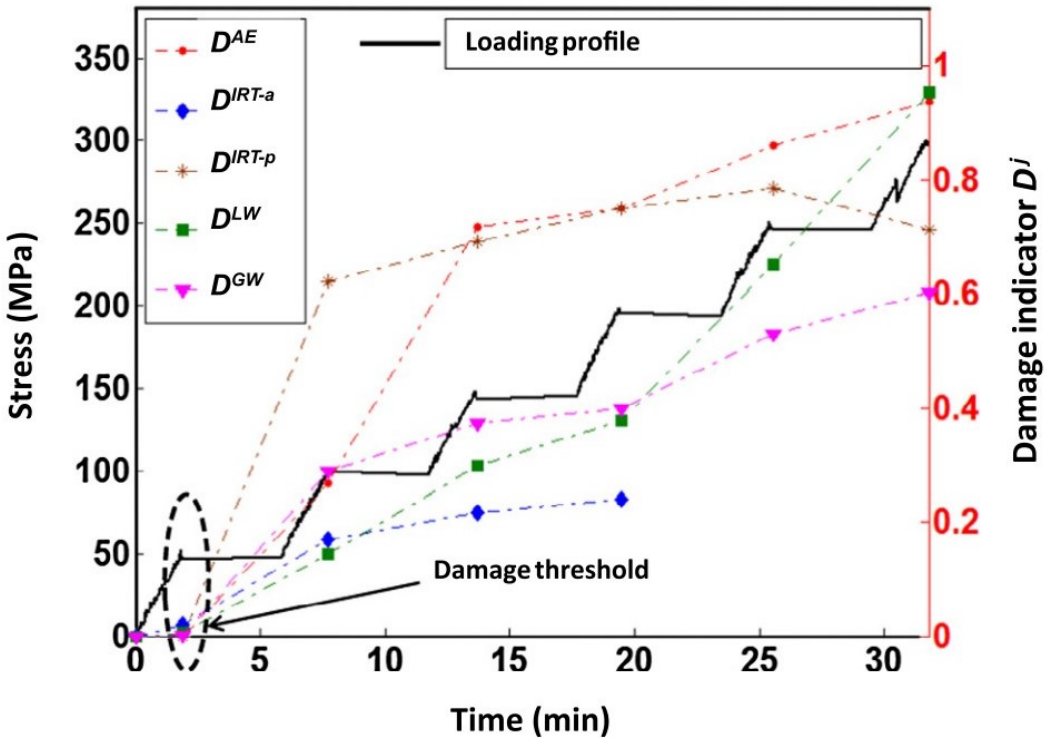


Figure 21: A comparison of damage indicators used by Chaki et al. for incremental static tensile loading of GFRP coupons for multiple monitoring techniques, including AE and GUWs [87].

Alternatively, Staszewski et al. applied the active (GUWs) and passive (AE) approaches to impact damage on composite aircraft structures [38]. GUWs were applied using a single piezoelectric actuator and detected using a 3D laser vibrometer. They were

able to successfully detect the location and gain estimates on the severity of the impact damage. On a different composite structure, they applied AE during impact tests to locate the damage using a genetic algorithm based optimization scheme, which appeared to be very accurate, although highly complex. One would think that they could have applied the tests to the same structure i.e. AE to record the initial impacts and subsequently GUWs to measure them afterwards. It may have been useful to combine the data from the two techniques to obtain more comprehensive evaluations of the severity of the damage.

Similarly, Torres-Arredondo et al. applied AE and GUWs to a variety of mechanical testing techniques to evaluate damage progression in GFRPs [67]. AE was applied to static tensile and DCB tests, while GUWs were applied to a sandwich structure with various damage types introduced. To process the waveform data and evaluate the damage, several techniques were applied, such as discrete wavelet transforms for feature extraction, “unfolding” the data from multiple sensors and applying them to a self-organizing map. The AE data was used to cluster events into various damage modes and the GUW data was used to detect and evaluate the damage introduced to the sandwich structure. Once again, it is surprising that the researchers chose not to conduct both techniques during the same tests and attempt to combine the data from the two to gain a greater understanding of how the results relate to each other.

Finally, Nasrollahi et al. did propose that it is certainly possible to combine multiple ultrasonic monitoring techniques to structures using the same piezoelectric sensors [88, 89]. They combined AE, GUWs and electromechanical impedance (EMI) techniques into a standalone system for monitoring structures. They showed that the three

techniques could be applied simultaneously, but only applied them to an aluminum plate with simulated damage. Pencil lead breaks were applied for AE to detect the location and aluminum blocks were glued to the plate to simulate damage for the GUWs and EMI techniques to detect. Still, this was a relatively simple approach. The techniques were not applied to actual mechanical testing and the datasets were no combined to make any specific predictions.

The previous paragraphs have shown that there is a notable interest in comparing and evaluating AE and GUW techniques, but researchers still have not considered the idea of combining the data from the two techniques. A whole host of statistical modeling techniques are available for making predictions using these techniques, so there must be well known data manipulation methods to combine the data into a singular predictive model.

Statistical Predictive Modeling

In the preceding sections of this chapter, a wide array of statistical modeling techniques have been discussed, from empirical predictive models to iterative models to highly complex artificial neural networks, self-organizing maps and unsupervised clustering techniques. For the purposes of this research, a relatively simple approach was taken. Multivariate linear regression analyses were the chosen method for making predictions, due to their interpretability and good fit to the data. This is further explained in the “Statistical Predictive Modeling Procedures” chapter.

Multivariate Linear Regression Modeling

Multivariate linear regression models are an extension of standard single variable linear regressions. Rather than observing linear correlations between single predictors and a response, multivariate regressions use multiple predictors simultaneously to predict their effects on the response. It is like applying a linear fit to a dataset in multiple dimensions. For example, if a linear fit of one predictor onto a response is a line in 2D space, a linear fit of two predictors onto a response can be shown as a plane in 3D space (see Figure 22). If the number of predictor variables is greater than two, then it cannot be displayed visually. The linear relationships between multiple variables and a response can be described by Equation 2, where Y is the response, β_i are the slope coefficients, X_i are the predictor variables and ϵ is a mean zero random error term. The slope coefficients can easily be determined via a least squares approach.

$$Y = \beta_0 + \beta_1 X_1 + \beta_2 X_2 + \cdots + \beta_i X_i + \epsilon \tag{2}$$

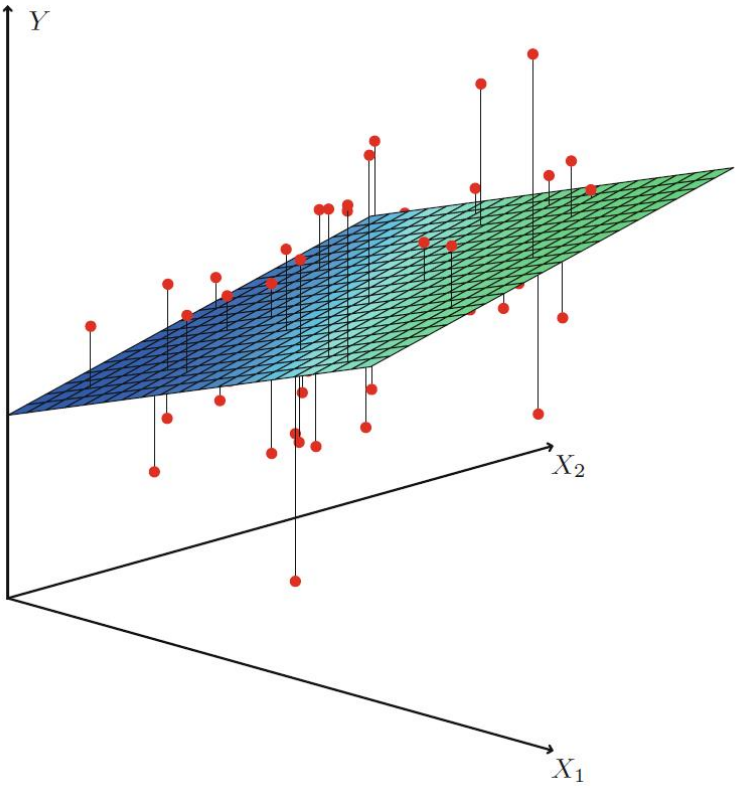


Figure 22: A representation of a two predictor linear regression onto a response – a 2D plane across 3D space [90].

Multivariate linear regressions assume that all predictor variables are related to the response, therefore, strategies must be applied to determine which variables should not be used and which ones are relevant. First of all, various model testing statistics can be applied to determine the performance of the model. For example, the F-statistic (F) is commonly used (see Equation 3, where TSS is the total sum of squares, RSS is the residual sum of squares, p is the number of predictor variables and m is the number of observations). The higher the F-stat, the more likely the variables are related to the response. In the case of multivariate analyses, the coefficient of determination (R^2) is not exactly relevant. The addition of any variable with even the slightest degree of correlation

will cause it to increase [90]. Instead, an adjusted R^2 (or R^2_{adj}) is typically used in multivariate analyses, which takes into account the number of predictor variables and is calculated using Equation 4. As well as these measures of fit, p-values from t-tests have shown to be very useful, whether it is a p-value for the overall fit of the dataset or, in the case of variable selection, p-values for each individual variable, although the idea of a "good" or "bad" p-value is rather subjective.

$$F = \frac{(TSS - RSS)/p}{RSS/(m - p - 1)} \tag{3}$$

$$R^2_{adj} = 1 - \frac{RSS/(m - p - 1)}{TSS/(m - 1)} \tag{4}$$

All of the model test statistics described above can be useful for determining whether or not predictor variables are useful for predicting the response. Perhaps the most useful are p-values [84]. The most relevant variables can be selected using either forward selection, backward selection or mixed selection. All three of these methods can be applied while tracking changes in F, R^2_{adj} and p-values to create the best fitting and most representative model. Forward selection is where the model starts with just the intercept term (β_0) and variables are added to the model iteratively until the test statistics are optimized. Backward selection is where all of the predictor variables are applied and the worst ones are iteratively removed until the model is optimized. Mixed selection is perhaps the most inefficient, especially when there are a lot of predictor variables, and all possible combinations of the predictor variables are tested.

The model test statistics are a good measure of how well a statistical model could make predictions, but they are not true tests of model performance, since the data used to train the model are also being used to test it. To truly test a model's predictive performance, a validation procedure must be applied. Hold out cross validation (HOCV) is a method commonly used by researchers to validate statistical models. In this case, a certain percentage of random data points (usually 10-20%) are withheld from the dataset and the remaining data points are used to train the model. The withheld data points can then be used to test the model's predictive capabilities. This process is then repeated by withholding different data points until all have been tested. The predictions from these tests can be compared with the actual responses from the dataset and a linear fit can be applied to determine coefficients of determination for each validation test, which can then be averaged to give an overall validation score. As well as validating the models themselves, this style of validation can also serve as a good measure of repeatability for experimental testing, especially when multiple tests are combined into a single dataset [91]. The data from each test can be withheld to validate the model and the changes in R^2 from test to test would be a good indication of how repeatable the test method actually is.

Although a relatively simplistic modeling approach, there are some issues to be wary of when applying multivariate linear regressions. First of all, it is of course a linear model, which assumes that every predictor variable shares a linear relationship with the response. This can be overcome by simply incorporating non-linear terms, such as squared or logarithmic terms, to Equation 2 (see Equation 5). There is also the additive assumption; variables are independent of each other, but their summation is equal to the

response. This is not always the case when many variables are being applied, which may be closely related to each other. In this case, certain interactions between variables can be added to Equation 2 (see Equation 6), but good knowledge of the underlying relationships between predictor variables is required to do this effectively.

$$Y = \beta_0 + \beta_1 X_1 + \beta_2 X_1^2 + \beta_3 X_2 + \cdots + \epsilon \tag{5}$$

$$Y = \beta_0 + (\beta_1 + \beta_3 X_2) X_1 + \beta_2 X_2 + \epsilon \tag{6}$$

The most concerning issue regarding statistical modeling of experimental datasets, which can be very common when used in conjunction with signal analysis techniques, is collinearity. This is where two or more predictor variables are closely related to each other. This makes it difficult to separate out the individual effects of each predictor variable on the response and can affect the least squares predictions as well as lead to instability in the β_i determinations. Figure 23 shows an example of how collinearity can affect coefficient calculations. On the left are two variables which show little correlation between each other and the right are two variables which display a high degree of collinearity. The axes show possible model coefficients for each variable and the ellipses are lines of constant RSS. The left plot shows that it is much easier for the least squares technique to determine accurate model coefficients, whereas the plot on the right shows how it can be difficult for the least squares approach to determine stable coefficients. In practice, this can cause large deviances in the coefficients determined for a collinear regression model. It can result in regression coefficients being negative when they should be positive and vice versa. In extreme cases it can also cause the standard error to grow rapidly and ultimately result in inaccurate predictions.

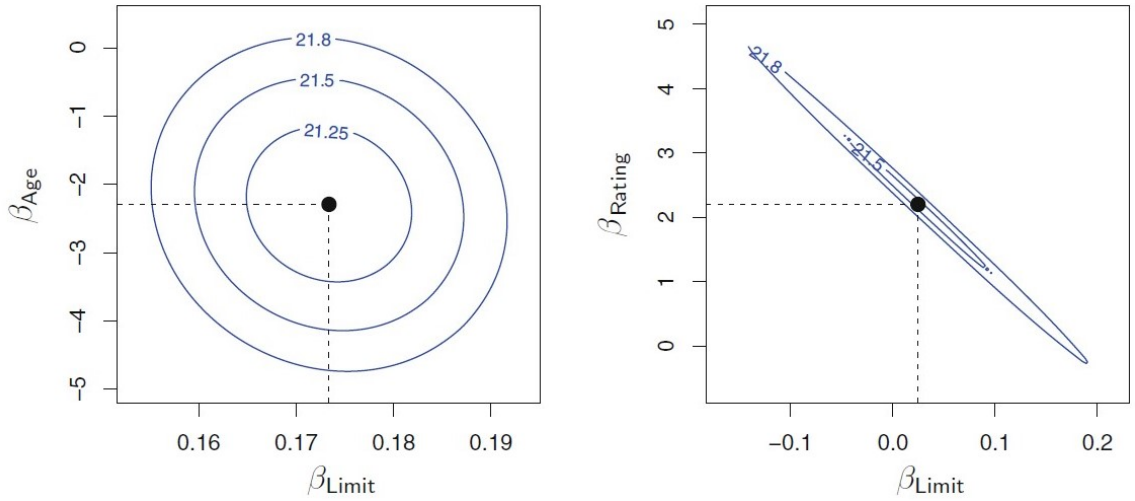


Figure 23: Plots of possible regression coefficients that are not collinear (left) and highly collinear (right) to show the instability that collinearity can cause. The ellipses are lines of equal RSS [90].

To detect collinearity, it is common to inspect the correlation matrix of all the variables, or to determine a variance inflation factor (VIF) matrix of all the predictor variables (see Equation 7). A VIF which is close to 1 is good and indicates there is very little relationship between two variables, but a VIF greater than 5 indicates significant collinearity between two variables. In cases like this, there are data manipulation methods available which can help avoid this kind of instability. A suitable dimension reduction method, such as principal component analysis, could be applied to account for variances and close relationships between predictor variables.

$$VIF_{ij} = \frac{1}{1 - R^2_{X_i|X_j}} \tag{7}$$

Principal Component Analysis

Principal component analysis (PCA) is a dimension reduction technique, which is a commonly used tool in exploratory data analysis and constructing predictive models. Principal components (PCs) are a series of orthogonal coordinate transforms of a dataset in the directions of maximum variance. Essentially, PCA turns a set of possibly correlated variables into a set of linear, uncorrelated variables [92]. The first PC has the largest possible variance and the proceeding PCs maximize variance under the constraint that they are orthogonal to the preceding PC [93].

To calculate PCs from a dataset, the dataset must first be normalized and each variable centered around its mean. This helps stability of the solution as well as better interpretability of the principal loading vectors [94]. The PC loading vectors can then be calculated through eigenvalue decomposition of a data covariance matrix or singular value decomposition of a data matrix. For eigenvalue decomposition, the PC loading vectors ($\underline{W}$) are eigenvectors of $\underline{X}^T\underline{X}$, if $\underline{X}$ is an $m \times p$ dataset. The eigenvector with the largest eigenvalue is the loading vector of the first PC and subsequent loading vectors are arranged in order of highest to lowest eigenvalue. The PC matrix ($\underline{T}$) can then be determined by Equation 8.

$$\underline{T} = \underline{X} \cdot \underline{W} \tag{8}$$

First of all, inspection of $\underline{W}$ can aid researchers in comparing relationships between variables and which variables have the largest contributions to the variance within the dataset [93]. For data reduction purposes, the lower variance PCs can be

removed from the dataset, while the higher variance PCs can be kept, leaving the majority of the important information in the dataset intact. Ultimately, this means there are fewer variables to process, with minimal effects on the results of the dataset.

For the purposes of this work, PCA was applied to multivariate regression analyses. Known as principal component regression (PCR), it can be a powerful tool for differentiating relationships between strongly correlated predictor variables and can potentially outperform the typical least squares approach for regression analyses [90]. PCR uses the PC dataset as variables in a multivariable regression model instead of the original variables. It can serve to constrain the estimated regression coefficients and can prevent overfitting of the model, but it is not a feature selection method, since each PC is still a linear combination of all the predictor variables. Once regression coefficients have been determined for the PCs, they can then be transformed back to the original dataset through Equation 9, where $\hat{Y}$ is the response variable, $\hat{\beta}_{PCA}$ is a vector of the PCR coefficients and $\hat{\beta}$ is a vector of regression coefficients in the original data space.

$$\hat{Y} = \underline{T} \cdot \hat{\beta}_{PCA} = \underline{X} \cdot \underline{W} \cdot \hat{\beta}_{PCA}$$

$$\hat{Y} = \underline{X} \cdot \hat{\beta}$$

$$\underline{X} \cdot \hat{\beta} = \underline{X} \cdot \underline{W} \cdot \hat{\beta}_{PCA}$$

$$\hat{\beta} = \underline{W} \cdot \hat{\beta}_{PCA} \tag{9}$$

In theory, the PCR should be able to remove statistical noise and irrelevant information from the dataset, rather than selectively removing variables, and should separate the effects of any collinear variables within the dataset. Despite this, the PCA

method does have its limitations. Of course, it is a series of linear transformations of the dataset, so it cannot accurately account for any degree of non-linearity within the dataset. Also, it is an unsupervised technique. In other words, the response variable is not accounted for in the analysis. The PCs only describe the relationships between the predictor variables and there is no guarantee that they are also the best way to describe the response. In light of this, it is possible to extend these concepts to a technique called the partial least squared method, which does take into account the response variable to determine new features within the dataset, which are also related to the response, but is currently beyond the scope of this research.

EXPERIMENTAL PROCEDURES

To test the potential of combining AE and GUW monitoring to predict degrading mechanical properties in composite laminates, an array of test methods and inspection techniques were applied. Testing techniques had to be derived so that changes in moduli could be measured accurately, whilst also implementing the AE monitoring and GUW techniques simultaneously. It was also required that the data obtained from the on-line damage monitoring was in a sufficient form for constructing the statistical models.

For the first half of this research the static loading case was tested and evaluated before continuing to more realistic loading scenarios i.e. fatigue loading. Significant efforts were made throughout the process to ensure consistency and acquire reliable results for the modeling portion of this research. This began by manufacturing high quality GFRP test samples of multiple layups, which were of sufficient dimensions to test in both static and fatigue loading, while also being large enough to acquire AE data, apply and record GUWs and take accurate load/strain measurements. Setting up the on-line damage monitoring systems also required a significant amount of preliminary testing and detailed inspection to ensure reliable results that were repeatable and truly representative of the damage occurring in the test samples, throughout the mechanical testing procedures. This section describes in detail the procedures used and the hurdles that were overcome to achieve the goals outlined in the introduction to this dissertation.

Specimen Manufacturing

All of the GFRP laminates used to produce the test coupons were manufactured in-house in the research group's composites manufacturing lab. The specific requirements for the manufactured laminates and, ultimately, the test coupons that were produced from them were as follows:

- GFRP laminates manufactured from fabrics and a matrix material that are representative of laminates that are currently being used in the wind energy industry.
- Apply a manufacturing technique that is also representative of the wind industry.
- Produce laminates that are of high quality, with consistently high fiber volume fractions, well aligned fiber tows and minimal porosity.
- Apply a variety of layups and ply orientations to achieve differing trends in damage progression, under the constraint that the laminates are similar thicknesses for consistent AE and GUW monitoring.
- Cut high quality tensile test coupons from the laminates that are of consistent dimensions and sufficiently large enough to arrange the on-line damage monitoring sensors.
- Ensure good gripping surfaces on the test coupons to avoid grip failures during mechanical testing.

Wind turbine blades typically use E-glass fiber reinforcements arranged in fabrics of various orientations, which are combined with room-temperature cure epoxies, via

resin infusion techniques. The manufacturing of test samples for this research aimed to follow these techniques as closely as possible.

The chosen fabrics for the laminates were Vectorply E-LT 3800 and PPG Devold 810 Biax, which are common choices for blade manufacturers. Manufacturers' datasheets for these two fabrics can be found in Appendix A. The Vectorply fabric is the primary fabric used to construct the laminates and is a stitched unidirectional fabric with a small percentage of backing tows and was used in all of the laminates that were manufactured. The longitudinal tows made up 90% of the overall areal weight of the fabric, while the transverse tows made up 9% and the stitching 1%. Although this fabric is commonly used in the industry, the backing tows do add complexity when trying to evaluate damage modes and progressions, when compared to purely unidirectional fabrics. On the other hand, the PPG fabric is a stitched ±45° fabric which was only used for the ±45° plies in one of the chosen layups. It is constructed of one layer of 45° tows stitched to a second layer of -45° tows. Figure 24 shows photos of the raw fabrics.

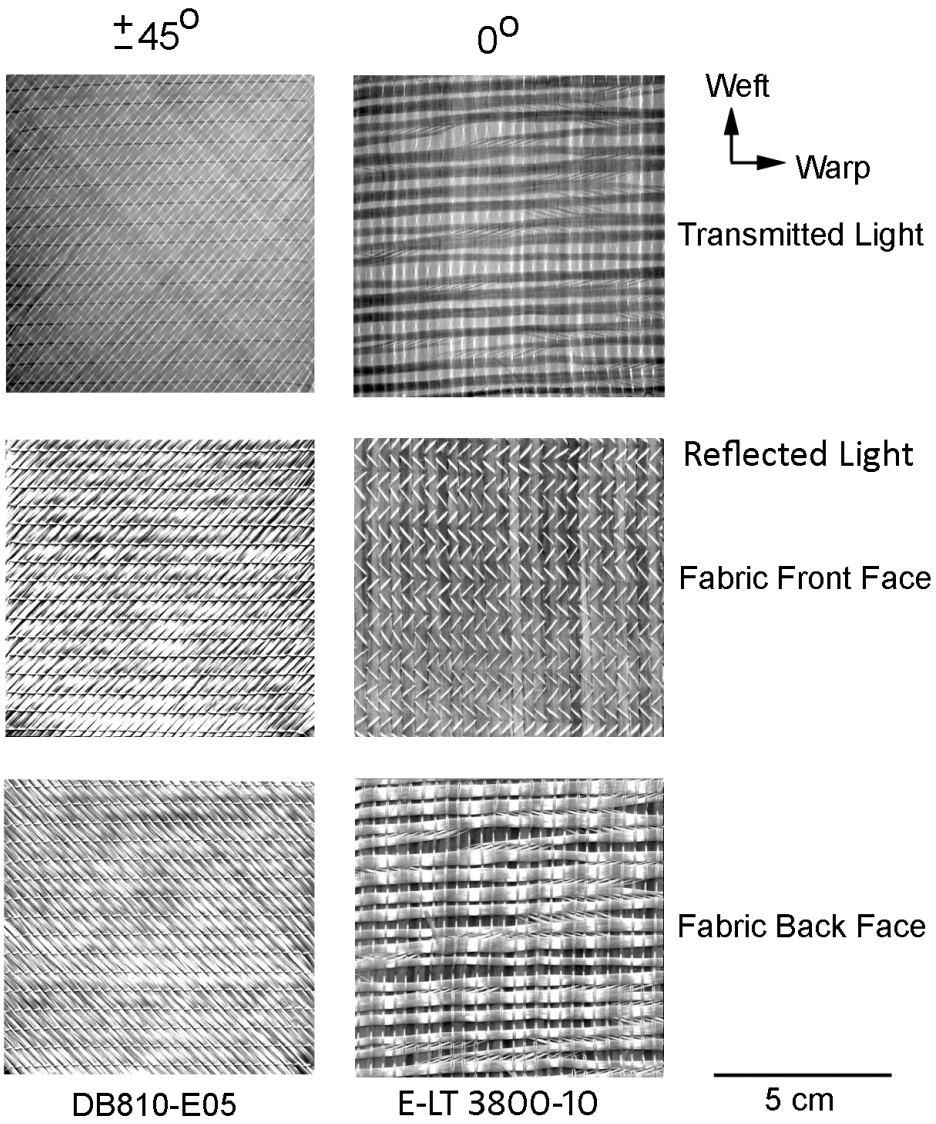


Figure 24: Transmitted light and reflected light front and back images of the PPG Devold Biax 810 fabric (left) and the Vectorply E-LT 3800 fabric (right).

The chosen matrix material for this research was a two-part, room-temperature cure epoxy system; Hexion Epikote™ RIMR 135 epoxy with Hexion Epicure™ RIMH 1366 hardener. Hexion's specification sheets for this epoxy can be found in Appendix A.

Several layups were chosen to achieve a variety of damage mechanisms and damage progression trends during mechanical testing. The chosen layups were as follows:

1. $[0/90]_S$
2. $[90/0]_S$
3. $[90_4]$
4. $[45/-45]_S$
5. $[0/90/\pm45]_S$

Layups 1 and 2 were chosen because they were expected to exhibit comparable strengths and moduli, but have different ply orientations for the outer plies where the AE and GUW sensors were mounted. This was to investigate the effect of surface ply orientations where the sensors were mounted for the application and monitoring of acoustic waves when damage was introduced. Layup 3 was a fully transverse layup, which was to emphasize the effects of transverse matrix cracking, and layup 4 was to emphasize shear failure modes. Finally, layup 5 was a quasi-isotropic layup, which was hoped to exhibit a combination of all composite failure modes. Note that all layups were constructed using the Vectorply fabric except layup 5, which used the PPG Biax fabric for the ±45° plies.

To stay consistent with wind blade manufacturing processes, laminates were manufactured using a vacuum assisted resin infusion molding (VARIM) technique. Figure 25 shows a schematic of the setup and materials used for the process. The materials were stacked on the aluminum mold, taking great care and attention when

laying down the fabrics to ensure the precise orientation of the tows. Vacuum was then applied through the vacuum port with the injection port closed off. When maximum vacuum had been pulled, the vacuum port was closed off and the plate left for at least 30 minutes to ensure there were no vacuum leaks present. Once this was confirmed, the resin was mixed to an epoxy:hardener weight ratio of 100:30 ± 2 as per the manufacturer's recommendation, for 5 minutes. The vacuum port was then opened again and the vacuum reapplied before slowly releasing the infusion port to allow the epoxy/hardener mix to flow into the mold and infuse into the glass fabric (see Figure 26). The resin was allowed to continue flowing across the mold until the fabric was fully wet out, whilst taking notes on the flow front and indicating any potential areas of porosity. The ports were then closed with the mold still under vacuum. The plates were then left to cure for 24 hours at room temperature (25°C). The mold was heated to ensure a constant 25°C in case of any dramatic changes in temperature within the lab. The cured plates were then removed from the mold and post-cured in a convection oven for 12 hours at 70°C, after which all the peel-ply and flow media etc. could be removed from the plates. It should be noted that all laminates were manufactured during the same time period (over the course of two months), to eliminate the possibility discontinuities from using resins and fabrics that are slowly degrading over time.

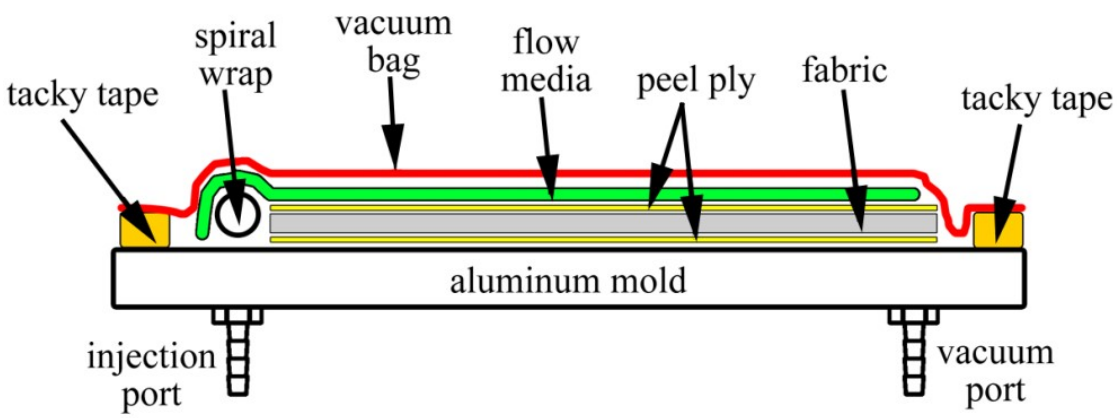


Figure 25: A schematic of the VARIM setup used to manufacture the laminates.

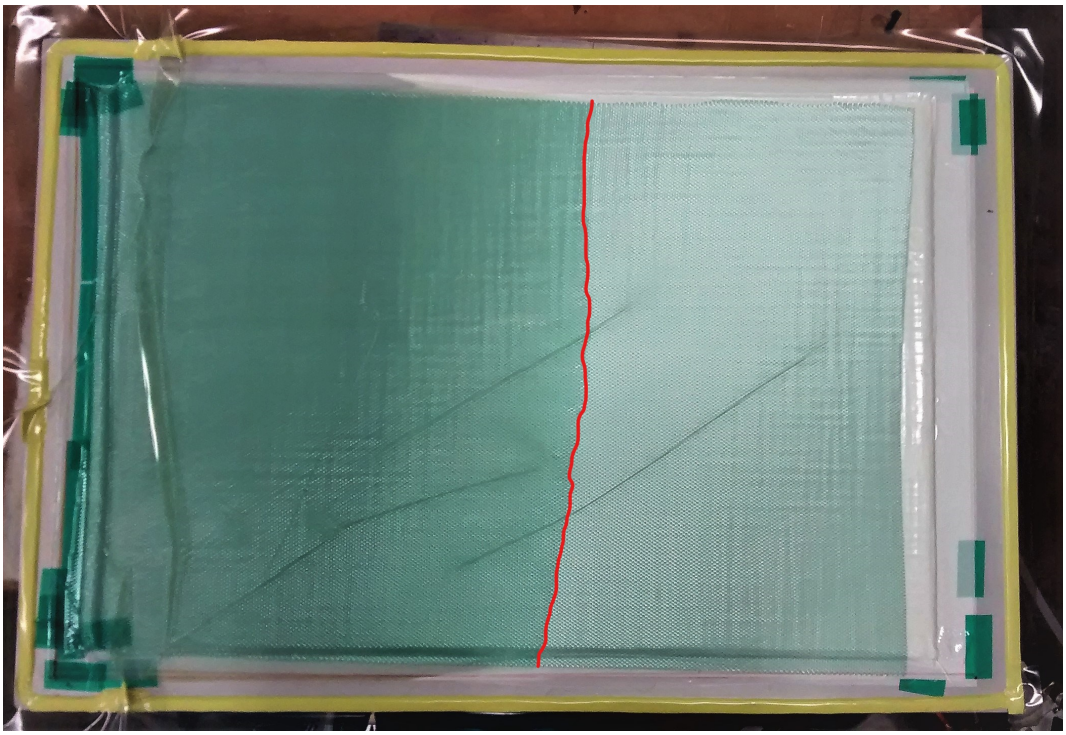


Figure 26: A photo of epoxy being infused into the fabric on the mold, with the red line indicating the flow front.

Before cutting test samples from the laminates, the quality of them was observed and quantified. Initially, the laminates were visually inspected to observe any possible areas of porosity. Matrix burn-off tests were then conducted on every laminate to

measure fiber volume fraction and observe tow alignments within the laminates (see Figure 27).

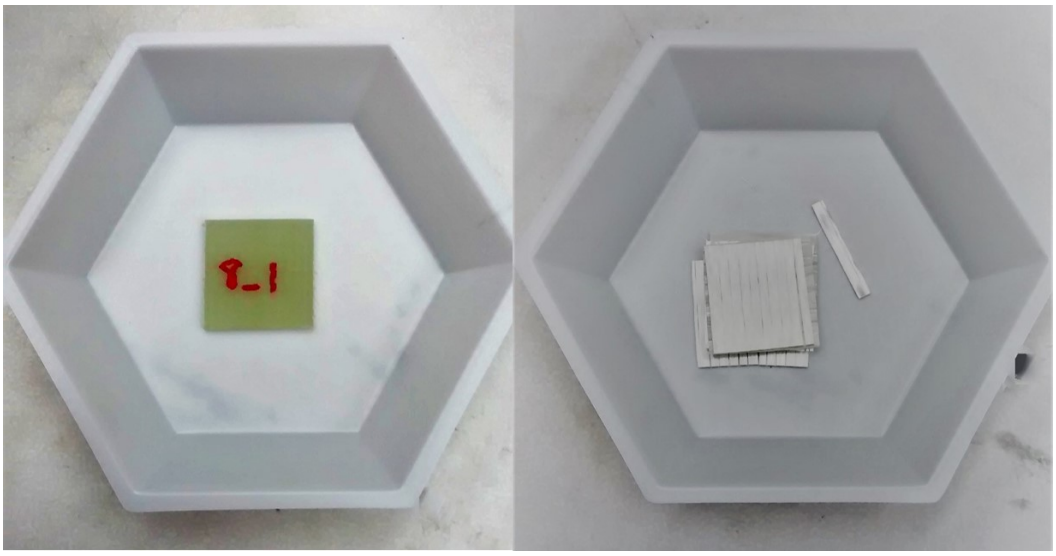


Figure 27: A test sample used for a matrix burn-off (left) and the sample once all the epoxy had been burnt off (right).

Once the quality of the laminates had been measured and verified, the laminates were cut into test coupons of dimensions 300x30 mm. These dimensions were deemed sufficient to allow for 50 mm of gripping on each end and space for the AE and GUW sensors within the gage section, as well as extensometers for strain measurements. End tabs were bonded to test coupons from some of the layups to ensure good shear load transfer from the grips to the gage section to avoid grip failures during tensile testing. These were primarily applied to the layups with 0° plies on the outside, but were found to be required for all layups used for fatigue testing. The tabs used were 50x32 mm sections of G10 fiberglass bonded with Armstrong A-12 two part epoxy adhesive, mixed to a 1:1 ratio, which was left to cure for 24 hours.

Every laminate that was manufactured was assigned its own four digit number and every coupon cut from each laminate was assigned a two digit number (in the form of LLLL_CC) to keep track of them all. All test coupons will be referred to by these numbers from this point onwards. Thickness and width measurements, to a precision of 0.01 mm, were taken for every coupon that was cut. For the purposes of stress calculations, the thickness used was the average coupon thickness of every coupon cut from the same laminate. Table 1 provides details of the numbers assigned to each manufactured laminate, their layup, the number of coupons cut from them, average thickness and V_f. Figure 28 is a photo of some of the final test coupons. Full dimensions and the tests conducted on each coupon, as well as manufacturing quality notes are provided in Appendix B.

Laminate Number	Layup	Number of Coupons	Average thickness (mm)	V_f (%)
4103	$[0/90]_S$	24	3.10	61.5
4107	$[0/90]_S$	12	3.11	59.5
4108	$[0/90]_S$	18	3.25	58.7
4109	$[90/0]_S$	20	3.18	60.0
4110	$[90/0]_S$	20	3.21	57.8
4111	$[90/0]_S$	20	3.20	59.5
4113	$[90_4]$	25	3.18	59.5
4114	$[90_4]$	28	3.24	58.7
4115	$[45/-45]_S$	14	3.26	58.2
4116	$[45/-45]_S$	14	3.37	55.6
4117	$[45/-45]_S$	17	3.31	56.8
4118	$[45/-45]_S$	20	3.24	56.9
4119	$[0/90]_S$	-	3.17	58.5
4120	$[0/90/\pm45]_S$	26	4.29	59.5
4121	$[0/90/\pm45]_S$	24	4.37	57.9

Table 1: Manufactured laminate numbers, layups, number of coupons cut, thicknesses and volume fractions.

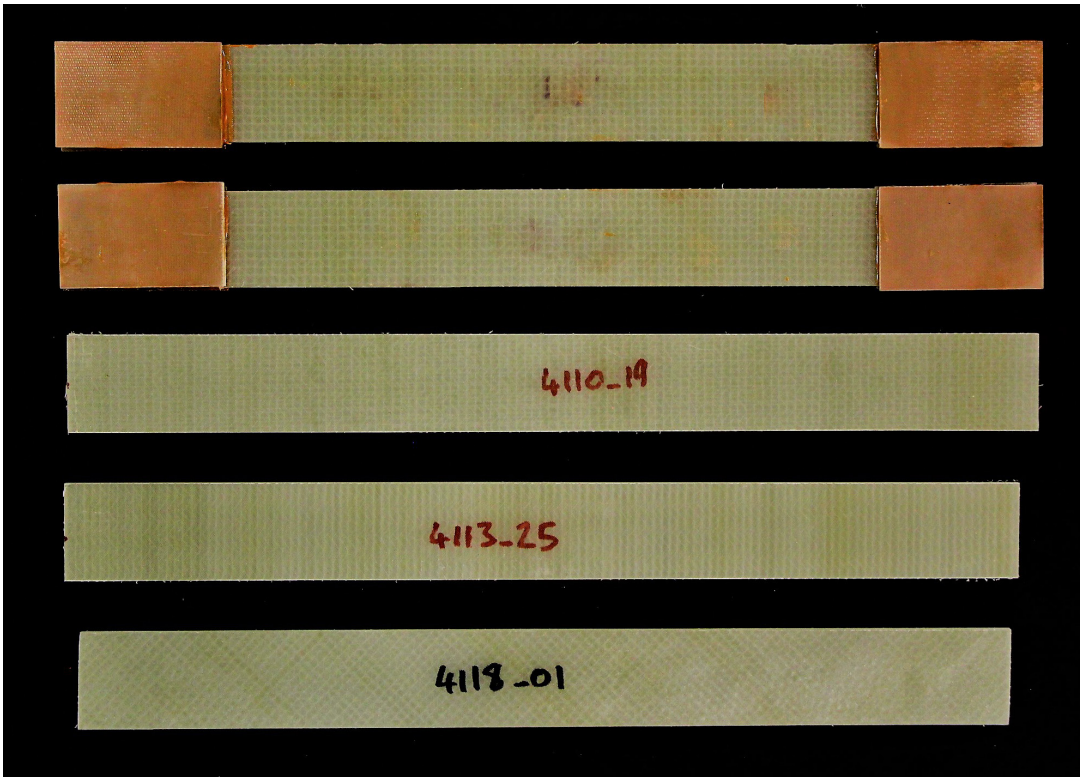


Figure 28: A photo as an example of the coupons that were produced with and without end tabs.

On-Line Damage Monitoring Setup

Setting up the on-line damage monitoring systems to acquire reliable and repeatable data throughout testing proved to be a complex task with several important considerations. Piezoelectric sensors needed to be applied to be capable of:

1. Detecting and locating AE events over the length of the coupons
2. Applying consistent and repeatable GUWs to the surface of coupons to travel along their lengths.
3. Detecting the GUWs that have propagated along the length of the coupons.

Given these constraints and the 200x30 mm gage section on every coupon, a three piezoelectric sensor setup was determined (see Figure 29). Two sensors were used on the top and bottom of the gage section for both acquiring and locating AE data and receiving the GUWs. The third sensor was placed in the center of the coupon with the sole purpose of being used as an actuator to apply the GUWs. All sensors were attached to the coupons using Dow Corning high vacuum grease as couplant to transfer elastic waves to and from the sensors with minimal attenuation. The sensors were always bonded to the flat mold side of the coupons, since the vacuum bagging side always exhibited a degree of waviness, due to the infusion process. The full details of setting up the systems as well as the best methods that were determined for attaching the sensors to the test coupons are described below.

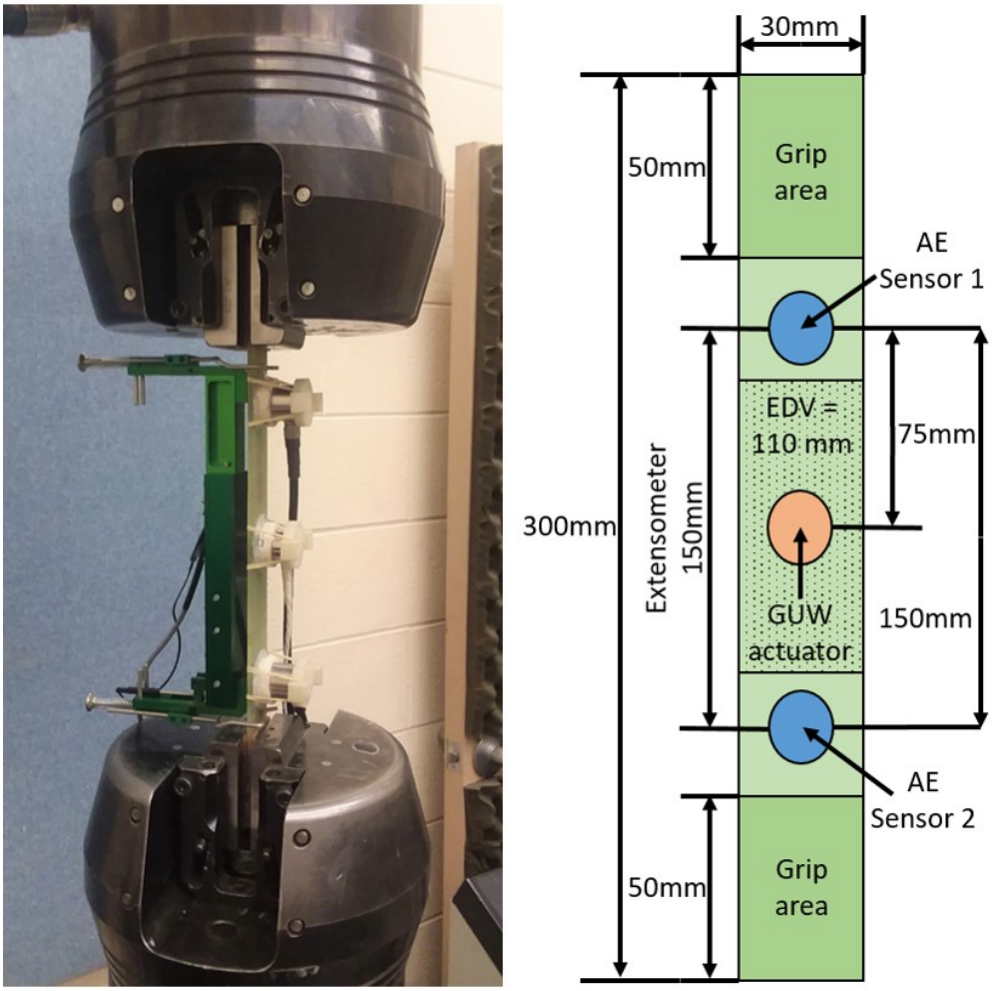


Figure 29: A photo of the test setup for static testing (left) and a schematic of the sensor setup, including dimensions related to the AE setup.

Acoustic Emission

As stated above, the AE monitoring system served the purposes of recording AE damage events in real-time throughout the loading of test coupons, receiving and recording the GUWs and recording parametric data throughout tests for moduli measurements and to link with the damage event data. For this study, a new AE system was used; Physical Acoustics 1283 USB-AE Nodes™ paired with AEWin™ for USB™ software and WSα wideband sensors. Full details can be found in Appendix C. The

previous system used by the research group is a Mistras PCI-Micro-II SAMOS system with AEWin™ for SAMOS E5.10 software and WD wideband sensors. Although very similar, there are fundamental differences between the two systems, which needed to be addressed. These differences are:

- The old system used differential sensors as opposed to single ended sensors used by the new system.
- The new system can acquire data at a higher sampling rate (10 MHz vs. 3 MHz).
- Different high pass and low pass analogue filters built into the systems.

The single ended sensors are perhaps the most important difference between the new and old systems. Single ended connections only measure a voltage difference between positive and negative wires, whereas differential sensors also have a ground connection to measure voltage differences. This means single ended connections are much more susceptible to electromagnetic noise, especially when testing with servo-hydraulic load frames. To inspect this, tests were conducted with the two systems to measure ambient electromagnetic noise in the testing lab. Both systems were set up with the same hit timing parameters (peak definition time, PDT, hit definition time, HDT, and hit lockout time, HLT), the sensor wires were connected without sensors and the thresholds reduced until they began defining ambient noise as hits. The frequency content and amplitudes of the noise were inspected and compared. Figure 30 shows the frequency content of the noise detected by the new system. It was already clear that the USB system was capable of detecting a large spike at approximately 1.4 MHz, due to its increased

sampling frequency (F_S) and despite having an analogue low pass filter (LPF) applied at 1 MHz. It was thought that this increased noise could affect the system's ability to detect events occurring in quick succession, because the signals would take longer to drop below the defined voltage threshold. Filtering below 1 MHz was thought to be the best course of action. Unfortunately, the system has a limited selection of analogue filters, which are based upon sampling frequency. For this reason, the sampling rate had to be reduced to 5 MHz to allow the second highest LPF of 600 kHz to be used. Consequently, an analogue high pass filter (HPF) of 100 kHz coincided with the LPF, which was deemed acceptable, since the WSα sensors lose sensitivity below this frequency (see Appendix C).

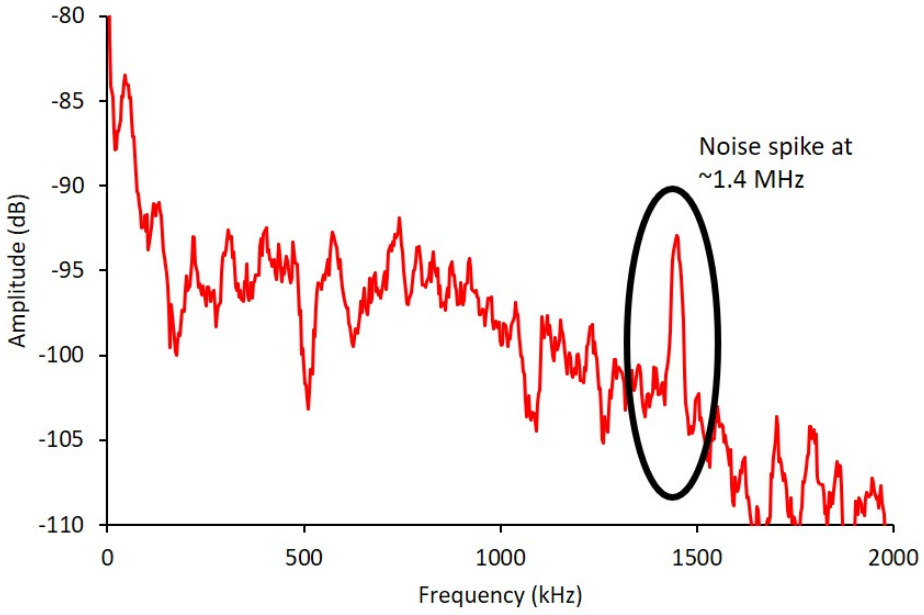


Figure 30: A Fourier transform of the electromagnetic noise detected by the USB system without sensors attached, show a significant spike at approximately 1.4 MHz.

Once the changes had been made, the noise spectrums detected by the two systems were compared again (see Figure 31). Note that the amplitudes for the new system are lower. This is due to the lower gain from the system's built-in amplifier (see Appendix C). The thresholds required to detect ambient noise as hits were 25 dB for the old system and 33 dB for the new system. For this reason, the decision was made to raise the voltage threshold of the USB system from 40 dB to 50 dB during the actual testing of coupons, so that a higher signal to noise ratio could be achieved when recording event waveforms. This was a compromise that was made, which means that the system records less low amplitude events and only the higher amplitude, more significant damage events. This was acceptable as long as the higher threshold was kept consistent throughout testing. It was assumed that the lower amplitude events are less relevant and would have little influence on the overall AE datasets.

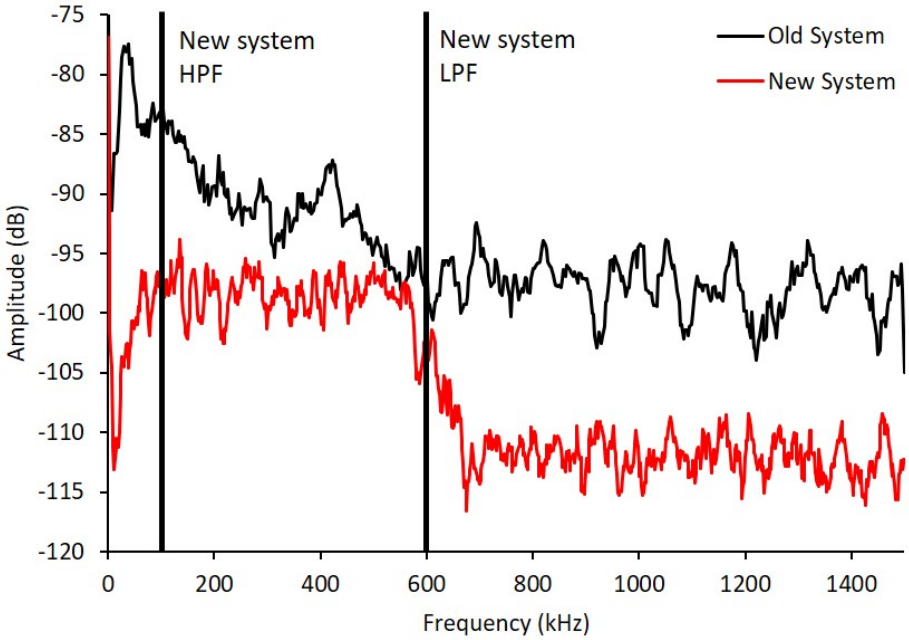


Figure 31: A comparison of the noise spectrums recorded from each system after the lower sampling rate and 600 kHz LPF had been applied to the new USB system.

The final system parameter that had to be defined in the AE software was the event definition value (EDV). This is a length based timing parameter which defines a window between the sensors in which hits are associated with events. Essentially, it allows the system to filter out any hits detected from outside of the sensors i.e. grip and machine noise. Since the sensors were spaced 150 mm apart, the EDV was set at 110 mm (see Figure 29). This allowed events to only be detected within a 110 mm window in the center of the coupon gage section and any events occurring outside of that location were discarded. This gave confidence that all damage events being recorded were definitely originating from the gage sections of the test coupons.

Finally, the system was set up to record parametric data from the load frames. For static testing, load and strain data were recorded to calculate moduli, determine ultimate failure loads and strains and associate them with the damage events that were acquired. For fatigue testing, crosshead displacement was also recorded as a backup for maximum strain measurements. All parametric data was recorded at 20 Hz (the maximum the system is capable of). As well as extracting parametric data for post-processing and evaluation, a multitude of waveform features and parameters were extracted for every damage event, with the most important being amplitude, energy content and frequency content. A number of parameters were also tracked as cumulative parameters throughout the tests to observe more generalized damage progression trends, such as cumulative energy, cumulative counts and the cumulative number of damage events detected. These parameters were used for comparisons and evaluations between tests, layups and ultimately to incorporate into the statistical modeling portion of this research.

Table 2 shows a comparison of the AE parameters used in this study for the USB system and the previous Mistras system. Slightly different thresholds and EDVs were used for the recording of the GUWs, which are explained in the proceeding section.

During testing, wave velocities through the test coupons had to be determined for the location monitoring and filtering of noise events. This was done by conducting pencil lead break (PLB) tests at known locations on the test coupons. Wave speeds were adjusted until the location monitoring was reading accurately. Since wave velocity is directly related to in-plane stiffness, each layup exhibited different wave velocities (see Table 3). These velocities were kept constant between coupons tested for each layup. In addition to assessing location accuracy, PLBs were used before every test to ensure that the event definition filter was operating correctly. PLB tests were conducted at the edges of the window where the system should be associating hits with damage events to verify that no waves originating from outside the window were defined as damage events.

Parameter	New USB System	Old Mistras System
F_S (MHz)	5	3
Threshold (dB)	50	40
PDT (μs)	50	50
HDT (μs)	100	100
HLT (μs)	500	500
Analogue HPF (kHz)	100	20
Analogue LPF (kHz)	600	400
EDV (mm)	110	110

Table 2: A comparison of AE system parameters used in this study for the new USB system with the previous Mistras system.

Layup	Wave Velocity (m/s)
$[0/90]_S$	3900
$[90/0]_S$	3900
$[90_4]$	3000
$[45/-45]_S$	3200
$[0/90/\pm45]_S$	3700

Table 3: A summary of the wave velocities used for the AE system for each layup tested, for location monitoring.

Guided Ultrasonic Waves

As shown in Figure 29, the GUWs were applied to the test coupons in the center of their gage section, to be detected by the AE sensors. The GUWs were intended to be applied at regular intervals throughout coupon tests as the coupons' damage states are increasing and their moduli and remaining usable life are decreasing. The actuator used was a WD wideband piezoelectric sensor from the old Mistras AE system, which was chosen to show that these techniques could be conducted by an array of AE sensors as part of a standalone system, with minimal additional hardware (the sensor's sensitivity curve can be found in Appendix C).

The voltage input to the GUW actuator was provided by a GW Instek AFG-2225 arbitrary function generator. For the waveform, a Dirac delta function was chosen, due to its simplicity and similarity to the waveforms produced by automatic sensors tests (ASTs) that some AE systems are already capable of conducting. It is analogous to using an impact hammer to test the vibrational response of machine parts, which is an older style of non-destructive evaluation. The voltage input was programmed as a square wave with a peak-to-peak voltage of 10 V, a duty cycle of 1% and a frequency of 2 kHz, resulting in a pulse duration of 5 μs and a primary frequency of 200 kHz. Other durations were

tested, but had negligible effects on the received waveforms, which verified that the input signal was in fact acting as an impulse. Figure 32 shows a voltage-time plot of the input signal compared with the signal received by the AE sensors, after a GUW had propagated through a coupon and been amplified by the receiving AE system.

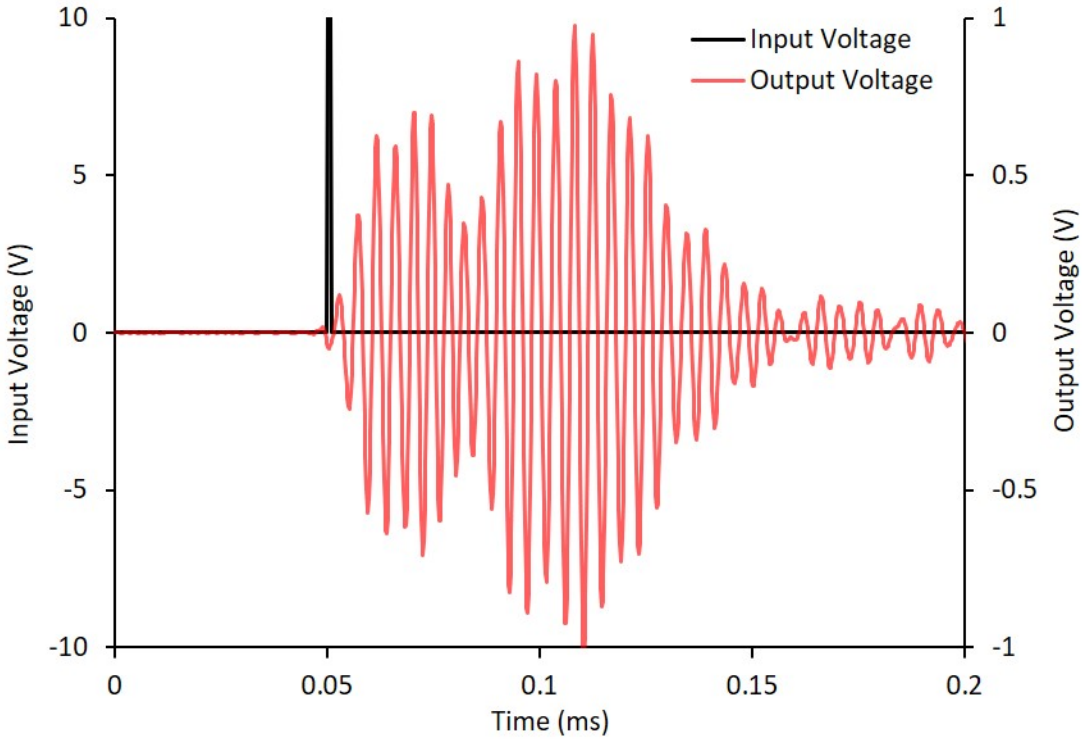


Figure 32: A comparison of the input voltage signal and the voltage signal received by the AE system after a wave has propagated through a test coupon.

To ensure repeatability between GUWs, the frequency content and respective magnitudes of subsequent GUWs were compared (see Figure 33). It was found that the received GUWs were highly repeatable, with negligible differences in frequency content and amplitude, although this was under the strict condition that the sensors were not removed and reattached or rotated throughout the duration of each test. Removing and reattaching the sensors, or even just rotating them, was found to cause notable changes in

the received waveforms. It is likely that these changes were caused by the vacuum grease couplant. Removing and reattaching or rotating the sensors could result in changing the thickness of the vacuum grease film on the sensor surfaces. When a sensor is reattached to a coupon, a slight change in clamping force could also result in a change in thickness of the vacuum grease film. The solution to this problem is explained in detail in the proceeding section. Because of this issue, the sensors were not adjusted or removed throughout the duration of each mechanical test. Despite their repeatability, five GUWs were applied during each interruption of mechanical tests for continuous validation of their repeatability during all tests.

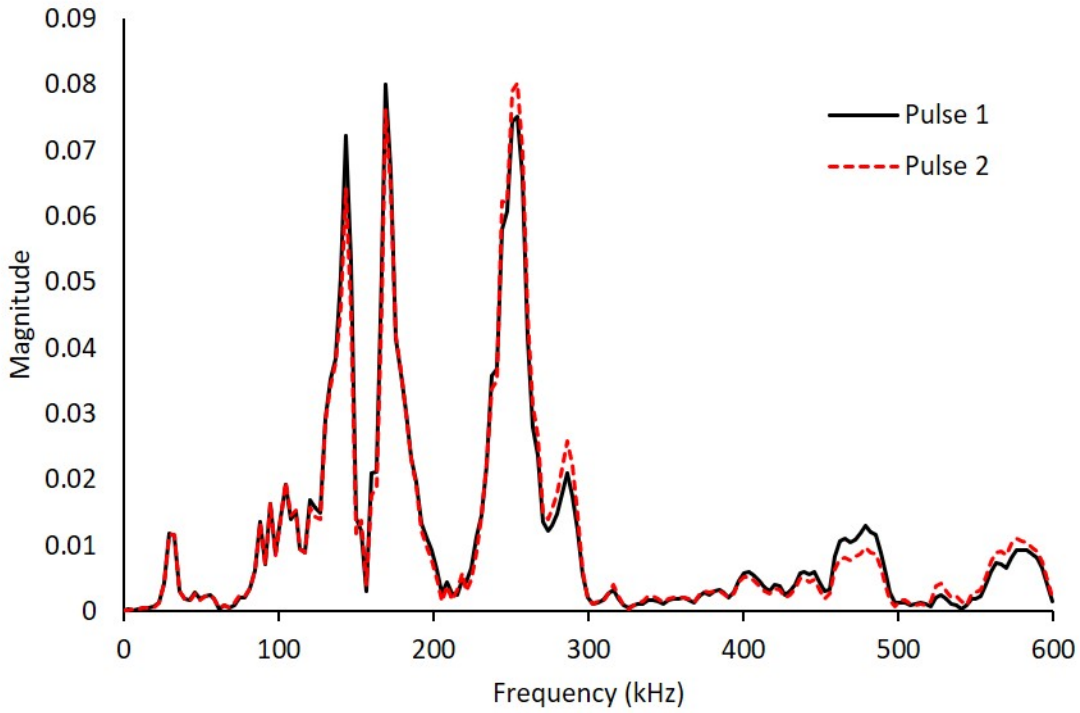


Figure 33: A comparison of frequency content and magnitude of two successive received GUW waveforms, using fast Fourier transforms.

Since the AE system was being used to detect the GUWs, it needed to be set up to do so. A small selection of parameters needed to be changed to account for certain abnormalities which arose during testing. Initial tests found that the GUWs were significantly attenuated near the end of tests, after large amounts of damage had accumulated within coupons. For this reason, the thresholds for recording the GUW data were reduced to 40 dB for static testing and 37 dB for fatigue testing. This was acceptable, since a known number of waveforms were to be recorded and any events originating from noise could easily be removed from the datasets manually. Initial testing also showed that the location monitoring significantly lost accuracy in the later stages of tests, due to the attenuation of the waves. This was because the system makes its location calculations based on the times the waveforms cross the specified threshold. Some waveforms showed that they actually started a noticeable amount of time before crossing the threshold, resulting in inaccurate location calculations (see Figure 34). If the location error exceeded the EDV window then the GUWs were not detected. Because of this, the EDV was increased to 140 mm (still smaller than the distance between the sensors) for recording the GUWs. Once again, additional noise detection was not a concern since noise events could easily be removed from the dataset. For these changes, a separate layout was made for the AEWin™ software which could easily be loaded during the interruptions to avoid any human errors in forgetting to revert system parameters when switching back to AE monitoring.

Like AE, a multitude of important waveform features and parameters were extracted during post-processing, such as amplitude, MARSE (measured area under the

rectified signal envelope) energy, absolute energy, rise time, duration, counts, peak frequency and centroid frequency. These parameters were used to make comparisons between tests, layups and ultimately for the modeling portion of this research.

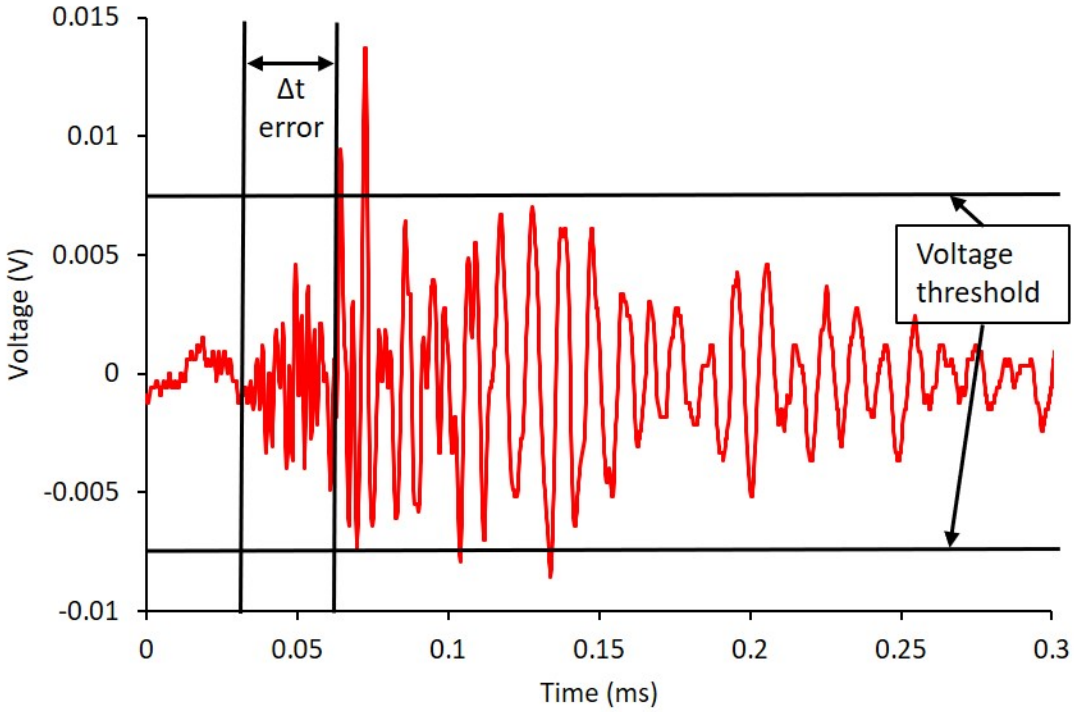


Figure 34: An example waveform showing how the location monitoring can become inaccurate after the GUWs have been significantly attenuated.

Sensor Attachment

As mentioned above, movement of the sensors during testing had noticeable effects on the GUW results, so close attention was paid to the method in which sensors were attached to the test coupons. For this, two main issues had to be addressed:

1. Damage to the sensors caused by explosive strain energy release when coupons fail (particularly laminates with 0° plies).

2. Inaccuracy of GUW measurements, due to slippage and movement of the sensors.

Previously within the research group, plastic hand clamps were used to attach the AE sensors to test samples (see Figure 35). It was suspected that these clamps led to variability in clamping forces, were too stiff so that the strain energy release at failure was transferred directly to the sensors, causing damage, and that the sensors can still slip and move during testing, due to the thin film of vacuum grease couplant beneath them.

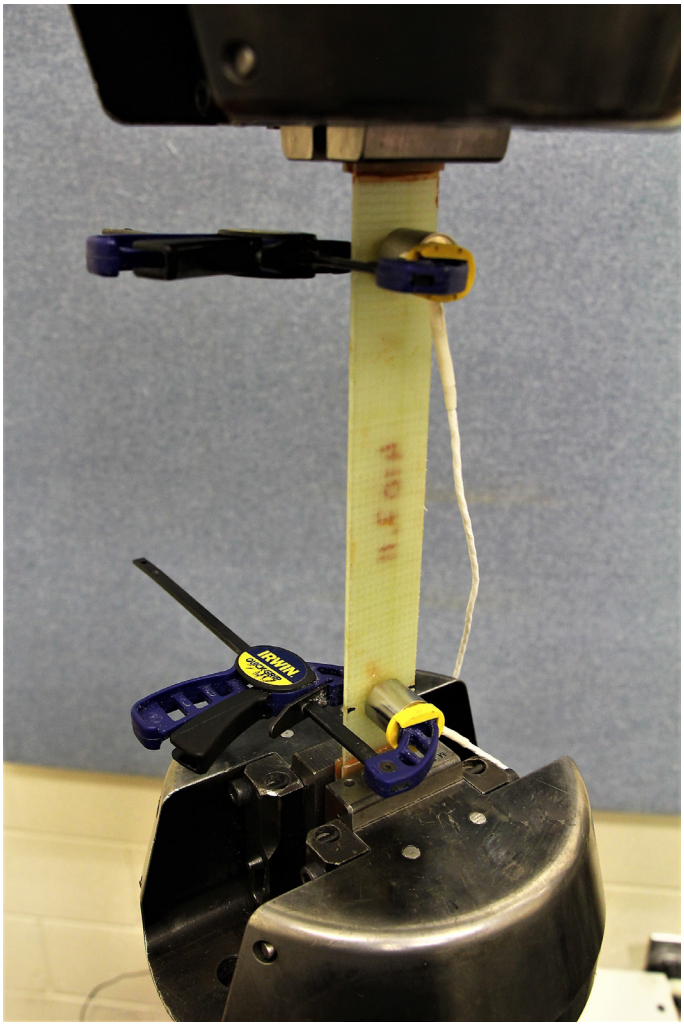


Figure 35: A photo of the previous hand clamp method used to attach the AE sensors to test coupons.

The first issue was overcome by developing a more compliant clamping method, which was still capable of applying sufficient pressure to the sensors to keep them in place. Small caps were manufactured by 3D printing, which would fit on top of the sensors. The caps had tabs on either side which allowed attachment and sufficient clamping force to be applied using rubber bands wrapped around the coupon (see Figure 36). It was also found that the rubber bands were compliant enough to allow the sensors to move during unexpected, explosive ultimate failures, meaning that the strain energy release was not transferred directly to the sensors and was absorbed by the rubber bands.

The second issue listed was remedied by machining cylindrical sleeves, which could be bonded to the surfaces of test coupons, for the sensors to slide into and be held in place (see Figure 36). For static testing they were bonded to the coupons using hot melt glue, which could be conducted quickly for each test. In fatigue testing it was clear that hot melt glue would not be sufficient to hold the sleeves in place throughout the duration of tests. Instead, a compliant silicon adhesive was used, which required 24 hours to cure. The sleeves proved to effectively prevent the sensors from slipping and mitigate the possibility of misleading results from the GUW data, particularly during long and sometimes erratic fatigue tests.

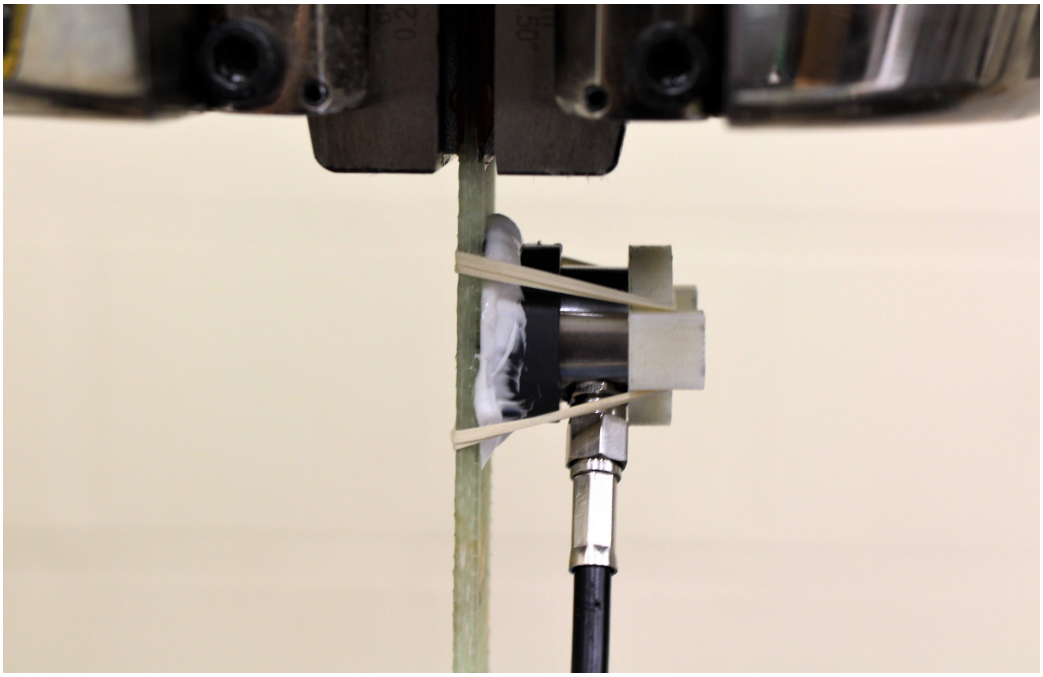


Figure 36: A photo of the sensor caps and sleeves used to attach a sensor to a test coupon using rubber bands.

Static Testing

Static tensile testing was ultimately used to test the concept of combining AE and GUWs to monitor damage progression and assess damage states, while also using the data to predict changes in moduli, due to damage. This testing was used as a starting point, before progressing to the more complex and realistic fatigue loading.

All of the static tensile testing was conducted on an electro-mechanical load frame with hydraulic wedge grips and an Instron 8562 controller. Testing generally followed ASTM D3039 standard test method for tensile properties of polymer matrix composite materials. All test coupons were loaded at a crosshead speed of 1.3 $mm.min^{-1}$.

Strain was measured using an Epsilon 3543 extensometer, with a 152 mm gage length (see Figure 37). Strain measurements were primarily used to calculate moduli, but

also proved useful for measuring ultimate failure strains. Usually, either strain gages or smaller gage length extensometers would be used to measure strains during tensile tests, but they only measure strains over small, localized areas of test coupons. Because AE and GUW data were being acquired over almost the full gage length of each coupon, the long gage length extensometer was thought to be more representative for the tests being conducted. Using the larger extensometer essentially meant that the measured strains and any discontinuities were averaged across the gage length of the coupons. Additionally, the large extensometer was much more robust than the smaller extensometers. The smaller extensometers usually have to be removed from the test coupon before ultimate failure to avoid them being damaged, due to explosive strain energy releases. The large extensometer could safely be left on the coupons during failure, which meant that ultimate failure strains could be recorded.



Figure 37: Epsilon 3543 extensometer with a 152 mm gage section used for all static tensile testing.

Benchmark Testing

Before combining the AE and GUW measurement techniques, it was important to gain an initial understanding of how the different layups failed under static tensile loading and to check for consistency and repeatability of the moduli measurements. Also, to apply the GUWs, tests needed to be interrupted. It was important to acquire this data to validate that interrupting the static tests would not have any effect on the final results and that tests conducted with interruptions are still representative of monotonic static tensile tests. There was a small possibility that the interruptions for applying the GUWs could affect the overall damage state of the test coupons, whether they are conducted under load (creep effects) or fully unloaded (fatigue effects). For this, initial moduli and failure stresses could be acquired to compare with the tests conducted with the GUWs to validate the testing procedures. Also, tangent moduli could be calculated from the stress strain curves to compare with the changes in moduli measured during the static tests with the GUWs.

AE monitoring was also used as a tool during the benchmark testing, since it is a continuous, passive monitoring technique that has no effect on the damage occurring within the test coupons. AE was implemented during this phase of testing to:

- Determine the stresses and strains of the onset of damage within each coupon.
- Track damage progression occurring within the coupons to compare with the stress-strain curves.

- Further validate the use of interruptions to apply the GUWs and ensure that the AE data trends are comparable between static monotonic loading and interrupted loading.

The same system and sensor setup described in the "Acoustic Emission" section of this chapter was used to ensure that accurate comparisons could be drawn. A summary of the coupons tested for this phase of testing are provided in Table 4.

Layup	Coupons Tested
$[0/90]_S$	4103_12
	4108_15
	4108_16
	4108_17
	4108_18
$[90/0]_S$	4109_11
	4109_12
	4109_13
	4110_05
	4110_06
$[0/90/\pm45]_S$	4120_04
	4120_05
	4120_06
	4120_07
	4120_20
$[45/-45]_S$	4116_05
	4116_06
	4116_07
	4116_08
	4116_09
$[90_4]$	4113_14
	4114_25
	4114_26
	4114_27
	4114_28

Table 4: A summary of the layups and coupons tested for acquiring benchmark stress-strain and AE data.

Load-Unload-Reload Testing

Continuing on from benchmark testing, a test method needed to be developed to acquire data to be applied to the statistical modeling portion of this research. The requirements for the test method were as follows:

- Incrementally increase damage states within the coupons through tensile loading until ultimate failure.
- Obtain accurate moduli measurements for each damage state.
- Track changes in the propagation of the GUWs for each damage state.
- Record AE data during the changes between subsequent damage states.

To provide increasing damage states within coupons, loads were applied incrementally. As stated previously, the tests needed to be interrupted to apply the GUWs. First, increasing load-unload-reload (LUR) test were conducted where the GUWs were applied under the applied load of each LUR step and under no applied load. This was to investigate the effects of applied load on the propagation of the GUWs; a phenomenon that has been investigated by several other researchers [42, 84-86]. A comparison of the results are shown in Figure 38. It was found that applied load did have a significant effect on the attenuation of the GUWs, which also appeared to be amplified after damage was introduced to the test coupons. Also, during the testing some creep effects were observed in the AE data. Events were still be detected when the load frame was paused and held at the specified loads. Therefore, GUWs were only applied when test coupons were fully unloaded for subsequent tests, to remove any possible

uncertainties from creep effects and to remove the effect of conducting the GUW tests under different applied loads.

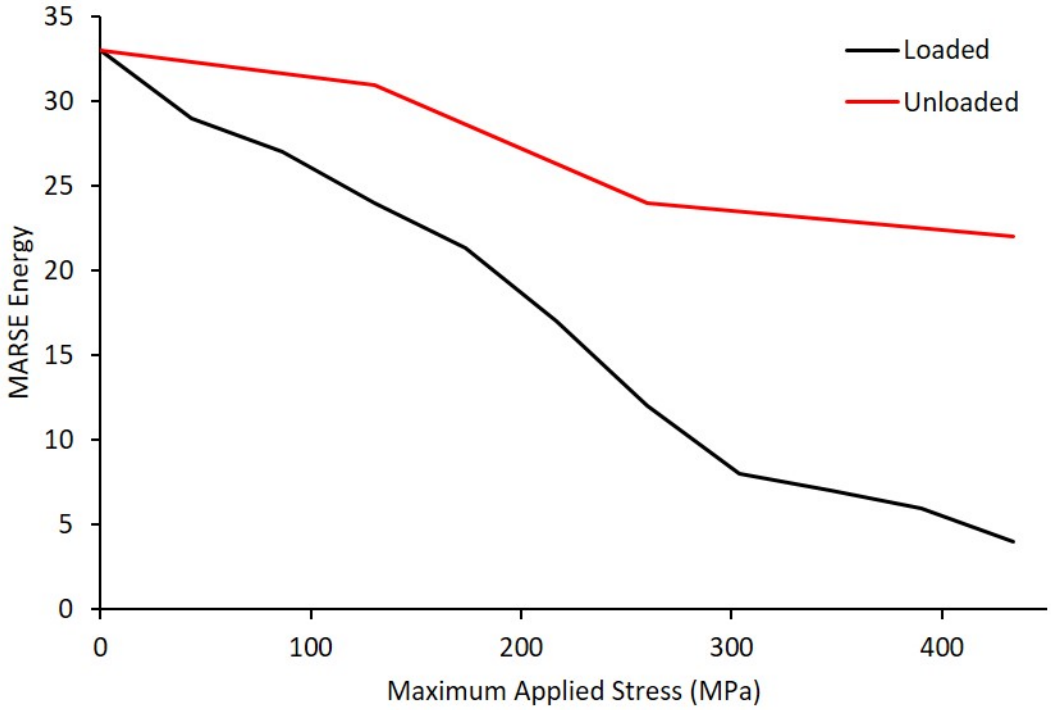


Figure 38: A plot of GUW energy attenuation against maximum applied load for an incrementally increasing LUR test to compare the effect of applied load on the attenuation of GUWs.

The influence of applied load on the attenuation of GUWs led to the finalized increasing LUR test method. Increasing damage states could be introduced to test coupons through incrementally increasing load steps, in which AE monitoring could also be applied, and the GUWs could be applied at the end of each unload to eliminate the effects of applied load. The loading steps also served the purpose of recording representative stress-strain data for each damage state, without the influence of additional damage being introduced. Figure 39 shows a strain-time plot indicating how AE and

GUW data were acquired. Originally, each LUR step was defined by maximum load, but was found to result in very specific groupings of moduli changes for certain layups (particularly the [90_4] layup). For this reason, strain steps were used instead. Increasing steps of 0.25% strain were used for each LUR cycle until ultimate failure. It should be noted that test coupons were still unloaded to zero load rather than zero strain. Once cracks had initiated and propagated, their surfaces did not mesh together properly during unloading, meaning that there was a noticeable amount of irrecoverable strain in the latter stages of tests. If the coupons were unloaded to zero strain then there was a possibility of introducing compressive stresses and buckling the test coupons.

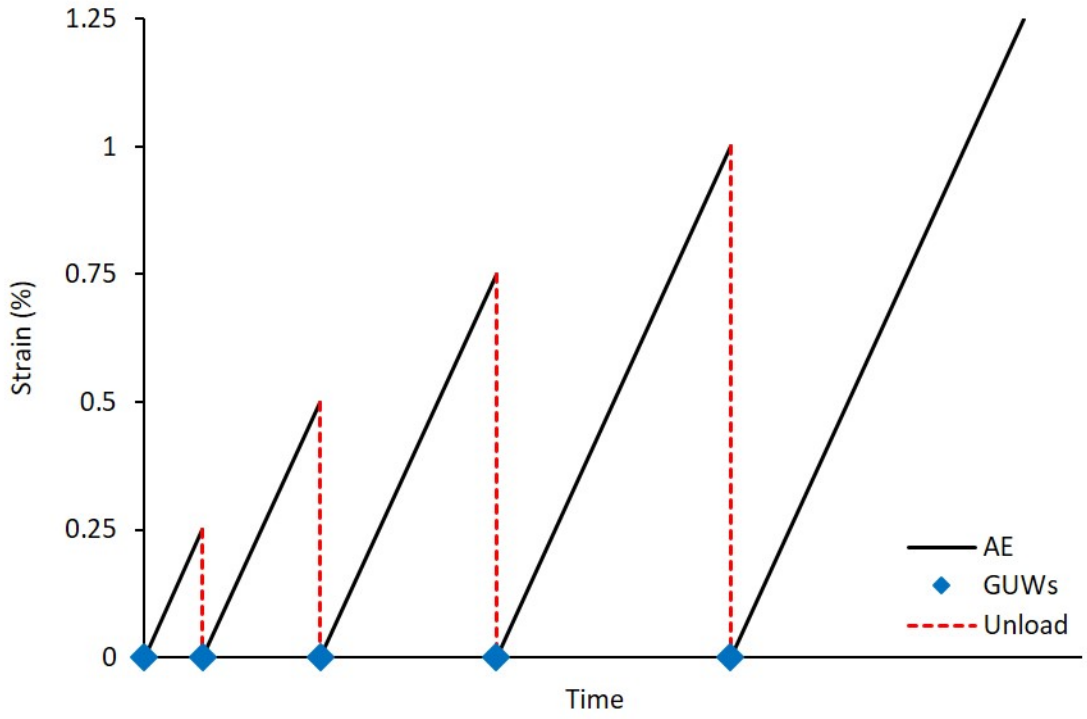


Figure 39: A strain-time diagram displaying how increasing damage states were introduced to coupons with the acquisition of AE and GUW data indicated.

Coupons of all layups except the $[45/-45]_S$ layup were tested using this procedure. Benchmark testing showed that they displayed highly non-linear stress-strain curves, even before damage had initiated (indicated by the AE data). Also, they exhibited very random, localized damage states, which resulted in ultimate failure. These phenomena are explained in detail in the proceeding chapter. Table 5 shows a summary of the final layups and coupons tested using the described procedure. Of course, far more coupons were tested to refine the procedure and several others had to be discounted, whether it was because of premature grip failures, the extensometer slipping and yielding inaccurate strain data, sensors becoming dislodged due to fiber tows splitting on the surface or simply human error during data acquisition. The data from the final coupons shown in Table 5 are the ones used for the statistical modeling portion of this research.

Layup	Coupons Tested
$[0/90]_S$	4103_01
	4103_03
	4103_04
	4103_05
	4103_06
	4103_07
	4103_11
$[90/0]_S$	4109_02
	4109_03
	4109_08
	4109_09
	4109_10
	4110_01
	4110_03
$[0/90/\pm45]_S$	4120_10
	4120_11
	4120_12
	4120_15
	4120_16
	4120_17
	4120_19
$[90_4]$	4113_06
	4113_07
	4113_08
	4113_09
	4113_10
	4113_11
	4113_12

Table 5: A summary of the layups and final coupons tested using the increasing LUR procedure, while acquiring AE and GUW data.

Fatigue Testing

The static tensile testing phase of this research was used as a proof of concept for combining the GUW and AE monitoring to evaluate laminate damage states and predict modulus degradation due to damage. The results were used to construct and evaluate the first set of statistical predictive models (see Predictive Modeling Results and Discussion). The models showed excellent predictive capabilities. Therefore, testing was continued to

fatigue loading, which is considered a more realistic loading scenario and is more representative of the loading histories experienced by real-life composite structures.

Fatigue tests were conducted on a servo-hydraulic load frame with hydraulic grips and an Instron 8500 controller. In this research, test coupons were only tested in tension-tension fatigue ($R = 0.1$). This was so that GUW data, AE data, moduli data and the respective statistical models constructed from them could be compared with the static tests. Also, compression samples are required to be a much smaller geometry to prevent buckling, meaning that it would not be possible to incorporate the piezoelectric sensors for AE and GUW monitoring.

Due to the flow rate limitations of the hydraulic pump, coupons could only be tested at a maximum of 0.85 cycles per second. This led to the decision to only conduct the tests with GUWs and AE at one stress level, as a further proof of concept. If one stress level worked well then there would be a possibility to expand to more stress levels in the future. This meant that full S-N curves could not be constructed from the test data. Ideally, a stress level had to be chosen that resulted in failure in approximately 10,000 to 20,000 cycles, so that each test took no longer than a day to complete.

Preliminary tests were conducted on each layup to determine the optimum maximum stresses to achieve failures in the 10,000-20,000 cycle range, whilst also applying the AE monitoring to track damage progressions. Initial stress estimations were based on S-N curves previously constructed for the Vectorply E-LT 5500 fabric (see Figure 40); very similar to the E-LT 3800, but with a higher areal weight. The results showed that a maximum first cycle strain of 1.2% was optimal for tension-tension fatigue

failures in the 10,000-20,000 cycle range. This was reflected by the $[90/0]_S$ layup which used the same stress level. For the $[0/90/\pm45]_S$ layup, stresses were originally reduced to meet the estimated 1.2% first cycle strain criteria, but it was found that failures consistently occurred above 20,000 cycles. Instead, the same maximum stress level as the $[0/90]_S$ and $[90/0]_S$ layups was used, which increased the maximum first cycle strain, but still resulted in failures close to 10,000 cycles. Table 6 shows the maximum stress levels used to test coupons from each layup.

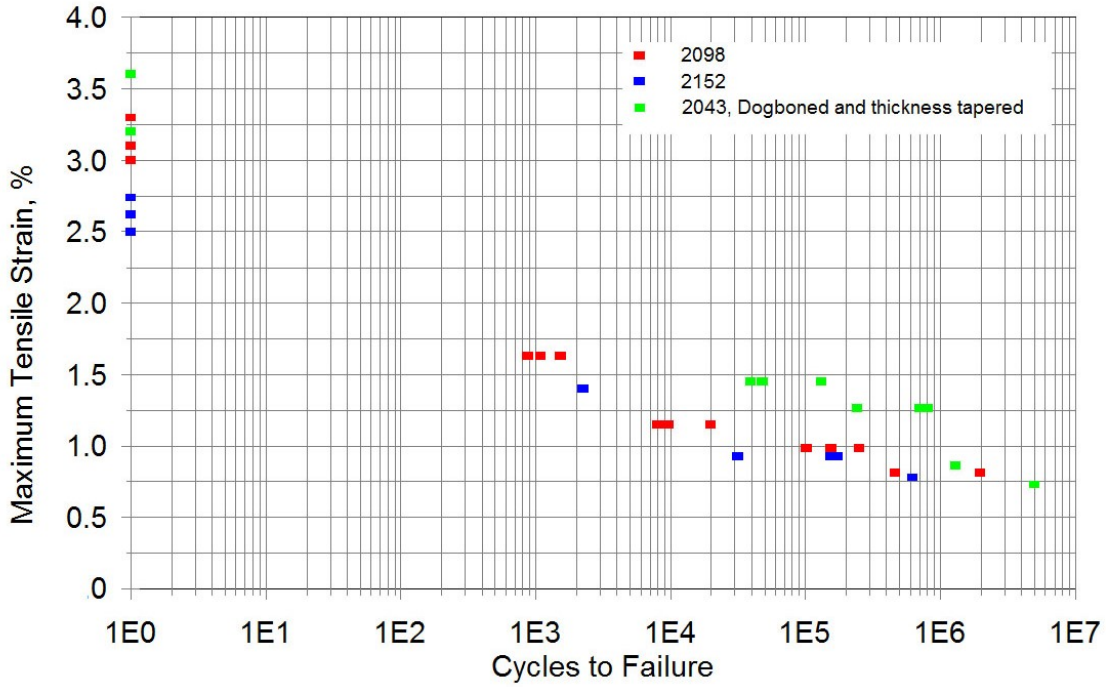


Figure 40: First cycle strain against cycles to failure for the Vectorply E-LT 5500 fabric with the Hexion 135/1366 resin system, constructed from previous tests conducted at MSU.

Layup	Coupon Tested	Maximum/Minimum Stress (MPa)	Test Type
$[0/90]_S$	4103_16**	482 / 48.2	AE only
	4103_17**	379 / 37.9	
	4103_18**	276 / 27.6	
	4103_19**		
	4103_20**		
	4103_21**		
	4103_22**	310 / 31	
	4103_23**		
	4103_24**		
	4107_01**		
	4107_02**		AE and GUWs
	4107_03**		
	4107_04**		
	4107_05		
	4107_06		
	4107_07		
	4107_08		
	4107_09		
	4107_10		
$[90/0]_S$	4110_08	310 / 31	AE only
	4110_09		
	4110_12		AE and GUWs
	4110_13		AE only
	4110_14		AE and GUWs
	4110_15		
	4110_17		
	4110_19		
$[0/90/\pm45]_S$	4120_21	275 / 27.5	AE only
	4120_22	310 / 31	
	4120_23		
	4120_24	275 / 27.5	
	4120_25	310 / 31	
	4121_01		AE and GUWs
	4121_02		
	4121_03		
	4121_04		
	4121_05		

Table 6: A summary of the layups, maximum stresses and coupons tested during the fatigue phases of testing.

** No crosshead displacement data recorded

The Epsilon extensometer used in static testing was not rated for fatigue, so could not be used for this portion of testing. It was also found to be too large to fit within the grips of the servo-hydraulic load frame. Instead, an Instron extensometer with a 12.7 mm gage section was used to monitor strain (see Figure 41). Preliminary tests found that strain measurements became inaccurate and sometimes erratic in later stages of the fatigue tests, particularly when test coupons exhibited large amounts of edge splitting, tow breaks and delaminations. Because of this, cross-head displacement was also measured as a backup. Although not ideal, often affected by grip slippage and possibly inaccurate due to machine compliance, it proved useful for tracking relative changes in displacement, which could loosely be extrapolated out to modulus degradation.

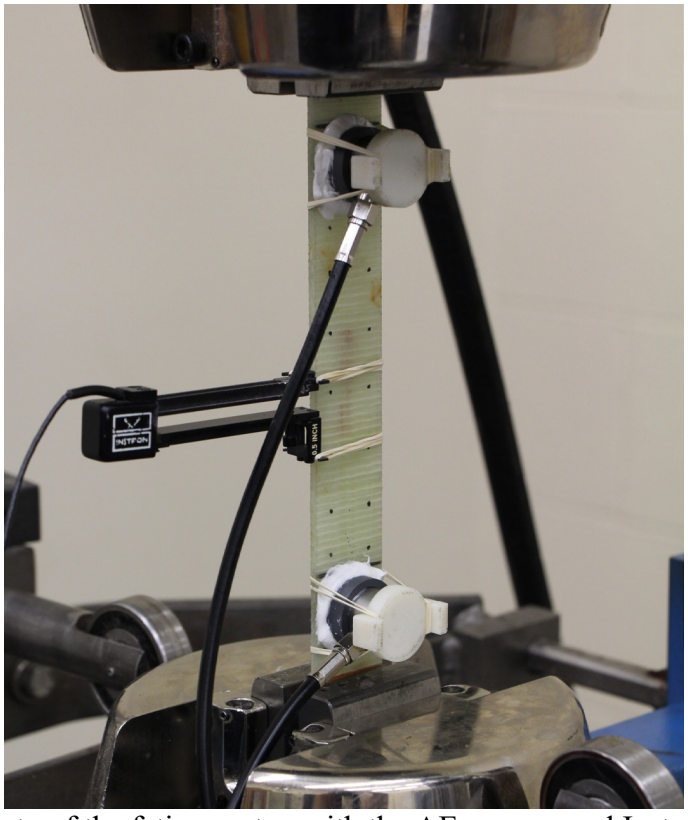


Figure 41: A photo of the fatigue setup with the AE sensors and Instron extensometer attached.

After the maximum stress levels had been determined and the test method refined, testing was continued to interrupted fatigue tests with the GUWs. Coupons were fatigue for a specified number of cycles, unloaded to apply the GUWs, reloaded up to their average load which recorded stress-strain data, and then fatigue cycles were continued. Initial cycle intervals were based on a logarithmic scale (i.e. 1, 10, 100, 500, 1000, 2000 cycles etc.) and then every 1000-2000 cycles. These intervals were continued until significant changes in the damage of the coupon were observed, such as large fiber tow failures and delaminations. At this point, interruptions were conducted when necessary. This interval process ensured that most measurements were taken at the points in the coupons' fatigue lives where they exhibited the most dramatic changes in moduli; approximately the first and last 10% (see Figure 9).

Overall, the experimental process applied to the fatigue testing made it less challenging to obtain consistent modulus degradation curves and relatively consistent numbers of cycles to failure, although it should be noted that fatigue tests generally exhibit a large degree of statistical scatter, which is best described on a logarithmic scale. Table 6 shows the layups tested, the stress levels used, the individual coupons tested and which tests were interrupted to include the GUW measurements. As stated earlier, significantly more of the $[0/90]_S$ coupons were tested to gain initial estimates in the stress levels required and to refine the test method. The $[90_4]$ layup was not tested in fatigue. Static testing showed that it exhibited unusual damage progression trends, which are not really representative of what might be expected in large composite structures, primarily due to the fabric architecture. It is not a true transverse layup, because of the backing

tows, and also showed a lot more variability in maximum strain to failure. The proceeding chapter provides more details on these phenomena.

Damage Observation Techniques

AE monitoring is a good tool for detecting damage events and tracking damage progressions in real-time, but it is still hard to gain a true understanding of the damage modes occurring within the laminates from the resulting waveforms. Because of this, other observation techniques were implemented to relate damage mechanisms back to the AE data and aid in assessing the trends in damage progressions observed.

Initial visual observations gave some insight into the final failure modes, but nothing more. Transmitted light scans of full coupons also proved to be a useful technique to observe crack directions and densities, as well as the extent of ply delaminations. Further optical microscopy of some coupons allowed for closer inspections of these cracks and delaminations. As shown in Figure 7, some test coupons exhibited more explosive failures, so it was not possible to conduct these techniques on coupons that had surpassed ultimate failure. Because of this, some test coupons were chosen to be loaded up to specific strains before ultimate failure to make closer observations of the damage mechanisms. In static testing, some test coupons were loaded up to damage initiation strains (~0.6% strain), and others were loaded close to ultimate failure (2.5% strain). Coupons loaded up to damage initiation strains were ground and polished through the thickness to observe the size and depth of cracks to refer back to AE data that was acquired. From these coupons, cross-sections were cut and cast in clear resin to be observed under the optical microscope (see Figure 42).

The same cross-sections were used for scanning electron microscopy (SEM) to further observe the extent to cracks, shapes, directions and positions within or between the fiber tows in more detail. Sanding a polishing the cast cross-sections to prepare them for SEM is a highly time consuming process, so not all layups could be observed for each loading scenario. Ultimately, the imaging and observation portion of this research is provided as supplementary details to the main research, to further understand the experimental data.

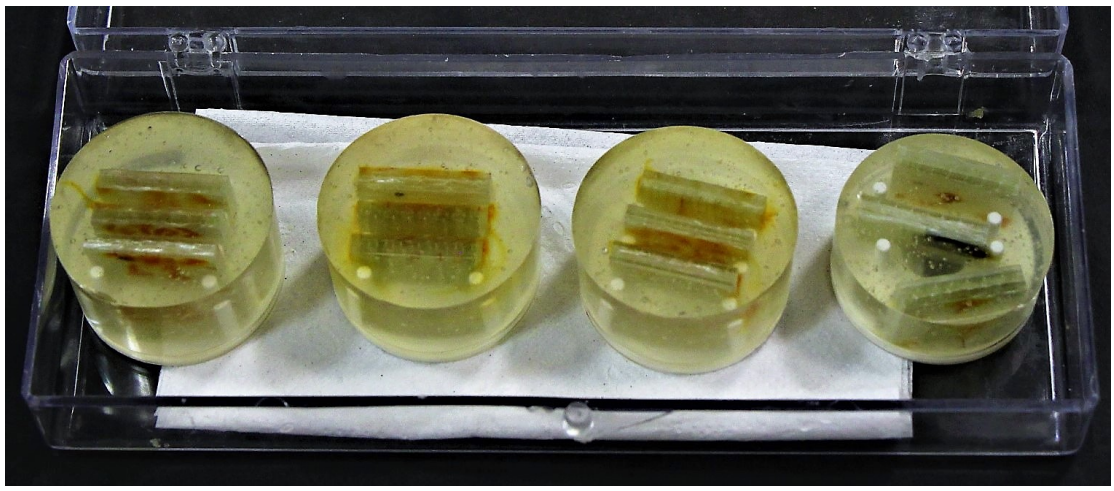


Figure 42: An example of a cross-section cast in clear resin and prepared for SEM observations.

STATIC TESTING RESULTS AND DISCUSSION

Static tensile testing was used as a starting point to acquire data to test the hypothesis that GUW and AE techniques can be combined to effectively track damage progressions and predict changes in moduli of GFRP laminates more accurately. This chapter provides a full evaluation of all the data acquired during static tensile testing, from benchmark monotonic static testing with AE, to the novel increasing LUR procedure to apply GUWs and AE monitoring while measuring moduli of incrementally increasing damage states. The benchmark test data is also used to validate the new LUR procedure, through comparing ultimate strengths, strains and AE data.

Benchmark Tests

To begin comparisons between layups, ultimate failure stresses (σ_{ult}) are compared (see Table 7). σ_{ult} was taken as the maximum stress attained by each coupon tested. As expected the $[0/90]_S$ and $[90/0]_S$ layups displayed very similar ultimate strengths, although there was a much larger degree of statistical scatter related to the $[90/0]_S$ tests. This was likely due to gripping issues. The $[90/0]_S$ coupons did not have end tabs, while the $[0/90]_S$ coupons did. The final failures of the coupons were not recognized as grip failures, but it is likely that the gripping effects could still have led to some premature failures. Naturally, the quasi-isotropic layup experienced lower ultimate stresses, due to the inclusion of the biaxial ±45° fabric, but did hold significantly more load because of its increased thickness. The most interesting comparison that can be drawn from the ultimate failure stresses are from the $[90_4]$ and $[45/-45]_S$ layups. The

transverse layup is noticeably stronger than the $[45/-45]_S$ layup. This can be explained by the Vectorply fabric architecture. The small percentage of transverse backing tows stitched into the fabric meant that the $[90_4]$ layup is still constructed of approximately 9% longitudinal fibers, which made a significant difference to its load carrying capacity. This feature of the fabric was also the likely cause of the increased experimental scatter for the $[90_4]$ layup. Figure 24 shows that the backing tows are randomly spaced and not very well aligned. This meant that some coupons may have had more tows aligned in the 0° direction than others, when cut from the manufactured laminates.

Layup	σ_{ult} (MPa)
$[0/90]_S$	572 ± 24
$[90/0]_S$	615 ± 39
$[0/90/\pm45]_S$	502 ± 18
$[90_4]$	104 ± 10
$[45/-45]_S$	80.4 ± 1.2

Table 7: A comparison of ultimate failure stresses for each layup, with standard deviations.

Figures 43-47 show the stress-strain plots for each layup of all the coupons tested during this phase of testing. All stress and strain data has been smoothed with a 10 point moving average to reduce the effects of noise during acquisition. It should also be noted that some stress-strain curves have been truncated due to the extensometer being knocked out of place when removing the AE sensors close to ultimate failure. The stress-strain plots show that layups generally exhibited consistent results between coupon tests. The plots for each test of each layup are tightly grouped before the onset of damage, which indicates the coupons were manufactured to an acceptable quality.

The $[0/90]_S$, $[90/0]_S$ and $[0/90\pm45]_S$ layups all exhibited very distinct bilinear trends, with knees at approximately 0.45% strain. These knees signify the initiation of damage, most likely in the form of matrix cracking, as stresses are transferred from the matrix to the 0° tows. Some major tow breaks can be observed at higher strains (seen as sudden drops in stress) in some of the tests, before ultimate failure. Figure 48 shows stress-strain curves for these three layups on the same axes to compare. Aside from the reduced stiffness of the $[0/90/\pm45]_S$ layup, they exhibit almost exactly the same trends. This suggests that the addition of the ±45° biaxial plies has very little effect on the damage progression of the laminate in static tensile loading, other than reducing its stiffness.

The $[90_4]$ stress-strain curves also exhibit a very significant knee at a similar strain level, but the curves show a lot more variation after this point. Once again, this is likely due to the more random distribution of backing tows, which are arranged in the loading direction. Significant amounts of transverse matrix cracking were observed around this point and all coupons experienced a large degree of softening, before loads were transferred to the backing tows. Once the coupons were saturated with transverse cracks, the stress-strain curves show that their stiffness seemingly increases again before ultimate failure.

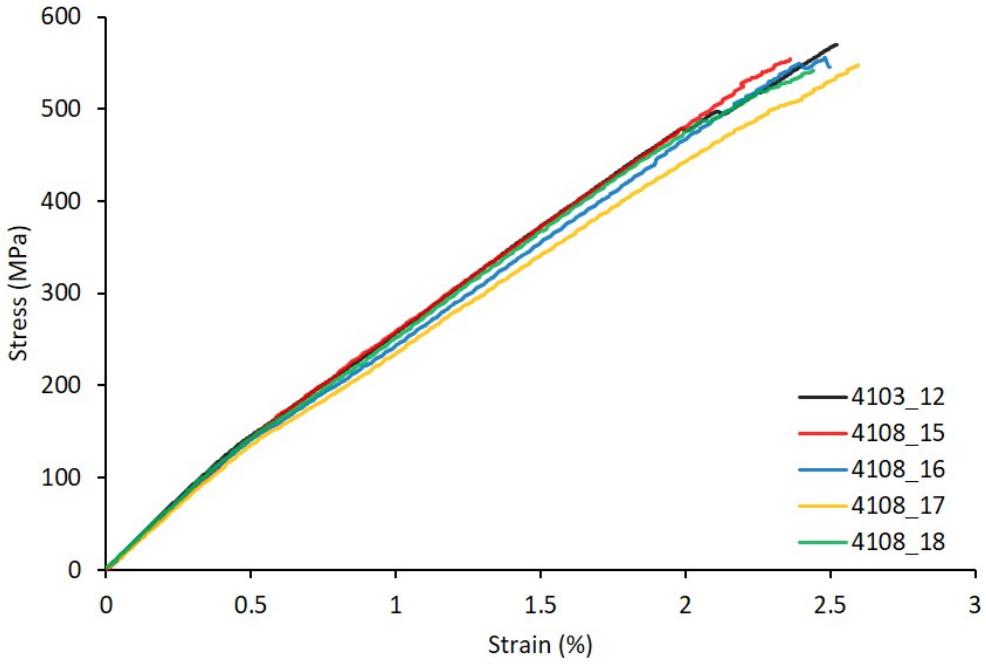


Figure 43: Stress-strain curves for the $[0/90]_S$ coupons tested under monotonic static tensile loading.

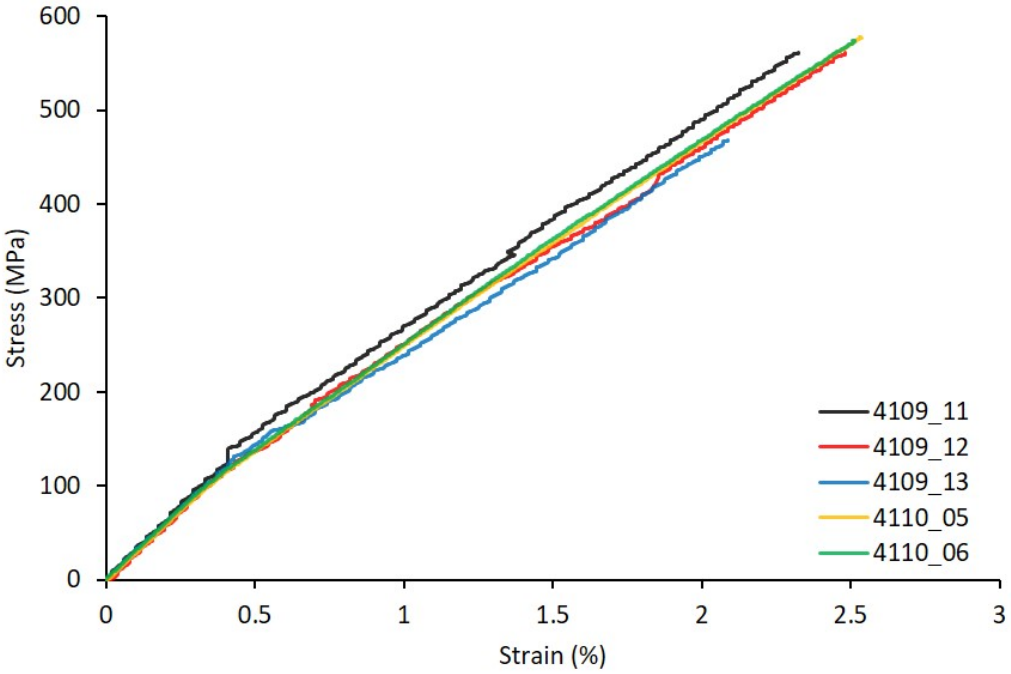


Figure 44: Stress-strain curves for the $[90/0]_S$ coupons tested under monotonic static tensile loading.

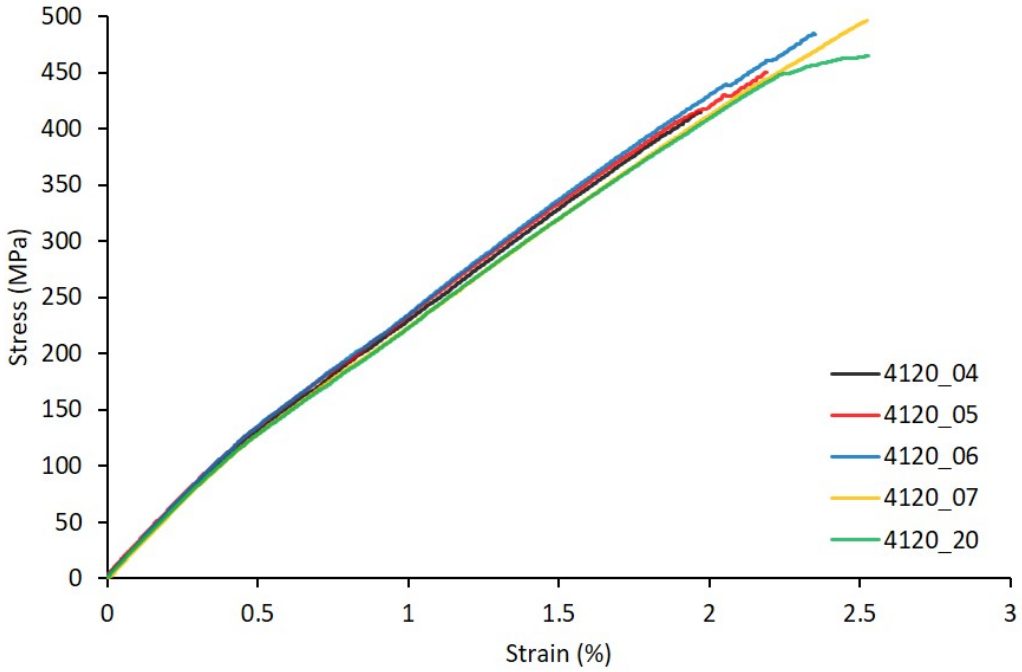


Figure 45: Stress-strain curves for the $[0/90/\pm45]_S$ coupons tested under monotonic static tensile loading.

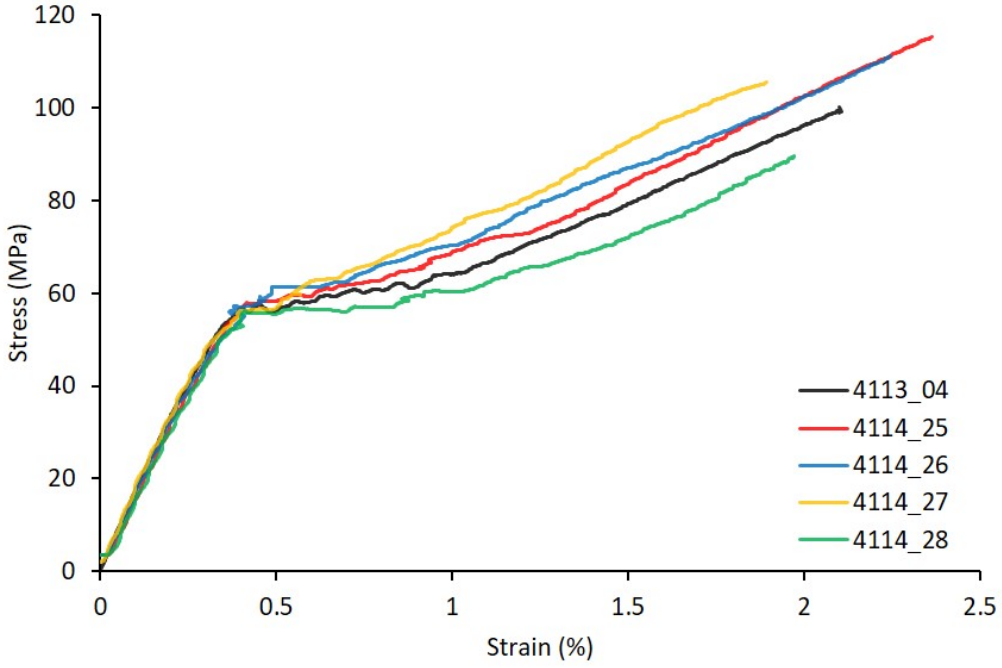


Figure 46: Stress-strain curves for the $[90_4]$ coupons tested under monotonic static tensile loading.

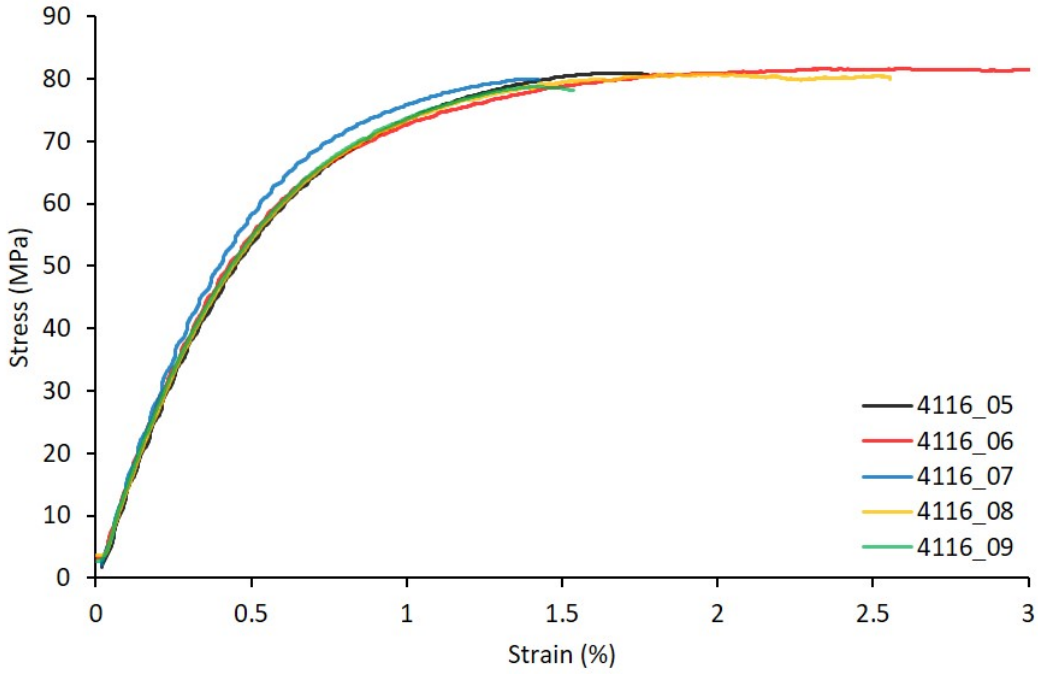


Figure 47: Stress-strain curves for the $[45/-45]_S$ coupons tested under monotonic static tensile loading.

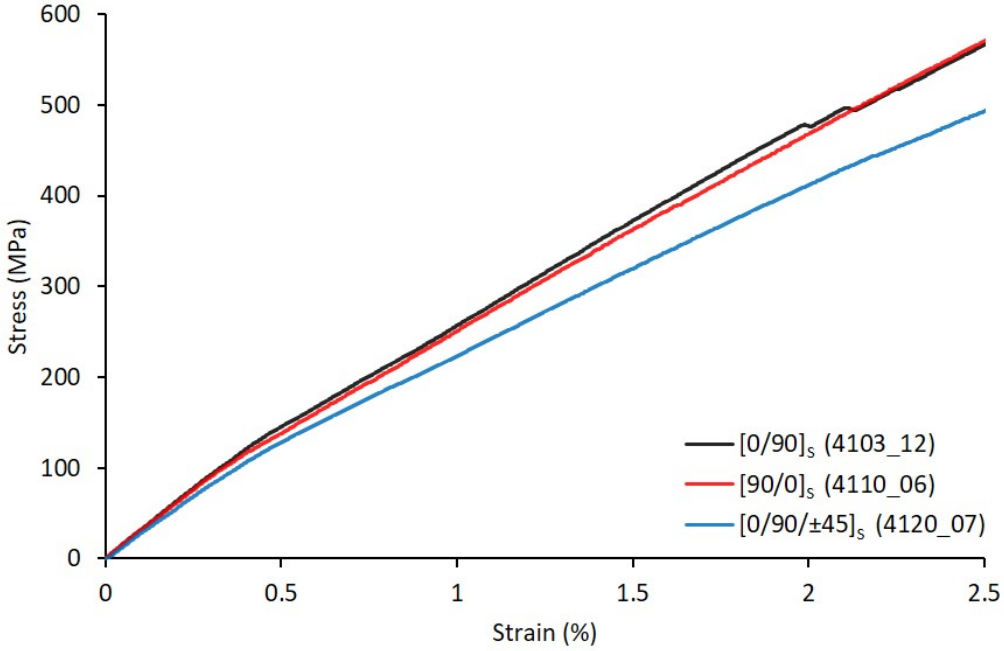


Figure 48: A stress-strain plot to compare trends between the $[0/90]_S$, $[90/0]_S$ and $[0/90/\pm45]_S$ layups.

The stress-strain plots for the $[45/-45]_S$ layup are very different to the other layups. All curves appear highly non-linear and it is not clear exactly where damage initiates. This problem was addressed using AE, which is further discussed in the proceeding sections. It is clear that the maximum strains to failure are highly variable. This is because coupons failed in a very localized manner (see Figure 49). The recorded maximum strains were highly dependent on the location of final failure. If failure occurred outside of the extensometer gage section, then strains would appear to reduce as the coupon's overall load carrying capacity degraded and the rest of the coupon contracted again. The non-linearity in the stress-strain curve and random locations of ultimate failure resulted in this layup not being used for further testing. It would be possible to encourage failure in the center of coupons through machining them into dog-bone geometries, but this would likely have a negative or unpredictable effect on the AE and GUW monitoring during testing.

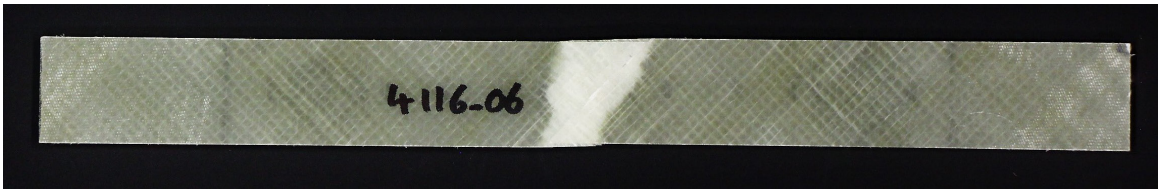


Figure 49: A photo showing the localized failure regions exhibited by the $[45/-45]_S$ coupons.

Moduli Measurements

Initial moduli have been calculated for all layups and are presented in Table 8 with standard deviations for comparison. These values were calculated by determining the slope of the stress-strain curves from 0.1-0.4%, where it was certain that no damage had occurred within the coupons.

All layups displayed good repeatability, with very low standard deviations. Once again, the $[0/90]_S$ and $[90/0]_S$ coupon tests are comparable and well within standard deviation of each other, as expected. The quasi-isotropic layup was calculated to be approximately 10% lower than the cross-ply layups, due to the addition of the ±45° biaxial plies. Also, the $[90_4]$ layup still exhibited a modulus greater than the $[45/-45]_S$ layup, due to the presence of the backing tows in the Vectorply fabric.

Layup	Initial Modulus (GPa)
$[0/90]_S$	29.3 ± 0.9
$[90/0]_S$	30.3 ± 0.7
$[0/90/\pm45]_S$	27.3 ± 0.5
$[90_4]$	14.5 ± 0.3
$[45/-45]_S$	12.1 ± 0.4

Table 8: A comparison of initial moduli for the five layups tested.

Since the primary focus of this research is on damage progression and property degradation of GFRPs, it is of more interest to observe changes in moduli throughout the static loading. One way to do this is to calculate tangent moduli across the stress-strain curves, or determining the changes in slope of the stress-strain curves up until ultimate failure. This was done by incrementally determining the slope of the curves across 0.3% changes in strain for 0.05% moving strain intervals. Although not the most accurate method, it does give a good indication of the progression of damage states within the layups. Figure 50 shows the results for each layup normalized against the initial moduli of each coupon. Plots for the rest of the coupons are shown in Appendix D. The first observation to make is that the moduli of all layups appear to begin to degrade at approximately 0.3-0.5% strain. The $[0/90]_S$, $[90/0]_S$ and $[0/90/\pm45]_S$ all appear to show

very similar trends, exhibiting sharp drops of approximately 20% initially and then steady declines with smaller drops at around 1.3% strain and less change before ultimate failure. The $[90_4]$ and $[45/-45]_S$ layups clearly showed much more severe modulus degradations up until failure. The $[90_4]$ layup exhibited a modulus reduction of almost 70% by 1% strain from when transverse matrix cracking initiated and became saturated at 1.3% strain. Its modulus then appeared to increase again, due to all stresses being transferred to the fabric's backing tows, which are oriented in the loading direction. A small decline near ultimate failure indicates where these backing tows began to fail, resulting in ultimate failure. The $[45/-45]_S$ also showed severe degradation of tangent modulus initiating from the same strain level. After the initiation, it appears to exhibit an exponential decay of tangent modulus, which then displays an additional sudden drop in modulus at approximately 1.3% strain before converging to zero. The additional step is not obvious in the stress-strain curve, but could suggest the initiation of significant damage. The phenomenon was further investigated with AE monitoring. This is also noticeable in the logarithmic growth-like trend of the stress-strain curves (see Figure 47). This is attributed to the localized damage growth shown in Figure 49. Once the main damage site begins to grow, the coupon's load carrying capacity converges at a maximum before the stress begins to decrease as the coupon is separated into two pieces. This is the point where the tangent modulus curve converges to zero.

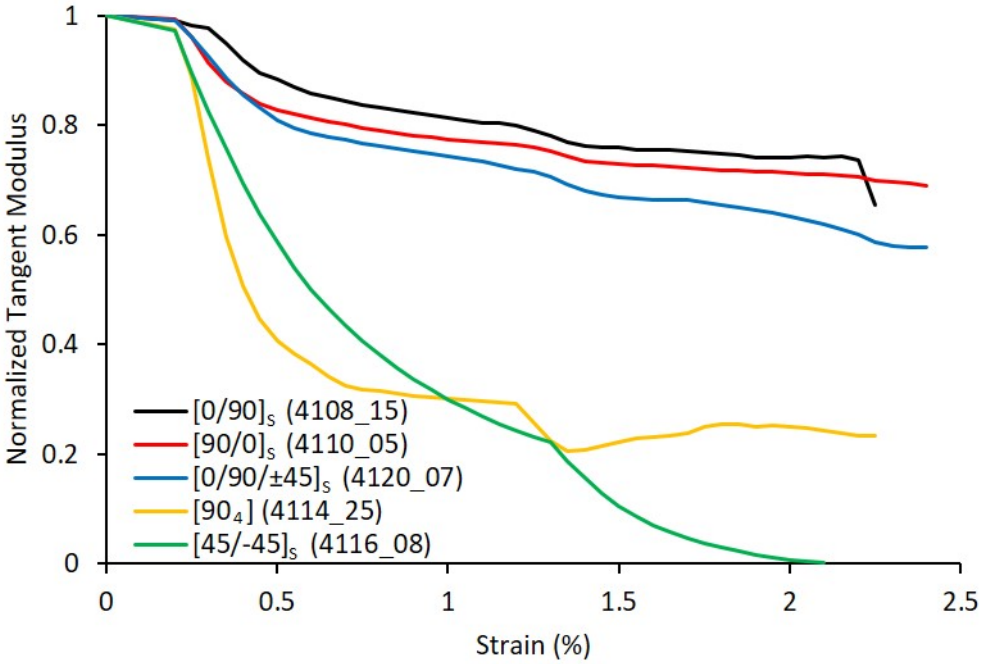


Figure 50: A comparison of normalized tangent moduli for a coupon of each layup.

Acoustic Emission

Acoustic emission data were recorded for all benchmark static tests for evaluation and to compare with data from the LUR tests for validation. The first observations and comparisons are accumulated absolute energy throughout the tests. To calculate this, the energy of each event recorded by each of the two sensors are added together and then accumulated throughout the test. Figure 51 and Figure 52 show the accumulated energy plots for coupons from each layup, with the stress-strain curves overlaid for comparisons. Plots for the other coupon tests can be found in Appendix D. Accumulated energies are plotted on a logarithmic scale because of large differences between coupons. They also begin at 1000 aJ because any events occurring with less energy than that can be considered as far less severe damage events. All layups except the $[45/-45]_S$ show that damage initiation occurred at the same levels as the knees observed in the stress-strain

curves, which validates the assumptions made in the moduli analyses. All appear to rise to an asymptote before final failure. Damage events occurring at final failure were not recorded, since the sensors had to be removed to prevent damage.

Most interestingly, the $[45/-45]_S$ exhibited much lower accumulated energies than the other layups and also suggest that damage did not initiate until much later than presumed, contrary to the tangent moduli plots. This could suggest that the initial non-linearities in the stress-strain curves are a feature of the stress distributions caused by the off-axis plies as opposed to damage occurring within the laminate.

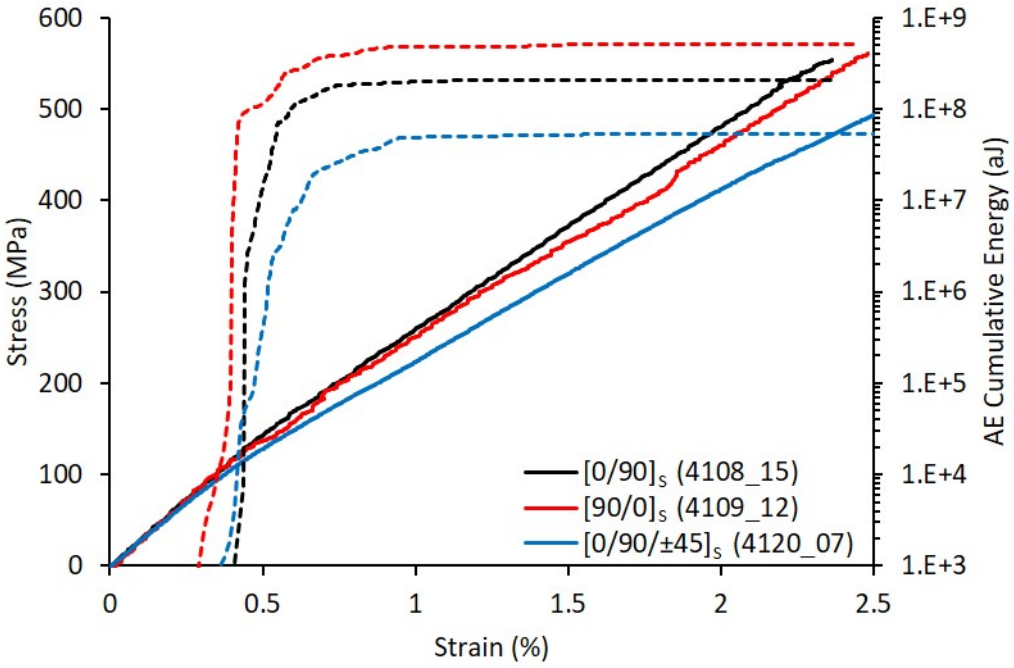


Figure 51: AE accumulated energy plots for the $[0/90]_S$, $[90/0]_S$ and $[0/90/\pm45]_S$ layups with their respective stress-strain curves.

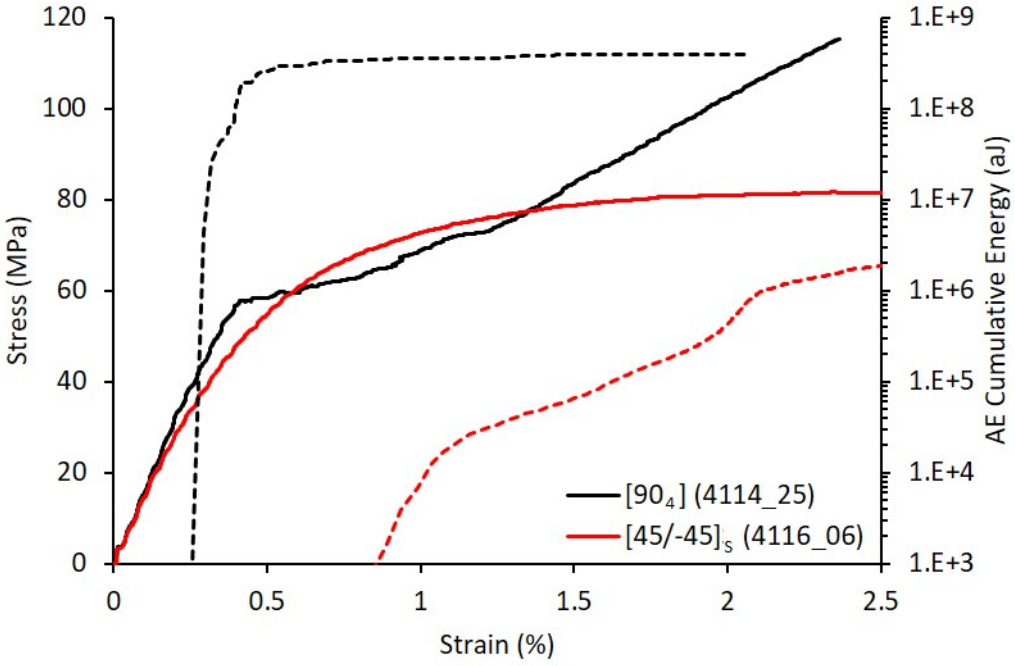


Figure 52: AE accumulated energy plots for the $[90_4]$ and $[45/-45]_S$ layups with their respective stress-strain curves overlaid.

Figure 53 shows a comparison of coupons from all layups, except the $[45/-45]_S$ layup. Total energies from the two layups with 90º plies on the outside are noticeably higher than the two with the 0º plies on the outside. The clearest comparison is between the $[0/90]_S$ and $[90/0]_S$ layups which should exhibit very similar trends in damage progression. The increased total energies for the $[90/0]_S$ and $[90_4]$ layups could be attributed to the more dominant, higher amplitude and energy antisymmetric waves, which could be initiated by transverse cracking of the 90º plies occurring further away from the mid-planes of the coupons, causing more prominent out-of-plane displacement. It could also be a case of how far cracks can propagate through the thickness of the laminates and the number of cracks resulting from it. For example, in the $[0/90]_S$ case, the transverse cracks in the 90° plies could propagate through both plies, whereas they may

be confined to single plies in the $[90/0]_S$ laminates, resulting in double the number of cracks. Conversely, the $[0/90/\pm45]_S$ displayed significantly less accumulated AE energy. This is likely due to the majority of damage events originating from the 90º and ±45º plies, which were arranged close to the mid-plane of the laminate, meaning lower energy, in-plane, symmetric waves were more prominent.

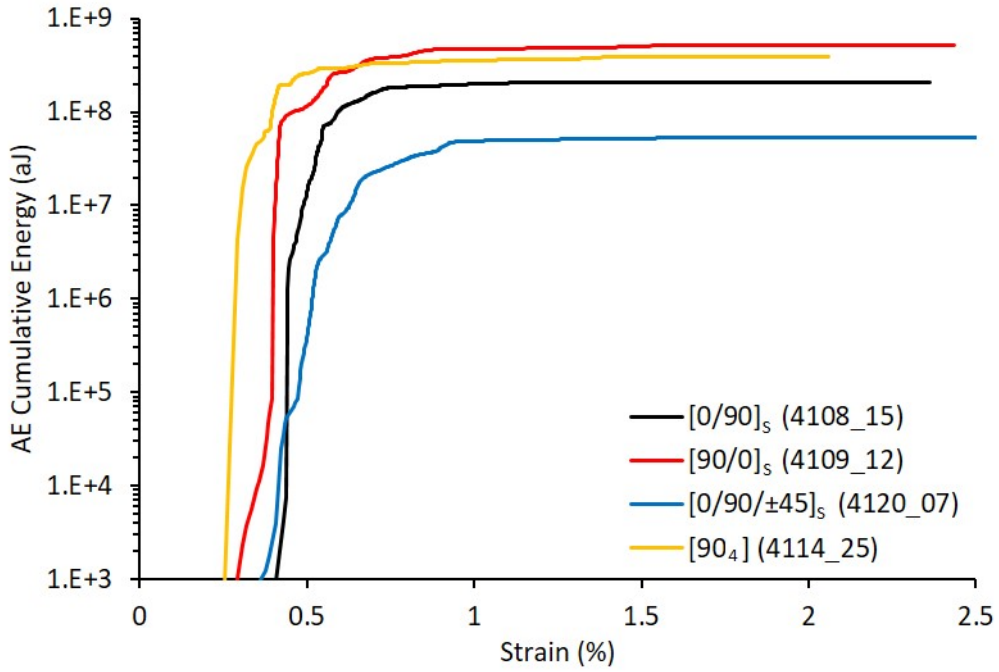


Figure 53: A comparison plot of AE accumulated energies for the $[0/90]_S$, $[90/0]_S$, $[0/90/45]_S$ and $[90_4]$ laminates.

Another useful variable for observing damage progressions with AE is peak frequency. Peak frequency is defined as the highest amplitude frequency determined from the fast Fourier transform of a received waveform from a damage event. Peak frequencies of damage events against the respective strains that the events occurred at are presented as scatter plots in Figures 54-58. Plots for the rest of the coupons tested can be found in Appendix D. Peak frequencies were taken from the sensor closest to the determined

location of each damage event. This method is limited by the fact that energies and amplitudes are not accounted for. On the scatter plots, high energy AE events originating from more severe damage mechanisms are not differentiated from lower energy, less significant events.

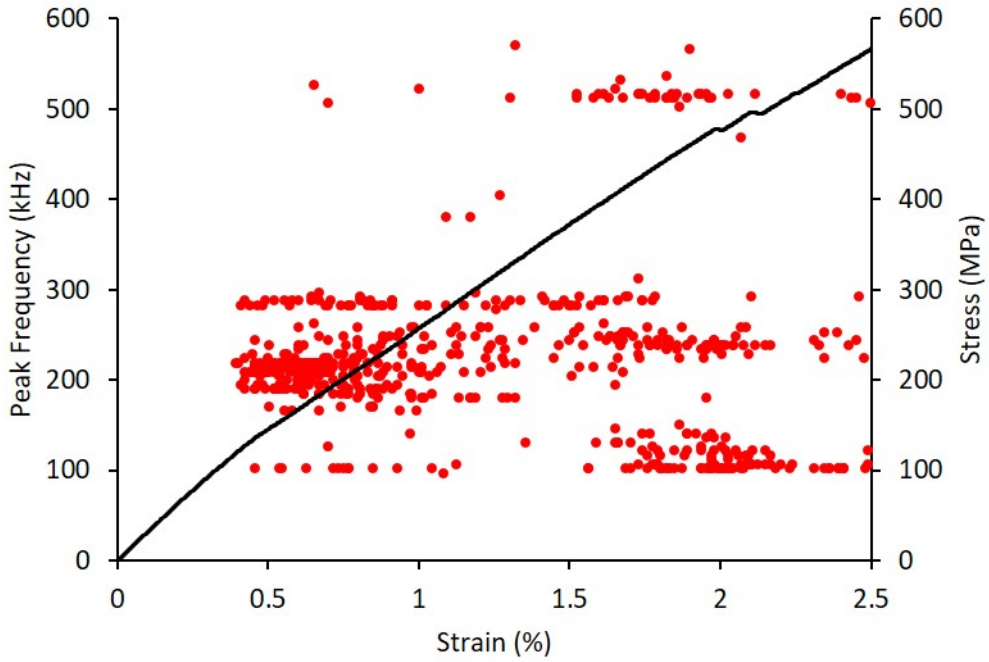


Figure 54: AE event peak frequency against strain for the $[0/90]_S$ (4103_12) layup with the respective stress-strain plot overlaid.

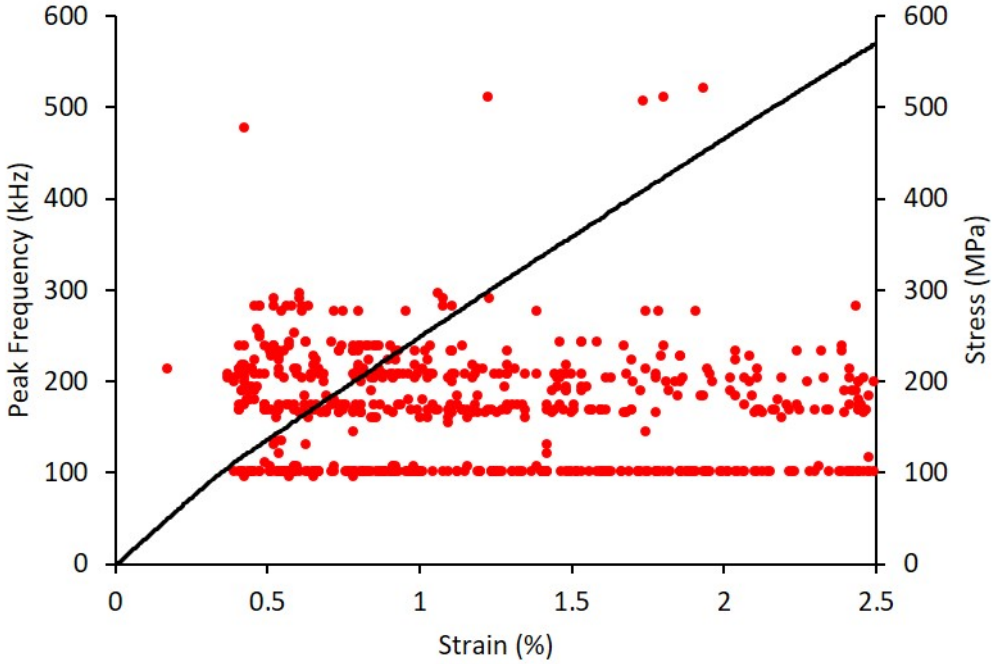


Figure 55: AE event peak frequency against strain for the $[90/0]_S$ (4110_05) layup with the respective stress-strain plot overlaid.

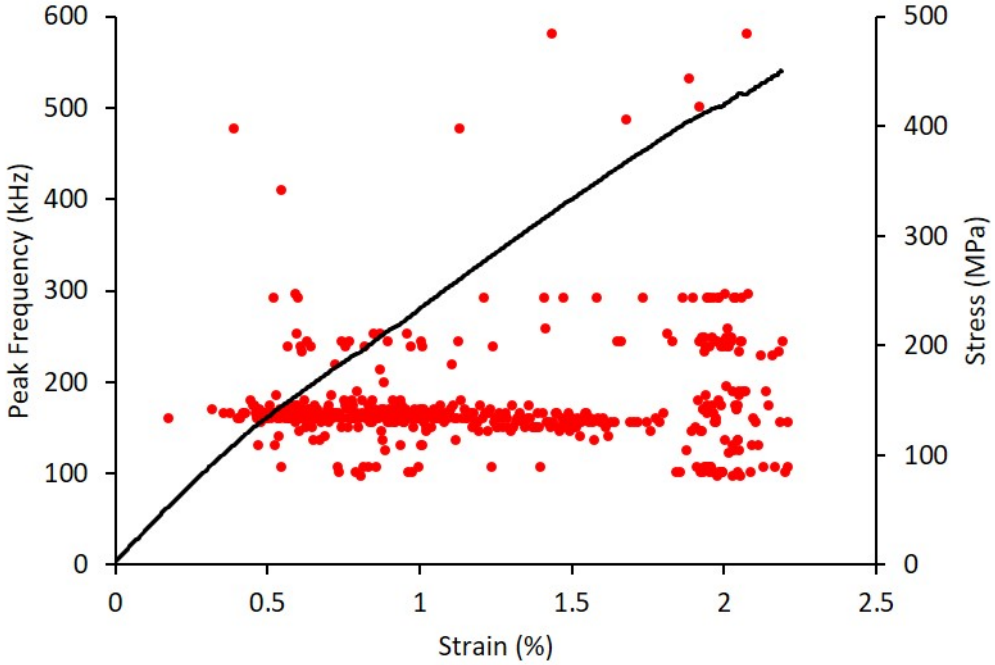


Figure 56: AE event peak frequency against strain for the $[0/90/\pm45]_S$ (4120_05) layup with the respective stress-strain plot overlaid.

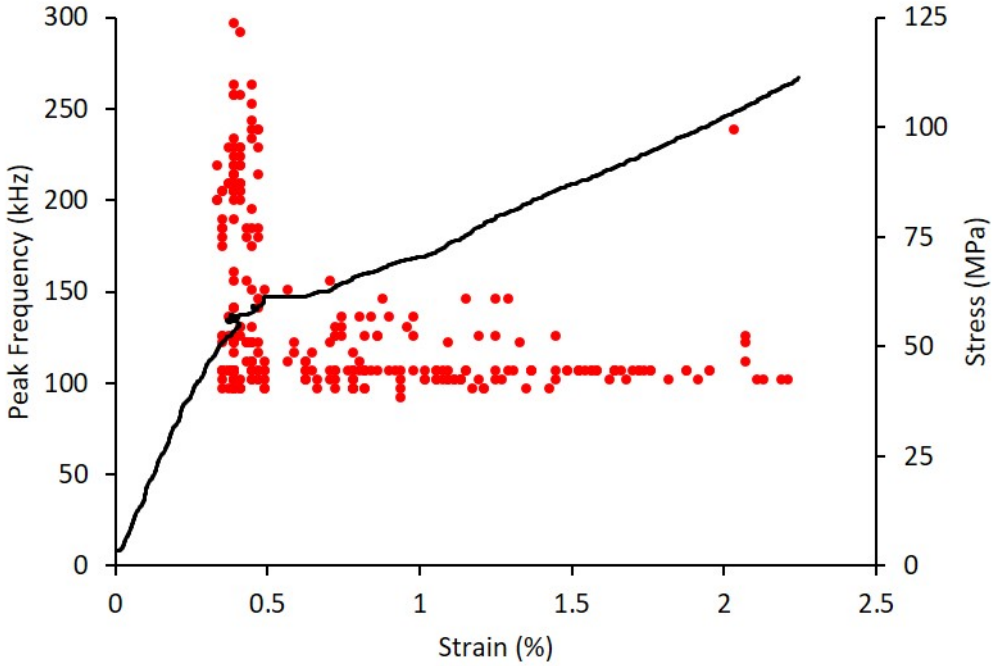


Figure 57: AE event peak frequency against strain for the [90_4] (4114_26) layup with the respective stress-strain plot overlaid.

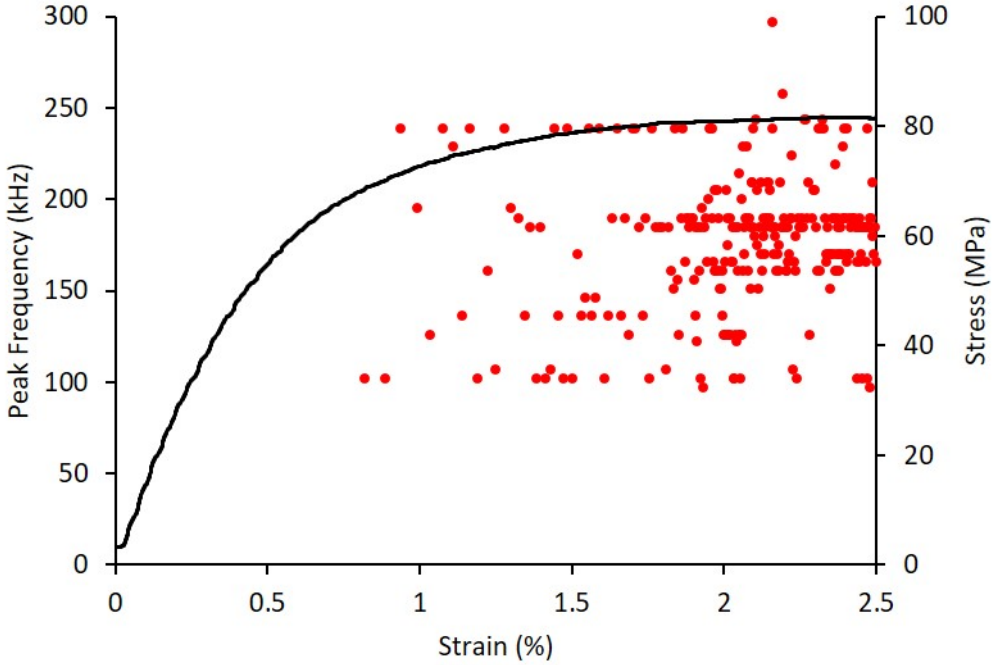


Figure 58: AE event peak frequency against strain for the $[45/-45]_S$ (4116_06) layup with the respective stress-strain plot overlaid.

The $[0/90]_S$, $[90/0]_S$ and $[0/90/\pm45]_S$ layups all exhibited similar trends in terms for frequency distributions, ranging from 100 kHz (the AE system's analogue HPF) to 550 kHz. For all three layups, damage initiation is signified by peak frequencies in the 100-300 kHz range. The $[0/90]_S$ and $[0/90/\pm45]_S$ layups appear to show more high frequency (500-600 kHz) events at higher strain levels, before ultimate failure, which may be related to fiber and/or tow failures. The $[90/0]_S$ layup shows significantly more events clustered close to 100 kHz. This could be a result of the lower frequency, out-of-plane wave modes originating from the 90º outer plies. Their peak frequencies are most likely lower than 100 kHz, but the waves are so dominant that the 100 kHz HPF has clustered them close to 100 kHz, rather than filtering them out completely. The $[0/90/\pm45]_S$ layups displayed the majority of the events in the middle frequency range (150-250 kHz), particularly close to final failure. Previous research has suggested that this intermediate frequency range can be attributed to fiber/matrix interface related damage modes [54-56] and likely originated from the ±45º biaxial plies. This is also reflected by the $[45/-45]_S$ scatter plot, where the majority of AE events are clustered in this range.

At the point of damage initiation, the $[90_4]$ scatter plot shows a broad range of peak frequencies (100-300 kHz) from the damage events, which quickly drops off to peak frequencies in the 100-150 kHz range. This is then reduced to events clustered closely around 100 kHz. The plot suggests that the matrix steadily becomes saturated with cracks until all the load is transferred to the backing tows oriented in the loading direction, before ultimate failure. The closely clustered events around 100 kHz also reflect the

hypothesis of the $[90/0]_S$ layup, that they originate from high energy antisymmetric wave modes and are likely to be lower frequencies, but have been shifted by the 100 kHz HPF.

Figure 58 also gives a good perspective on the damage initiation strain for the $[45/-45]_S$ layup. No damage events were detected until approximately 0.75% strain. Once again, this would suggest that the non-linearity observed early on in the stress-strain curve my not be caused by damage initiation, but a different progression of shear stress distribution within the off-axis plies. Also, in some cases, the initiation of AE events occurred at similar strains to the additional dip observed in the tangent modulus plots (see Figure 50), suggesting that tangent modulus may give a better indication of damage initiation than the stress-strain curves themselves. True validation of this required microscopy. Results are presented at the end of this chapter.

Load-Unload-Reload Tests

As described in the previous chapter, the increasing (LUR) static tensile testing technique was used with the purpose of allowing continuous AE monitoring, applying the GUWs at zero load and measuring modulus degradation for increasing damage states. The main purpose was to acquire data for each of the four chosen layups to be applied to statistical models for predicting the measured changes in moduli. This section first validates the LUR procedure before comparing and discussing the modulus degradation results. Various AE and GUW signal parameters are compared and discussed in preparation for applying them to the predictive modeling portion of this research.

Load-Unload-Reload Validation

To ensure consistency between the increasing LUR procedure and monotonic tensile loading, the LUR procedure was validated by comparing several trends and parameters from the monotonic test data. This was predominantly to inspect for any potential fatigue effects from multiple LURs and to ensure that the AE data was not affected by multiple load cycles.

To determine there were no significant fatigue effects or strength degradation from the LURs, ultimate tensile strengths are compared in Table 9. There are some minor variations between results, as is expected from static ultimate tensile strength testing of composite laminates, but the results were still well within standard deviation of each other. Stress-strain curves were also compared for two of the layups to evaluate consistency between the damage progression trends. Figure 59 and Figure 60 show comparisons for the $[0/90/\pm45]_S$ and $[90_4]$ layups. They display very close trends and are well within the statistical variation of multiple coupons tests. It can be seen that subsequent loading cycles consistently meet where the stress-strain curve left off at the end of the previous loading step.

Test Type	$[0/90]_S$	$[90/0]_S$	$[0/90/\pm45]_S$	$[90_4]$
Monotonic Strength (MPa)	572 ± 24	615 ± 39	502 ± 18	104 ± 10
LUR Strength (MPa)	595 ± 23	637 ± 21	492 ± 12	107 ± 6

Table 9: A comparison of static tensile strengths determined from monotonic and increasing LUR loading for all four layups, with standard deviations.

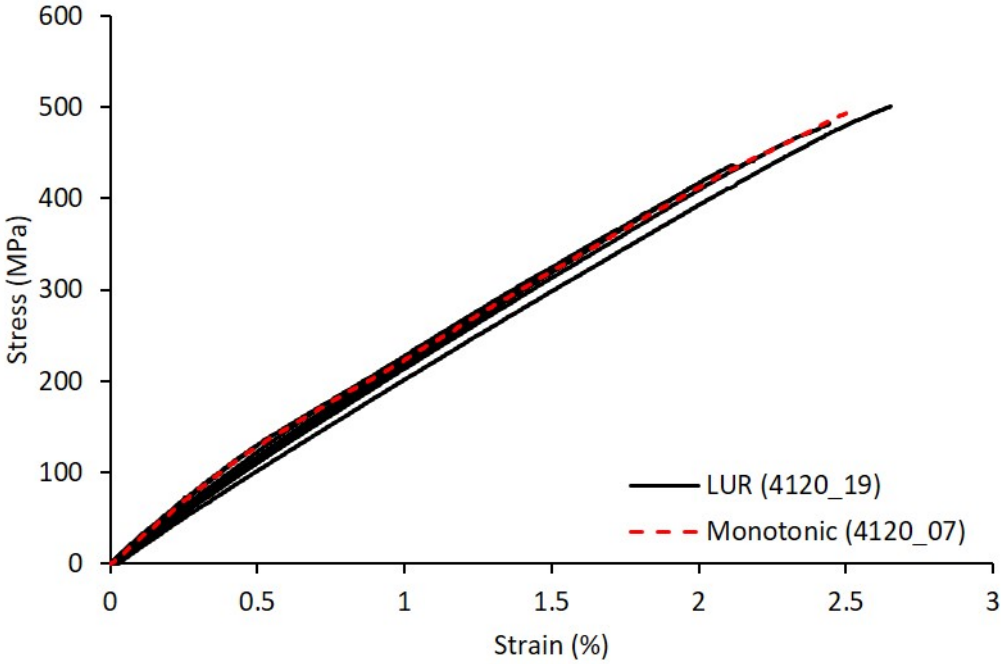


Figure 59: A comparison of stress-strain curves from an increasing LUR test and a monotonic static test for the $[0/90/\pm45]_S$ layup.

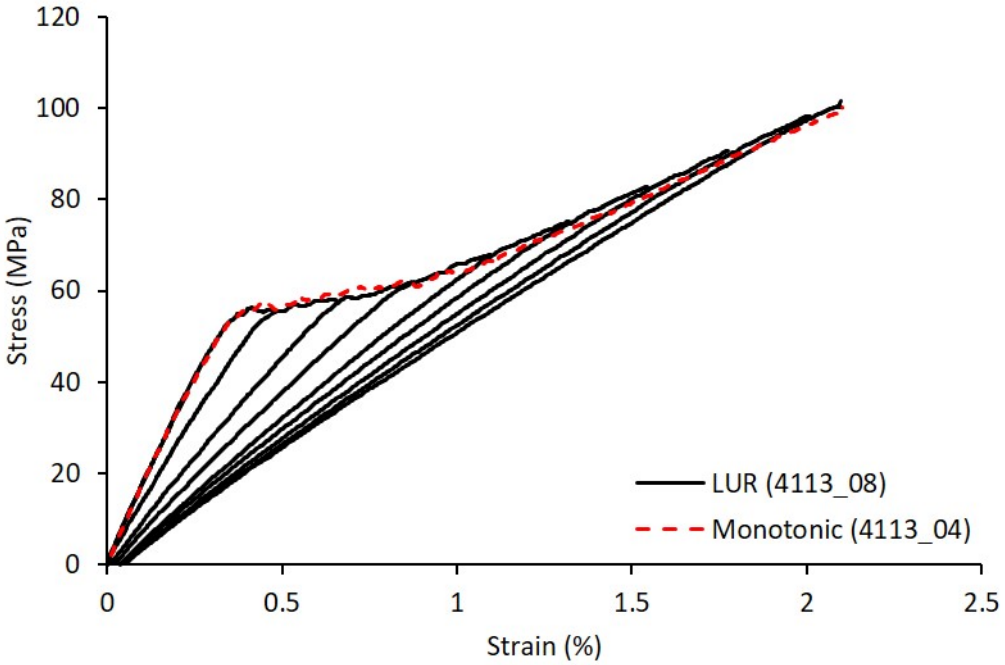


Figure 60: A comparison of stress-strain curves from an increasing LUR test and a monotonic static test for the $[90_4]$ layup.

Finally AE energy trends were compared for all four layups. Observations during the LUR tests showed edge splitting occurred at higher strain levels (>2% strain) for coupons from the $[0/90]_S$ and $[0/90/\pm45]_S$ layups. Initial inspection of the AE data showed that these edge splits were resulting in events being detected at much lower strain levels during subsequent load steps, caused by friction of the two fracture surfaces rubbing together. Because of this, event datasets were filtered to remove any events that occurred at strains lower than 90% of the maximum strain of the previous load cycle; a technique commonly used to filter out frictional events detected during fatigue testing with AE [45]. This filter was applied to all layups for consistency. Figure 61 and Figure 62 show the monotonic to LUR comparisons for AE accumulated energy, after frictional events were filtered out of the LUR datasets. All layups show close trends and reach comparable maximum values before failure.

The comparisons made between ultimate tensile strength, stress-strain curves and AE accumulated energy have validated that, aside from frictional AE events originating from edge splits, there are no significant differences in the data acquired from monotonic static tensile tests and increasing LUR static tensile tests. Therefore, increasing LURs are an acceptable method for applying the GUWs and measuring moduli of the test coupons as their damage states are increased.

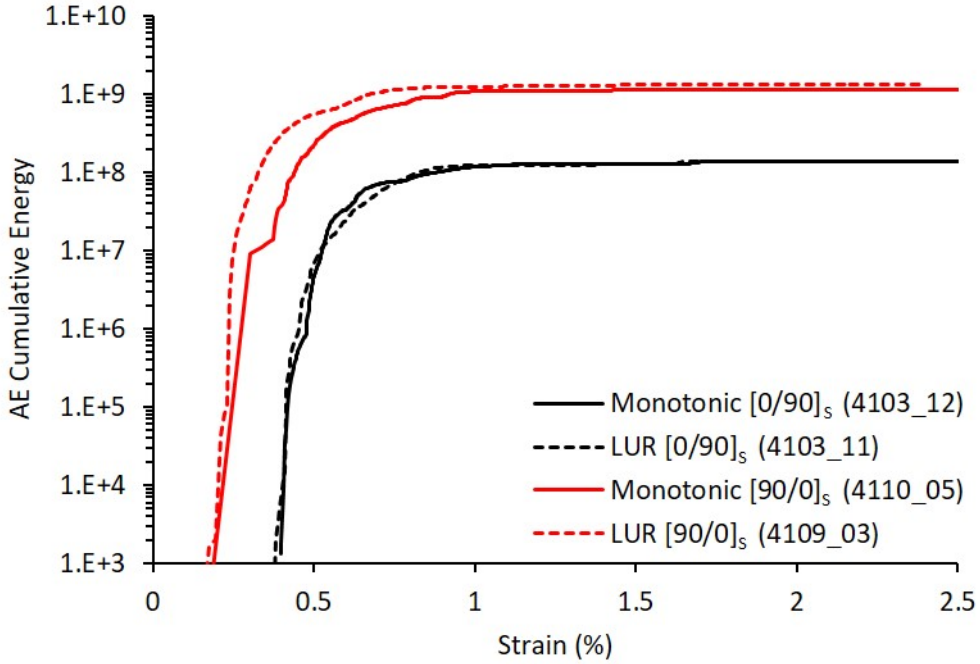


Figure 61: A comparison of AE accumulated energies between the monotonic and LUR loading procedures for the $[0/90]_S$ and $[90/0]_S$ layups.

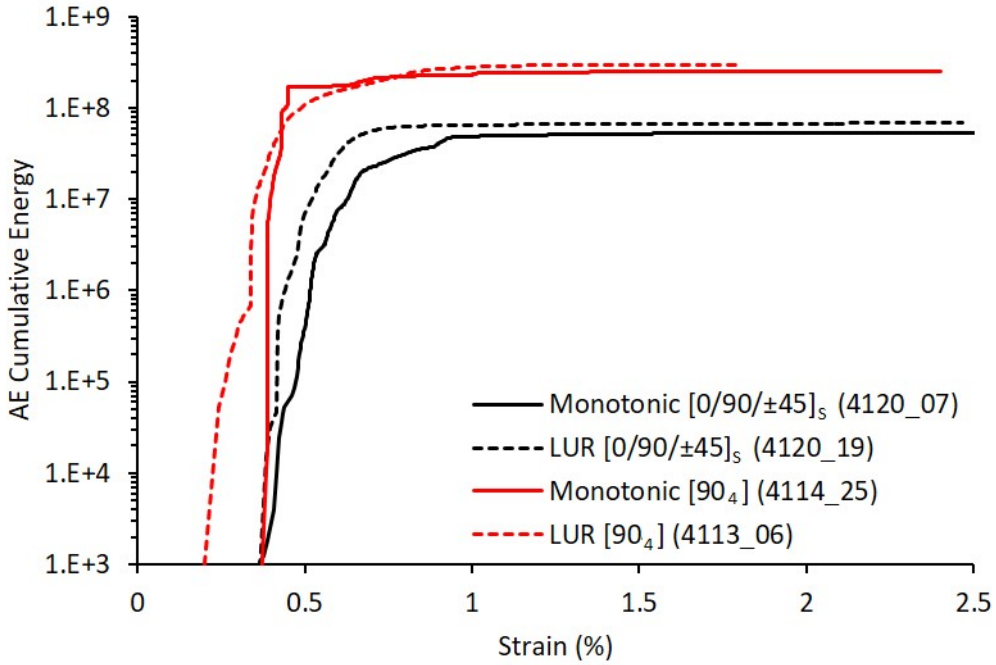


Figure 62: A comparison of AE accumulated energies between the monotonic and LUR loading procedures for the $[0/90/\pm45]_S$ and $[90_4]$ layups.

Moduli Degradation

For the statistical modeling portion of this research, modulus degradation was the main variable to be predicted from the AE and GUW data, so it is of importance to understand the degradation trends exhibited by each layup. Strictly speaking, the moduli recorded during the LUR tests are defined as the secant moduli (as opposed to tangent), since they are always calculated from linear portions of the stress-strain curves, but are mainly referred to as modulus is this research. Figure 63 shows the degradation results averaged over all seven coupon tests for each of the four layups. Standard deviation bars are included, but some are too small to observe in many cases. Results are normalized based on the initial modulus for each coupon test, for better comparisons between layups.

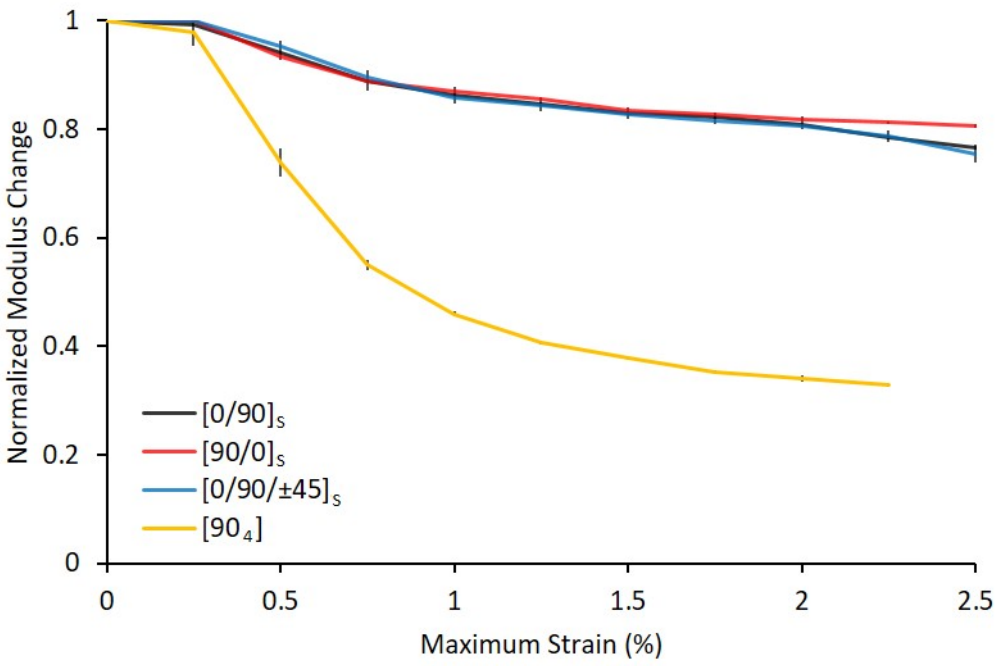


Figure 63: A comparison of normalized modulus change averaged over all seven coupon tests for each layup, with standard deviation error bars included.

The $[0/90]_S$, $[90/0]_S$ and $[0/90/\pm45]_S$ layups exhibited almost exactly the same trends in modulus degradation. They show a reduction of approximately 10-15% from damage initiation to 1% strain and only a shallow, steady decline afterwards, as stresses are transferred to the longitudinal fibers. The $[0/90]_S$ and $[0/90/\pm45]_S$ layups also show a further 5% drop from 2-2.5% strain, which is likely due to the aforementioned edge splitting from the 0° plies, close to ultimate failure. The $[90/0]_S$ layup did not show the phenomenon, since the 0° plies are constrained within the 90° plies, which prevented misaligned tows at the edge of the coupon from splitting and no longer being able to hold any load.

The $[90_4]$ layup shows a more exaggerated trend of the other three layups. It consistently exhibited up to a 55% drop in modulus from damage initiation to 1% maximum strain. The modulus steadily declined after this point until a total of 65% reduction in modulus before ultimate failure. This is consistent with the idea that this layup rapidly becomes saturated with matrix cracks after damage initiation. Once saturation was reached, the majority of the tensile stresses had been transferred to the backing tows, oriented in the loading direction, before ultimate failure.

Figure 64 shows a comparison of the secant moduli degradations described above, with the tangent moduli estimations from the benchmark static testing, to determine if it is a viable method for calculating moduli degradations from static stress-strain curves. It can be observed that the tangent method is more unstable and consistently over estimates the amount of degradation by 20-30% at some strain levels. Despite this, the tangent modulus plots generally do show comparable trends in degradation. This indicates that

the tangent modulus method is less accurate, but can still give an insight into moduli degradations with significantly less testing time required.

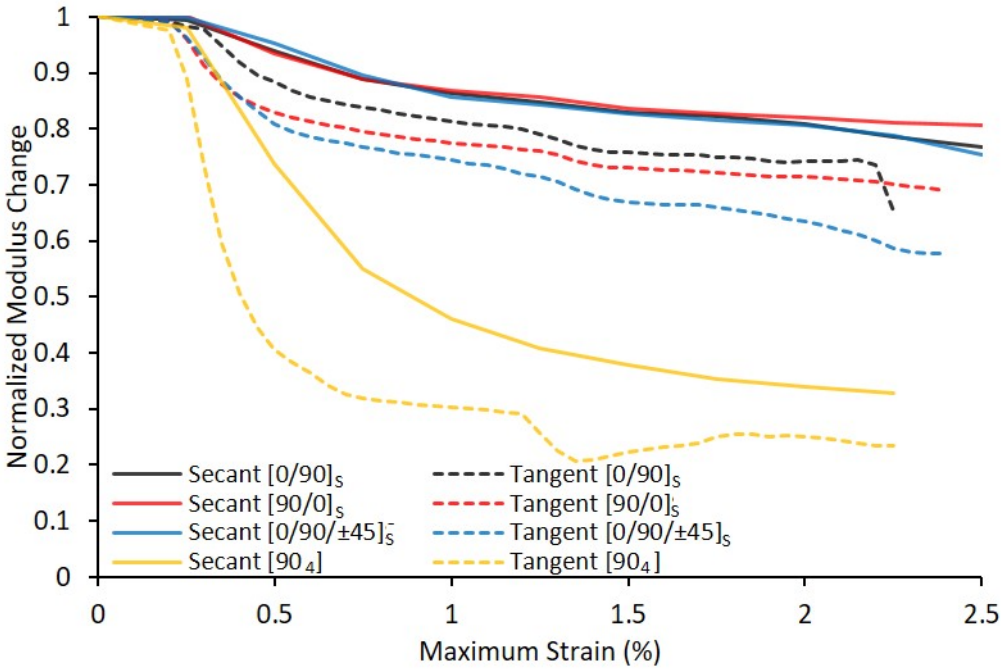


Figure 64: A comparison of secant and tangent moduli degradations from the increasing LUR and monotonic static tensile testing procedures.

Acoustic Emission

AE was one of the two in-situ damage monitoring techniques to be used to predict the moduli degradations presented in Figure 63. To compare the acquired AE data with the moduli degradations, it had to be summarized over each LUR step. Because of this, only cumulative parameters were used to compare with moduli degradations. For each load step, several event parameters were accumulated from the events recorded from all previous load steps of each test to compare with the moduli degradations.

Figures 65-67 show scatter plots of cumulative absolute energy, cumulative counts and cumulative number of events against changes in moduli for each of the four

layups. The data from all seven coupon tests for each layup have been combined to account for differences between each test. The data for each AE variable showed noticeable linear trends, so linear regression fits have been included for each layup. This is particularly important to note for the statistical modeling procedures that were applied to the data and is described in more detail in the proceeding chapters.

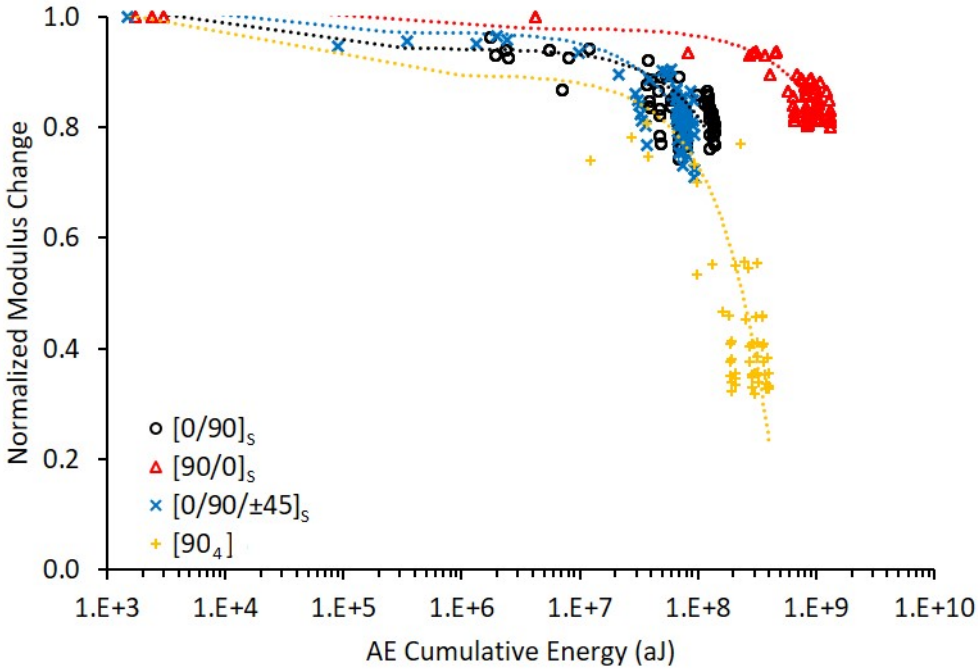


Figure 65: A scatter plot of modulus degradation against AE cumulative absolute energy for all seven coupons tested from each of the four layups.

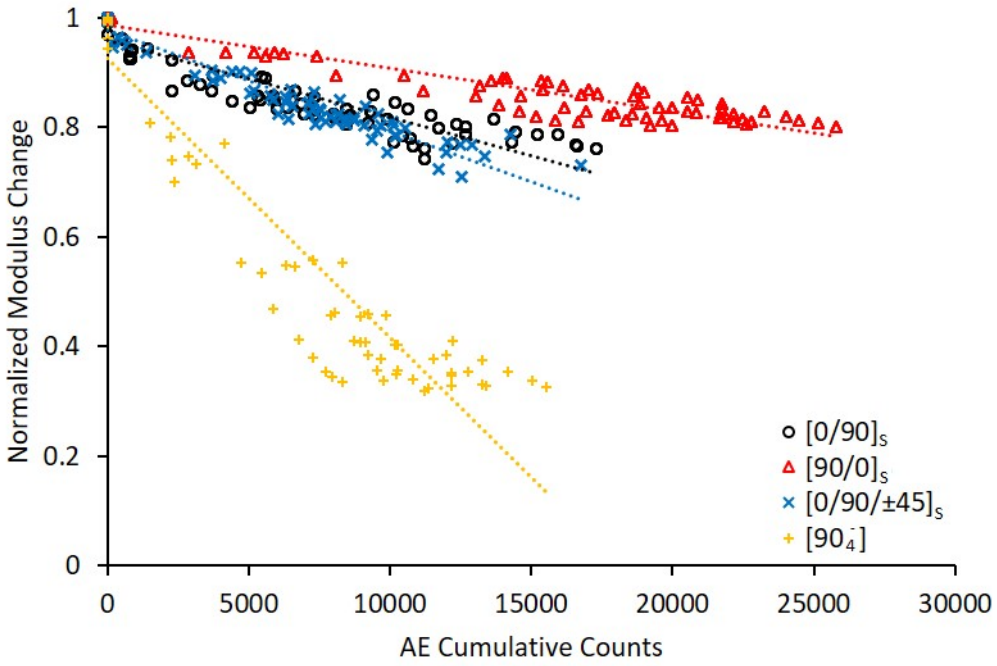


Figure 66: A scatter plot of modulus degradation against AE cumulative counts for all seven coupons tested from each of the four layups.

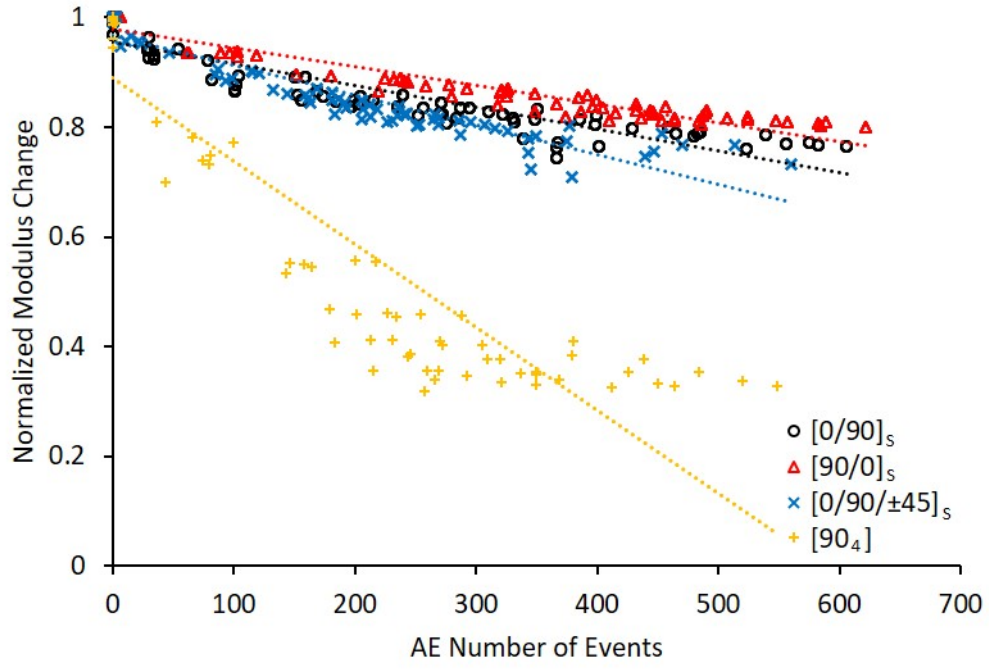


Figure 67: A scatter plot of modulus degradation against AE cumulative number of events for all seven coupons tested from each of the four layups.

Figure 65 is plotted on a logarithmic scale for easier interpretation. It is clear that the $[90/0]_S$ coupons consistently accumulated significantly more energy than the other three layups. This is comparable to the trends observed during the benchmark static testing. The two layups with 0º plies on the outside exhibited lower accumulated energies, despite showing very similar trends in modulus degradation. Also, the $[90_4]$ coupons show far less energy accumulation relative to the amount of modulus degradation that they exhibit. This suggests that the impact of each damage event on the modulus is far more severe, despite showing relatively similar absolute energies.

Figure 66 shows the cumulative counts against changes in modulus for the four layups, which reflect the relationships of cumulative energy. Once again, the $[90/0]_S$ layups shows far more cumulative counts than the other three layups. Interestingly, the $[90_4]$ layup shows slightly less cumulative counts at larger moduli changes, despite the higher accumulated energies. Counts are directly related to frequency content of AE events, so this suggests that the AE events for the $[90_4]$ layups generally have a lower frequency content than those exhibited by the other three layups, which was verified by the peak frequency plot (see Figure 57). This idea is reflected by the cumulative number of AE events presented in Figure 67. All four layups show similar totals of number of AE events at maximum moduli degradations, so the number of counts per event is likely to be lower for the $[90_4]$ layup in comparison to the other three.

Overall, the $[0/90]_S$, $[90/0]_S$ and $[0/90/\pm45]_S$ layups showed relatively good and consistent linear correlations for all three of the cumulative AE variables presented. On the other hand, the $[90_4]$ layup appears to be less linear and exhibit more statistical

scatter, particularly at larger changes in moduli. For this layup, other fitting methods may be better to describe the trends, such as exponential decays or logarithmic functions. These observations are particularly important for using the datasets to predict the changes in moduli in the modeling portion of this research.

Guided Ultrasonic Waves

The secondary in-situ damage monitoring technique applied to the increasing static LUR tests were the GUWs. They were applied by the piezoelectric actuator in the center of the coupons' gage sections at zero load, after each LUR cycle. GUW monitoring is based on the principal that damage and cracks will affect the propagation of the ultrasonic waves, primarily in the form of attenuation, which should be reflected by changes in various signal parameters, such as signal energy, amplitude and frequency content. Therefore, these changes should be proportional in some way to damage state and crack density, which are related to changes in moduli. Because of large changes in signals from coupon to coupon, all data were normalized to the data acquired from the initial references pulses applied to the undamaged coupons. Rather than observing absolute values, differences between the undamaged and damaged states are compared.

First, fast Fourier transforms and short term Fourier transforms were applied to some of the GUW waveforms received from coupons in their undamaged states to verify that the GUWs were in fact Lamb waves and the modes being excited. Figure 68 shows the results from one of the received waveforms. On inspection of the fast Fourier transform, the main frequencies excited were approximately 185 kHz and 240 kHz. Using the minimum laminate wave velocity presented in Table 3, the minimum wavelength of

the GUWs can be calculated to be approximately 12.5 mm. This is significantly larger than the thickness of all the laminates that the GUWs were applied to. Therefore, it can be safely assumed that the GUWs propagating through the laminates were Lamb waves as opposed to Rayleigh surface waves [76]. Inspection of the short term Fourier transform presented in Figure 68 shows the peak frequency of the arriving wave to be 185 kHz. At approximately 150 µs a second wave appears to arrive, which can be attributed to a reflection, possibly from the end of the test coupon. Previous short term Fourier transform analysis has shown that these frequencies can safely be related to the in-plane, extensional wave mode (S_0) for the coupon geometries that were tested [95].

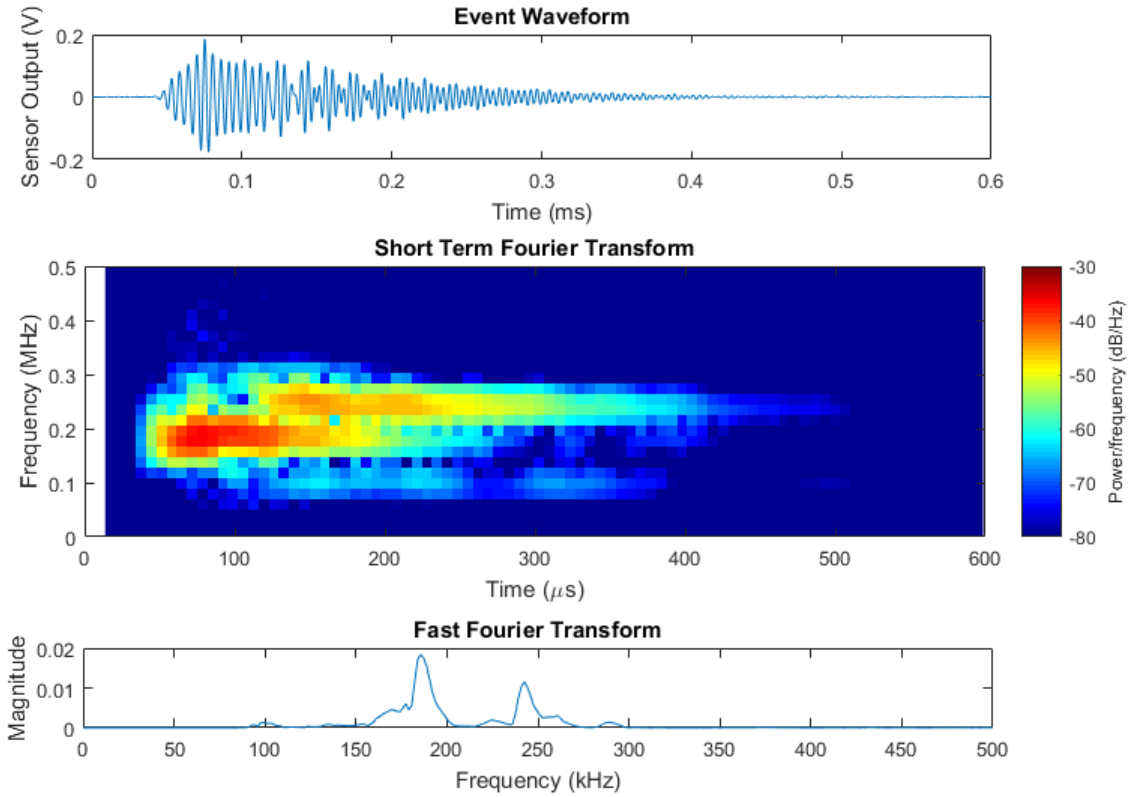


Figure 68: Plots showing the voltage signal, short term Fourier transform and fast Fourier transform of a received GUW applied to an undamaged coupon.

Figures 69-72 show several of the normalized GUW signal parameters plotted against the measured changes in moduli. Again, data from all seven coupon tests for each layup are combined in each plot. Linear regression fits are also included as visual aids for the modeling portion of this research. Plots of all the other signal parameters can be found in Appendix D.

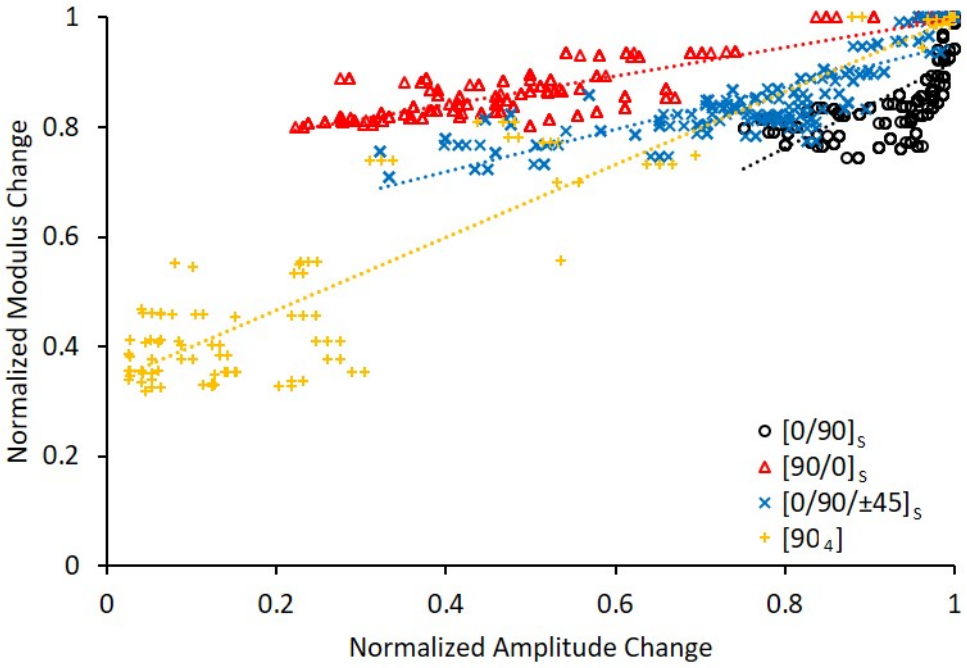


Figure 69: A scatter plot of modulus degradation against GUW normalized amplitude change for all seven coupons tested from each of the four layups.

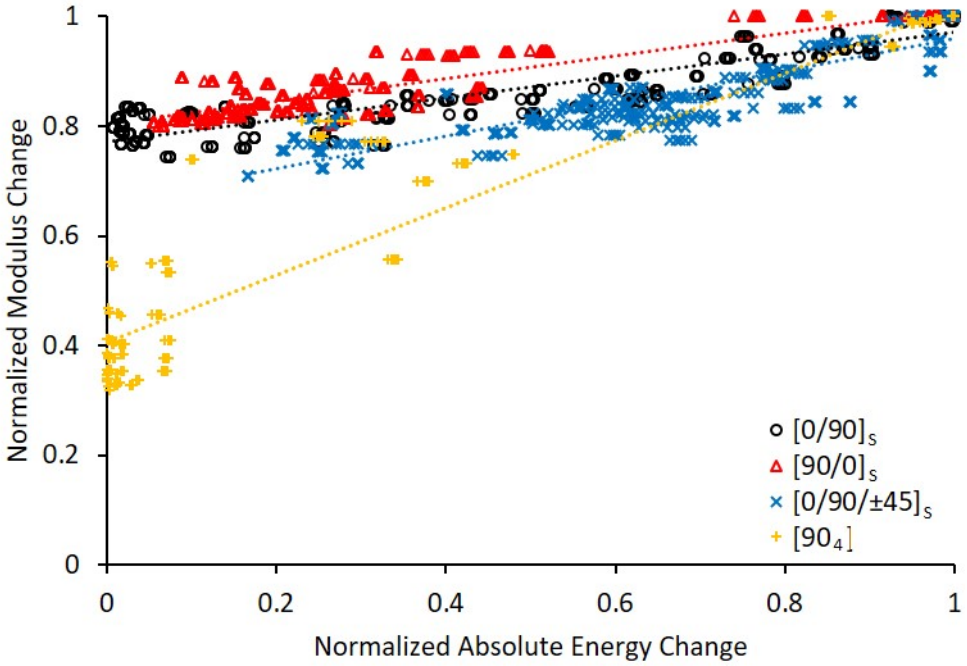


Figure 70: A scatter plot of modulus degradation against GUW normalized absolute energy change for all seven coupons tested from each of the four layups.

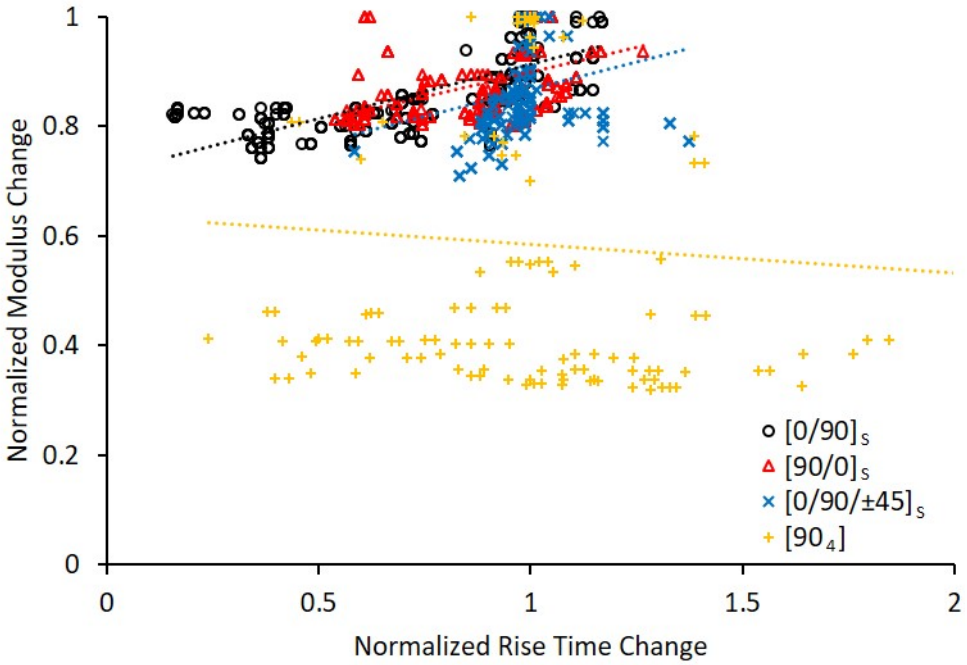


Figure 71: A scatter plot of modulus degradation against GUW normalized rise time change for all seven coupons tested from each of the four layups.

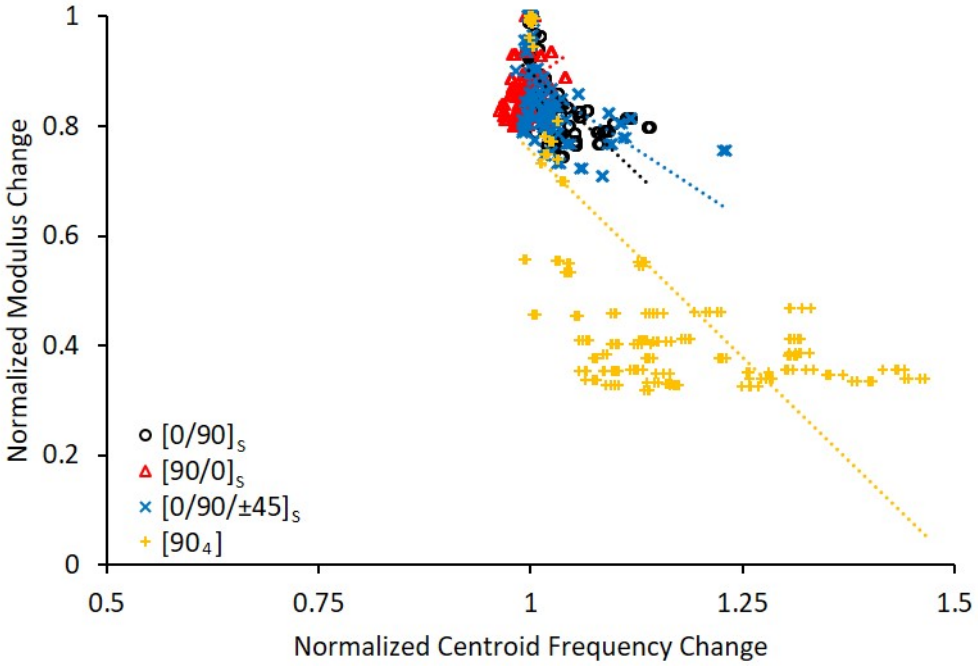


Figure 72: A scatter plot of modulus degradation against GUW normalized centroid frequency change for all seven coupons tested from each of the four layups.

Figure 69 shows modulus change against GUW amplitude reduction. It is evident that the $[0/90]_S$ layup showed much smaller reductions in amplitude than the other three layups. It was expected that the $[90/0]_S$ layup would show larger changes, due to the sensors being bonded to the 90° plies, which exhibited extensive amounts of transverse cracking before failure. Despite this, damage within the $[0/90/\pm45]_S$ layup resulted in much larger reductions in GUW amplitude than the $[0/90]_S$ layup. This could be explained by large delaminations which propagated along the coupons at higher strain levels. More information on this failure mode is provided in the proceeding section. Of course, damage progression of the $[90_4]$ layup resulted in significant attenuation of the GUW amplitudes, especially at maximum modulus degradation, where amplitude reductions of up to 98% were observed. Although larger amplitude reductions were

observed, the reductions relative to modulus reduction are actually less than the other three layups.

The features observed for amplitude reduction are more exaggerated in Figure 70 showing absolute energy reduction for the four layups. In terms of energy, signals get almost completely attenuated by damage within the coupons, so much so that the $[90_4]$ data appears to reach zero at large moduli reductions. This would suggest that the data, at least for the $[90_4]$ layup, may fit better on a logarithmic scale. In contrast, the other three layups show much more comparable linear trends, with similar gradients.

Both amplitude and absolute energy reductions appear to show good linear correlations with regards to modulus reduction, without excessive statistical scatter. On the other hand, rise time (see Figure 71) is far more unpredictable. It was expected that rise time should decrease with reductions in moduli. Attenuation due to damage causes amplitudes to decrease, therefore the time between the voltage signal crossing the voltage threshold and reaching its peak should also decrease. Very loose correlations are shown by the $[0/90]_S$, $[90/0]_S$ and $[0/90/\pm45]_S$ layup data, which do reflect this hypothesis, but the $[90_4]$ layup data show almost no correlation at all. Rise times for the $[90_4]$ layup both increased and decreased from the undamaged reference pulses at larger modulus reductions. In general, there is too much statistical scatter to draw any real conclusions.

Figure 72 shows changes in centroid frequency with respect to moduli changes. Centroid frequency is a function of both magnitude and frequency of the Fourier transform of the received GUW waveforms, analogous to the center of mass of the frequency content. It was expected that centroid frequency would decrease with

increasing damage states and modulus reduction. Frequency-based attenuation of in-plane wave modes is a function of wavelength in relation to the thickness of an interface that a wave is propagating through. Therefore, as the GUWs propagate through crack interfaces, higher frequencies should be attenuated more so than the lower ones. The centroid frequency plot does not reflect this hypothesis. In fact, centroid frequencies actually changed very little and more noticeably increased with increasing damage states, particularly for the $[90_4]$ layup. One explanation for this may be that the wavelengths of the GUW frequencies propagating through the coupons are too large in relationship to the size of the crack interfaces under zero load. Higher input frequencies or conducting the GUWs under applied load, so the crack interfaces are separated, may result in more noticeable trends. It could also be that the Dirac delta function input signal is exciting the natural frequency response of the coupons, resulting in different wave modes propagating through the coupons, which were less affected by crack interfaces. In this case, different input waveforms would likely show different results. For example, frequency based attenuation may be more obvious when a frequency sweep or chirp input signal is applied.

As shown in Figures 69-72, some GUW waveform signal parameters showed good linear correlations with changes in moduli of the layups tested, whereas other features showed little to no correlation of any kind. Particularly in the case of energy and amplitude attenuation, statistical scatter can be attributed to the attachment of the sensors to the coupons. Although steps were taken to mitigate the variations in the attachment of the sensors, it still may have been possible for the thickness of the vacuum grease

couplant to vary during loading and unloading of the test coupon. Cracks propagating beneath the sensors may have also resulted in variations in responses received by the sensors. Despite this, all GUW data and variables were still applied to the statistical modeling portion of this research to be processed and removed if necessary in an indiscriminate manner. Further discussion on which variables proved most useful for predicting changes in moduli are provided in the "Predictive Modeling Results and Discussion" chapter.

Imaging and Microscopy Observations

To provide further validation and supplementary information for all the data acquired during static testing, various observation techniques were applied to assess the failure and damage modes of the laminates tested. These observations led to a better understanding of what was to be expected during the fatigue testing. The observation techniques applied were in the form of visual inspections, transmitted light, optical microscopy and SEM. Some coupons were loaded to the point of damage initiation to observe initial damage mechanisms and others were loaded to close to ultimate failure before making observations, as well as analyzing the failure mechanisms of coupons which had underwent ultimate failure.

Several coupons from each layup were loaded in static tension with AE monitoring, until damage events were being detected. For all but the $[45/-45]_S$ layup, coupons were loaded to 0.6% strain before being removed from the load frame and cross-sections prepared for SEM imaging. Since damage events were detected at much higher strains for the $[45/-45]_S$ coupons, they were loaded to 1.5% strain and then removed.

Figure 73 shows an SEM image of the cross-section of one of the $[0/90]_S$ coupons that was tested. Only small transverse cracks between the 0° tows can be observed and they do not appear to have propagated through the thickness of the plies. It also appears that the 0° plies and backing tows act as crack barriers to prevent the cracks from propagating through the thickness of the laminate, as was expected.

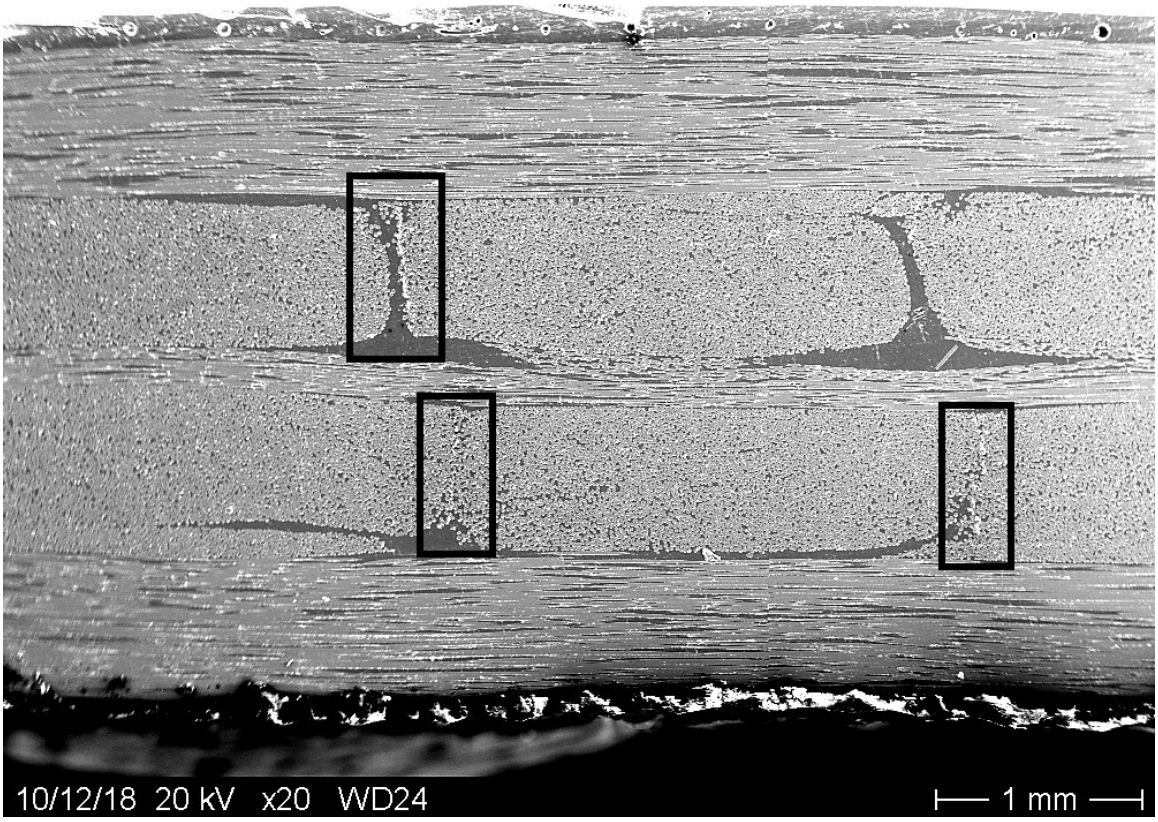


Figure 73: An SEM image looking through the transverse direction of a $[0/90]_S$ coupon (4107_12), which had been loaded to 0.6% strain, with the faint cracks highlighted in the black boxes.

Figure 74 shows an SEM image of the cross section of one of the $[90/0]_S$ coupons that was loaded up to damage initiation. It shows similar, small, faint transverse cracks between the outer 90° tows, which do appear to have propagated through the entire thickness of the tows and have been arrested by the inner 0° tows. Figure 75 shows the

same phenomena in a $[0/90/\pm45]_S$ coupon that was tested. No cracks were observed in the ±45° plies. Figure 76 shows an SEM image of one of the $[90_4]$ coupons tested. It is particularly interesting to note that most of the cracks in the $[90_4]$ coupon have propagated through the fiber tows, rather than between them. This may be caused by the stitching that is only barely visible in some of the resin rich areas between the tows. It is highly plausible that these cracks initiated in the stitching and found the path of least resistance through the tows rather than around them. The distortion of the fiber tows caused by the stitching can also be observed.

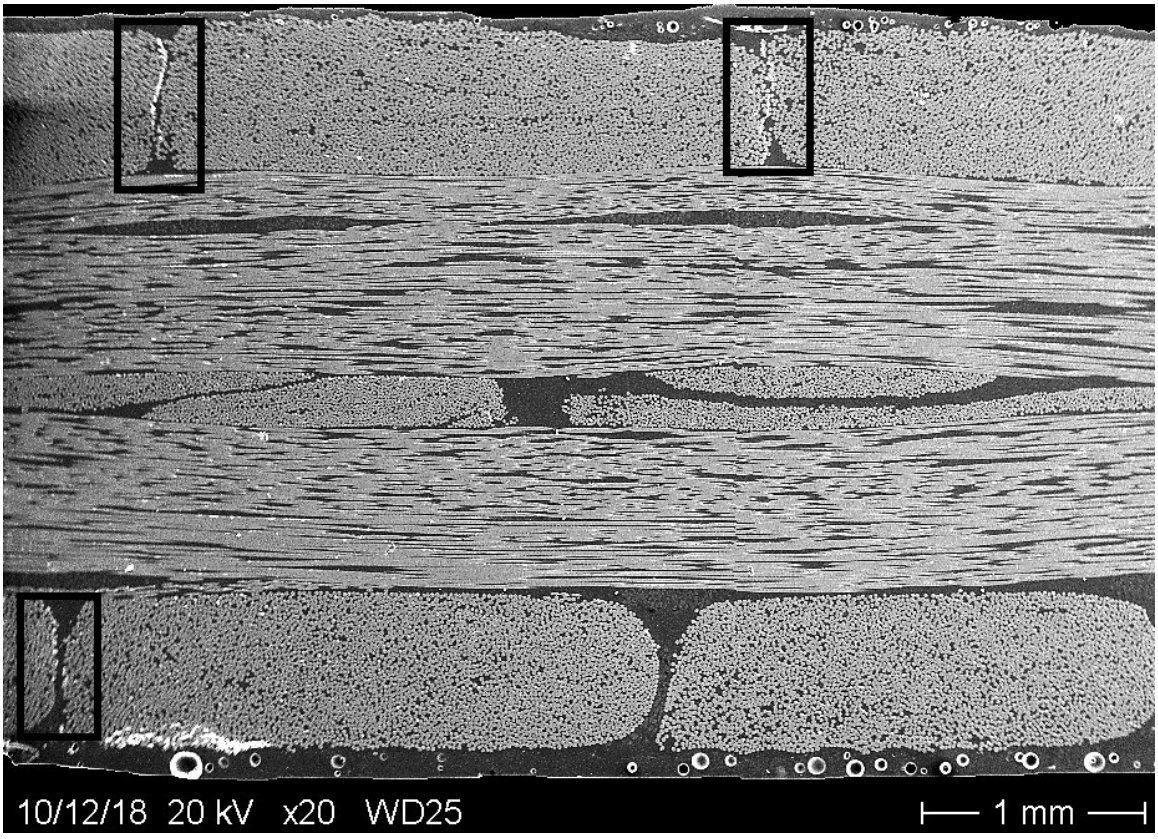


Figure 74: An SEM image looking through the transverse direction of a $[90/0]_S$ coupon (411_02), which had been loaded to 0.6% strain, with the faint cracks highlighted in the black boxes.

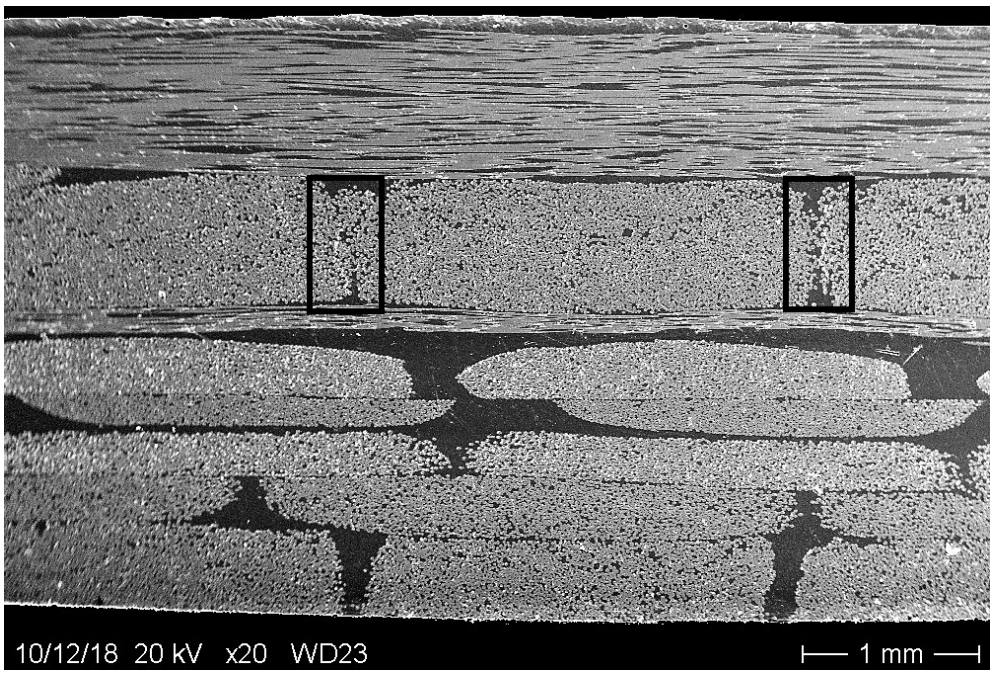


Figure 75: An SEM image looking through the transverse direction of a $[0/90/\pm45]_S$ coupon (4121_07), which had been loaded to 0.6% strain, with the faint cracks highlighted in the black boxes.

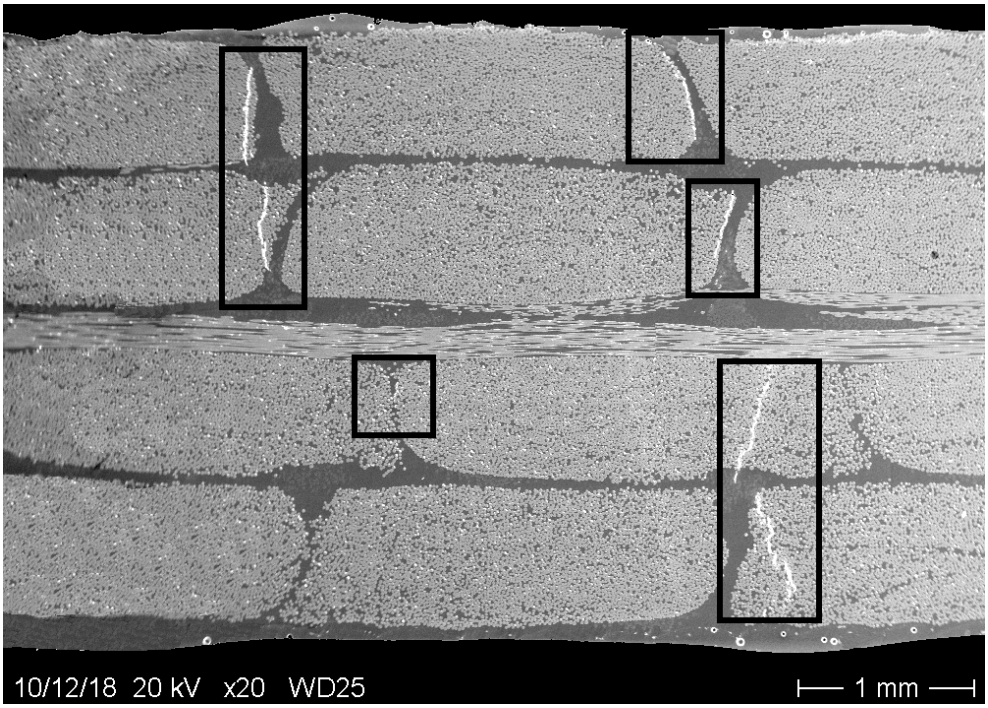


Figure 76: An SEM image looking through the transverse direction of a $[90_4]$ coupon (4113_18), which had been loaded to 0.6% strain, with the faint cracks highlighted in the black boxes.

Finally, Figure 77 shows an SEM image of a cross section of one of the $[45/-45]_S$ coupons loaded up to 1.5% strain. Very few cracks were found in the coupon, which would verify the acquired AE data, where very few damage events were actually detected away from the main failure region. It is unknown as to why this layup was able to sustain significantly higher strains than the other layups tested without large amounts of damage being accumulated. Figure 77 only shows two cracks. The top one appears to have initiated under strain, but the V-shape of the bottom crack was likely due to damage, which was already present in the coupon. The horizontal portion of the crack was likely caused by the removal of the peel-ply material after manufacturing of the laminate. The application of tensile stress appears to have caused the crack to propagate into the thickness of the coupon. Again, the stitching can be faintly observed in the resin rich areas of the laminate and its influence on the distortion of the fiber tows.

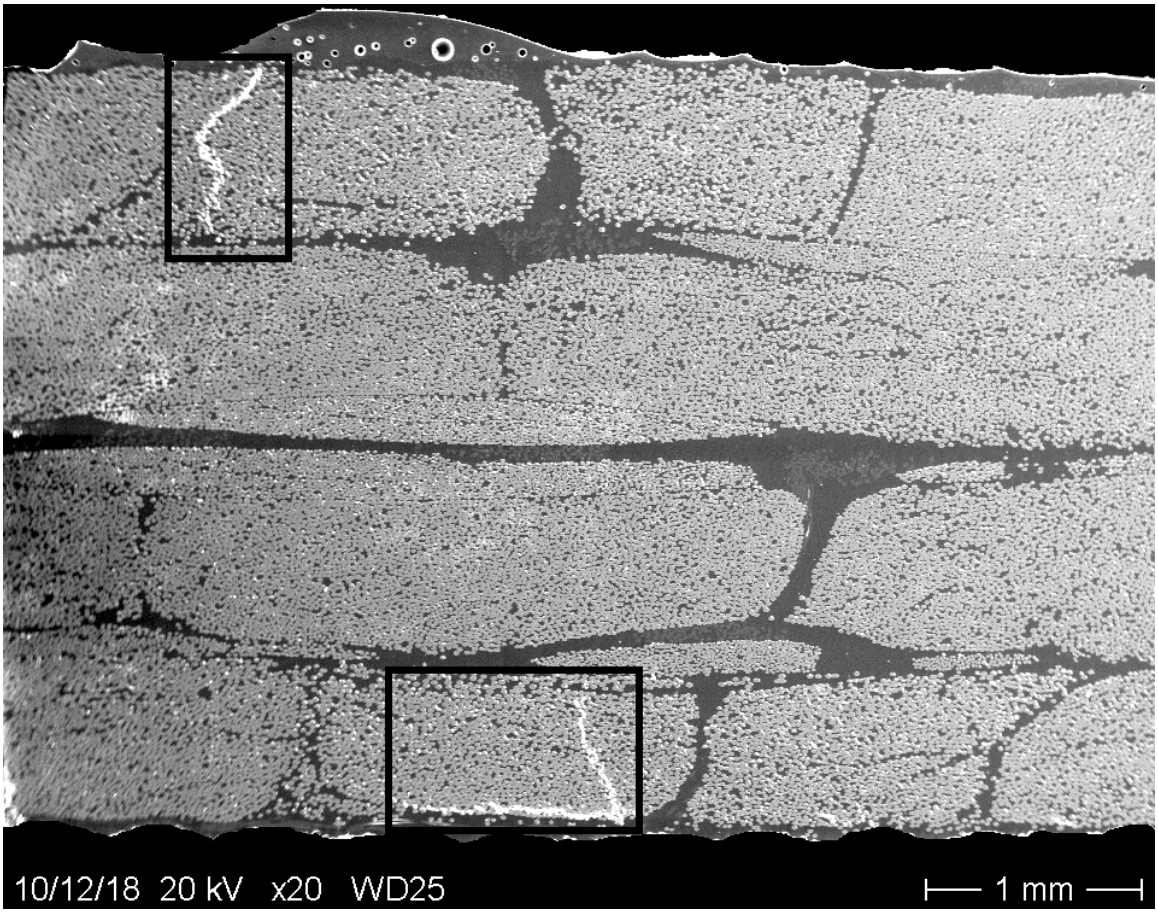


Figure 77: An SEM image looking through the transverse direction of a $[45/-45]_S$ coupon (4115_05), which had been loaded to 1.5% strain, with the faint cracks highlighted in the black boxes.

Figure 78 shows transmitted light photos of coupons from all layups, except the $[45/-45]_S$, which were loaded to 2.5% strain . Note that the $[90_4]$ layup was actually loaded to ultimate failure, since all coupons failed prior to 2.5% strain, although they exhibited a much more localized failure, so could still be inspected.

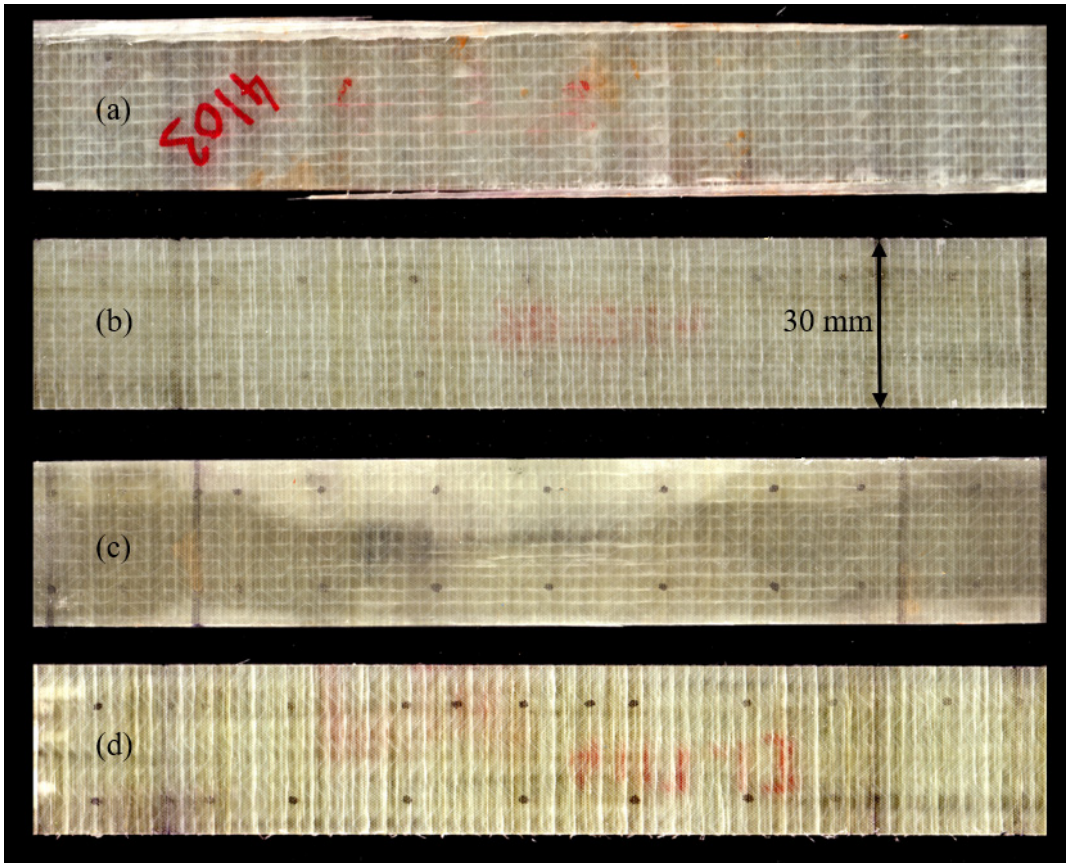


Figure 78: Transmitted light photos of coupons from the (a) $[0/90]_S$, (b) $[90/0]_S$, (c) $[0/90/\pm45]_S$ and (d) $[90_4]$ layups which had been loaded up to 2.5% strain.

Figure 78(a) clearly shows the previously described edge splitting, which manifested close to final failure, causing the final small drops in moduli for both the $[0/90]_S$ and $[0/90/\pm45]_S$ layups, which were not observed in the $[90/0]_S$ layup. Also, longitudinal cracking can be observed between the 0° fiber tows. Transverse cracks are faint, so they may only be present in the 90° center plies. This was further investigated using SEM.

The $[90/0]_S$ coupon shows the opposite (see Figure 78(b)). There was no visible edge splitting and the transverse cracking, assumed to be between the fiber tows, was much more prominent on the surface of the coupon. Instead, the longitudinal cracks were

less visible, which were most likely only present in the 0° plies in the middle of the coupon.

Figure 78(c) for the $[0/90/\pm45]_S$ coupon shows similar longitudinal and transverse cracking to the $[0/90]_S$ layup, with the addition of significant delaminations appearing to initiate from the edges of the coupon (shown as milky discolorations). It was suspected that the delaminations were most likely caused by interlaminar shear stresses originating from the contraction of the ±45° biaxial plies, although SEM showed that this was not actually the case.

Finally, the $[90_4]$ coupon (Figure 78(d)) exhibited significant amounts of transverse matrix cracking across its entire length. The density of cracks appears to be greater than the density of fiber tows, suggesting that cracks have also propagated through the tows as well as in between them, but it could also be a result of cracking between tows in the other 90° plies below the surface. SEM imaging was required to validate this.

To validate the damage phenomena observed in Figure 78, closer observations were required. SEM imaging was conducted to investigate the features described above in more detail. Figure 79 and Figure 80 show SEM images of the cross section of a coupon from the $[0/90]_S$ layup loaded up to 2.5% strain, looking in the longitudinal and transverse directions respectively. Figure 79 shows a small amount of longitudinal cracks both between and within the 0° tows. The cracks have clearly been arrested by the transverse tows, which prevented further propagation into the laminate. Figure 79 shows far more extensive transverse cracks, both between the tows and within them at relatively

regular intervals. The cracks do appear to have been arrested by the 0° backing tows, but they do line up closely between the two plies so may have actually propagated around the backing tows in the center. This is a feature that cannot be observed using 2D imaging and would require a far more sophisticated technique, such as CT scanning.

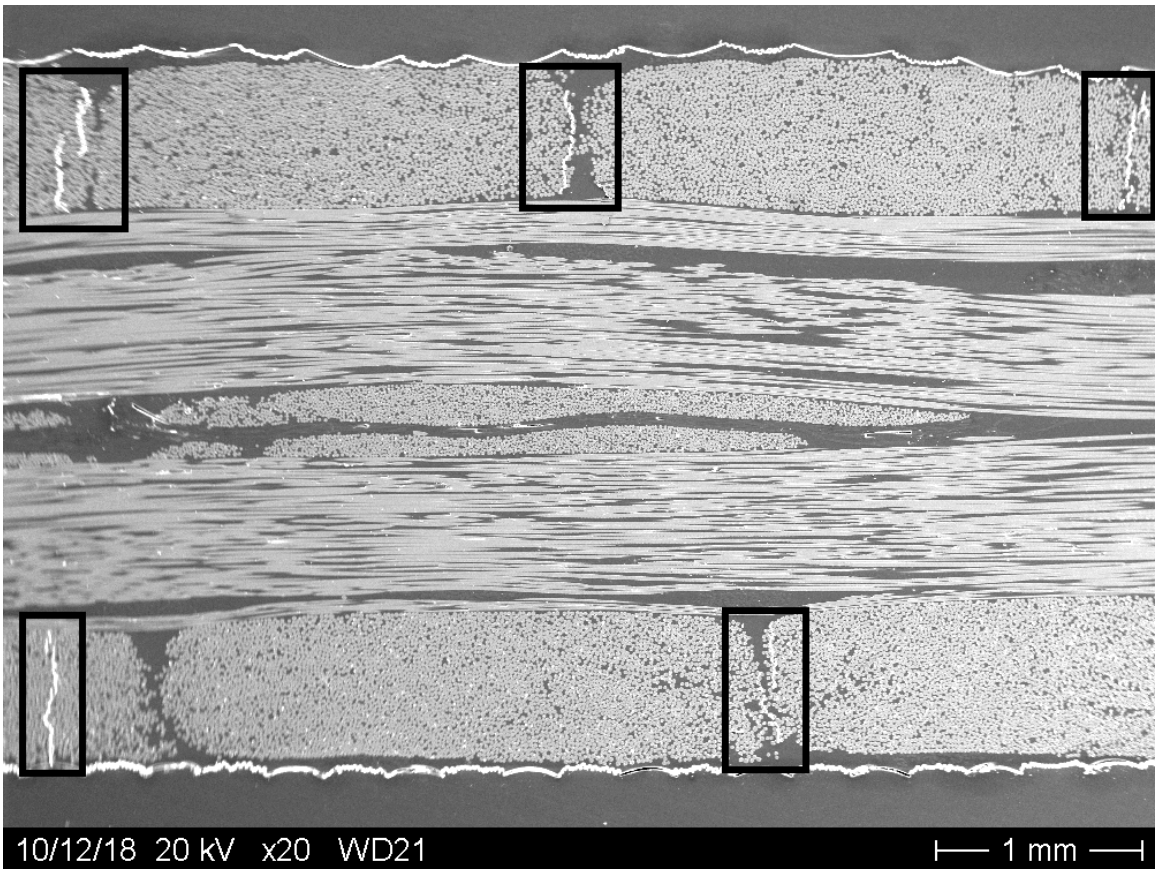


Figure 79: An SEM image of a $[0/90]_S$ coupon (4103_12), which had been loaded up to 2.5% strain, looking in the longitudinal direction.

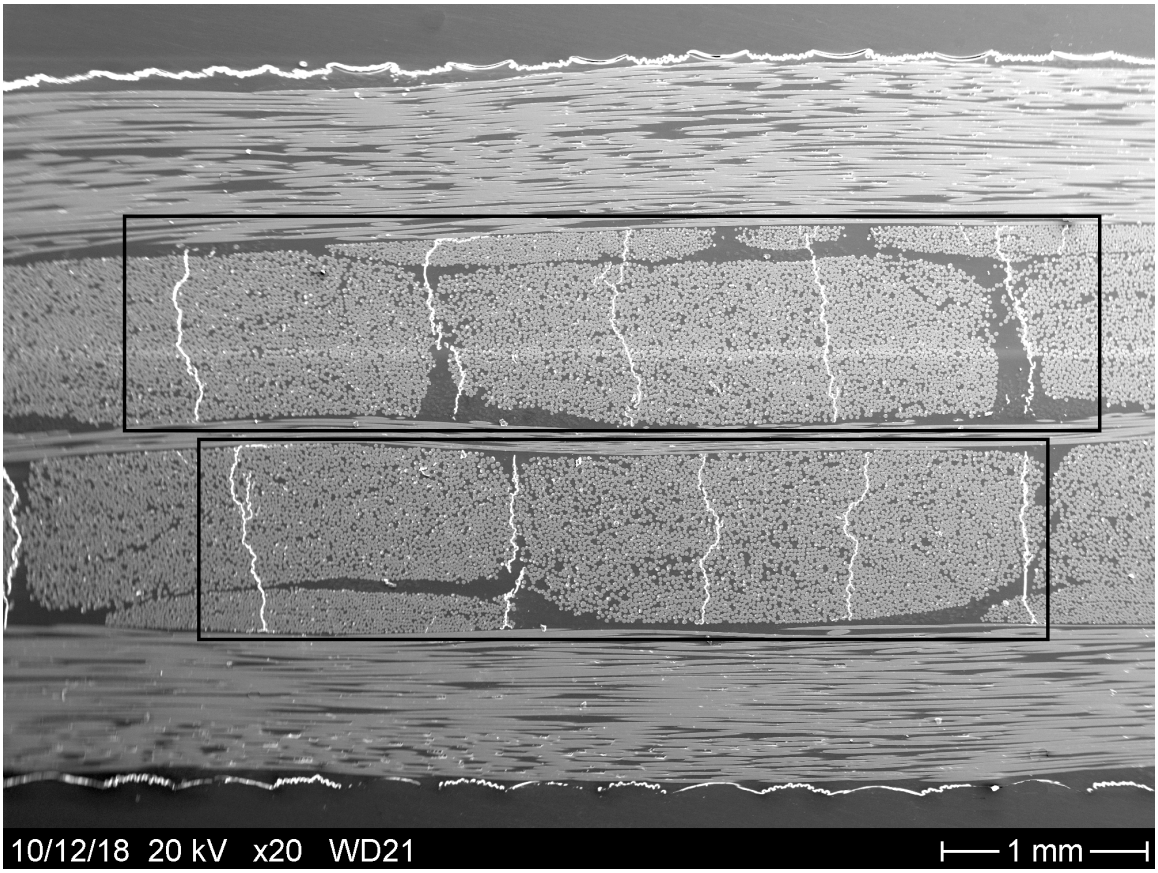


Figure 80: An SEM image of a $[0/90]_S$ coupon (4103_12), which had been loaded up to 2.5% strain, looking in the transverse direction.

Figure 81 shows an SEM image of a $[90/0]_S$ coupon taken looking through the transverse direction. The transverse cracking in the outer 90° plies is certainly less extensive than in the $[0/90]_S$ coupon that was observed. The cracks appear to be far less regular and some have not propagated through the full thickness of the tows. Once again, cracks can be observed between and within the tows, suggesting the influence of the stitching and resin rich regions between the tows were not the paths of least resistance for the cracks to initiate and propagate.

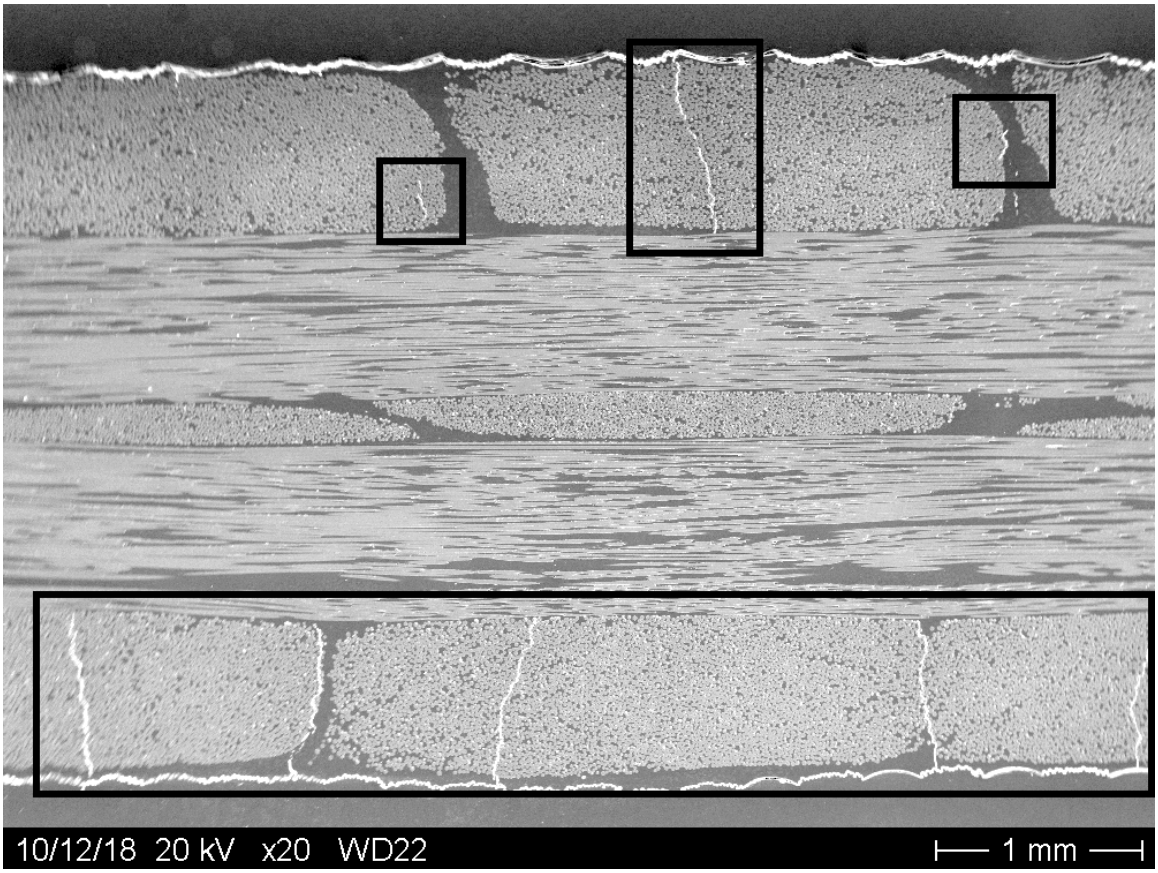


Figure 81: An SEM image of a $[90/0]_S$ coupon (4110_06), which had been loaded up to 2.5% strain, looking in the transverse direction.

Figure 82 shows an SEM image of the cross section of the $[0/90/\pm45]_S$ coupon shown in Figure 78(c) looking in the transverse direction, providing a more detailed look at the delaminations. Two delaminations are clearly visible It was originally expected that the delaminations had propagated between the 90° and ±45° biaxial plies, but Figure 82 shows that they actually propagated within the 90° plies; between the main fiber tows and their backing tows, which were oriented in the longitudinal loading direction. Another interesting feature is that the delaminations do not actually follow a straight path between the tows. They appear to be deflected by between the main fiber bundles. This is most likely due to the stitching holding the tows together and deflecting the cracks as they

propagated along the coupon. The stitching is barely visible in this SEM image because it is polyester, which is a very similar density to epoxy, so it blends in with the resin rich areas between the tows. Extensive transverse cracks in the 90° tows can also be observed, which all link up to the delaminations. These cracks also appear to have propagated into the backing tows of the 0° plies. Interestingly, in the top half of the laminate, the cracks do not show up in the resin rich regions between the 90° ply's main tow and the 0° ply's backing tow. Again, this could be the fabric's stitching influencing the propagation path of the cracks. No cracks can be observed in the ±45° biaxial plies.

Figure 83 shows an SEM image of the same laminate looking in the longitudinal direction. The delaminations are still present, but not as clear as Figure 81. Longitudinal cracks can be observed in the upper 0° ply, but a not as extensive as the transverse cracking. Part of a transverse crack in the upper 90° ply can also be seen. This image does show evidence of a small amount of cracking within the ±45° plies.



Figure 82: An SEM image displaying a closer look at the delaminations and other damage modes in a $[0/90/\pm45]_S$ coupon (4120_07), looking in the transverse direction.

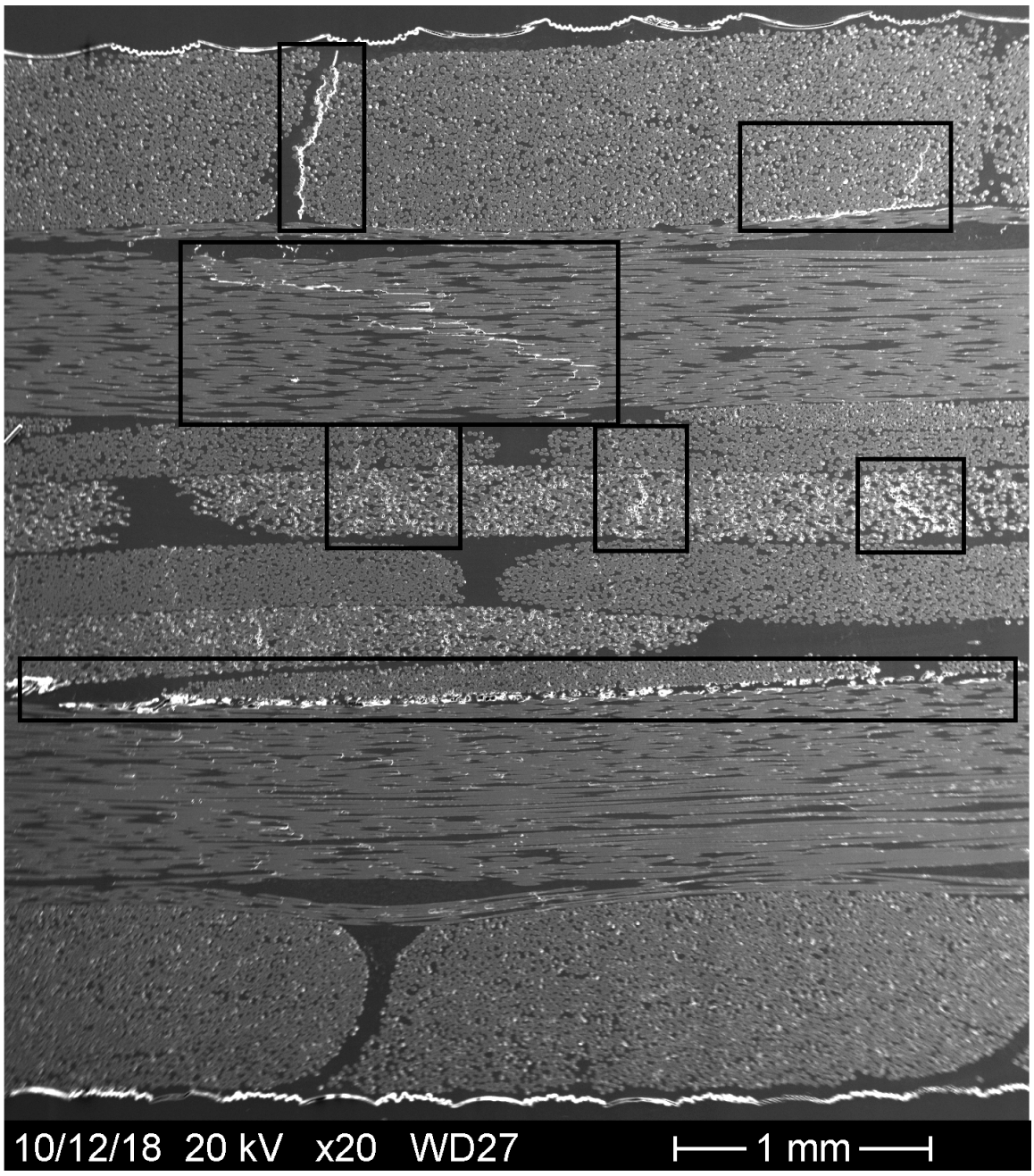


Figure 83: An SEM image displaying a closer look at the delaminations and other damage modes in a $[0/90/\pm45]_S$ coupon (4120_07), looking in the longitudinal direction.

Figure 84 and Figure 85 show SEM images of a $[90_4]$ coupon, which has been loaded to ultimate failure, in the longitudinal and transverse directions respectively. The longitudinal image shows very little evidence of damage in the coupon. Small sections of

delaminations or longitudinal cracks are highlighted between the main plies and their backing tows. The transverse images shows only transverse cracks. Some are small and had barely propagated through the thickness of one tow, whereas others have propagated through almost half the thickness of the laminate. The cracks do not appear to be regularly distributed, like those in the $[0/90]_S$ coupon. From observation of Figure 78 it was expected that there would be a crack between every fiber tow, but this was not the case. The cracks appear to have primarily initiated and propagated through the fiber tows, rather than between them.

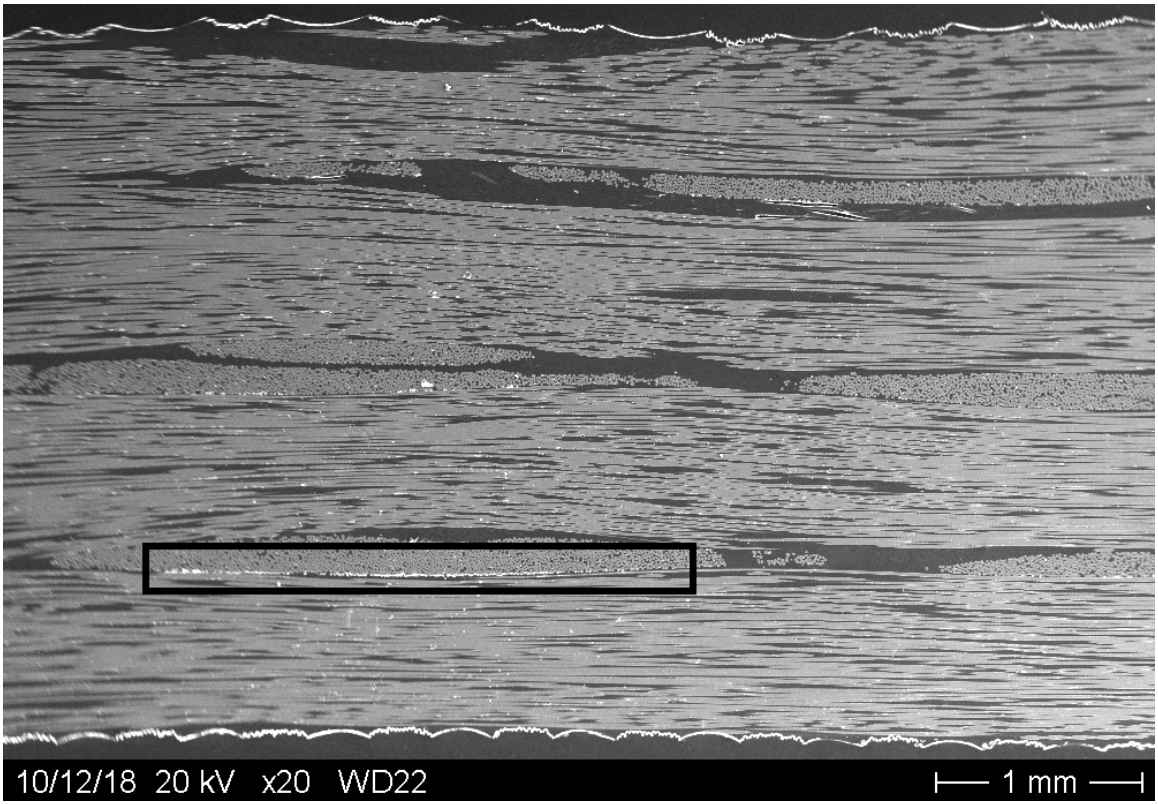


Figure 84: An SEM image of a $[90_4]$ coupon (4113_13), which had been loaded up to ultimate failure, looking in the longitudinal direction.

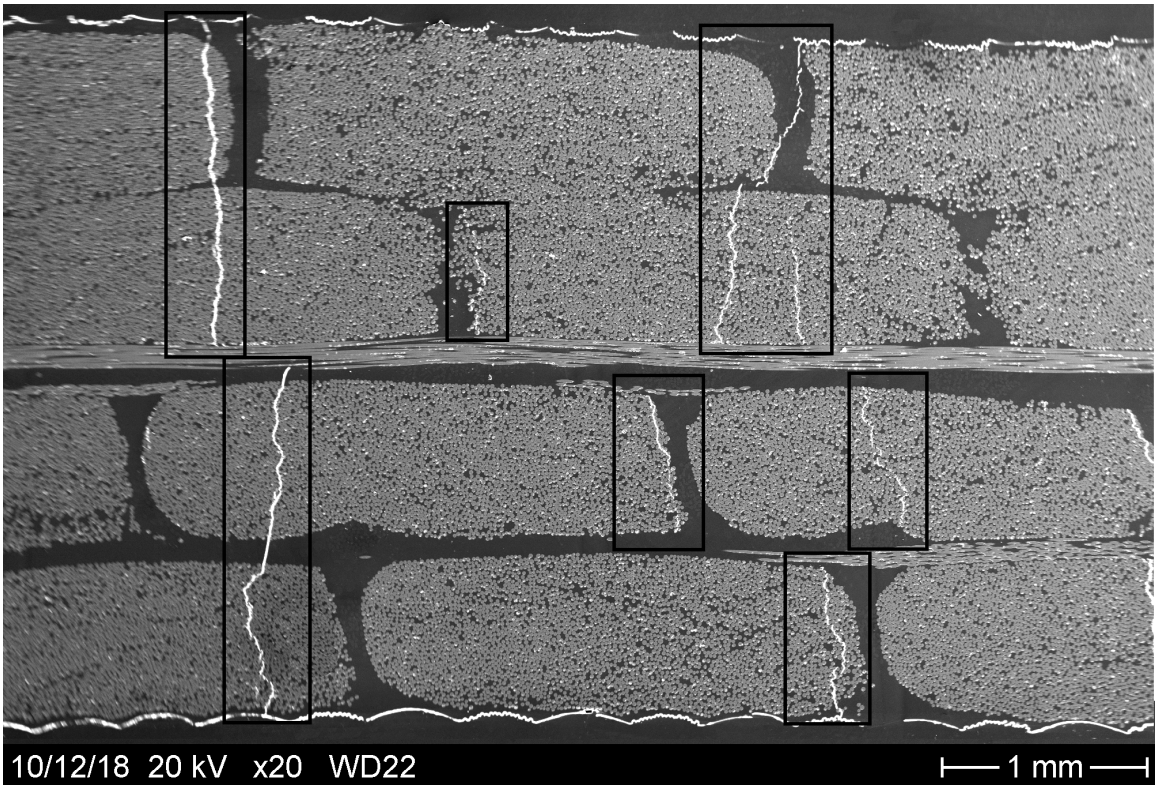


Figure 85: An SEM image of a [90_4] coupon (4113_13), which had been loaded up to ultimate failure, looking in the transverse direction.

Figure 86 shows a photo of the final failures of coupons from all five layups tested. The three layups with 0° plies in them exhibited very explosive failures, due to rapid strain energy releases, when the 0° tows failed almost simultaneously or in quick succession. The $[0/90]_S$ and $[0/90/\pm45]_S$ coupons displayed significant amounts of brooming on the outside from the 0° tows delaminating away from the 90° plies, leaving the 90° plies almost intact apart from a single crack splitting them in two. Conversely, the $[90/0]_S$ coupon shows less extensive brooming, but significant amounts of spalling from the 90° outer plies. The resulting strain energy release from the inner 0° plies caused large delaminations and explosive release of the outer plies from the surface of the coupons.

The $[90_4]$ coupons demonstrated much more localized final failures. Coupons broke in two from single transverse failures. As described earlier, the majority of stresses are transferred to the fabric backing tows oriented in the loading direction before final failure. Figure 24 shows that the fabric's backing tows are much more misaligned and chaotic than the main tows. It is highly probable that final failure occurs at the random point in the coupon where the backing tows are most severely misaligned.

Finally, the $[45/-45]_S$ coupons also failed in a very localized manner, through cracks and delaminations following the tow directions. In comparison to the $[90_4]$ coupons, very little damage could be observed in the coupon, aside from the main failure region, as was validated by the SEM imaging (see Figure 77). During testing, very slow and progressive final failures were observed, as opposed to the sudden and sometimes explosive failures exhibited by the other four layups. This was predominantly because of fiber bridging between the cracks which continued to hold load, as the coupons were slowly pulled apart.

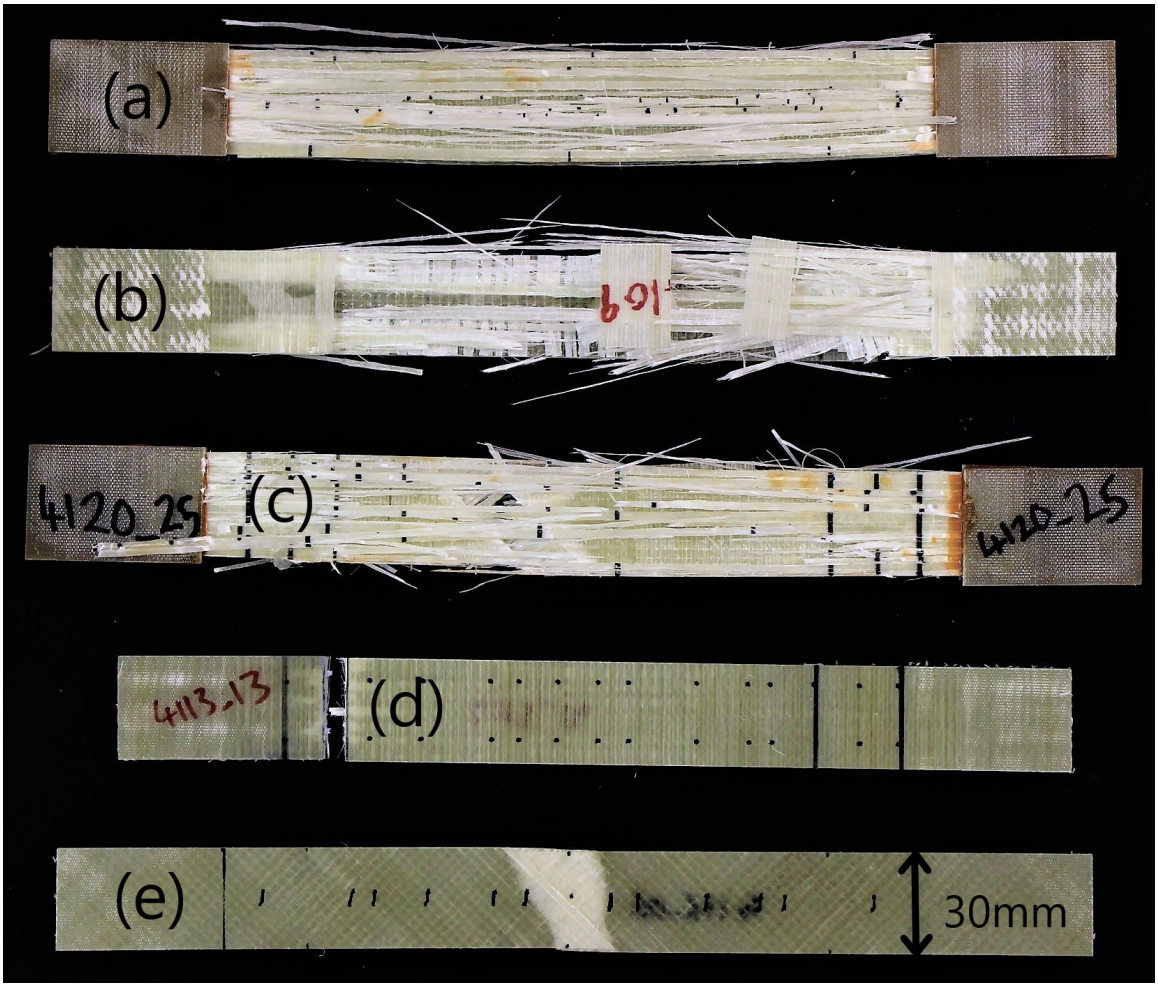


Figure 86: A photo showing coupons from all five layups which had underwent ultimate failure - (a) $[0/90]_S$, (b) $[90/0]_S$, (c) $[0/90/\pm45]_S$, (d) $[90_4]$ and (e) $[45/-45]_S$.

FATIGUE TESTING RESULTS AND DISCUSSION

Interrupted fatigue testing was conducted as a continuation of the static testing phases of this research, to apply the AE and GUW monitoring techniques to a more realistic loading scenario. The $[90_4]$ layup was not used in this phase of testing, due to its damage characteristics not being particularly relatable to real-life composite structures. This section provides the results, analysis and discussions with regards to the phenomena that were observed, the difficulties that were overcome and the challenges that may need to be addressed in the future.

Fatigue Life Results

As described previously, preliminary tests were conducted to obtain stress levels which would result in fatigue lives of approximately 10,000-20,000 cycles to failure, so that tests would not be too time intensive for each layup. Figure 87 shows the S-N plot for all three layups, including the data points for the preliminary and final tests (excluding premature grip failures), as well as the static testing results. Calculated S-N curves are not included, since not enough tests were conducted at each stress level, meaning it would not be possible to draw accurate conclusions from them.

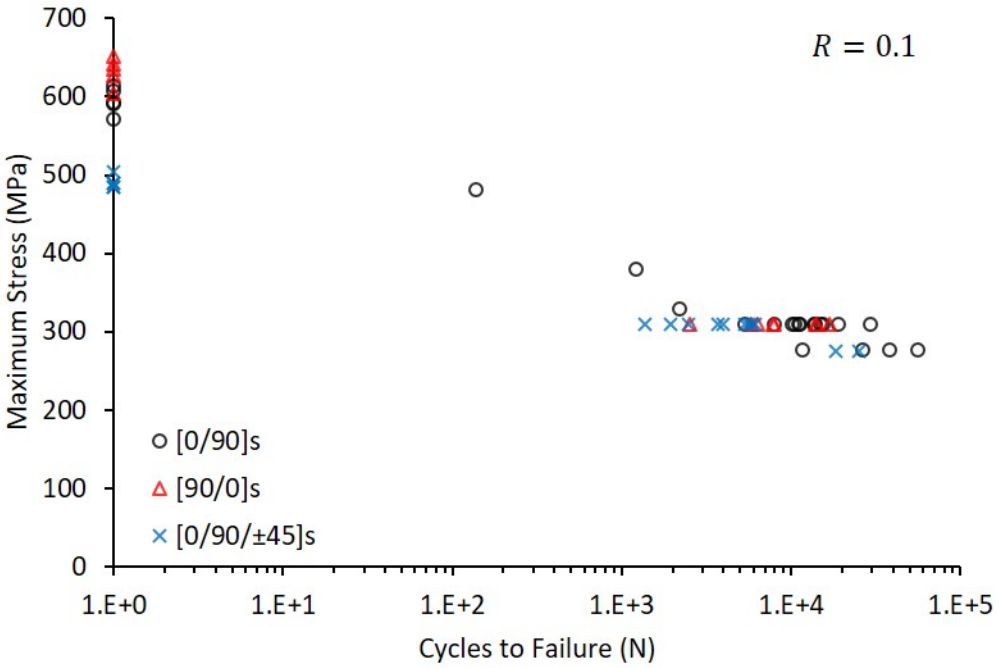


Figure 87: S-N plot for all fatigue tests that were conducted ($R = 0.1$), excluding premature grip failures and including the static tensile strengths, for all three layups tested.

The $[0/90]_S$ layup had the most data points, since it was the first layup to be tested to find approximate stress levels, for the desired fatigue life of this study. The plot shows that a stress level of 310 MPa was ideal for achieving a fatigue life in that range. Because the $[0/90]_S$ and $[90/0]_S$ layups were very similar, with comparable ultimate strengths, the same stress level of 310 MPa was also used for the $[90/0]_S$ layup. Initially, the $[90/0]_S$ coupons were tested without end tabs, but this consistently resulted in premature grip failures, despite the tabs not being required for the static tensile tests. What was particularly interesting, was that even with end tabs, the $[90/0]_S$ coupons still appeared to be much more sensitive to gripping issues than the other two layups tested. To prevent further grip failures, the end tabs had to be sanded to be parallel within a tolerance of 0.05 mm. This procedure was not required for the other two layups tested. It may be that

the combination of the tabs and the 90° outer plies were too soft for adequate gripping across the gripping area, causing slippage and uneven stress distributions. Perhaps thinner tabbing material would have resulted in less premature failures.

On average, the $[90/0]_S$ coupons still appeared to have a slightly shorter fatigue life than the $[0/90]_S$ coupons tested at the same stress level, despite showing a slightly higher static tensile strength. It is suspected that the full S-N curve would be slightly steeper for the $[90/0]_S$ layup in comparison to the $[0/90]_S$ layup, but this would require more testing at the intermediate and lower stress levels.

Despite the $[0/90/\pm45]_S$ layup showing a slightly lower fatigue life at 310 MPa maximum stress (2,000-8,000 cycles), the final interrupted tests were conducted at this stress level for consistency and better comparisons between layups. What is interesting is that the trend in fatigue life with respect to maximum stress appears to be much flatter for the $[0/90/\pm45]_S$ layup in comparison to the two cross-ply layups tested. It appears that the fatigue life may begin to converge or even surpass the cross-ply layups at lower maximum stresses, despite having a significantly lower static tensile strength. One explanation for this may be that the inclusion of the ±45° plies in the mid-plane of the laminate could act as crack barriers to a certain degree. They may slow the propagation of cracks through the thickness of the coupons, from one side to the other. This could have resulted in better stress distributions between the outer 0° plies, preventing the earlier onset of ultimate failures. More fatigue tests at the intermediate and lower stress levels would be required to draw more accurate conclusions on this point.

Overall, more fatigue tests at maximum stresses above and below 310 MPa would be required to draw more conclusive comparisons between the fatigue lives of the three layups tested. These tests were not completed during this study, due to testing limitations. The test coupons had to be of sufficient length to incorporate the AE and GUW sensors for the damage monitoring portion of this research. This meant that the cycle speed had to be significantly reduced, because of the limitations of the load frame used. Testing to one million cycles would have been infeasible with the current coupon geometry.

Modulus Degradation

Modulus degradation over the fatigue lives of laminates is an important parameter, which has been shown a lot of interest for SHM applications. Obtaining accurate moduli measurements throughout the fatigue life of the laminates tested proved to be difficult, with certain factors causing significant errors in the results. Initially, an extensometer was used on the edge of the coupons to acquire changes in strain for every fatigue cycle, but appeared to slip and become unstable after significant damage had been introduced to the coupons. Because of this, extensometer moduli measurements were only taken at each interruption when the GUWs were conducted. Even still, at later stages in the fatigue lives of the coupons, delaminations and significant tow splits were present, particularly in the $[0/90]_S$ and $[0/90/\pm45]_S$ coupons, which made it almost impossible to acquire accurate strain measurements. These delaminations and tow splits would result in the plies extending at different rates, resulting in the unstable and inaccurate measurements. Because of this, a combination of extensometer and crosshead displacement measurements were used to calculate moduli changes. During the earlier

stages of the fatigue tests, moduli were calculated from the extensometer strain measurements, before significant damage had occurred within the coupons and the measurements had become unstable. After this point, crosshead displacement measurements were then used until final failure. This assumed that the end tabs had had enough time to fully settle into the wedge grips and no significant grip slippage was occurring. Therefore, only the final five interrupted fatigue tests for each layup were used to produce modulus degradation curves. Figures 88-90 show the resulting normalized modulus degradation curves for each layup respectively and Figure 91 shows a comparison of the representative curves for each layup.

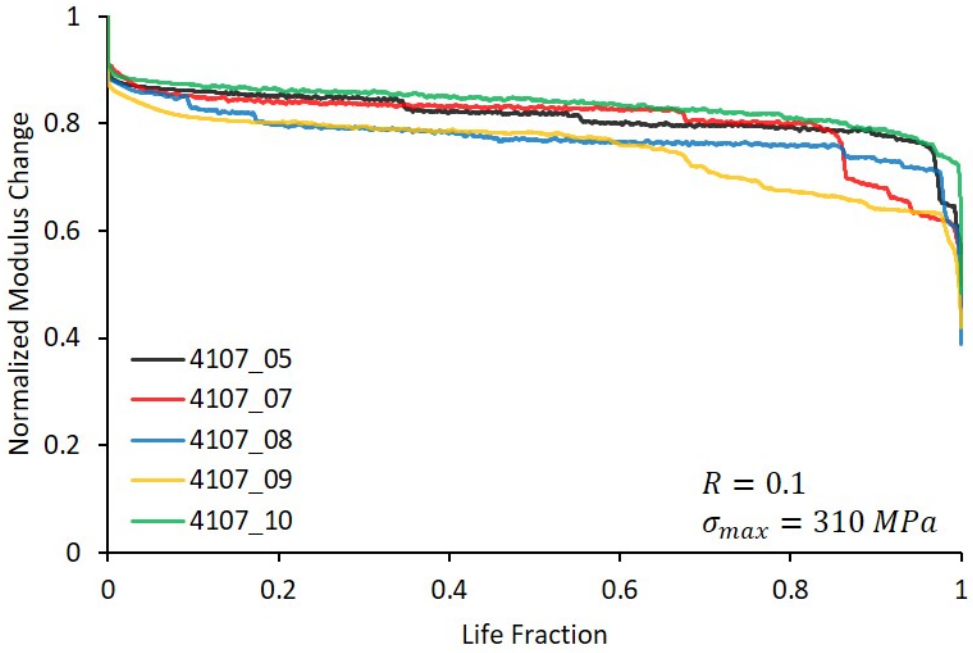


Figure 88: Normalized modulus degradation curves for the final five $[0/90]_S$ fatigue test coupons.

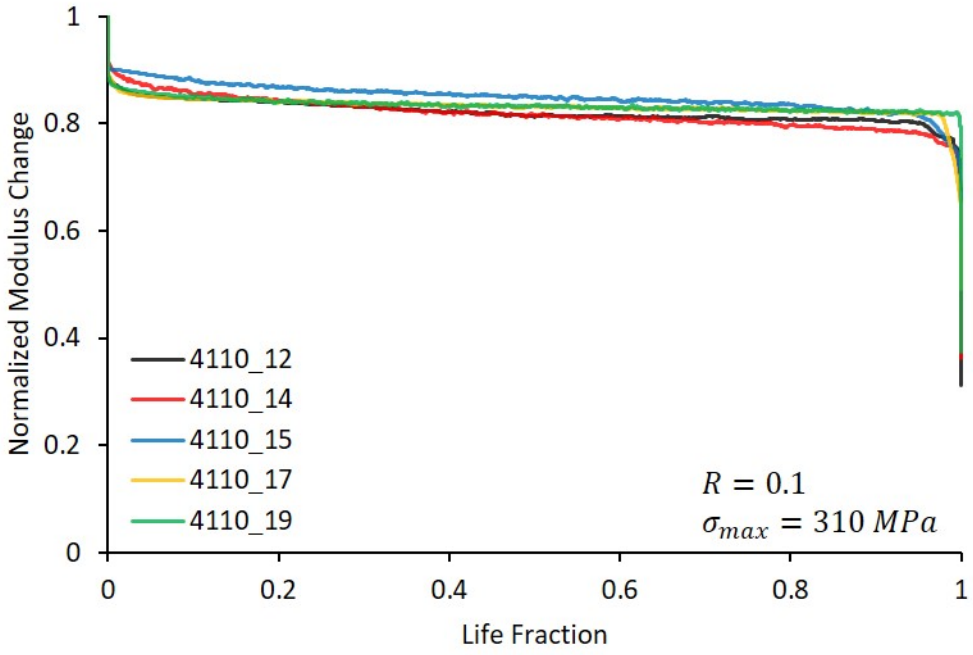


Figure 89: Normalized modulus degradation curves for the final five $[90/0]_S$ fatigue test coupons.

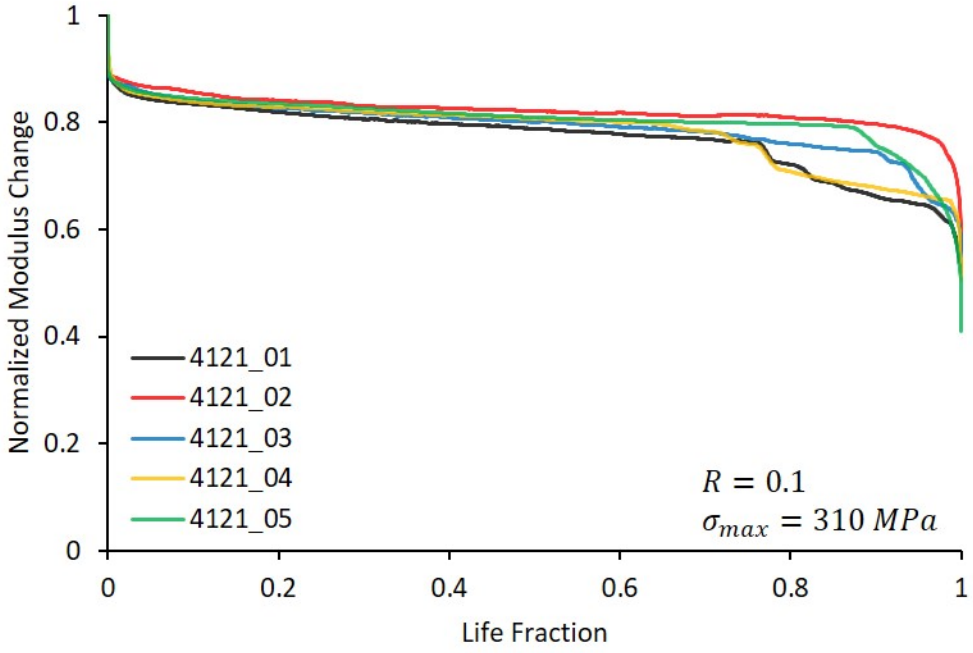


Figure 90: Normalized modulus degradation curves for the final five $[0/90/\pm45]_S$ fatigue test coupons.

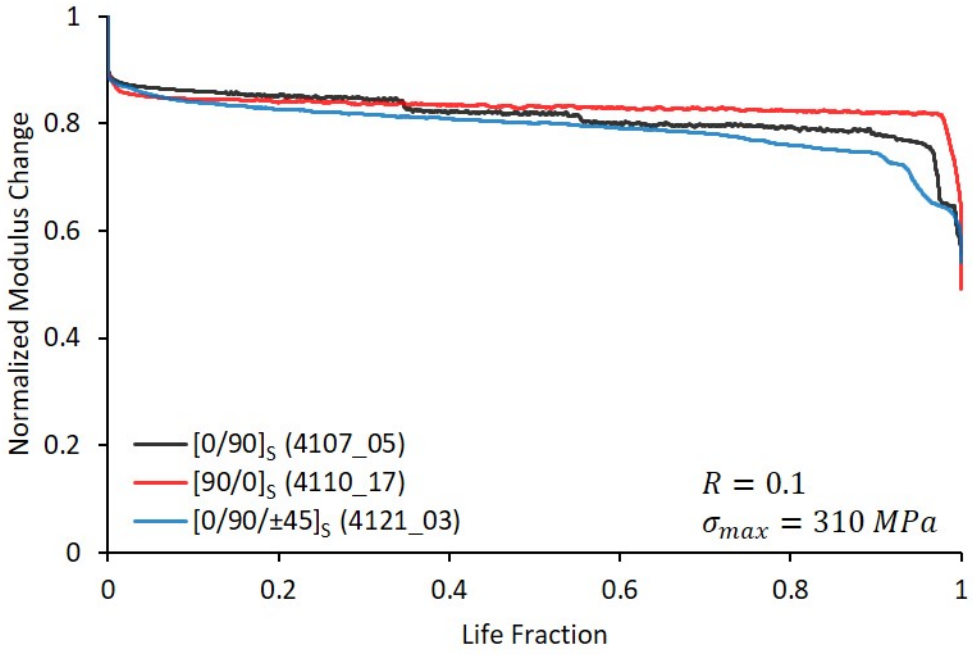


Figure 91: A comparison of normalized modulus degradation curves for one representative coupon from each of the three layups tested in fatigue.

The $[0/90]_S$ plot shows there was a noticeable amount of variation between tests (see Figure 88). All coupons showed approximately a 10-15% drop after the first fatigue cycle and then the curves appeared to flatten out after the first 10% of their fatigue life. Generally, little change was observed from this point until about 85% of fatigue life, when significant degradation began to occur, before final failure. Up to this point the coupons would typically exhibit a modulus drop of up to 20%, before dropping off to failure. Noticeable step changes in moduli can be observed over the length of the curves, which can be related to failure of 0° tows in the outer plies. Stresses would then be redistributed between the intact tows, resulting in uneven stress distributions across the coupons and a slow, progressive, cascading failure over the life of the coupons, leading to final fatigue failure.

The $[90/0]_S$ layup showed much more repeatable results (see Figure 89). The modulus degradation curves are grouped much closer together. Once again, the coupons experienced approximately a 10-15% drop in modulus over the first fatigue cycle. After this point, the curves flatten out significantly and the coupons experienced almost negligible changes in moduli before final failure. The most noticeable feature was how suddenly the moduli degraded at final fatigue failure. The moduli were observed to only severely degrade within less than the final 1% of the coupons' fatigue lives, or 5-10 fatigue cycles before final failure. These sudden failures can be explained by the fact that the main, load bearing 0° plies are constrained by the 90° outer plies. These constraints allowed the stresses to be redistributed much more evenly when the 0° tows did fail. This explains the flat portion of the modulus degradation curves and the much more sudden cascading failure and the end of the coupons' fatigue lives, when compared to the $[0/90]_S$ fatigue tests.

The $[0/90/\pm45]_S$ coupons showed very consistent modulus degradation results from the first cycle to approximately 80% of their fatigue lives, where the trends begin to deviate (see Figure 90). No obvious steps in degradation can be observed up until this point, unlike the $[0/90]_S$ curves, suggesting that significant tow breaks did not occur until later in the fatigue lives of the coupons tested. This may be a reflection of the lower fatigue lives exhibited by the $[0/90/\pm45]_S$ coupons at the same 310 MPa maximum stress level.

When comparing the general trend of the three layups (see Figure 91), all three show similar modulus degradations over the first fatigue cycle, which is consistent with

the results obtained during static testing up to the same stress level. This provides further validation that the increasing static tensile LUR test method resulted in no significant fatigue effects. The $[0/90]_S$ and $[0/90/\pm45]_S$ then continue to degrade at similar rates before significant drops within the final 10% of their fatigue lives. The $[90/0]_S$ showed a much slower rate of degradation, with the significant changes in modulus only occurring within the final 1% of fatigue life.

Overall, the results presented have shown that the three layups exhibited varying trends in modulus degradation throughout their fatigue lives. Perhaps the most important feature to note is the consistency between coupon tests, which showed that using extensometer strain measurements in the earlier stages of the tests and crosshead displacement measurements in the later stages was an acceptable method for reliable and repeatable moduli measurements for producing modulus degradation curves from fatigue test data.

Acoustic Emission

Similar to its use in the static testing phases of this research, AE monitoring was applied to detect crack initiation and propagation throughout the duration of fatigue testing. After the first load cycle, event data was filtered to only include damage events which were detected above 90% of maximum stress. This was to remove noise from events originating from the friction of fracture surfaces rubbing together during loading and unloading, in an attempt to only include waveforms which originated from actual damage events, for the analyses.

Figures 92-94 show the accumulated absolute energy trends for each coupon tested for each respective layup and Figure 95 shows a comparison of representative curves for each layup.

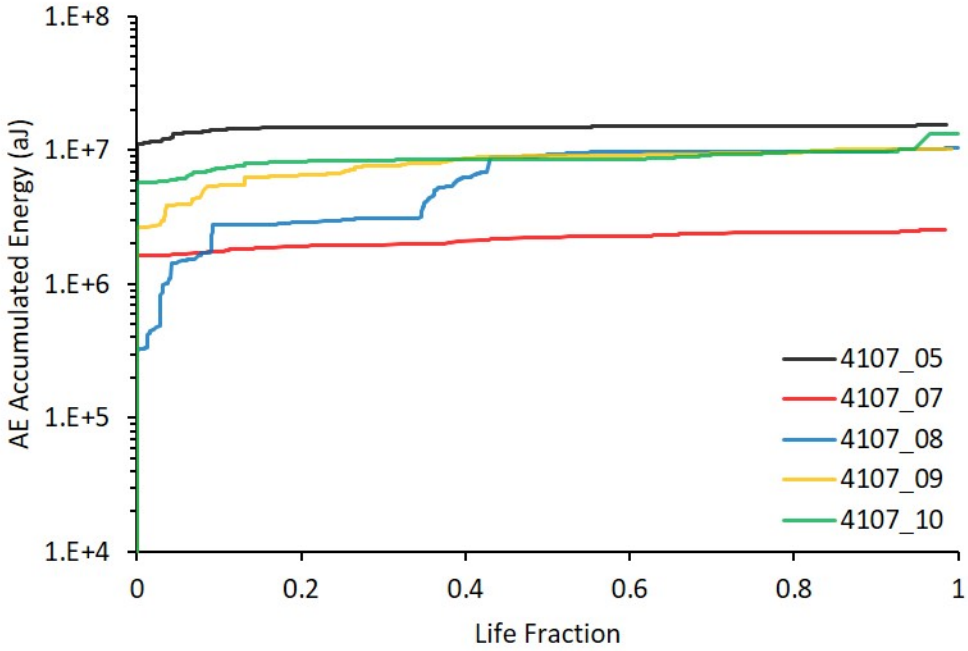


Figure 92: AE accumulated absolute energy (aJ) curves for the final five coupons tested for the $[0/90]_S$ layup.

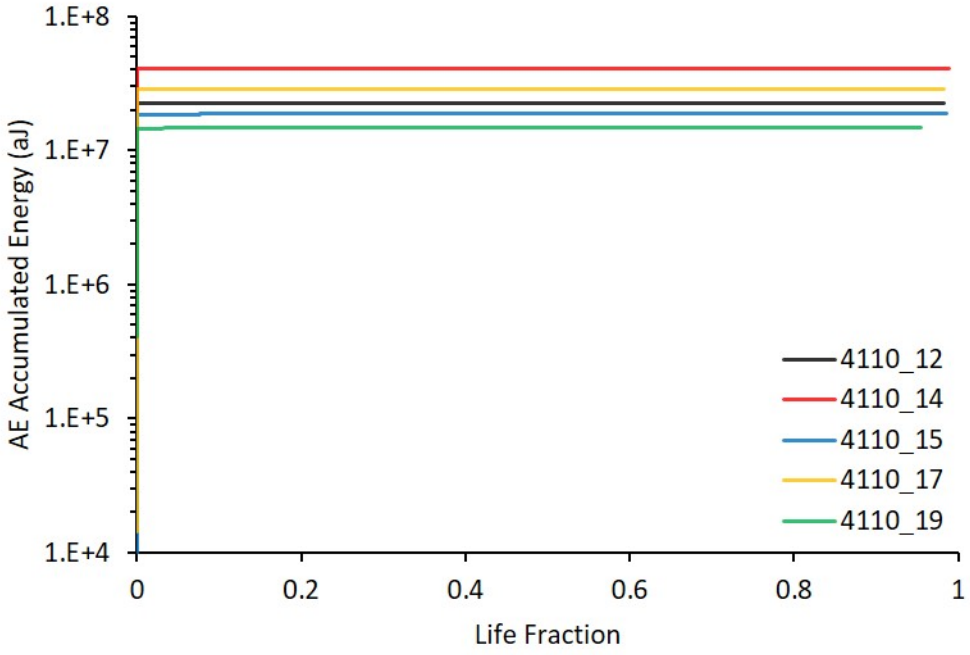


Figure 93: AE accumulated absolute energy (aJ) curves for the final five coupons tested for the $[90/0]_S$ layup.

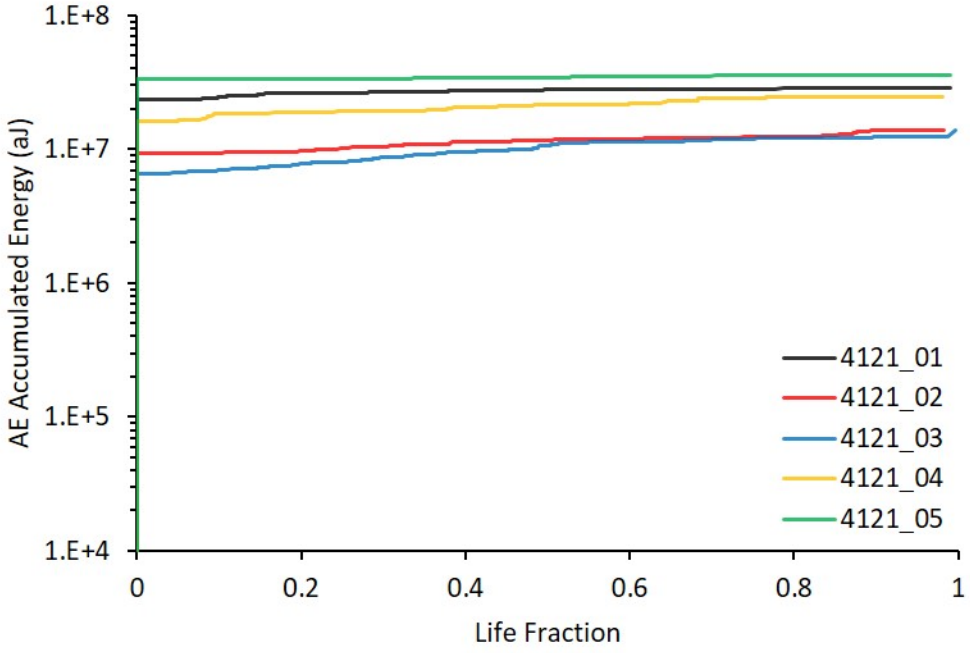


Figure 94: AE accumulated absolute energy (aJ) curves for the final five coupons tested for the $[0/90/\pm45]_S$ layup.

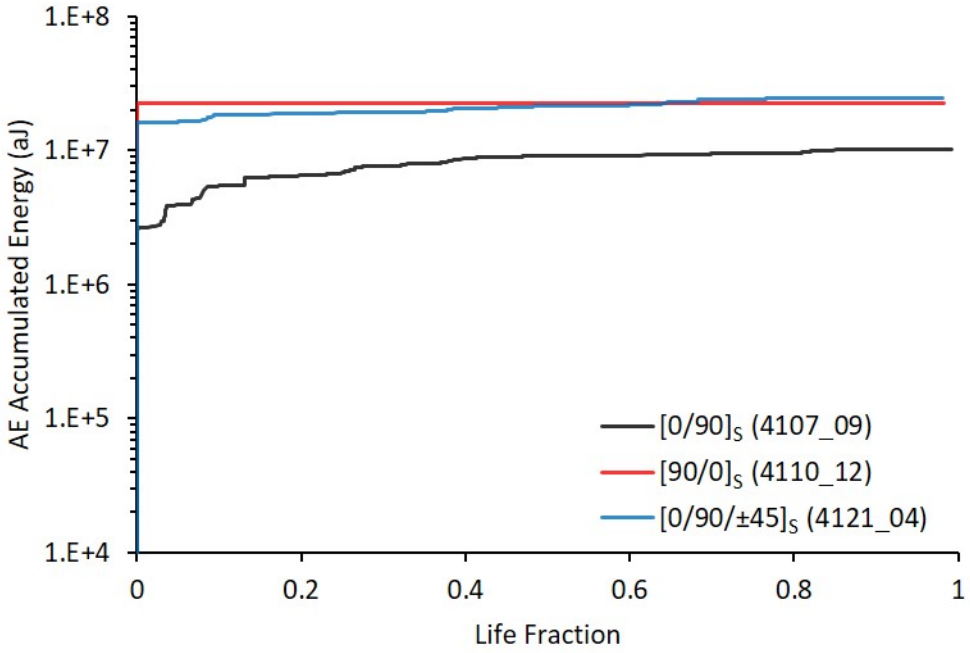


Figure 95: A comparison of representative AE accumulated energy trends for each of the three layups tested in fatigue.

The $[0/90]_S$ coupons showed large differences in event energy accumulated after the first fatigue cycle, ranging from approximately 3×10^5 to 10^7 aJ (see Figure 92). From this point, the changes observed were not as significant, apart from the 4107_08 coupon, which exhibited large changes throughout the fatigue test. It could be that the large tow failures described previously typically originated from the grips, so could not be detected by the AE sensors. These tow breaks also showed a significant possibility of affecting the placement of the AE sensors. Once the tows split they began to buckle and straighten with every load cycle (see Figure 96). When the broken tows were in line with the sensors, they would buckle underneath the sensors, causing them to become dislodged. This may be an explanation for some of the significant differences observed between tests.

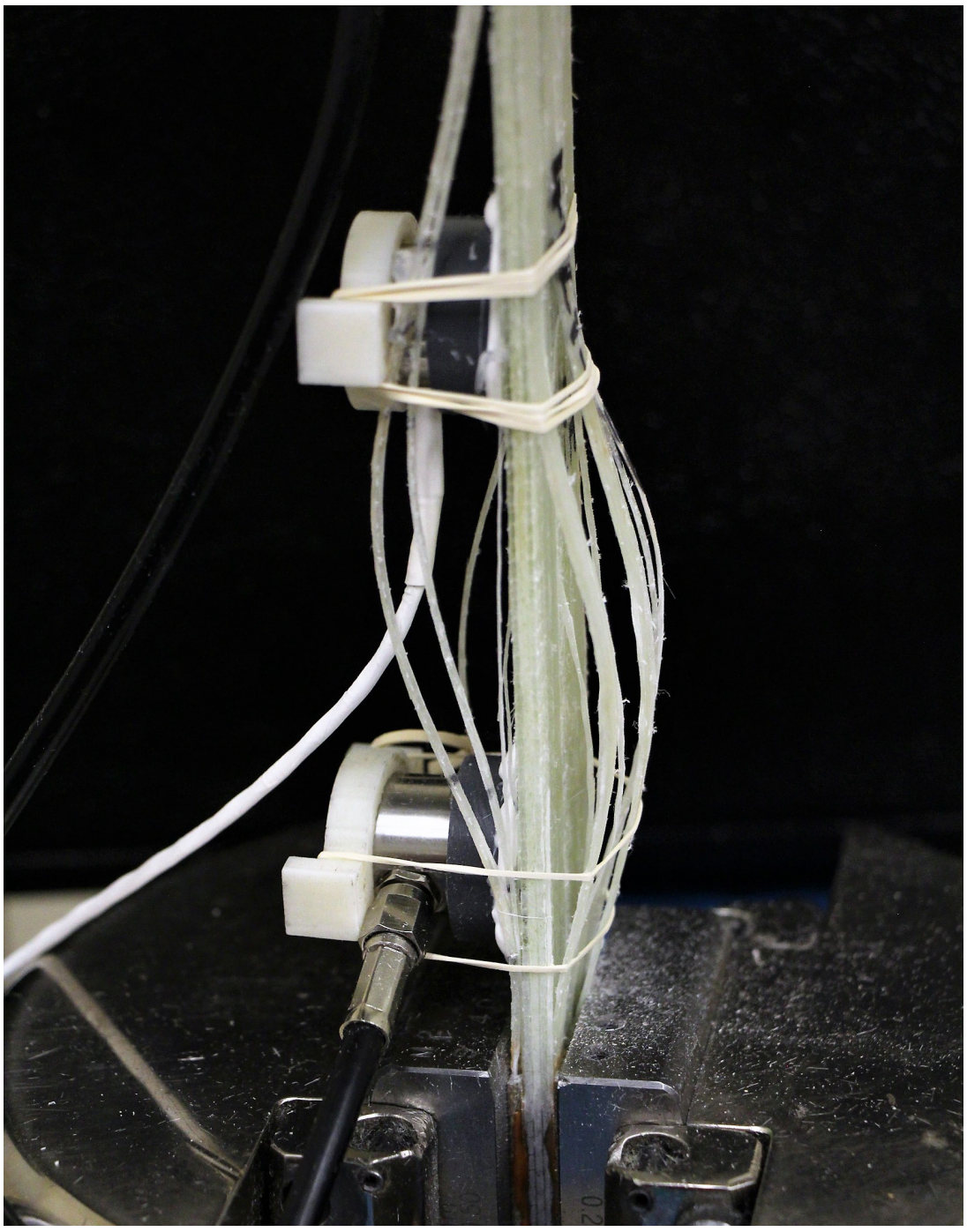


Figure 96: A photo showing buckling of tows close to the AE sensors, which had the potential to dislodge them.

On the other hand, the $[90/0]_S$ coupons showed closer relationships from test to test (see Figure 93). The trends were much closer together after the first fatigue cycle.

The most striking feature of this plot is how flat the trends were after the first fatigue cycle. This would suggest that the majority of the damage occurred during the first fatigue cycle, which would be consistent with the modulus degradation trends. Despite this, one would expect a final increase in energy during the final failure of the coupons, but this was not observed. It can also be observed that the 4110_19 test did not even detect any damage events after 95% of the fatigue life. Once again, this is likely due to final failure of the 0° initiating within the gripping areas of the coupons, so final damage events could not be detected.

The $[0/90/\pm45]_S$ coupons showed similar results to the other two layups (see Figure 94), but more consistent than the $[0/90]_S$ tests and less so than the $[90/0]_S$ tests. This was likely due to similar reasons, with tow failures occurring within the gripping areas. Despite this, the tow failures generally occurred during the later stages of the coupons' fatigue lives, so had less of an influence on the sensor placements than with the $[0/90]_S$ coupons.

The comparison of accumulated AE energies showed some interesting differences between the three layups (see Figure 95). Overall, significantly less AE energy was accumulated over the $[0/90]_S$ tests in comparison to the other two layups. The $[90/0]_S$ and $[0/90/\pm45]_S$ layups showed more comparable trends, with similar total accumulated energies. This is particularly surprising when compared with the static testing AE results. In static tensile testing, the $[0/90/\pm45]_S$ coupons generally accumulated noticeably less energy than the other two layups and the $[90/0]_S$ coupons significantly more than the $[0/90]_S$ and $[0/90/\pm45]_S$ coupons. The fatigue AE data showed the opposite of these

trends. It is also important to note that the total accumulated energies for the fatigue tests were significantly less than those acquired during the static tests. Initially, it was expected that the accumulated energy results would exhibit trends similar to the trends presented by Reifsnider's fatigue damage models [10], with the most significant changes in energies being observed in the first and last 10% of the coupons' fatigue lives. The results presented show that this was not the case. There may be several explanations for these significant differences.

One explanation may have been the setup of the AE system's event timing parameters. During the first fatigue cycle of each test, the AE system generally only detected 30-50 damage events. This is noticeably less than what was detected during the static tensile tests to a comparable stress level. The fatigue load cycles were conducted at a much higher strain rate than the static tests, meaning that all the initial damage events occur over a much shorter period of time. The AE system may have gotten overloaded with event waveforms and would not have been able to differentiate between them. A solution to this could be to reduce the HLT timing parameter in an attempt to more quickly differentiate between waveforms occurring in very quick succession, but could run the risk of detecting reflections as damage events and convoluting existing damage event waveforms.

Another possible cause of the reduced accumulated energies could be the attenuation of stress waves originating from damage events, resulting in reduced energies or damage events not being detected at all. Observation of the GUW data from the static testing has already shown that the presence of damage within composite laminates can

have a significant effect on the propagation of ultrasonic stress waves. This may have had a severe effect on the energy of the detected waveforms and the number of damage events which were actually detected. There are many compensation strategies associated with GUWs, such as applied load, temperature and humidity [42, 77, 83-86, 96, 97], but only distance based attenuation strategies for AE [98, 99]. Damaged based attenuation could have a profound effect on the results obtained from AE monitoring, particularly in constant amplitude fatigue loading, but seems to have been severely overlooked by the AE research community.

Similar to the static testing results presented in this research, information can be gained from observing trends in frequency content of the resulting AE damage event waveforms. Figures 97-99 show peak frequency scatter plots against fatigue life fraction for one coupon test from each layup, with their respective modulus degradation curves overlaid. Peak frequency plots for the rest of the final coupon tests conducted in fatigue can be found in Appendix E.

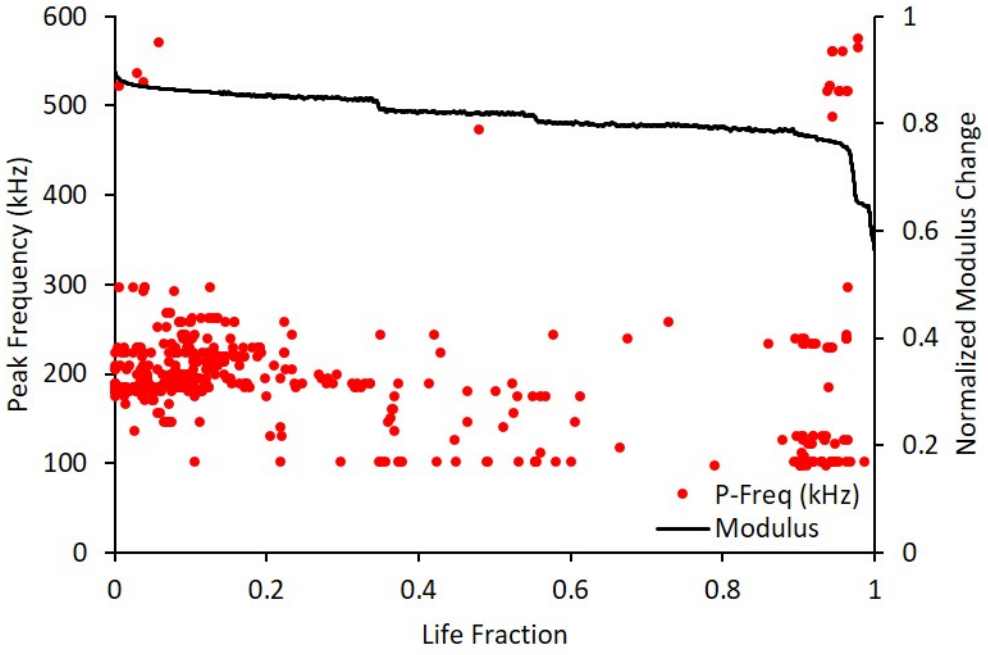


Figure 97: A peak frequency plot against life fraction for a $[0/90]_S$ coupon fatigue test (4107_05), with its respective modulus degradation curve overlaid.

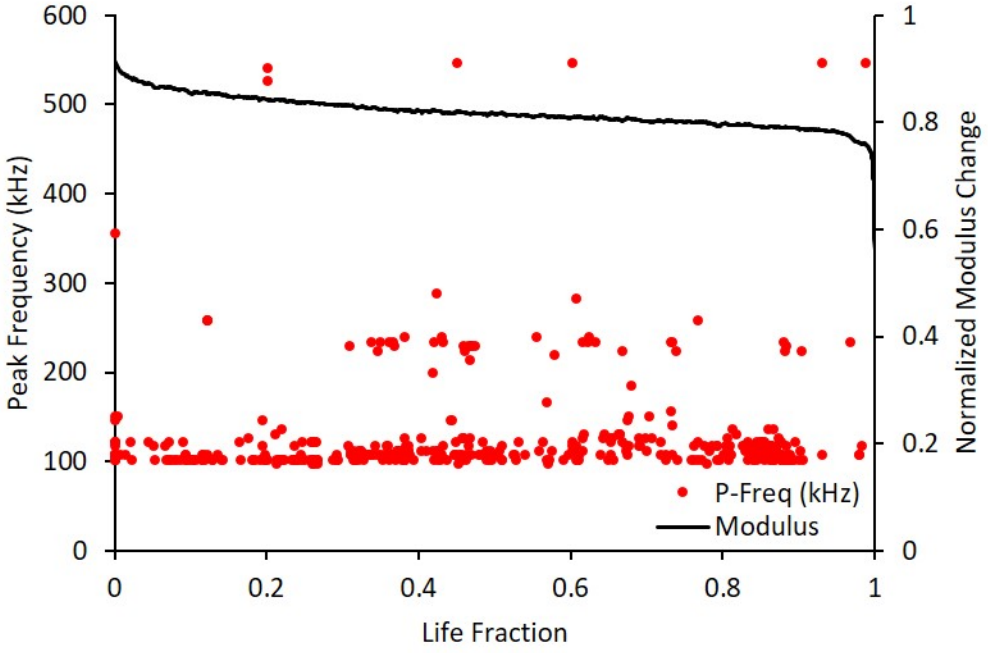


Figure 98: A peak frequency plot against life fraction for a $[90/0]_S$ coupon fatigue test (4110_14), with its respective modulus degradation curve overlaid.

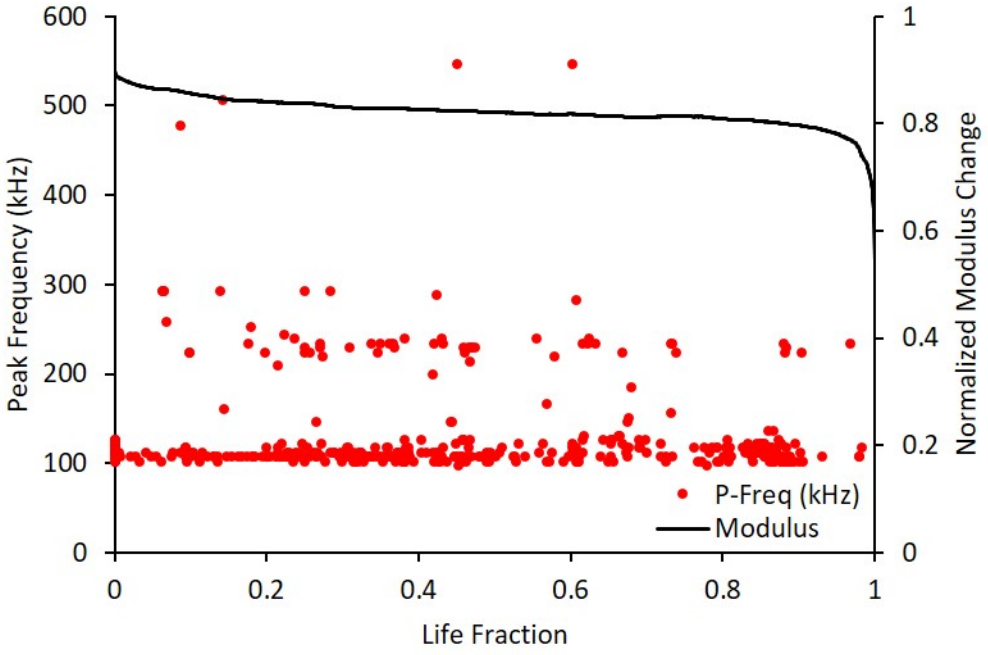


Figure 99: A peak frequency plot against life fraction for a $[0/90/\pm45]_S$ coupon fatigue test (4121_02), with its respective modulus degradation curve overlaid.

The plot for the $[0/90]_S$ coupon test (see Figure 97) shows that the majority of the AE events were clustered in the 150-300 kHz range for the first 20% of the coupon's fatigue life, which may be attributed to interface damage and is similar to the AE data acquired during static testing. A small number of events can be observed in the 500-600 kHz range, which may be related to fiber breaks in the 0° tows. Interestingly, very few events were detected with a peak frequency below 150 kHz. Events appear to become much less frequent after 20% life fraction, but activity picks back up again around 90% life fraction, which coincides with the severe drop in modulus at the end of the coupon's life. At this point more events below 150 kHz are detected as well as another cluster of events in the 500-600 kHz range, which may be related to final fiber breaks. Another noticeable feature is that almost no events were detected in the 300-400 kHz range, which

was also shown in the static testing results. All layups in both static and fatigue testing have exhibited this phenomenon.

On the other hand, the $[90/0]_S$ coupon plot shows significantly more low frequency events throughout the life of the coupon (see Figure 98), which is what was also observed during static testing. These frequencies were suspected to be caused by dominant out-of-plane flexural waves originating from transverse matrix cracks in the 90° outer plies. In comparison, very few events in the 500-600 kHz range were observed. This would be consistent with tow failures only being observed in the gripping areas of the $[90/0]_S$ coupons, which is outside the gage length of the AE sensors.

The $[0/90/\pm45]_S$ scatter plot (see Figure 99) shows a very similar trend to the $[90/0]_S$ plot, with the majority of the events being in the 100-150 kHz range. A larger number of mid-frequency (150-300 kHz) events can be observed throughout the life of the coupon, which may be caused by the inclusion of the ±45° plies. Many of these events may originate from interface damage within the off-axis plies, which would be consistent with the static testing results.

Since one of the goals of this research is to apply the acquired AE data to predict changes in moduli in fatigue loading scenarios, accumulated absolute AE energy and the number of detected AE events have been plotted against changes in moduli, to observe possible trends. Figure 100 and Figure 101 show these results as a combination of all five final fatigue tests for each layup. Each scatter point relates to the interruptions when moduli measurements were taken and the GUWs were applied. Further plots of changes in moduli against other cumulative AE parameters can be found in Appendix E.

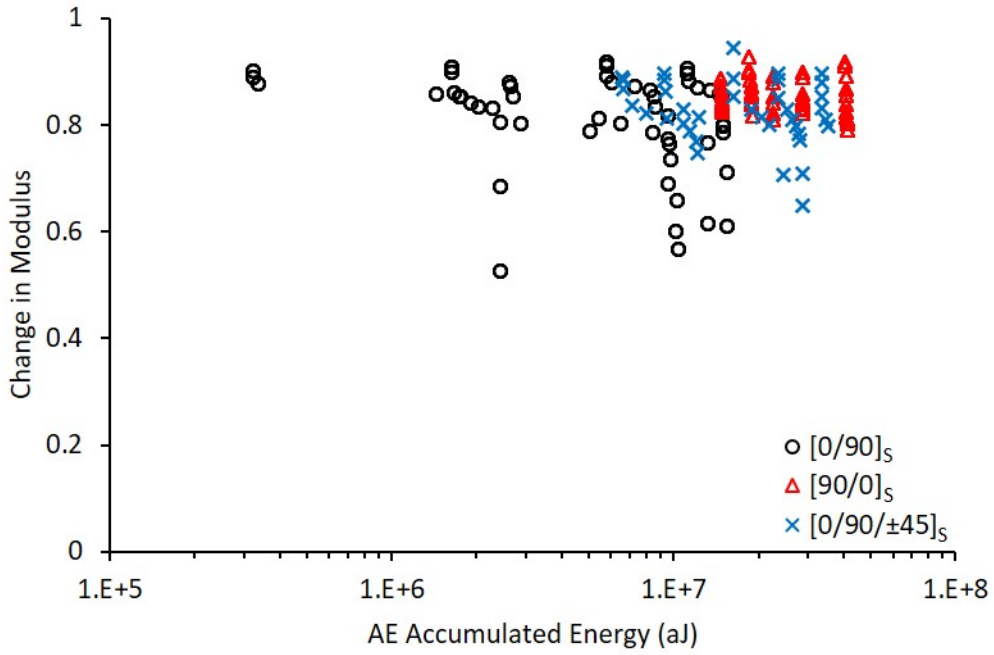


Figure 100: Changes in moduli plotted against accumulated absolute AE energy for all five coupon tests for each respective layup tested in fatigue.

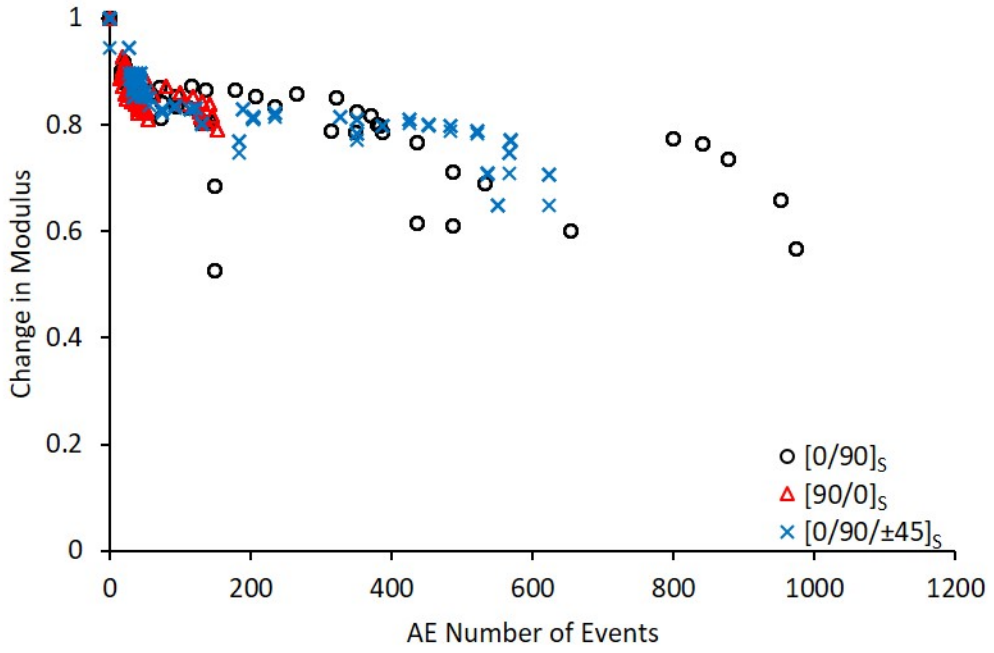


Figure 101: Changes in moduli plotted against accumulated number of AE events for all five coupon tests for each respective layup tested in fatigue.

As would be expected from the rest of the AE data presented in this section, there is a significant degree of statistical scatter caused by differences between tests. The accumulated energy plot (see Figure 100) shows the most variation, with no significant trends relating to modulus degradation for each of the three layups. The accumulated number of AE events (see Figure 101) does show better trends with respect to changes in moduli, but they were certainly not linear when compared with the static testing results. These significant differences and variations, when compared to the static testing results, can be attributed to issues with the AE test method when applied to fatigue testing, which have been discussed previously in this section. It is suspected that if the suggested corrections and compensation strategies are applied to the AE test data, the relationships between changes in moduli and the cumulative AE variables would show much better linear correlations, similar to the static testing results.

Guided Ultrasonic Waves

To stay consistent with the static testing procedures, fatigue tests were interrupted at specified intervals to apply the GUWs at zero applied load. Once again, five GUWs were triggered at each interruption. All the same signal parameters were extracted from the resulting waveforms and normalized to the initial reference pulses, which were acquired when the coupons were in their undamaged state. Figures 102-104 show normalized modulus change plotted against normalized absolute energy change, amplitude change and counts change respectively. Linear regression fits have been included to show the linear relationships of the variables with respect to modulus change,

similar to the static testing GUW results. Plots of the other extracted variables can be found in Appendix E.

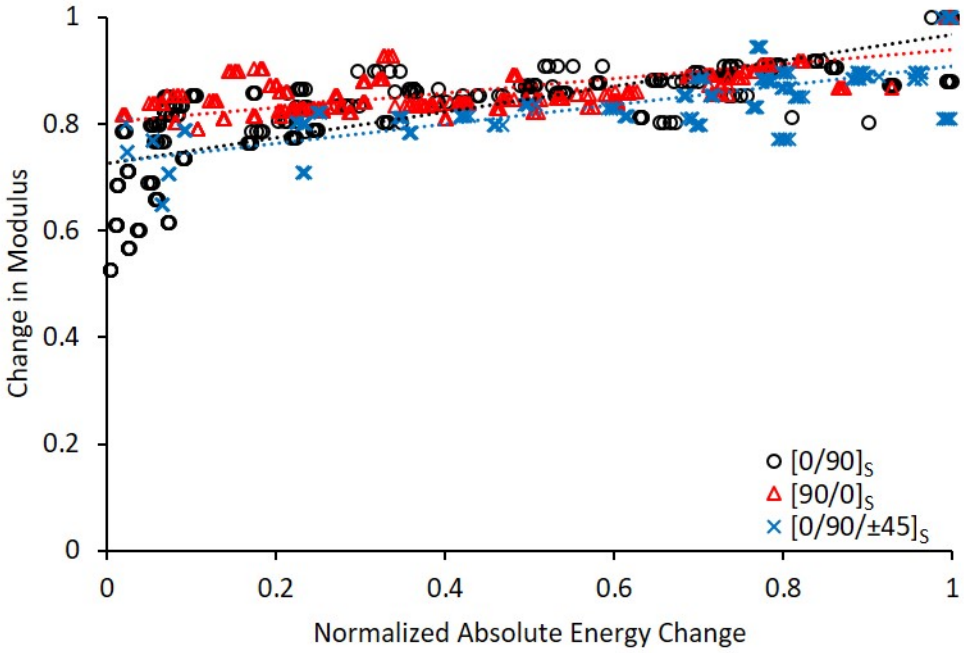


Figure 102: Changes in moduli in fatigue plotted against GUW normalized absolute energy change for all five coupons tested for the three layups, with linear regression fits included.

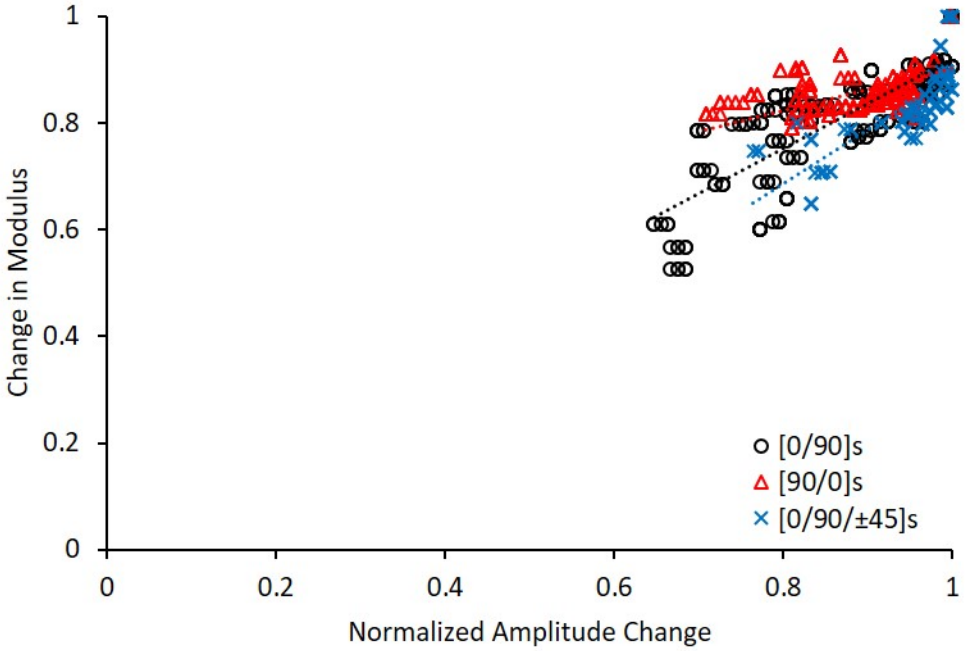


Figure 103: Changes in moduli in fatigue plotted against GUW normalized amplitude change for all five coupons tested for the three layups, with linear regression fits included.

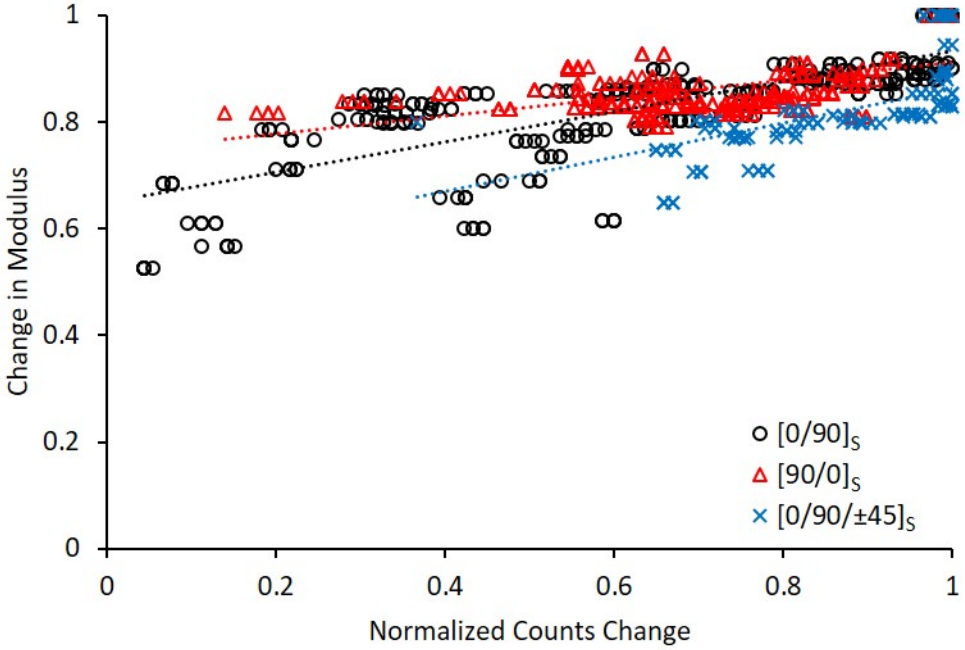


Figure 104: Changes in moduli in fatigue plotted against GUW normalized counts change for all five coupons tested for the three layups, with linear regression fits included.

Changes in absolute energy were noticeably linear for all three layups (see Figure 102) and were comparable to the static testing results (see Figure 70). The gradients were also comparable to the static testing results, or even slightly lower i.e. changes in absolute energy were more severe with respect to changes in moduli. The $[0/90]_S$ dataset showed more data points for more significant changes in moduli. This is an artefact of the $[0/90]_S$ coupon fatigue lives being slightly longer than the other two layups, so more data points could be acquired in the final 10% of the coupons' fatigue lives. At these more severe modulus degradations, the trend appears to become non-linear. Of course, energies cannot fall below zero, so a logarithmic fit may have been more accurate for more severe modulus degradations, but linear fits appeared more accurate overall for the acquired results.

Comparisons between moduli changes and changes in GUW amplitude also showed loose linear trends (see Figure 103). The $[0/90]_S$ and $[90/0]_S$ datasets showed the most significant amplitude changes, whereas the $[0/90/\pm45]_S$ dataset showed the smallest amplitude changes. This was not consistent with the static testing results (see Figure 69), where the $[90/0]_S$ and $[0/90/\pm45]_S$ layups showed the largest changes in amplitude and the $[0/90]_S$ layup showed the smallest. In fatigue the $[0/90]_S$ data certainly exhibited the most statistical scatter, when compared with the other two layups.

Changes in GUW counts also showed some noticeable correlations with changes in moduli (see Figure 104). Although there was significantly more statistical variation than the other two waveform variables presented, changes in counts showed better correlations in fatigue than the data acquired during static testing (see Appendix D). The

$[90/0]_S$ data showed the least statistical scatter, whereas the $[0/90]_S$ data showed the most. The most important feature of the GUW count data to note is the cluster of data points close to 1 on the x-axis, but below no change in modulus (change in modulus = 1), particularly for the $[0/90/\pm45]_S$ dataset. This would suggest that the number of GUW counts did not change after the first fatigue cycle. Reasons for this are unknown.

Overall, the GUW results have shown significant amounts of statistical scatter, but there are several explanations for this, in relation to the attachment of the sensors to the coupons. As was described in the AE results section, the failure and subsequent buckling of outer 0° tows on the $[0/90]_S$ and $[0/90/\pm45]_S$ coupons would occasionally dislodge the AE sensors. The phenomenon would also affect the GUW actuator, compounding the errors in the results. Additionally, constant loading and unloading of the coupons would have resulted in movement of the coupon surface beneath the sensors, due to strain. This may have resulted in slight changes in the thickness of the vacuum grease film beneath the sensors, which could have affected the results to some degree. This may explain the significant differences between the static testing and fatigue testing GUW results. The only remedy to this would be to use a permanent adhesive, such as epoxy, to bond the sensors to the coupons. This would be a good solution for real-life SHM scenarios, but was deemed too impractical and risky for lab testing. Removing the sensors after ever test would significantly increase the probability of damaging them. This would be completely infeasible for the hundreds of tests that were conducted throughout this study.

STATISTICAL PREDICTIVE MODELING PROCEDURES

A significant amount of AE, GUW and modulus degradation data was acquired from increasing static tensile LUR tests and interrupted tension-tension fatigue tests, which has been analyzed in depth in the previous two chapters. The goal of this was to process the data in such a way, so that it could be combined and used to construct and train statistical models to predict modulus degradation of composite laminates. Originally, it was anticipated that the data could have been used to predict remaining fatigue life, as well. The results presented in the previous chapter showed that there was far too much variation for this application, but it is certainly worth considering for the future. Models were constructed as a starting point to making the combination of the two techniques applicable to the SHM of large composite structures, such as wind turbine blades.

Modeling procedures and decisions were developed through observations of the data acquired during static testing. It was hoped that the models produced would still be applicable to the fatigue loading cases, since the fundamental ideas behind the formation and propagation of ultrasonic waves have not changed. This chapter describes the procedures developed and a summary of the models that were constructed.

Model Selection

As was shown in the “Background” chapter of this dissertation, a whole host of signal processing techniques and statistics based models have previously been applied to AE and GUW data to evaluate composite laminate damage states, determine damage

mechanisms and predict degrading laminate properties. The chosen model had to fit the following requirements:

- Be capable of combining the data from the two monitoring techniques in a logical and suitable way.
- Fit the data in a representative manner, while also avoiding overfitting.
- Be easily interpretable, so fundamental understandings of the data can be obtained.
- Provide room for expansion and added complexities, if this research in continued to larger composite structures with more complex sensor arrays.

Figures 65-72 show that several variables from both the AE and GUW data in static testing exhibited prominent linear trends against modulus degradation for all four layups tested. For this reason, multivariate linear regressions were the chosen models for making predictions. They are capable of combining variables from both techniques in a logical manner. Also, being a relatively simple style of predictive modeling, they allow for easy interpretation of the results, unlike the commonly used artificial neural networks, which can possess many hidden layers to them. Finally, they provide a good starting point for gaining deeper understandings of the datasets and relationships between variables and would allow for expansions, if this research is to be continued to larger, more complex sensor arrays and structures.

Multivariate Linear Regression Modeling

Before constructing the multivariate linear regression models, relevant signal parameters had to be extracted and the data had to be processed in a logical manner to

combine the two techniques and obtain meaningful predictions. From the GUW datasets, many signal parameters from the received waveforms were extracted, which were rise time (μs), counts, amplitude (dB), duration (μs), MARSE energy (based around 100 kHz), absolute energy (aJ), peak frequency (kHz) and centroid frequency (kHz). Since two sensors were used to receive the GUWs, variables from the resulting waveforms were averaged over the two sensors. All variables were normalized to the waveforms obtained from the GUWs applied to the undamaged coupons, since it is of interest to compare the response of the damaged coupons to the same undamaged coupons.

On the other hand, data acquired from the AE monitoring had to be summarized over the coupons' lives up until the points that the respective GUWs had been applied. This meant that cumulative variables had to be used, which were cumulative absolute energy (aJ), cumulative MARSE energy (based around 100 kHz), cumulative counts and cumulative number of events. Cumulative totals were calculated by the sum of these variables from both AE sensors and all damage events that had been detected up to each point where the GUWs were applied. These variables could not be normalized against the undamaged state, since they all begin at zero and end at unspecified totals.

Changes in moduli were also normalized against the initial moduli measured at the beginning of each test. Separate models for each layup were constructed, so the datasets from each of the coupon tests (seven for static and five for fatigue) from each layup were stacked to account for variability between tests. Finally, an arbitrary constant variable was added to each dataset to account for the β_0 intercept term in Equation 2. Plots of all processed variables against modulus change for each coupon test for each

layup can be found in Figures 65-72 and Appendix D for the static cases and Figures 100-104 and Appendix E for the fatigue loading cases.

Initially, models were constructed for each layup separately, with all predictor variables present. Variable coefficients were calculated to fit Equation 2 using a maximum likelihood estimation procedure, through built-in functions in MATLAB. The β_i coefficients were then applied to the datasets to calculate the modulus changes and then compared to those measured during testing. From these comparisons, various fit quality measures were calculated, such as R^2_{adj}, F-statistic, overall p-value and individual p-values for every variable applied to the models. These fit characteristics were used as measures of how well the calculated coefficients can be used to fit the data to changes in moduli, when compared to the training data.

Model Validation

Although R^2_{adj}, F-statistic and p-values are good measures of how well a predictive model has been trained, they do not truly validate a model's predictive capabilities. They only test the model's ability using the same response data that was used to train it. Therefore, certain validation procedures had to be adopted to properly assess the effectiveness of the models.

Hold out cross validation (HOCV) was the chosen method. To conduct this procedure for a given dataset, the data points from one coupon test were withheld and the remaining data points were used to train the model. Using the coefficients determined from training, the withheld coupon dataset was then used to test the model and determine its predictive capabilities. By comparing the predicted modulus changes to those

measured in the withheld dataset, an R^2 value was calculated. This procedure was then repeated by withholding different coupon tests from the dataset, until all had been evaluated. The resulting R^2 values were then averaged to give an overall score for the model (R^2_{HOCV}).

This served as a non-biased way to evaluate the predictive performance of each model that was constructed, as well as providing a good measure of the repeatability of the testing procedures implemented for acquiring the data [91].

Variable Reduction

As shown in Appendices D and E, not all GUW and AE variables correlated well with changes in modulus. To remove these statistically noisy variables and prevent overfitting of the data, a non-biased procedure had to be developed.

Backward selection was the chosen method. First, models were constructed using all of the available variables. Individual p-values were compared for all of the predictor variables. The variable with the highest p-value was removed from the dataset and the model re-trained. The changes in R^2_{HOCV} were observed and this process was repeated iteratively until R^2_{HOCV} was maximized.

Although a non-biased process, it did result in different variables being finalized for different layups and models. Comparisons of the final selected variables allowed for discussion on how different layups affected the different features of the GUW and AE data.

Layup Independence

All the procedures described above have stated that models were constructed for each layup separately. It would be much more universal to have a single model which is capable of making accurate predictions for any given layup in any orientation, as would be encountered when monitoring large composite structures.

To test the possibility of constructing a singular model, datasets from the three main layups ($[0/90]_S$, $[90/0]_S$ and $[0/90/\pm45]_S$) were combined for producing singular static models. The $[90_4]$ layup was not used, since it is an unrealistic layup to be used for composite structures. The HOCV procedure was slightly modified so that three coupon datasets were withheld from training rather than one each time, to keep within the idea that 15-20% of the data should be used for validation each time.

First a model was constructed and tested without making any modifications to Equation 2. It was hypothesized that certain interaction parameters based on various laminate properties could be incorporated into Equation 2 to obtain better layup independent predictions. Inspection of the variables against changes in moduli for the static data showed that the AE cumulative variables exhibited the biggest differences in linear gradients between layups, particularly cumulative energies and counts. As discussed in the "Static Testing Results and Discussion" chapter, the most likely causes of these differences are the propagation and amplitudes of both S_0 and A_0 wave modes i.e. S_0 is related to in-plane stiffness (E_L), whereas A_0 is related to bending stiffness (E_B). Because of this, it was decided that an interaction parameter should be a function of both E_L and E_B, which were calculated using Equations 10 and 11, using the A_{ij} and D_{ij} terms

which can be calculated using classical laminate plate theory [100]. Two different functions were chosen to test the possibility of an improved layup independent model, which are shown in Equation 12. These functions were applied as interaction parameters to modify Equation 2 into the form of Equation 13, where X_1, X_2 and X_3 are AE cumulative absolute energy, AE cumulative MARSE energy and AE cumulative counts respectively and t is the laminate thickness. All GUW variables and AE number of events were still included in the model and the same variable reduction procedure was applied.

$$E_L = \frac{A_{11}A_{22} - A_{12}^2}{tA_{22}} \tag{10}$$

$$E_B = \frac{12(D_{11}D_{22} - D_{12}^2)}{t^3 D_{22}} \tag{11}$$

$$f(E_L, E_B) = \frac{E_B}{E_L} \; and \; f(E_L, E_B) = \frac{1}{E_L E_B} \tag{12}$$

$$Y = \beta_0 + f(E_L, E_B)(\beta_1 X_1 + \beta_2 X_2 + \beta_3 X_3) + \beta_4 X_4 + \cdots + \beta_i X_i + \epsilon \tag{13}$$

Collinearity and Principal Component Analysis

Collinearity is a common issue when constructing statistical models from datasets extracted from waveform and AE data. For example, waveform amplitudes and frequency content are closely related to waveform energy content and AE cumulative number of events are of course closely related to AE cumulative energy and counts. It is possible for these close relationships to affect the stability of multivariate linear regression coefficients and their overall predictive capabilities. Because of this, various techniques, including PCA, were applied to the static testing datasets to produce separate models in the hopes of mitigating possible collinearity effects.

First, VIFs were calculated using Equation 7 to compare the linear relationships between every variable for each of the datasets and understand which variables were likely to cause issues. Continuing from this, PCA was applied. All variables were first normalized and centered around their means for stability. PC loading vectors were then calculated from the datasets. Observations of these matrices allowed for better understanding of how each predictor variable contributed to the overall variances of the datasets. From this point, the datasets were transformed into principal component space using Equation 8. Note that all variables were included in these techniques. In theory, PCA should be capable of removing statistical noise through removal of the higher PCs, which account for the least amount of variance, without affecting any of the input variables.

From the datasets in principal component space, regression models were constructed and validated using the same HOCV procedure and an average R^2_{HOCV} value was determined. Next the PC with the least variance (the last one) was reduced to zeros and the models were reconstructed and the R^2_{HOCV} score was redetermined. This was repeated incrementally until only one PC remained, while tracking the changes in R^2_{HOCV} scores. In theory, the results should have improved as more PCs were removed until the RSS was minimized, indicating that as much statistical noise as possible had been removed, to optimize the models.

Finally, the PC regression coefficients could be transformed back to the original dataspace using Equation 9. This should have resulted in optimized models and regression coefficients that were stable and free from the effects of collinearity.

Model Summaries

In this chapter, a whole host of modeling procedures have been described for both the static and fatigue testing data acquired during this research. As will be evident in the proceeding chapter, not all models performed as well as anticipated, so not all of the same procedures applied to the static datasets were applied to the fatigue datasets.

To summarize, the predictive capabilities of models constructed from just the AE variables and just the GUW variables separately were first assessed for each layup in static testing. The data from the two techniques were then combined to construct full models for each layup to analyze their predictive capabilities and to provide a full assessment and interactions within the datasets. They also served to validate that combining the two techniques was superior to using the datasets separately.

From this point, the datasets from the $[0/90]_S$, $[90/0]_S$ and $[0/90/\pm45]_S$ layups were combined to explore the possibility of a layup independent model with no interaction parameters. As well as combining the datasets, the functions described in Equation 12 were applied as interaction parameters to the AE variables to construct further models and assess their accuracies. Finally, with regards to static testing, principal component regression (PCR) models were constructed for each of the layups to evaluate their predictive accuracy and the possibility of them reducing any collinearity effects that were present within the datasets, when transformed back to the original coordinate spaces of the datasets. This also served as an alternative to using the variable reduction procedure for the regular models. In theory, reduced PCs in a PCR should have similar effects to removing noisy, unwanted variables.

Continuing to the fatigue datasets, new predictive models were constructed and assessed for each of the three layups tested. Because of limited success with layup independent and PCR models for the static test data, the same procedures were not applied to the fatigue data. This is further explained in detail in the proceeding chapter. In addition, the static regression model coefficients were also applied to the fatigue AE and GUW datasets, to test the possibility of making residual modulus predictions from static testing. Since AE response, GUW response and modulus reduction have shown close relationships with crack density, both in the current research and from other researchers, there was a possibility that the static testing results could hold true in fatigue loading. If this was the case, then the models constructed from static test data could be used to save significant testing time for future researchers. It would also serve as the ultimate validation of the fatigue test results.

Table 10 and Table 11 provide full summaries of the models constructed from each loading scenario respectively, the predictor variables applied, the response variables, the layups tested and additional descriptions.

Response Variable	Predictor Variables	Layup	Description
Modulus change	AE only	$[0/90]_S$ $[90/0]_S$ $[0/90/\pm45]_S$ $[90_4]$	AE only model
Modulus change	GUWs only	$[0/90]_S$ $[90/0]_S$ $[0/90/\pm45]_S$ $[90_4]$	GUW only model
Modulus change	AE & GUWs	$[0/90]_S$ $[90/0]_S$ $[0/90/\pm45]_S$ $[90_4]$	Combined AE & GUWs
Modulus change	AE & GUWs	$[0/90]_S$, $[90/0]_S$ and $[0/90/\pm45]_S$	Layup independent (no interactions) $f_1(E_L, E_B)$ $f_2(E_L, E_B)$
Modulus change	AE & GUWs	$[0/90]_S$ $[90/0]_S$ $[0/90/\pm45]_S$ $[90_4]$	PCR

Table 10: A summary of the models constructed using the AE and GUW datasets, acquired during the static tensile LUR tests.

Response Variable	Predictor Variables	Layup	Description
Modulus change	AE & GUWs	$[0/90]_S$ $[90/0]_S$ $[0/90/\pm45]_S$	Combined AE & GUWs
Modulus change	AE & GUWs	$[0/90]_S$ $[90/0]_S$ $[0/90\pm45]_S$	Static models for fatigue predictions

Table 11: A summary of the models constructed using the AE and GUW datasets, acquired during the interrupted tension-tension fatigue tests.

PREDICTIVE MODELING RESULTS AND DISCUSSION

Previous chapters have outlined in detail the previous research, testing techniques and data that have led to this point in attempting to combine AE and GUW data to predict degrading laminate properties for SHM applications. This chapter outlines the results of all the models constructed and provides and in depth analysis of their effectiveness and how they can be improved upon for future research.

Static Data Modeling

Static tensile testing through incrementally increasing LUR cycles provided the initial test case for combining the AE and GUW techniques, while measuring reductions in moduli. Multivariate linear regression models were constructed to evaluate the predictive accuracies and potential for combining the datasets from the two different monitoring techniques. First, the two techniques were evaluated separately and then the data combined to form singular models, to compare their predictive capabilities. The possibility of creating layup independent models was also explored, as well as principal component regressions to observe variables' contributions to variance within the datasets, reduce collinearity effects and as an alternative to the variable reduction techniques applied to the other models.

As a starting point, R^2 values for each extracted variable from the datasets, for each layup, for linear fits against changes in moduli were evaluated and compared (see Table 12). It is already evident that some variables show good correlation with changes in moduli, whereas others show very low to no correlation at all for some layups. For

example, changes in GUW MARSE and absolute energies consistently showed good correlation, but changes in rise time, peak frequency (P-Freq) and centroid frequency (C-Freq) showed no correlation at all in some cases. The cumulative AE variables all showed good correlations with changes in moduli, particularly cumulative number of events and cumulative counts. These initial evaluations gave a good indication of which variables were likely to be significant in the linear regression models and which variables were likely to be removed from the models.

Variable	$[0/90]_S$	$[90/0]_S$	$[0/90/\pm45]_S$	$[90_4]$
Rise Time	0.498	0.190	0.055	0.004
Counts	0.533	0.614	0.512	0.671
MARSE Energy	0.725	0.838	0.704	0.923
Duration	0.535	0.425	0.492	0.606
Amplitude	0.480	0.783	0.624	0.850
Abs. Energy	0.838	0.854	0.780	0.907
P-Freq.	0.007	0.193	0.004	0.004
C-Freq.	0.326	0.053	0.216	0.478
Cumulative Abs. Energy	0.597	0.779	0.759	0.786
Cumulative MARSE Energy	0.734	0.826	0.882	0.868
Number of AE Events	0.839	0.930	0.881	0.821
Cumulative Counts	0.835	0.910	0.925	0.892

Table 12: A summary of R^2 values for each extracted variable for each layup when compared with changes in moduli (GUW variables are on top and AE variables are below and separated by the dotted line).

Acoustic Emission vs. Guided Ultrasonic Waves

Before constructing full regression models, the AE and GUW datasets were evaluated separately. The same validation and variable reduction techniques described in the previous chapter were applied and the appropriate fit characteristics were calculated. Results are presented for the AE and GUW models in Table 13 and Table 14 respectively. Figures 105-108 also show plots of the validation results to display the

models' predictions against the measured values acquired during testing. The lines of best fit show the ideal case where predicted modulus change is equal to the measured modulus change. These results show that the models were able to make good predictions in some cases, with R^2_{HOCV} values above 0.9 for the $[0/90/\pm45]_S$ layup AE model and $[0/90]_S$ and $[90_4]$ layups GUW models, but R^2_{HOCV} values of less than 0.75 in other cases. Another interesting feature is that no layup displayed good results for both the AE and GUW cases. It appeared that each layup seemed to favor one technique over the other. These inaccuracies are reflected in Figures 105-108, showing large amounts of deviation from the actual results acquired during testing. Despite this, the plots do not really show any obvious outliers, which deviate significantly in comparison to the other data points. The $[90_4]$ layup appears to show the most inaccurate predictions, due to modulus changes being much more significant, particularly for the AE dataset. At maximum modulus reductions, the AE model predicted much more severe degradations than were actually measured; upwards of 20% error.

Model Statistics	$[0/90]_S$	$[90/0]_S$	$[0/90/\pm45]_S$	$[90_4]$
Number of Observations	380	380	380	340
Number of Predictors	2	2	3	1
RMSE	0.0304	0.0172	0.0195	0.0867
R^2_{adj}	0.821	0.931	0.942	0.879
F-Statistic	868	2556	2030	2447
Overall p-value	$< 10^{-322}$	$< 10^{-322}$	$< 10^{-322}$	$< 10^{-294}$
R^2_{HOCV}	0.734	0.887	0.921	0.753

Table 13: A summary of fit characteristics and HOCV results for models constructed using only AE data for each of the layups tested in static tension.

Model Statistics	$[0/90]_S$	$[90/0]_S$	$[0/90/\pm45]_S$	$[90_4]$
Number of Observations	380	380	380	340
Number of Predictors	5	4	5	4
RMSE	0.0215	0.0233	0.0303	0.0575
R^2_{adj}	0.917	0.866	0.845	0.950
F-Statistic	838	609	411	1591
Overall p-value	$< 10^{-322}$	$< 10^{-322}$	$< 10^{-322}$	$< 10^{-322}$
R^2_{HOCV}	0.900	0.741	0.676	0.925

Table 14: A summary of fit characteristics and HOCV results for models constructed using only GUW data for each of the layups tested in static tension.

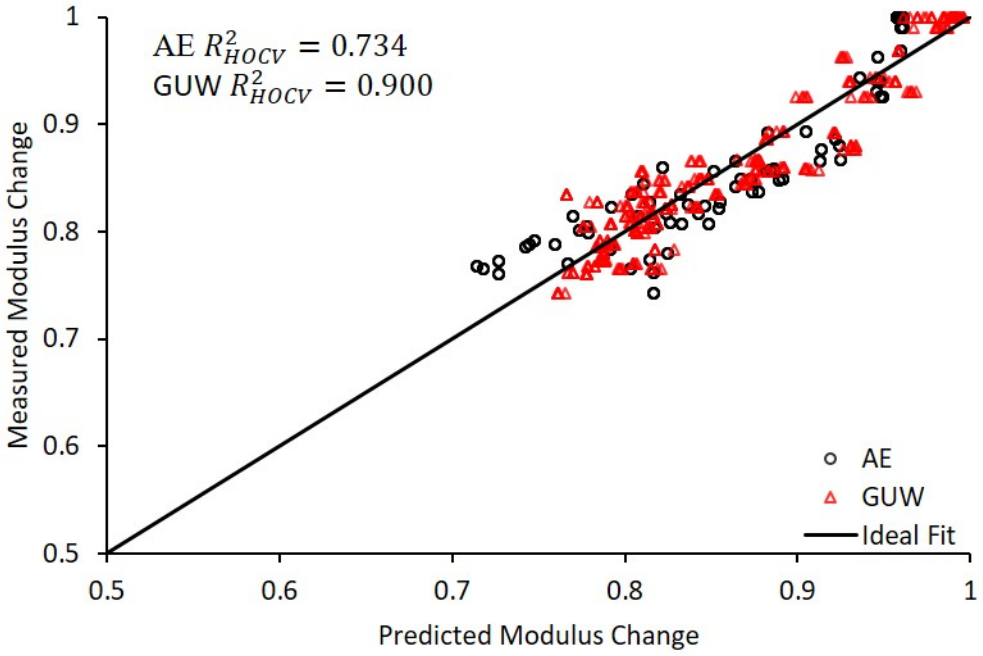


Figure 105: A scatter plot of the HOCV prediction results for the separate AE and GUW models for the $[0/90]_S$ layup.

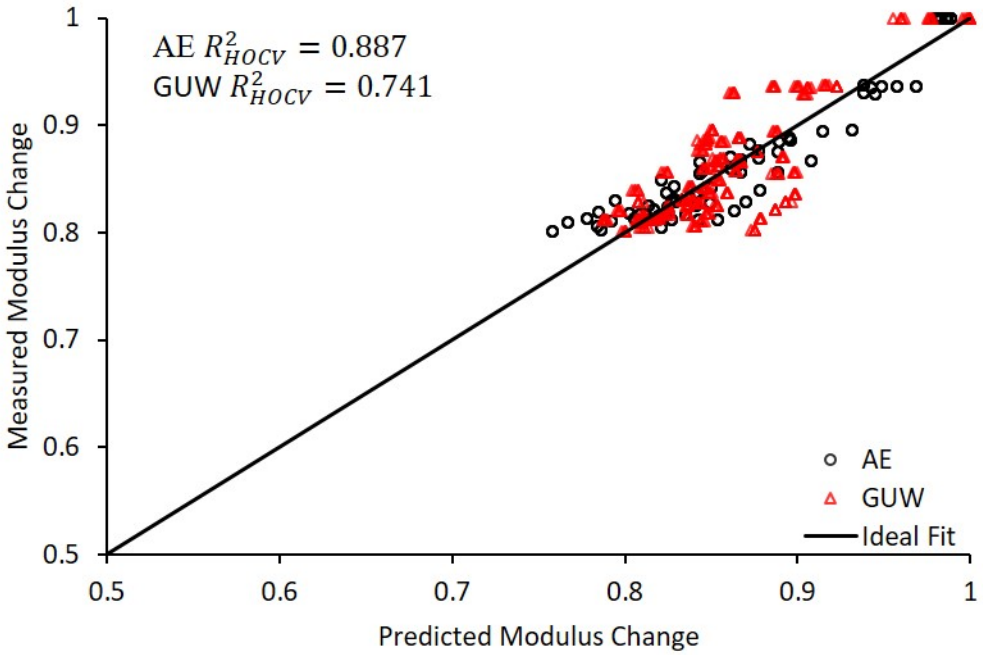


Figure 106: A scatter plot of the HOCV prediction results for the separate AE and GUW models for the $[90/0]_S$ layup.

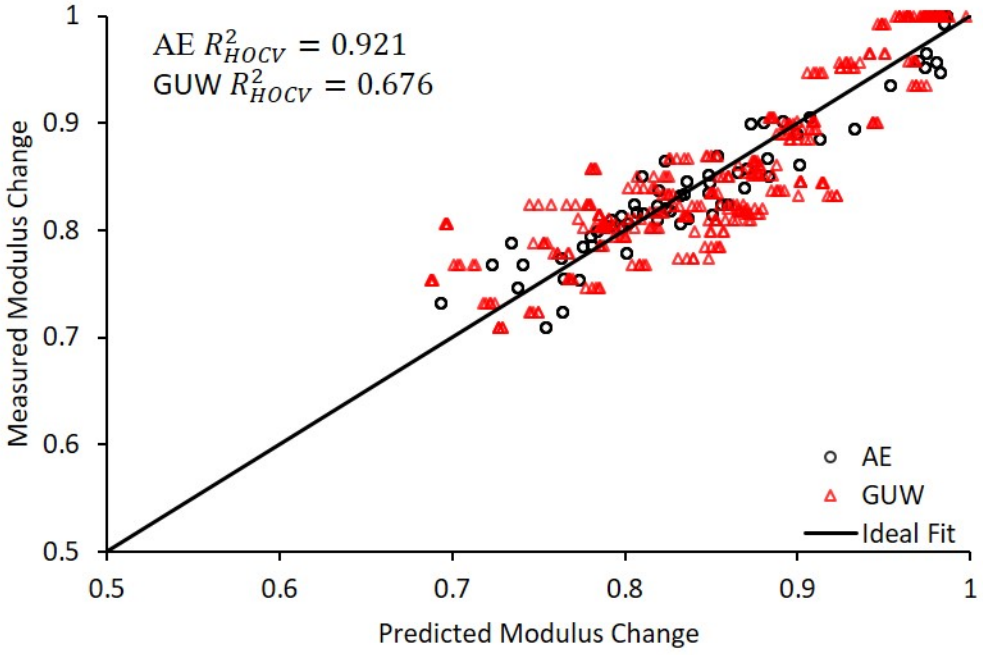


Figure 107: A scatter plot of the HOCV prediction results for the separate AE and GUW models for the $[0/90/\pm45]_S$ layup.

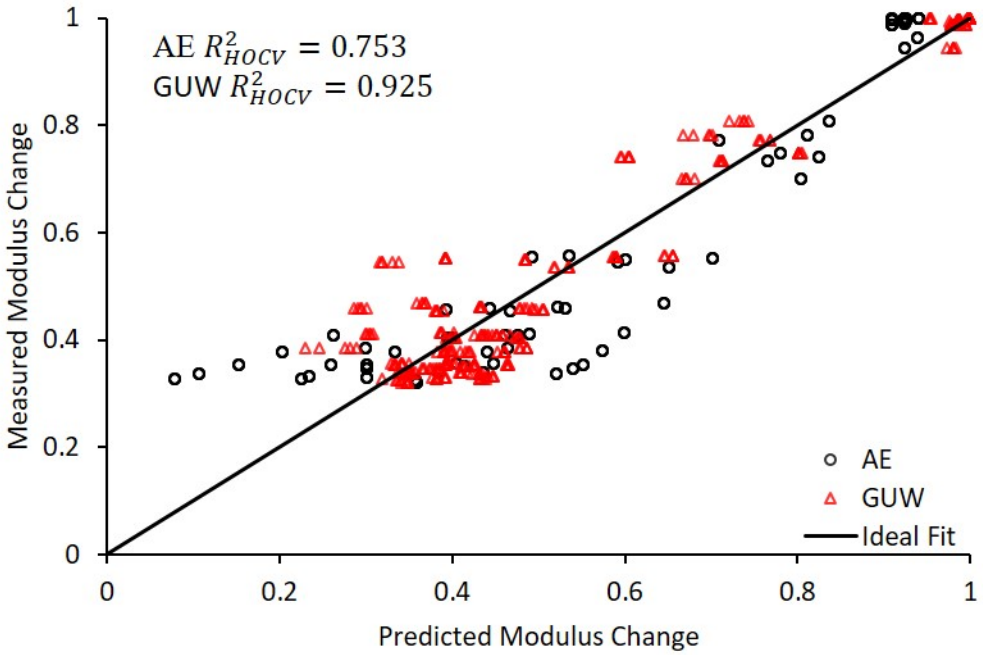


Figure 108: A scatter plot of the HOCV prediction results for the separate AE and GUW models for the [90_4] layup.

As a final comparison for the separate technique models, Table 15 shows the coefficients calculated for the models and the variables that were applied to determine the models. For the GUW models, it can be observed that some variables were consistently chosen for making the best predictions, such as absolute energy change. Change in counts and C-Freq were both chosen for three out of the four models. With regards to the AE models, the cumulative number of AE events proved to be the most useful, but cumulative absolute energy was only applied to the $[90/0]_S$ model. Despite this, either MARSE energy or absolute energy variables were chosen for all the GUW and AE models apart from the [90_4] AE model. Interestingly, this model found that only AE cumulative counts was of use for making the most accurate predictions.

Variable	$[0/90]_S$	$[90/0]_S$	$[0/90/\pm45]_S$	$[90_4]$
Rise Time			-0.135	-0.0777
Counts	0.252	0.0324	0.0964	
MARSE Energy	-0.285	0.0655		
Duration				
Amplitude	-0.621			1.302
Abs. Energy	0.442	0.144	0.403	0.300
P-Freq	0.211		-0.468	
C-Freq		0.745	1.104	0.486
Constant	0.992	0.0227	-0.0238	-1.011
Cumulative Abs. Energy		-2.58×10^{-11}		
Cumulative MARSE Energy	-3.25×10^{-6}		-1.55×10^{-5}	
Number of AE Events	-3.11×10^{-4}	-2.94×10^{-4}	-7.50×10^{-4}	
Cumulative Counts			2.44×10^{-5}	-5.10×10^{-5}
Constant	0.959	0.983	0.983	0.926

Table 15: A comparison of variables selected for each respective model and their associated coefficients, β_i (GUW and AE models are split by the double solid line divider).

Prediction Accuracy

The AE and GUW datasets were then combined for each layup to construct singular, standalone models to assess their performances. Table 16 shows a summary of the models' fit characteristics and final HOCV results. Furthermore, Table 17**Error! Reference source not found.** shows the individual HOCV R^2 scores when each coupon test was removed from the datasets for training the models. Figures 109-112 show plots of the HOCV predictions against the measure moduli changes during testing. Once again, the ideal fit line represents the case where the predictions are equal to the measured changes.

Comparison of the R^2_{HOCV} values from Table 16 with Table 13 and Table 14 clearly shows that combining the AE and GUW datasets to construct singular models results in far better predictions in all cases. The maximum R^2_{HOCV} value from using the

techniques separately was 0.925, whereas the minimum R^2_{HOCV} value from the combined models was 0.948. This showed the benefits and effectiveness of applying multiple monitoring techniques into singular predictive models, rather than using them separately.

All four models were shown to predict changes in moduli to a superior degree of accuracy, with minimal outliers. The $[90/0]_S$ layup showed the best accuracy with a R^2_{HOCV} score of 0.982 and the lowest average residual error. This is particularly interesting, since its R^2_{HOCV} scores for the separate AE and GUW models were not the best in either case. The $[90_4]$ layup model also showed some of the best validation results ($R^2_{HOCV} = 0.979$). Despite this, the $[90_4]$ layup showed some of the largest residual errors (2.8%). This is likely due to the moduli changes spanning a much larger range than the other three layups.

Further validation of the predictive accuracy of the models is shown by the scores produced by each individual HOCV test. All 28 validation tests scored R^2 values above 0.91. This was a good indication that the AE and GUW data acquired during testing is highly repeatable and gives confidence that accurate predictions could still be made if more tests were conducted.

Model Statistics	$[0/90]_S$	$[90/0]_S$	$[0/90/\pm45]_S$	$[90_4]$
Number of Observations	380	380	380	340
Number of Predictors	7	6	7	6
RMSE	0.0139	0.0072	0.0153	0.0253
R^2_{adj}	0.967	0.989	0.965	0.991
F-Statistic	1574	5429	1465	5073
Overall p-value	$< 10^{-322}$	$< 10^{-322}$	$< 10^{-322}$	$< 10^{-322}$
R^2_{HOCV}	0.954	0.982	0.948	0.979
Ave. Residual Error	1.4 ± 0.9%	0.7 ± 0.6%	1.6 ± 1.0%	2.8 ± 2.2%

Table 16: A summary of fit characteristics and HOCV results for models constructed when combining the AE and GUW datasets for each of the layups tested in static tension.

Test Number	$[0/90]_S$	$[90/0]_S$	$[0/90/\pm45]_S$	$[90_4]$
1	0.940	0.961	0.952	0.997
2	0.953	0.972	0.919	0.970
3	0.976	0.996	0.979	0.955
4	0.941	0.991	0.935	0.988
5	0.944	0.989	0.963	0.982
6	0.977	0.987	0.916	0.975
7	0.948	0.980	0.971	0.987
Ave. R^2_{HOCV}	0.954	0.982	0.948	0.979

Table 17: R^2 values for each of the HOCV tests conducted for each layup, where each coupon was removed from the training datasets to validate the models.

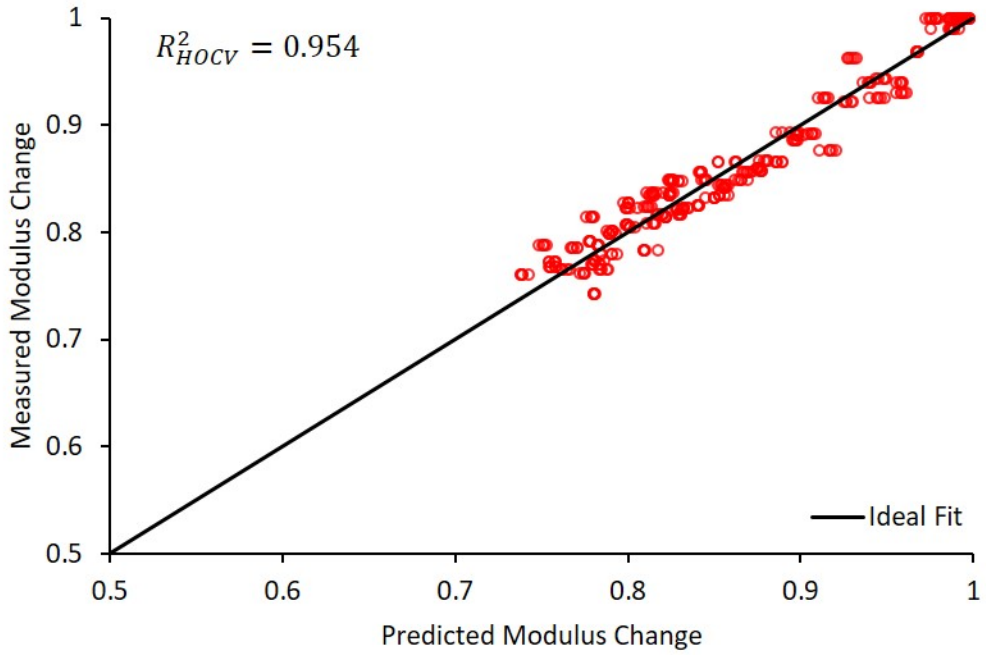


Figure 109: A scatter plot of the HOCV prediction results for the combined AE and GUW models for the $[0/90]_S$ layup.

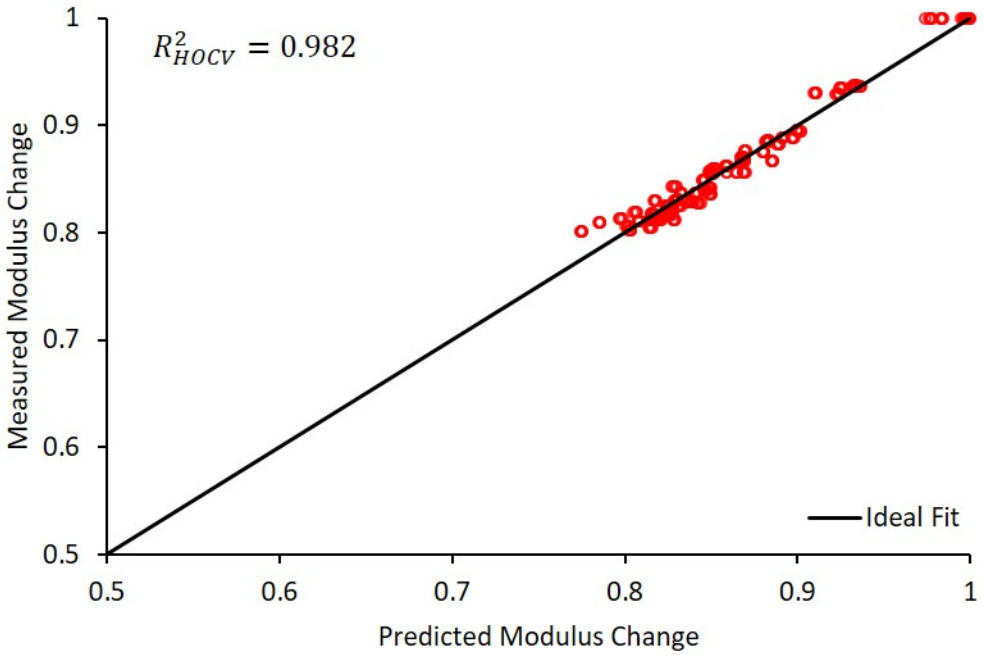


Figure 110: A scatter plot of the HOCV prediction results for the combined AE and GUW models for the $[90/0]_S$ layup.

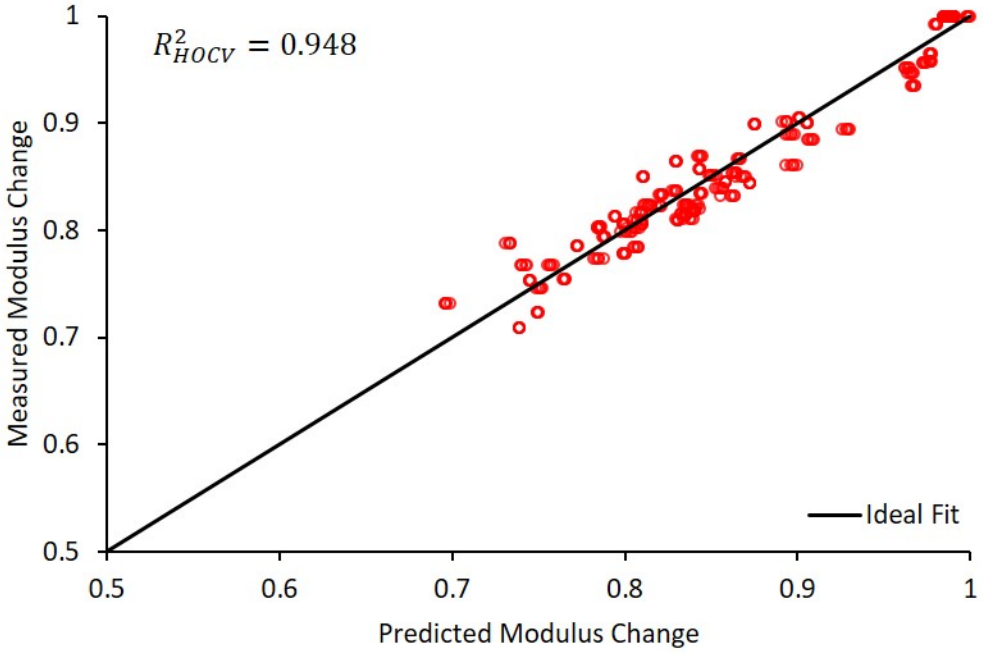


Figure 111: A scatter plot of the HOCV prediction results for the combined AE and GUW models for the $[0/90/\pm45]_S$ layup.

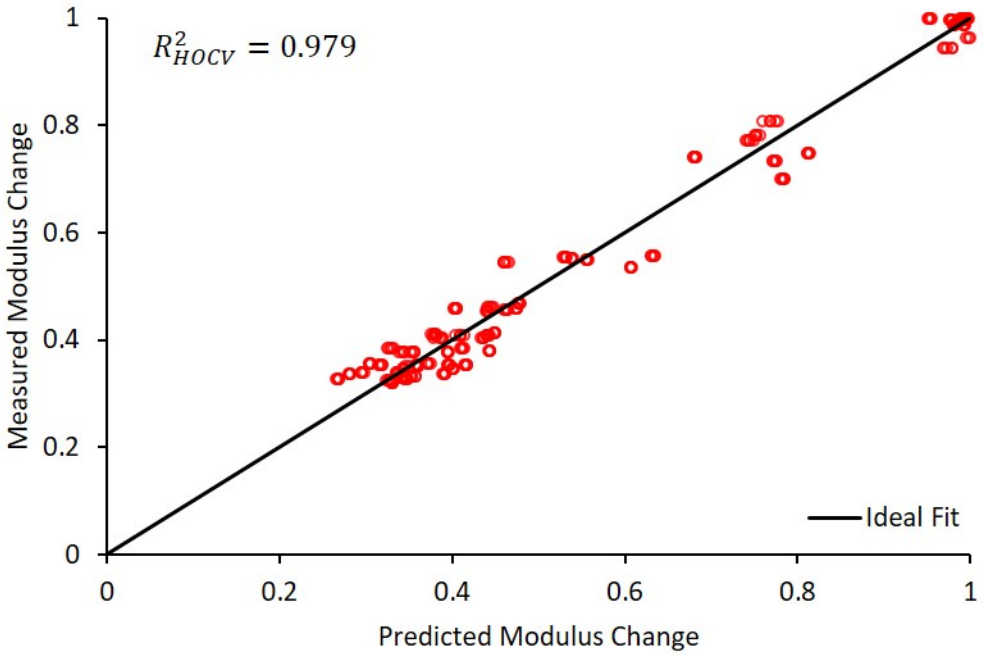


Figure 112: A scatter plot of the HOCV prediction results for the combined AE and GUW models for the [90_4] layup.

Absolute residual error plots are shown in Figures 113-116. All layups show a good distribution of residual errors with minimal significant outliers. Perhaps the most important feature to note is that all plots show many data points clustered around a measured modulus change of 1 (where no changes in moduli have occurred). This is particularly prominent for the [90_4] layup, where there is a large cluster of data points with minimal residual error. This could explain why the [90_4] layup exhibited such a high R^2_{HOCV} score, despite showing a larger average residual error.

A likely cause of these clusters is a feature of the test method. LUR cycles were incrementally increased by 0.25% strain each time. Therefore, for the first LUR cycle, coupons were loaded up to 0.25% strain and then unloaded again for GUW and moduli measurements to be taken. At such a low strain, no damage had occurred within any of

the coupons, which was evident in the AE datasets. In light of this, it may have been beneficial to remove all the data points acquired during the first load cycle. This could have resulted in the models making better predictions for more severe changes in moduli, where accurate predictions would be much more important in real life SHM scenarios.

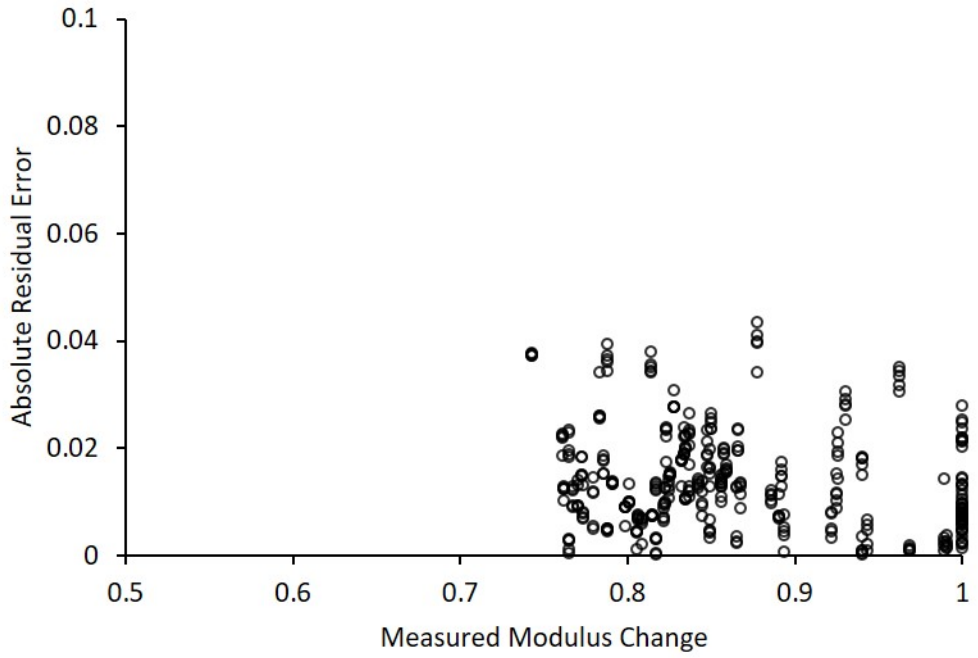


Figure 113: An absolute residual error plot for the $[0/90]_S$ model HOCV results.

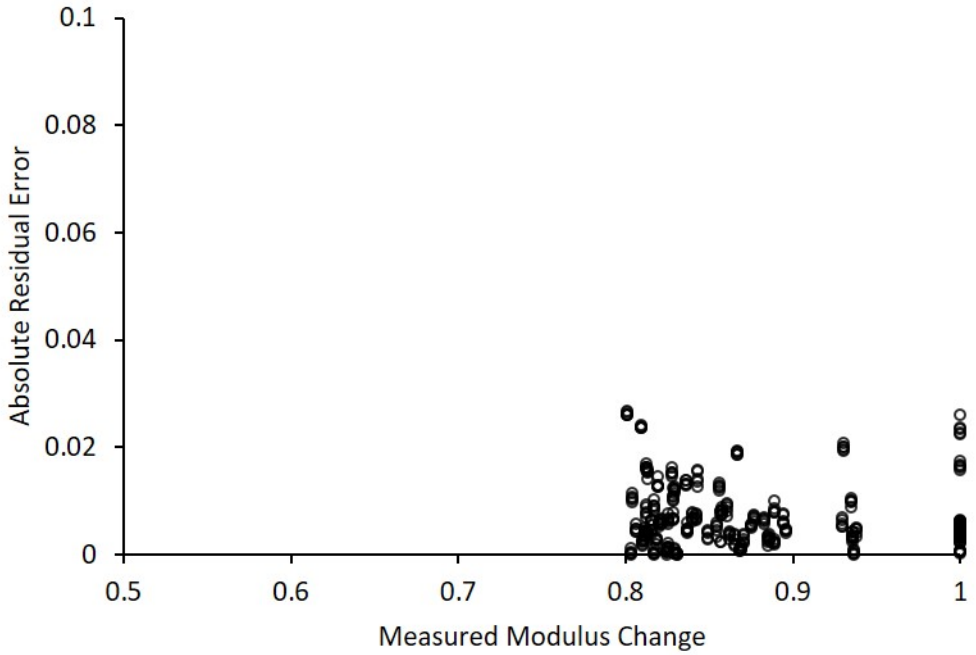


Figure 114: An absolute residual error plot for the $[90/0]_S$ model HOCV results.

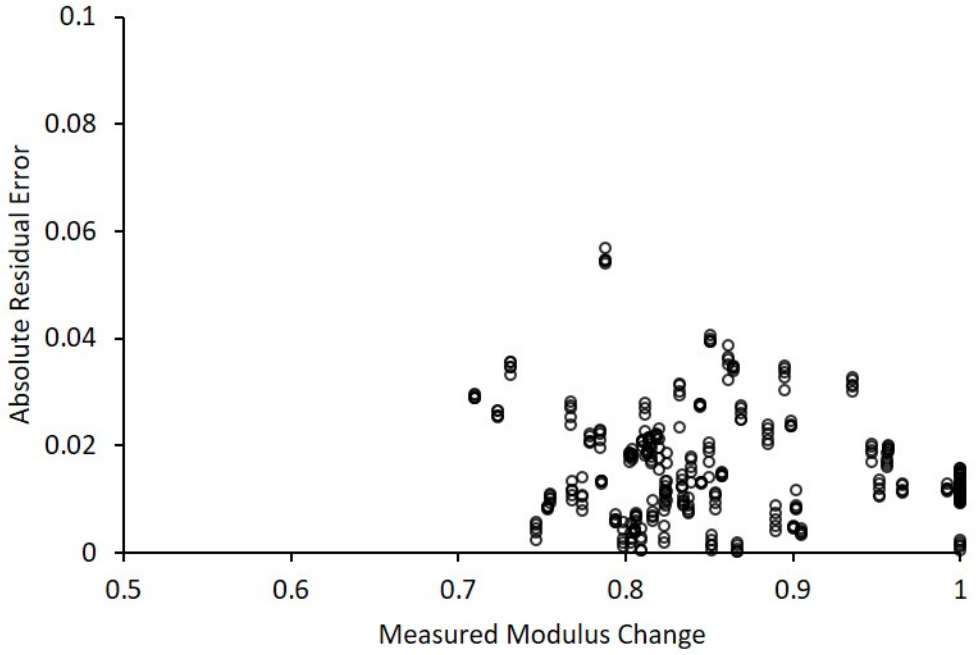


Figure 115: An absolute residual error plot for the $[0/90/\pm45]_S$ model HOCV results.

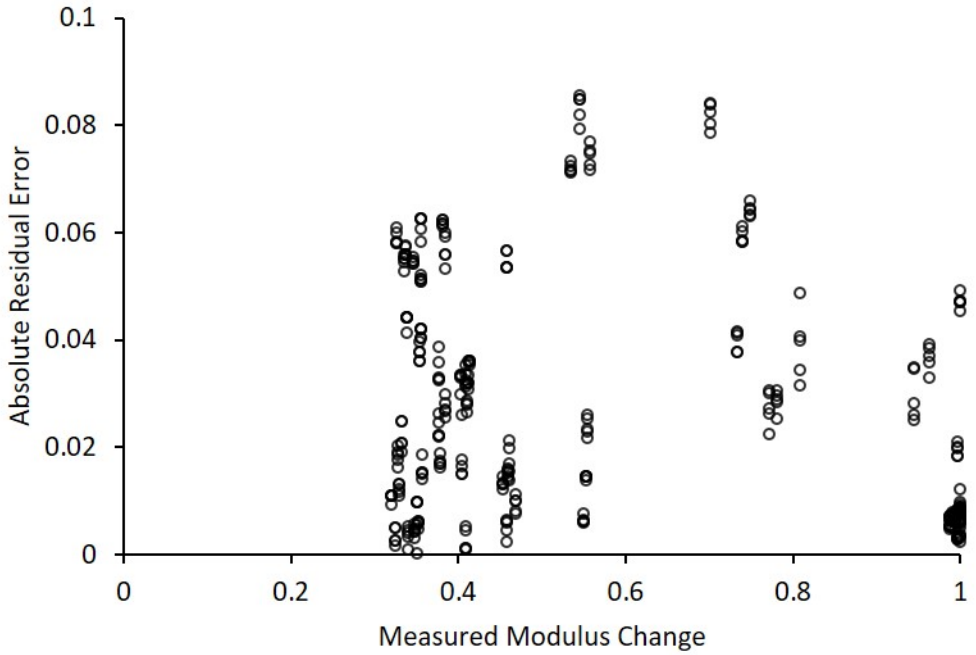


Figure 116: An absolute residual error plot for the [90_4] model HOCV results.

Coefficient Comparisons

Table 18 shows a summary of the variables selected and their final coefficients (β_i) for each model. The first thing to note is that not all the same variables from the separate AE and GUW models (see Table 15) were used for the combined models for each layup. Changes in GUW absolute energy was selected for all four layup models, which consistently showed good correlation in relation to changes in moduli. Each model selected one or even both cumulative absolute and MARSE energies from the AE datasets. Duration was discarded from all four models, despite exhibiting acceptable correlation in relation to changes in moduli, especially when compared with some of the variables that were not discarded. Interestingly, some variables which displayed little to no correlation with changes in moduli, such as changes in GUW rise time, P-Freq and C-Freq, were selected for some of the models. These phenomena are difficult to explain, but

could be as a result of complex underlying interactions, between the GUW variables, which cannot be described by simple linear regression analyses.

Variable	$[0/90]_S$	$[90/0]_S$	$[0/90/\pm45]_S$	$[90_4]$
Rise Time	0.025		-0.026	
Counts	0.201	0.033		0.116
MARSE Energy	-0.648	-0.153		
Duration				
Amplitude				0.228
Abs. Energy	0.577	0.197	0.148	0.221
P-Freq			-0.165	-0.087
C-Freq		0.418	0.330	
Cumulative Abs. Energy	-8.32×10^{-10}	1.67×10^{-11}		4.11×10^{-10}
Cumulative MARSE Energy	1.84×10^{-5}		-1.28×10^{-5}	-8.34×10^{-6}
Number of AE Events		-2.51×10^{-4}	-4.99×10^{-4}	-4.98×10^{-4}
Cumulative Counts	-1.92×10^{-5}		1.86×10^{-5}	
Constant	0.838	0.511	0.702	0.515

Table 18: A summary of the variables selected and their respective coefficients for each layup for the combined static models.

The most noticeable feature of the coefficients was where one variable might have shown a positive coefficient value for one layup, but a negative coefficient value for a different layup. For example, the coefficient for cumulative absolute energy was negative for the $[0/90]_S$ model, but positive for the $[90/0]_S$ and $[90_4]$ models. From inspection of the datasets, it was obvious that all the AE variables show a negative relationship with changes in moduli, therefore should have negative coefficients, and certain GUW variable, such as changes in amplitude, MARSE energy and absolute energy, share a positive relationship with changes in moduli and should have positive coefficients. These changes in sign were an indication of collinearity between closely related variables, which was expected, although the final prediction results of the models did not show any

signs of instability. Further inspection and a more detailed analysis of this phenomenon is provided later on in this chapter.

Layup Independent Model

Constructing statistical models to make accurate moduli degradation predictions on a layup-by-layup basis from test data is certainly useful, but a layup independent model would be much more beneficial in practical applications. Therefore, the datasets from the $[0/90]_S$, $[90/0]_S$ and $[0/90/\pm45]_S$ layups were combined to construct three new models; one with no interaction parameters and two with $f_1(E_L, E_B)$ and $f_2(E_L, E_B)$ applied to the cumulative absolute energy , MARSE energy and cumulative counts AE variables (see Equation 12).

Table 19 shows a comparison of R^2 values of variables against changes in moduli, with the variables of particular interest indicated in bold. On observations of the "No Interactions" column, the first thing to note is that the R^2 values of every variable suffer when the layup datasets are combined, due to additional scatter and differences being introduced. Clearly the AE variables in bold suffer the most, with cumulative absolute and MARSE energies showing little to no correlation at all. This is particularly apparent when observing Figure 65, where absolute energies are plotted on a logarithmic scale. There was almost a difference of a decade in accumulated absolute energies between layups, especially the $[90/0]_S$ layup. Application of interaction function f_1 resulted in improved coefficients of determination for all three variables of interest, with cumulative counts showing the most notable improvement. This function aided in closing the large differences between data points for each layup. $f_2(E_L, E_B)$ on the other hand, showed

decreases in R^2 values, suggesting that it was not an appropriate function to describe the differences in AE data between layups.

Variable	No Interactions	$f_1(E_L, E_B)$	$f_2(E_L, E_B)$
Rise Time	0.196	0.196	0.196
Counts	0.464	0.464	0.464
MARSE Energy	0.565	0.565	0.565
Duration	0.436	0.436	0.436
Amplitude	0.413	0.413	0.413
Abs. Energy	0.624	0.624	0.624
P-Freq	0.008	0.008	0.008
C-Freq	0.150	0.150	0.150
Cumulative Abs. Energy	**0.075**	**0.117**	**0.060**
Cumulative MARSE Energy	**0.141**	**0.280**	**0.097**
Number of AE Events	0.755	0.755	0.755
Cumulative Counts	**0.524**	**0.849**	**0.301**

Table 19: A comparison of R^2 values for each variable with respect to changes in moduli. Variables of interest for the interaction functions are shown in bold.

Table 20 and Table 21 show regression coefficients and training statistics and validation results respectively for the three models. All three models showed very similar variable selections, with the "No Interactions" model and f_2 model showing the same variables and highly comparable coefficients. The f_1 model instead selected cumulative counts over C-Freq. This is a reflection of its significantly improved R^2 value for cumulative counts. It should also be noted that the effects of collinearity were still present in the fit coefficients of these models.

Overall, the validation scores for each model show relatively good results, with the "No Interactions" model showing an average R^2_{HOCV} of 0.893. Application of interaction function f_1 led to slight improvements in the training and validation statistics, resulting in a R^2_{HOCV} of 0.915. It was a slight improvement, but barely significant.

Application of interaction function f_2 showed a slight decrease in training and validation statistics, which was expected from observations of Table 19.

Variable	No Interactions	$f_1(E_L, E_B)$	$f_2(E_L, E_B)$
Rise Time			
Counts	0.105	0.085	0.107
MARSE Energy	-0.293	-0.209	-0.311
Duration			
Amplitude	-0.388	-0.277	-0.367
Abs. Energy	0.315	0.257	0.330
P-Freq			
C-Freq	-0.201		-0.196
Cumulative Abs. Energy	3.55×10^{-10}	3.83×10^{-10}	2.77×10^{-7}
Cumulative MARSE Energy	-4.70×10^{-6}	-5.11×10^{-6}	3.42×10^{-3}
Number of AE Events	-2.63×10^{-4}	-1.37×10^{-4}	-2.98×10^{-4}
Cumulative Counts		-2.69×10^{-6}	
Constant	1.45	1.13	1.45

Table 20: A summary of the regression coefficients for each layup independent model.

Model Statistics	No Interactions	$f_1(E_L, E_B)$	$f_2(E_L, E_B)$
Number of Observations	1140	1140	1140
Number of Predictors	8	8	8
RMSE	0.0216	0.0196	0.0221
R^2_{adj}	0.914	0.930	0.909
F-Statistic	1506	1894	1420
Overall p-value	$< 10^{-322}$	$< 10^{-322}$	$< 10^{-322}$
R^2_{HOCV}	0.893	0.915	0.888
Ave. Residual Error	2.0 ± 1.5%	1.8 ± 1.3%	1.8 ± 1.3%

Table 21: A summary of fit characteristics and HOCV results for models constructed when combining the $[0/90]_S$, $[90/0]_S$ and $[0/90/\pm45]_S$ static tension LUR datasets.

Figures 117-119 show plots of the validation results and Figures 120-122 show their respective absolute residual error plots. As one would expect, there were only small differences in the plotted HOCV results. Of course, the results for f_1 were clustered slightly closer to the ideal fit line. Observations of the absolute residual error plots show that the errors were again relatively well distributed, but still highlight a key point that

was explained for the previous models. A large portion of significant errors were shown where no moduli changes had been measured. Once again, this likely stemmed from the measurements taken after coupons had been loaded to 0.25% strain, where no damage had occurred. This effect was noticeably amplified when the data from 21 coupon tests were considered in a single dataset in this case. This again leads to the suggestion that measurements, except the GUW reference pulses and initial moduli, should only be taken after damage has initiated for further tests to train more accurate models in the future.

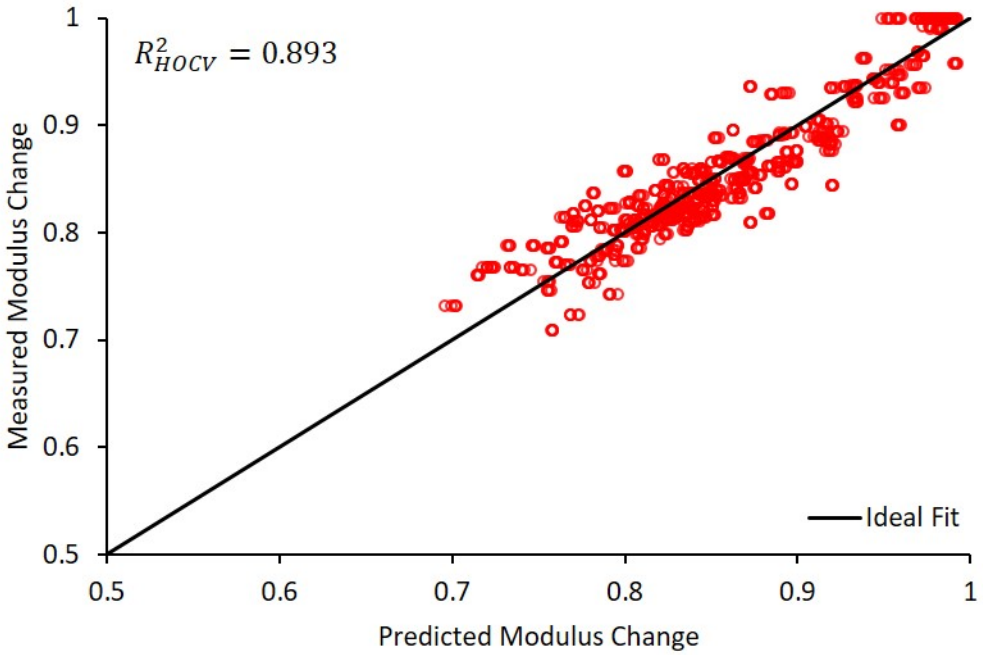


Figure 117: A scatter plot of the HOCV prediction results for the layup independent model with no interaction function applied to the AE data.

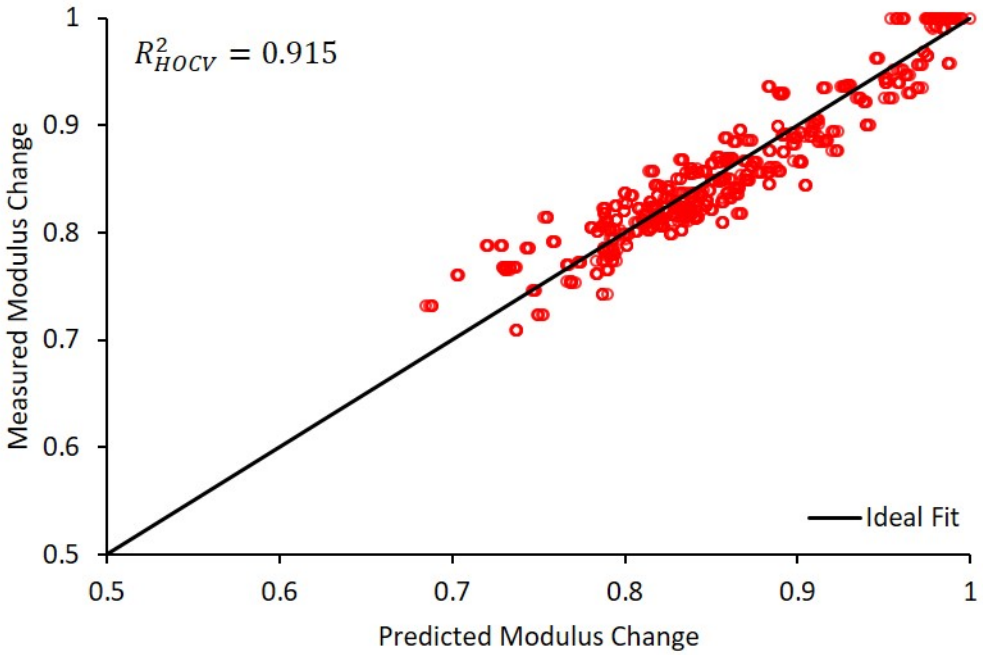


Figure 118: A scatter plot of the HOCV prediction results for the layup independent model with interaction function $f_1(E_L, E_B)$ applied to the AE data.

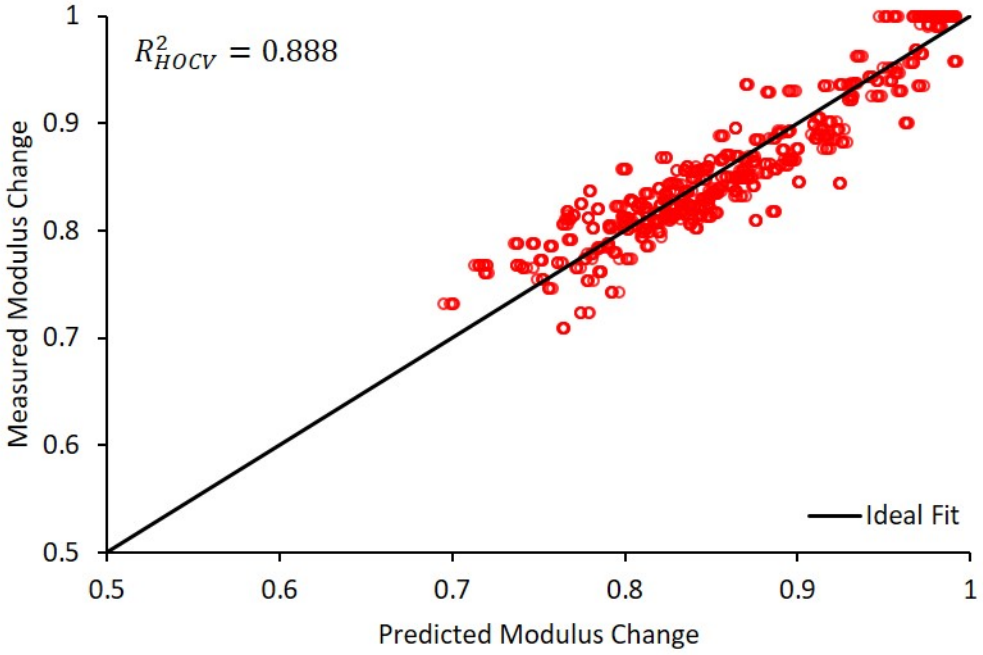


Figure 119: A scatter plot of the HOCV prediction results for the layup independent model with interaction function $f_2(E_L, E_B)$ applied to the AE data.

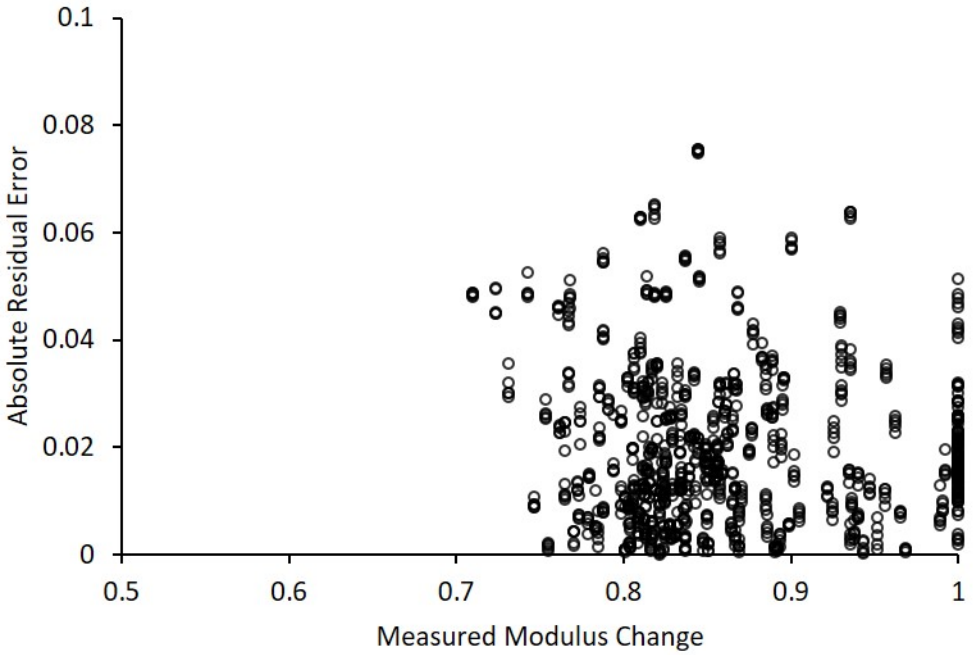


Figure 120: An absolute residual error plot for the HOCV results of the layup independent model with no interaction parameters.

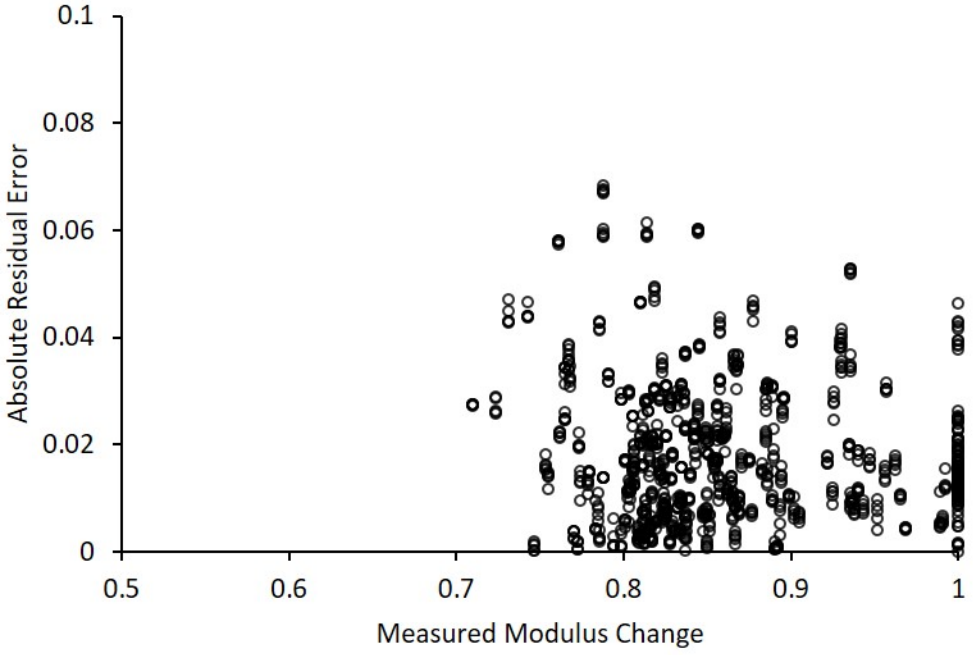


Figure 121: An absolute residual error plot for the HOCV results of the layup independent model with interaction function $f_1(E_L, E_B)$.

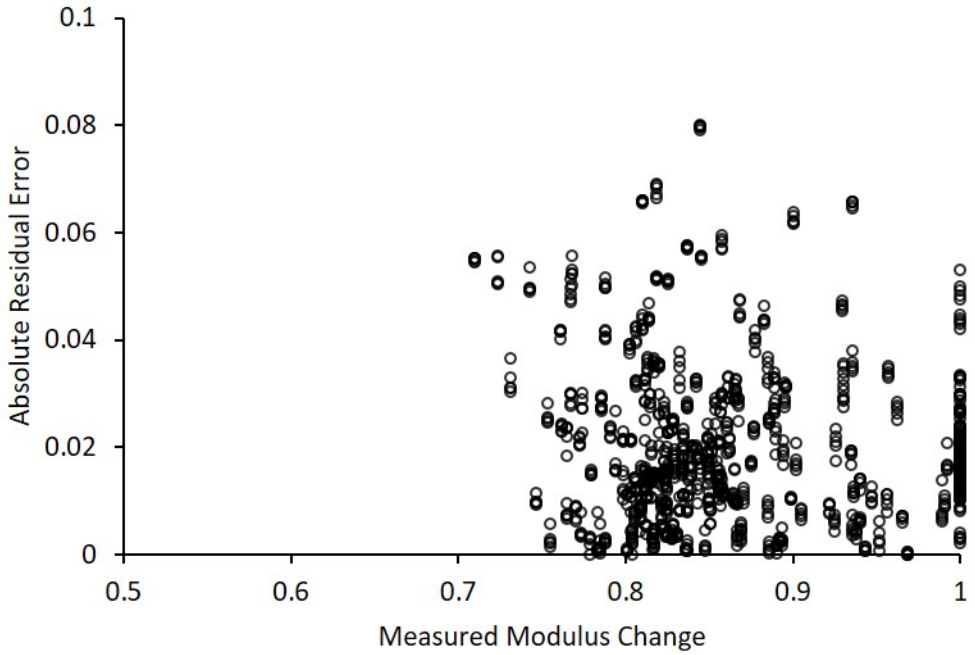


Figure 122: An absolute residual error plot for the HOCV results for the layup independent model with interaction function $f_2(E_L, E_B)$.

Overall, three layup independent models were constructed using the datasets from the $[0/90]_S$, $[90/0]_S$ and $[0/90/\pm45]_S$ static LUR tests. The results were acceptable, but certainly not as accurate as those where the layups were considered separately. Application of interaction function f_1 did lead to slight improvements, but they were not significant. For the interaction functions, only analytical values for E_L and E_B, which were calculated from ABD matrices, determined through classical laminate theory [100], were applied. The calculated values for E_L were close to the initial moduli measured during testing, but not exact. Using actual test values for E_L and E_B for each layup may have resulted in larger improvements, but the significance of changes were so small that it was not worth the additional testing time to determine actual E_B values for each of the layups, through three or four-point bend tests, in this case.

However, this does not mean that a better layup independent model cannot be constructed, but does suggest that linear regression models may not be the appropriate choice on this occasion. An artificial neural network (ANN) style model may have been the better choice in this instance. E_L, E_B, layup, plate thickness, V_f, ABD values and any other laminate parameters could be included as additional variables to the datasets in the analysis. An ANN algorithm would be able to find and scale the interactions between these inputs and the GUW and AE variables as interaction parameters automatically, wherever it deems necessary to obtain the best fits and much more accurate results. Despite this, there is very little theoretical basis to models of this style and the reasons for a better fit would be difficult to interpret and explain.

Collinearity and Principal Component Analysis

Initially, it was expected that certain predictor variables within the AE and GUW datasets would share close relationships with each other, or collinearity. These relationships can sometimes affect coefficients in the multivariate linear regression solutions and may even result in unstable predictions. The coefficients presented for the models described previously (Table 18 and Table 20) do show some evidence of collinearity effects with some coefficients being determined as negative when they should be positive and vice versa. Despite this, the models still appeared relatively stable and mode good predictions.

Tables 22-25 show variance inflation factors (VIFs) calculated for every variable comparison, using Equation 7, for each layup dataset. Cells with VIFs greater than 8 are highlighted in yellow, to indicate significant collinear relationships. All four datasets

show the same variables highlighted; GUW MARSE energy, GUW amplitude, GUW absolute energy, AE cumulative absolute and MARSE energies and AE cumulative counts. Interestingly, GUW counts and GUW duration also showed a significant collinear relationship for the $[0/90]_S$ dataset. These results are no surprise when considering how these variables are calculated from their respective waveforms.

Table 26 shows a comparison of the regression coefficients calculated for each of the seven HOCV tests conducted on the $[0/90]_S$ static dataset. The coefficients that exhibited the incorrect signs are highlighted in yellow. This showed that, although the coefficients were clearly showing significant indications of collinearity, they were not noticeably unstable when calculating the solutions. This also includes observation of the other collinear variables, which showed the correct sign, as well as the additional variables which were included in the model. Despite this, PCA techniques were still applied to the datasets in the hopes of "fixing" the offending coefficients. These techniques were also applied to test the possibility of using them as an alternative method to the variable reduction techniques used in previous models, as suggested by previous literature [90, 92-94].

Variable	(2)	(3)	(4)	(5)	(6)	(7)	(8)	(9)	(10)	(11)	(12)
(1)	1.6	2.3	1.7	1.6	2.4	1.0	1.3	1.4	1.6	2.0	1.8
(2)		7.1	9.0	14	4.0	1.3	6.3	1.8	2.0	3.0	2.4
(3)			5.9	9.2	27	1.2	3.3	1.8	2.2	5.0	3.1
(4)				7.5	4.0	1.2	4.3	1.7	1.9	2.6	2.2
(5)					4.4	1.3	7.5	1.6	1.7	2.7	2.0
(6)						1.1	2.3	2.1	2.6	5.4	3.7
(7)							1.5	1.0	1.0	1.0	1.0
(8)								1.5	1.6	1.8	1.6
(9)									13	2.3	3.4
(10)										4.0	9.7
(11)											17

Table 22: A comparison of VIFs for all the variables for the $[0/90]_S$ dataset, with significant relationships highlighted in yellow (numbers in parentheses relate to the variables in the order presented in previous tables).

Variable	(2)	(3)	(4)	(5)	(6)	(7)	(8)	(9)	(10)	(11)	(12)
(1)	1.0	1.1	1.1	1.1	1.1	1.0	1.0	1.1	1.1	1.2	1.2
(2)		3.2	2.0	3.4	2.7	1.4	1.0	1.6	1.8	2.1	2.1
(3)			2.0	17	37	1.2	1.0	3.3	4.2	3.8	4.9
(4)				1.8	1.9	1.1	1.0	1.5	1.5	1.6	1.8
(5)					9.2	1.2	1.0	2.6	3.2	3.3	3.7
(6)						1.1	1.0	3.7	4.4	3.5	4.8
(7)							1.2	1.0	1.1	1.2	1.1
(8)								1.0	1.0	1.0	1.0
(9)									72	4.4	13
(10)										5.5	24
(11)											15

Table 23: A comparison of VIFs for all the variables for the $[90/0]_S$ dataset, with significant relationships highlighted in yellow (numbers in parentheses relate to the variables in the order presented in previous tables).

Variable	(2)	(3)	(4)	(5)	(6)	(7)	(8)	(9)	(10)	(11)	(12)
(1)	1.4	1.2	1.2	1.3	1.1	1.1	1.2	1.0	1.0	1.1	1.0
(2)		3.4	3.0	3.7	2.6	1.0	1.6	1.4	1.4	2.0	1.7
(3)			4.1	7.9	27	1.0	2.3	1.8	1.9	2.7	2.6
(4)				3.4	3.3	1.0	2.1	1.4	1.4	1.8	1.6
(5)					5.9	1.0	2.7	1.6	1.8	2.4	2.2
(6)						1.0	1.9	2.0	2.4	3.5	3.2
(7)							1.2	1.0	1.0	1.0	1.0
(8)								1.2	1.1	1.3	1.2
(9)									14	2.4	3.8
(10)										4.3	10
(11)											25

Table 24: A comparison of VIFs for all the variables for the $[0/90/\pm45]_S$ dataset, with significant relationships highlighted in yellow (numbers in parentheses relate to the variables in the order presented in previous tables).

Variable	(2)	(3)	(4)	(5)	(6)	(7)	(8)	(9)	(10)	(11)	(12)
(1)	1.0	1.0	1.1	1.0	1.0	1.0	1.0	1.0	1.0	1.0	1.0
(2)		4.1	6.8	6.5	2.8	1.0	3.3	1.6	1.9	1.5	1.7
(3)			3.7	8.8	33	1.0	2.1	2.9	3.7	2.7	3.5
(4)				3.9	2.7	1.0	2.8	1.6	1.7	1.3	1.5
(5)					4.6	1.0	4.6	2.2	2.7	2.3	2.6
(6)						1.0	1.7	3.1	3.7	2.8	3.8
(7)							1.0	1.0	1.0	1.0	1.0
(8)								1.3	1.4	1.3	1.3
(9)									26	2.8	8.6
(10)										6.0	19
(11)											21

Table 25: A comparison of VIFs for all the variables for the $[90_4]$ dataset, with significant relationships highlighted in yellow (numbers in parentheses relate to the variables in the order presented in previous tables).

Variable	(1)	(2)	(3)	(4)	(5)	(6)	(7)
Rise Time	0.0411	0.0207	0.0192	0.0217	0.0175	0.0266	0.0180
Counts	0.190	0.178	0.178	0.189	0.236	0.232	0.209
MARSE Energy	-0.651	-0.619	-0.591	-0.626	-0.720	-0.689	-0.635
Abs. Energy	0.563	0.561	0.544	0.570	0.622	0.595	0.575
Cum. Abs. Energy ($\times 10^{-10}$)	-8.54	-8.78	-6.62	-7.27	-9.24	-8.43	-6.20
Cum. MARSE Energy ($\times 10^{-5}$)	1.86	1.83	1.53	1.70	1.98	1.97	1.45
Cum. AE Counts ($\times 10^{-5}$)	-2.03	-1.89	-1.71	-1.85	-2.00	-2.06	-1.62
Constant	0.848	0.852	0.843	0.839	0.838	0.829	0.825

Table 26: A comparison of linear regression coefficients for each HOCV test for the $[0/90]_S$ model to demonstrate stability. Effects of collinearity of specific variables are highlighted in yellow.

PC loading vectors were then determined from the datasets. Figure 123 shows a plot of cumulative percentage variance that the number of PCs account for, in descending order of variance. It shows that the first PC for each dataset accounted for approximately 80% of the total variance and over 95% of the total variance was accounted for by the first five PCs for each dataset. This would suggest that PCA could be used as a good variable reduction technique to aid in reducing calculation time, if larger datasets were used in the analyses. Table 27 shows a summary of the first two PC loading vectors for each of the datasets, which accounted for 85-90% of the total variance in all four cases. Inspections of these loading coefficients could be used to assess which variables made significant contributions to the variances of the datasets. Generally, all of the first PC loading vectors suggested that most of the variables were significant in contributing to the total variances of the datasets. GUW rise time, P-Freq and C-Freq consistently showed the lowest values for the first components, suggesting that they contributed very

little to the overall variances of the datasets and bared little significance. The AE variables generally showed comparable contributions to the variances between each other, but particularly for the $[90/0]_S$ and $[0/90/\pm45]_S$ datasets, which may explain why they favored the AE data over the GUW data in the "Acoustic Emission vs. Guided Ultrasonic Waves" modeling section. The GUW amplitudes and energies were also consistently high, as expected.

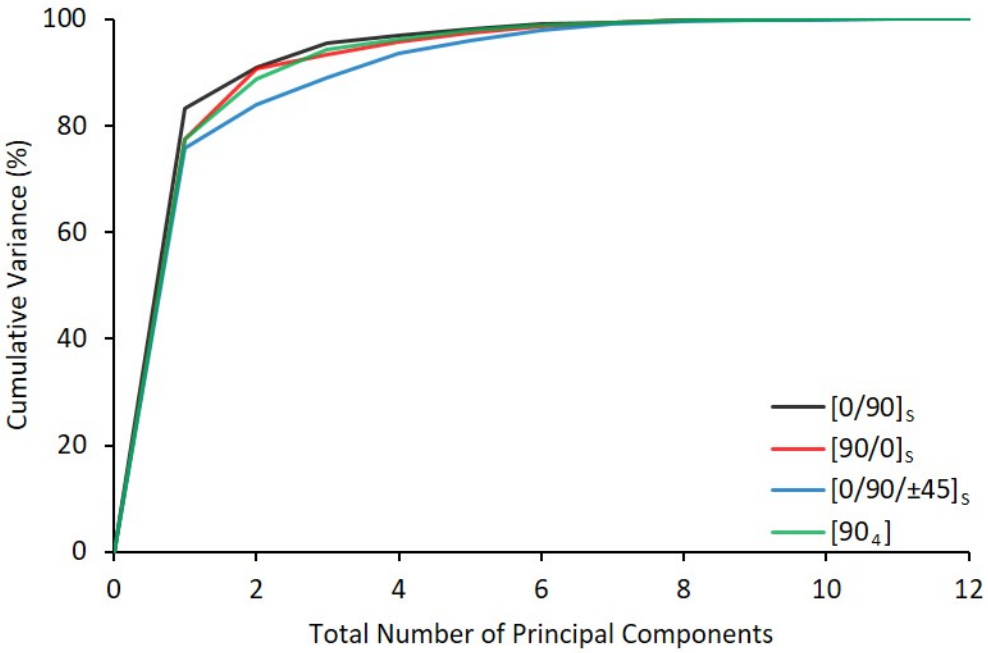


Figure 123: A plot of cumulative variance against the number of principal components for each of the four layup datasets.

Variable	$[0/90]_S$		$[90/0]_S$		$[0/90/\pm45]_S$		$[90_4]$	
	1	2	1	2	1	2	1	2
Rise Time	0.23	-0.31	-0.09	-0.15	0.06	0.13	0.00	0.12
Counts	0.44	0.26	-0.34	0.63	0.31	0.29	0.38	0.45
MARSE Energy	0.36	0.02	-0.30	0.12	0.37	0.17	0.33	0.07
Duration	0.37	0.21	-0.21	0.26	0.37	0.37	0.31	0.41
Amplitude	0.47	0.41	-0.31	0.20	0.44	0.26	0.39	0.23
Abs. Energy	0.30	-0.13	-0.28	0.05	0.34	0.06	0.30	-0.01
P-Freq	-0.04	-0.14	-0.09	0.38	0.00	-0.05	0.03	-0.07
C-Freq	-0.10	-0.12	-0.03	0.03	-0.07	-0.09	-0.15	-0.24
Cum. Abs. Energy	-0.22	0.49	0.37	0.39	-0.35	0.59	-0.33	0.40
Cum. MARSE Energy	-0.20	0.45	0.38	0.32	-0.32	0.50	-0.38	0.39
Number of AE Events	-0.20	0.20	0.34	0.11	-0.20	0.12	-0.22	0.29
Cum. Counts	-0.19	0.31	0.40	0.23	-0.21	0.21	-0.28	0.32

Table 27: A summary of the first two principal component loading vectors for each layup dataset.

The PC loading vectors presented in Table 27 were then used to transform the original datasets and apply the multivariate linear regression techniques. The PCs were removed one at a time in order of smallest to largest contributions to the total variance and the relevant training and validation statistics were calculated for each iteration. Figures 124-127 show the changes in R^2_{adj}, RMSE and R^2_{HOCV} against the number of PCs included in the PCRs for each layup respectively.

With respect to R^2_{adj}, only small reductions were observed until the models had been reduced to 5 PCs or less. In the case of the $[90_4]$ layup, negligible reductions were observed, even when only one PC was included in the model. The RMSE showed the inverse of these trends, as expected. The R^2_{HOCV} results against the number of PCs are the most important to note. Theory suggested that the statistical noise caused by poorly correlated variables, could be reduced by removing the least significant PCs from the regression models. Ideally, this would have served as a less biased approach to the

variable reduction procedures applied previously. The results did reflect this to some degree. The R^2_{HOCV} results were maximized when the number of PCs were reduced, except for the $[0/90]_S$ dataset (R^2_{HOCV} = 0.919). The $[90/0]_S$ validation results were maximized with 11 PCs (R^2_{HOCV} = 0.957), the $[0/90/\pm45]_S$ dataset with 5 PCs (R^2_{HOCV} = 0.934) and the $[90_4]$ dataset with 7 PCs (R^2_{HOCV} = 0.987).

In comparison to the original reduced variable models, the maximized results were significantly lower for the $[0/90]_S$ and $[90/0]_S$ datasets, slightly lower $[0/90/\pm45]_S$ dataset and increased for the $[90_4]$ dataset. Overall, the use of reduced PCR models instead of a suitable, non-biased variable reduction procedure resulted in less adequate predictions. The apparent increase in validation results for the $[90_4]$ layup reduced PCR model may be a reflection of the desired effects from the reduced number of PCs or simply a random variation within the test data.

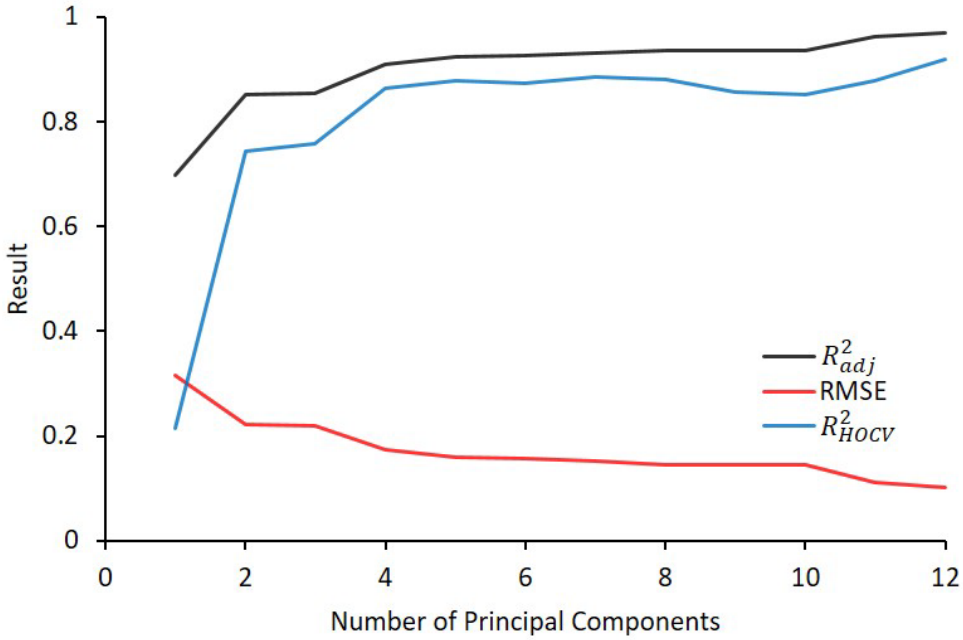


Figure 124: A plot showing changes in R^2_{adj}, RMSE and R^2_{HOCV} against the number of principal components used for the $[0/90]_S$ PCR models.

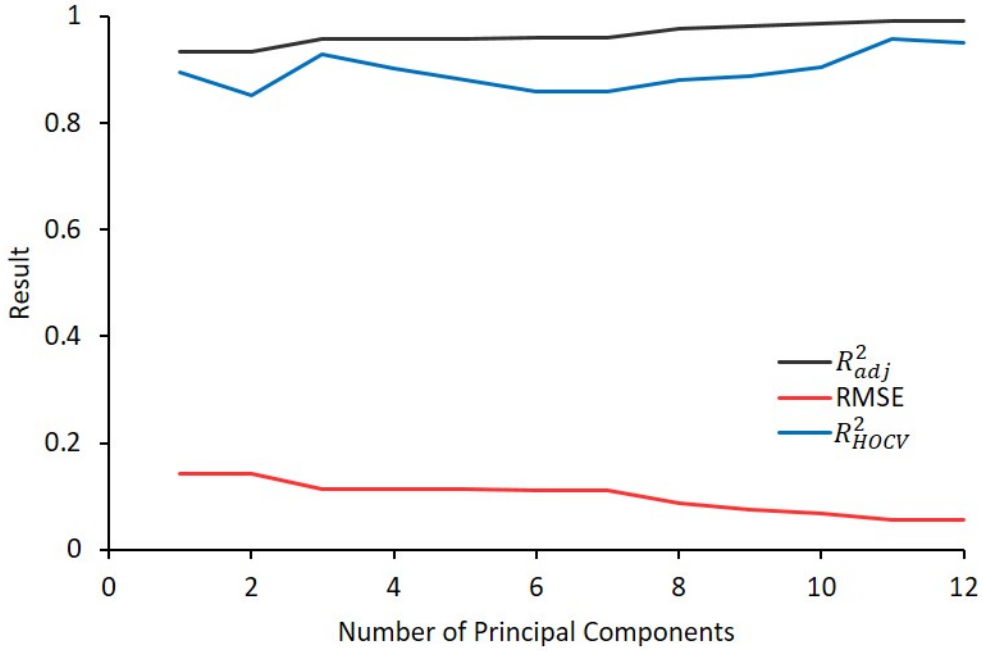


Figure 125: A plot showing changes in R^2_{adj}, RMSE and R^2_{HOCV} against the number of principal components used for the $[90/0]_S$ PCR models.

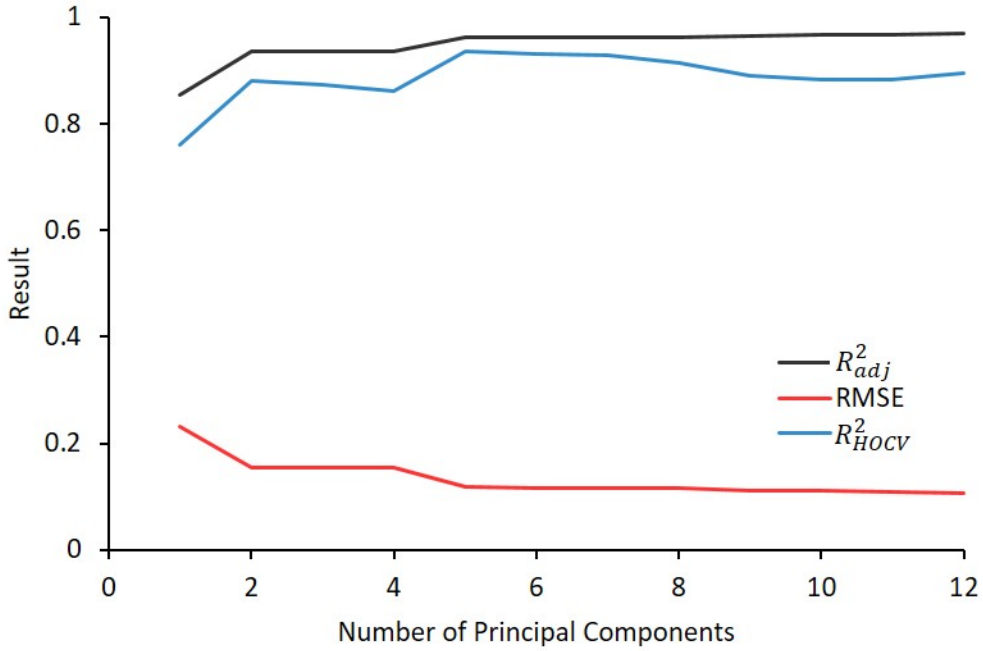


Figure 126: A plot showing changes in R^2_{adj}, RMSE and R^2_{HOCV} against the number of principal components used for the $[0/90/\pm45]_S$ PCR models.

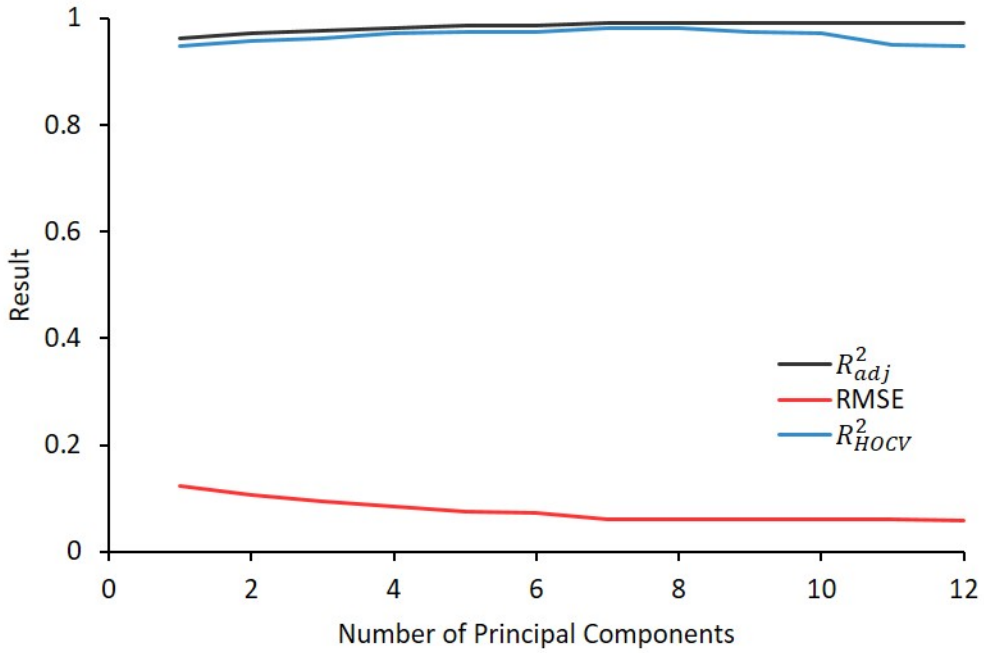


Figure 127: A plot showing changes in R^2_{adj}, RMSE and R^2_{HOCV} against the number of principal components used for the [90_4] PCR models.

Finally, the PCR coefficients were transformed back to the original dataspace and rescaled to be used with the original non-normalized, non-centered datasets to determine if the collinearity effects had been fixed. Table 28 presents the transformed coefficients for the original datasets when no PCs were removed for the PCR analysis. Table 29 show the transformed coefficients for the optimized models with reduced PCs. Since the $[0/90]_S$ layup dataset was optimized with all 12 PCs, the coefficients for the model with the second highest R^2_{HOCV} are presented (7 PCs).

With all PCs included in the PCR, the resulting transformed coefficients still exhibit the effects of collinearity. At least two variable coefficients from each layup model exhibited the incorrect signs. In fact, the coefficients presented are exactly the same as those obtained when applying a regular multivariate linear regression procedure,

without removing any of the variables. On one hand, this showed that the PCR had no influence on the collinearity effects, but on the other hand, it may serve as a good validation that the solutions were in fact stable.

The transformed coefficients for the reduced PCR model did exhibit some alleviation of the collinearity effects, but not completely. All layups, except the $[90/0]_S$ only showed one coefficient which had the incorrect sign. These variables were the ones which displayed the most significant VIFs presented in the tables at the beginning of this section. In fact, the only models which did not exhibit any collinearity effects were the ones which had been reduced to significantly less PCs. At this point, the validation results had already began to suffer.

In conclusion, PCRs could serve to fix, or at least alleviate, the collinearity effects observed between specific variables, but at the expense of the predictive accuracies. Despite this, several different observations had indicated that the original solutions were actually stable, even with the incorrect coefficient values, so there was little cause for concern under these circumstances. Despite this, PCRs are still worth considering for further modeling efforts in the future, if more variables are to be added to the models.

Variable	$[0/90]_S$	$[90/0]_S$	$[0/90/\pm45]_S$	$[90_4]$
Rise Time	0.0200	0.0158	-0.0405	-0.0033
Counts	0.216	0.0290	0.0447	0.0787
MARSE Energy	-0.588	-0.200	0.0604	-0.204
Duration	0.0145	0.0071	0.0445	0.104
Amplitude	-0.127	0.155	-0.265	0.394
Abs. Energy	0.540	0.207	0.105	0.351
P-Freq	0.0597	0.0435	-0.183	-0.0987
C-Freq	0.0696	0.388	0.348	0.0876
Cumulative Abs. Energy	-8.67×10^{-10}	2.71×10^{-11}	-8.08×10^{-12}	6.57×10^{-10}
Cumulative MARSE Energy	1.79×10^{-5}	-7.66×10^{-8}	-1.17×10^{-5}	-1.38×10^{-5}
Number of AE Events	-3.11×10^{-5}	-2.06×10^{-4}	-3.86×10^{-4}	-7.66×10^{-4}
Cumulative Counts	-1.72×10^{-5}	-1.31×10^{-6}	1.36×10^{-5}	1.56×10^{-5}
Constant	0.787	0.361	0.876	0.286

Table 28: A summary of coefficients from the PCRs when all PCs were applied and transformed back to the original data space. Cells highlighted in yellow indicate coefficients affected by collinearity and green indicates coefficients that were not.

Variable	$[0/90]_S$	$[90/0]_S$	$[0/90/\pm45]_S$	$[90_4]$
Rise Time	-0.0210	0.0161	-0.0240	-0.0125
Counts	-0.0629	0.0301	0.0831	0.0779
MARSE Energy	0.100	-0.183	0.0588	0.110
Duration	0.0765	-0.0077	0.0030	0.0644
Amplitude	-0.4958	0.1737	-0.218	0.227
Abs. Energy	0.111	0.196	0.0577	0.119
P-Freq	0.0218	0.0507	0.0290	-0.0648
C-Freq	0.118	0.387	0.0551	0.0209
Cumulative Abs. Energy	-7.48×10^{-12}	-2.02×10^{-12}	-2.43×10^{-10}	1.25×10^{-10}
Cumulative MARSE Energy	-1.80×10^{-6}	7.30×10^{-7}	-4.48×10^{-6}	-1.73×10^{-6}
Number of AE Events	-9.51×10^{-5}	-1.75×10^{-4}	-1.04×10^{-4}	-3.55×10^{-4}
Cumulative Counts	-3.16×10^{-6}	-3.26×10^{-6}	-3.37×10^{-6}	-1.31×10^{-5}
Constant	1.13	0.342	0.942	0.449

Table 29: A summary of coefficients from the PCRs transformed back to the original data space for models with reduced PCs, where R^2_{HOCV} was maximized; 7 PCs for $[0/90]_S$, 11 PCs for $[90/0]_S$, 5 PCs for $[0/90/\pm45]_S$, 7 PCs for $[90_4]$. Cells highlighted in yellow indicate coefficients affected by collinearity and green indicates coefficients that were not.

Fatigue Data Modeling

As presented in the "Fatigue Testing Results and Discussion" chapter, the AE and GUW results with respect to changes in moduli showed significant statistical variation and less clear linear trends. Reasons for this were explained in detail. Despite this, the same multivariate linear regression modeling approach was applied to the datasets to attempt to make predictions of modulus degradation in fatigue loading.

Table 30 shows the R^2 values for each of the variables for the three layups tested, when linear regressions were fit against changes in moduli. In comparison to the static testing results, the R^2 values were noticeably lower, as was expected. Despite this, changes in GUW MARSE and absolute energies were quite good, as well as changes in GUW amplitude. Other variables, such as GUW counts and duration, showed good correlations for some layups, but not so much others. Again, GUW peak and centroid frequencies showed little to no correlation with respect to changes in moduli.

When inspecting the extracted AE variables, cumulative absolute energy showed poor correlations for all three layups. The other three variables showed much better correlations. It is interesting to note that the R^2 values for cumulative MARSE energies were consistently higher than those for cumulative absolute energy. Since MARSE energy is an energy measure normalized to a base frequency 100 kHz, it would suggest that frequency content had a significant effect on the AE results, resulting in either more statistical scatter or much more prominent non-linearities. Overall, the AE data for the $[90/0]_S$ layup showed the worst correlations, with no R^2 values exceeding 0.5. The

$[0/90/\pm45]_S$ showed significantly better correlations with respect to changes in moduli, with all but cumulative absolute energy having R^2 values above 0.65.

Variable	$[0/90]_S$	$[90/0]_S$	$[0/90/\pm45]_S$
Rise Time	0.134	0.019	0.021
Counts	0.591	0.295	0.358
MARSE Energy	0.695	0.460	0.539
Duration	0.633	0.143	0.280
Amplitude	0.668	0.257	0.517
Abs. Energy	0.601	0.518	0.553
P-Freq.	0.095	0.006	0.009
C-Freq.	0.307	0.030	0.081
Cumulative Abs. Energy	0.207	0.261	0.306
Cumulative MARSE Energy	0.525	0.436	0.801
Number of AE Events	0.515	0.388	0.685
Cumulative Counts	0.534	0.392	0.711

Table 30: A summary of R^2 values for each extracted variable for each layup when compared with changes in moduli in fatigue testing (GUW variables are on top and AE variables are below and separated by the dotted line).

Prediction Accuracy

Table 31 shows a summary of the fitting statistics and HOCV results for the predictive models constructed for each of the three layups tested. The results show significantly worse fit characteristics and validation results for all three layups, when compared with the static modeling results. This is not surprising, given the increased amounts of statistical error within the datasets. Less observations were used when compared to the static results, since only five coupons were tested instead of seven and the differences between layups were dependent on the number of cycles to failure for each individual coupon test. The training statistics, such as RMSE, R^2_{adj} and F-statistic were worse than the static models, particularly the $[0/90]_S$ model. The $[90/0]_S$ model showed the best training statistics. The R^2_{HOCV} results were of most importance, as a true

test of the models' predictive capabilities. The $[0/90]_S$ showed very poor predictions, with a R^2_{HOCV} score of 0.46, and the $[0/90/\pm45]_S$ model resulted in the best, with a R^2_{HOCV} score of 0.82, despite exhibiting worse training statistics than the $[90/0]_S$ model. This would suggest that the $[90/0]_S$ dataset had larger differences between tests, despite exhibiting better linear correlations overall, which affected the HOCV results when individual coupon tests were withheld.

Model Statistics	$[0/90]_S$	$[90/0]_S$	$[0/90/\pm45]_S$
Number of Observations	299	280	214
Number of Predictors	7	8	5
RMSE	0.0507	0.0152	0.0271
R^2_{adj}	0.680	0.903	0.865
F-Statistic	91.0	326	273
Overall p-value	$< 10^{-322}$	$< 10^{-322}$	10^{-309}
R^2_{HOCV}	0.462	0.728	0.822
Ave. Residual Error	4.8 ± 4.0%	2.4 ± 1.9%	2.6 ± 1.8%

Table 31: A summary of fit characteristics and HOCV results for models constructed when combining the AE and GUW datasets for each of the layups tested in fatigue.

Figures 128-130 shows the results of the HOCV tests with measured modulus changes plotted against predicted changes in modulus, with the line of ideal fit included for comparison. The $[0/90]_S$ model appears to make good predictions at smaller moduli changes, but made significant under-estimations at larger modulus changes (see Figure 128). This would not be ideal for real-life SHM scenarios, where accurate predictions are of most importance for the most severe degradations. The $[90/0]_S$ model appears to be much more conservative (see Figure 129). The outliers were much less significant, as reflected by its R^2_{HOCV} score and average residual error, and more importantly makes over-predictions at more severe modulus changes. Despite this, an important thing to note

is that the $[90/0]_S$ coupons failed so suddenly (see Figure 89) that no GUW measurements were taken during the most severe final phases in moduli degradation. In reality this would be incredibly hard to capture and react to in real SHM monitoring scenarios. The $[0/90/\pm45]_S$ showed similar results, but did appear to make relatively accurate predictions for the most severe changes in moduli (see Figure 130).

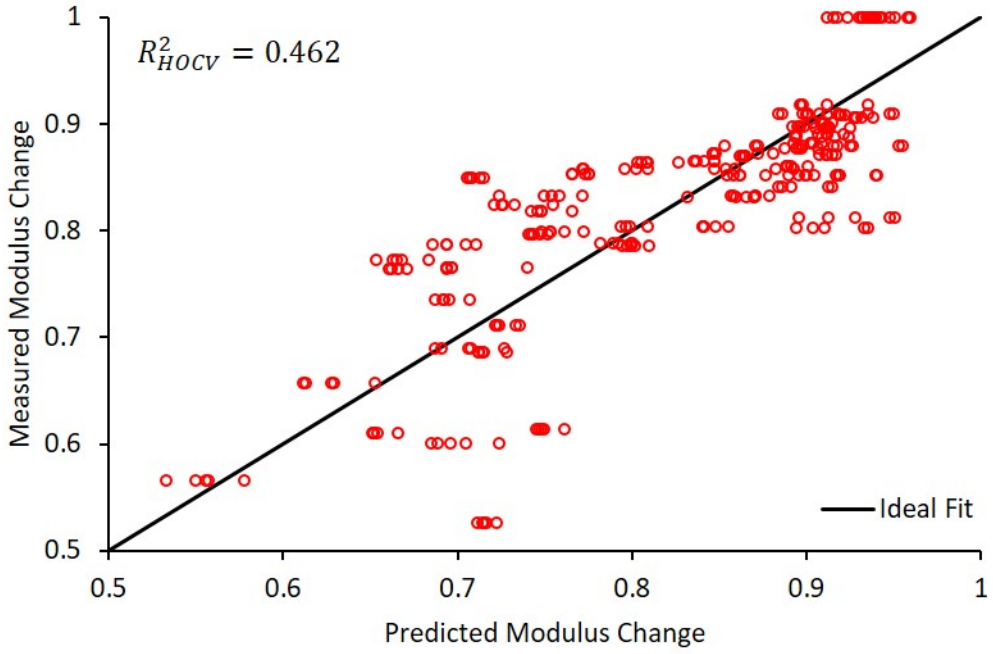


Figure 128: A scatter plot of the HOCV prediction results for the combined AE and GUW in fatigue for the $[0/90]_S$ layup.

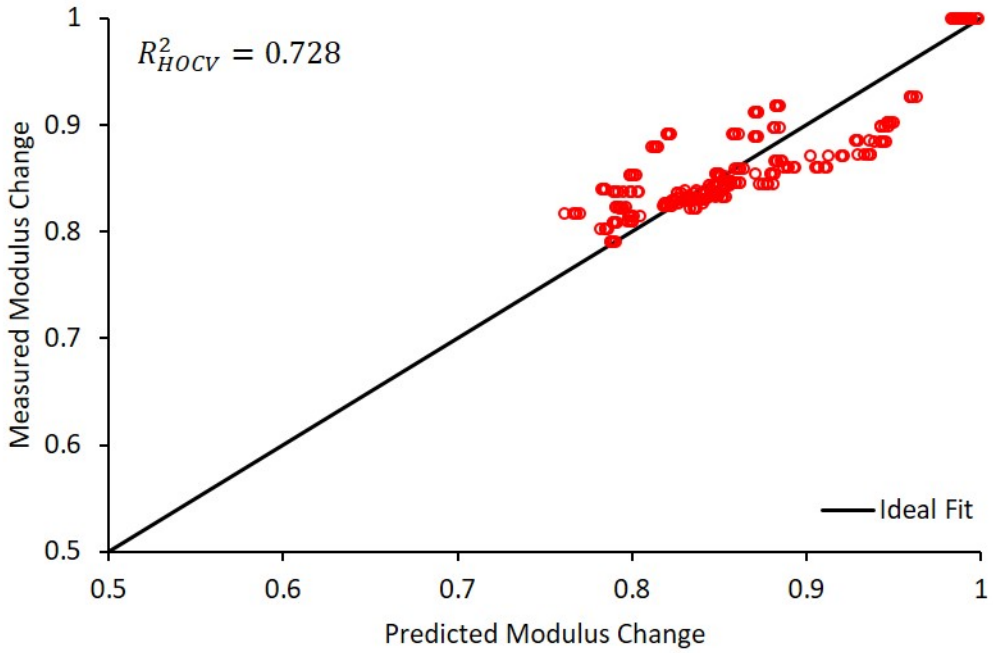


Figure 129: A scatter plot of the HOCV prediction results for the combined AE and GUW in fatigue for the $[90/0]_S$ layup.

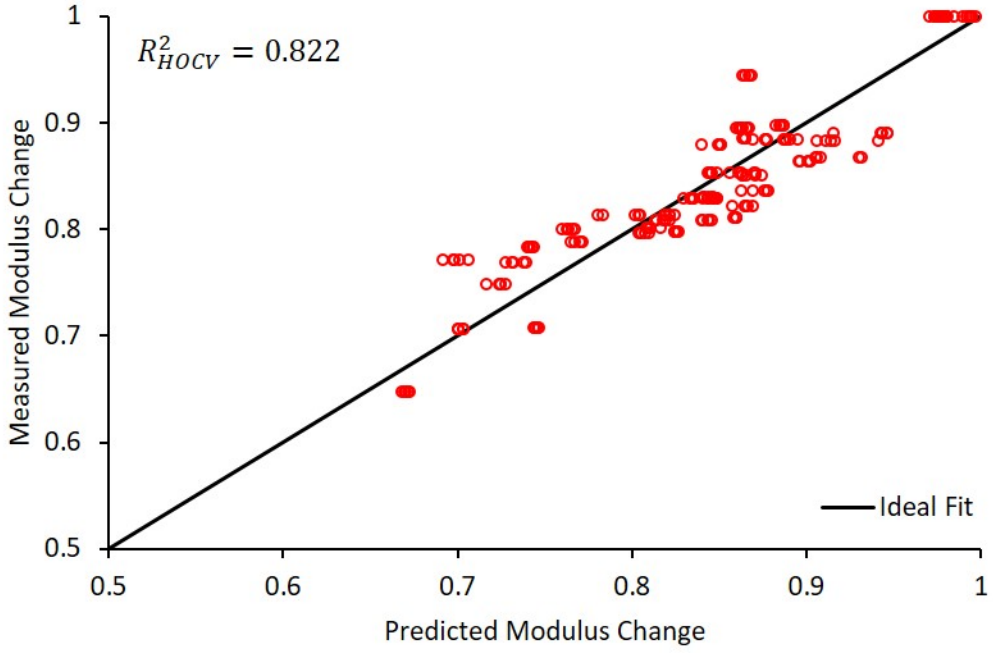


Figure 130: A scatter plot of the HOCV prediction results for the combined AE and GUW in fatigue for the $[0/90/\pm45]_S$ layup.

Figures 131-133 show plots of absolute residual errors of the three models respectively, to gain more insight into the inaccuracies of the models. The $[0/90]_S$ residual plot shows large errors of 15-20% for the largest changes in moduli (see Figure 131). Large errors can also be observed at a measured modulus change of 1 (no modulus degradation had occurred). Once again, this would suggest that it may be possible to improve the predictions for the more severe cases by omitting the initial data points from the training datasets, for the coupons in their undamaged states. The $[90/0]_S$ and $[0/90/\pm45]_S$ residual plots show much smaller errors, which do not exceed 8% (see Figure 132 and Figure 133). It can be observed that the measured modulus changes span a larger range for the $[0/90/\pm45]_S$ dataset, in comparison to the $[90/0]_S$ dataset. Overall, the results appear to show a good normal distribution across the ranges of measured moduli changes, suggesting that the linear models were still an appropriate choice for the datasets.

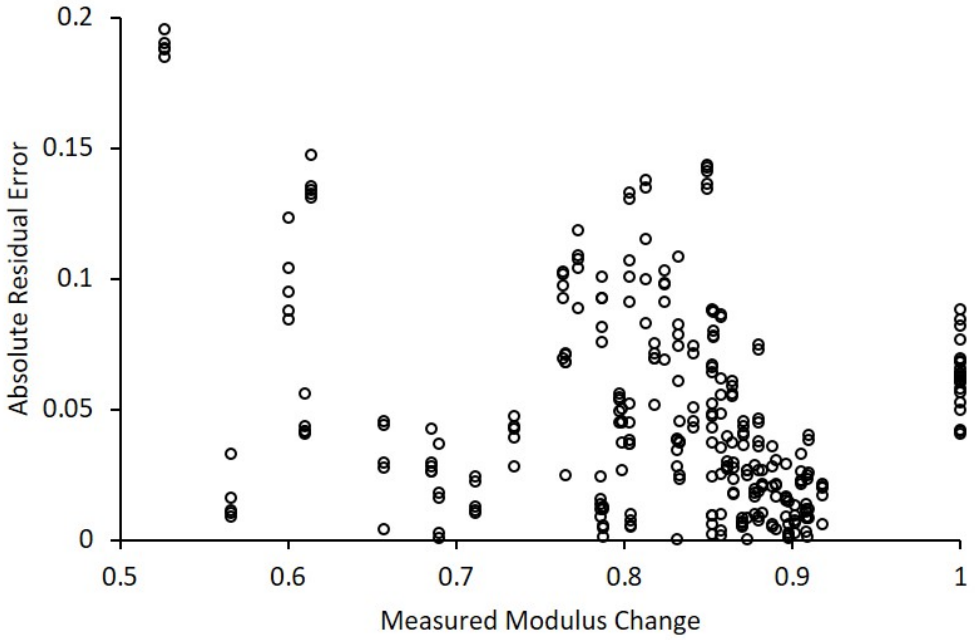


Figure 131: An absolute residual error plot for the HOCV results of the $[0/90]_S$ fatigue model.

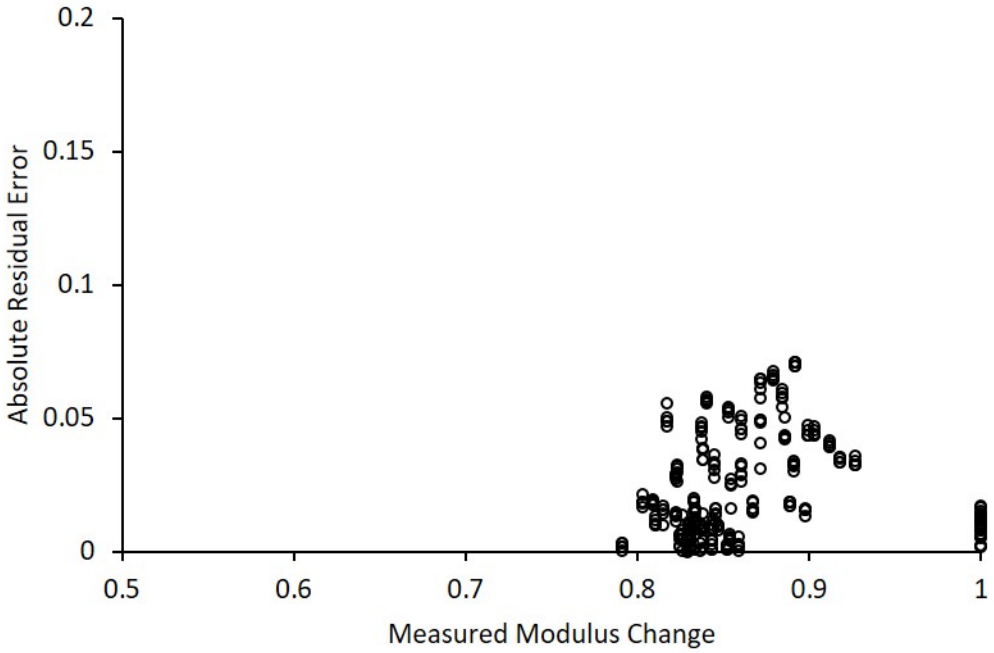


Figure 132: An absolute residual error plot for the HOCV results of the $[90/0]_S$ fatigue model.

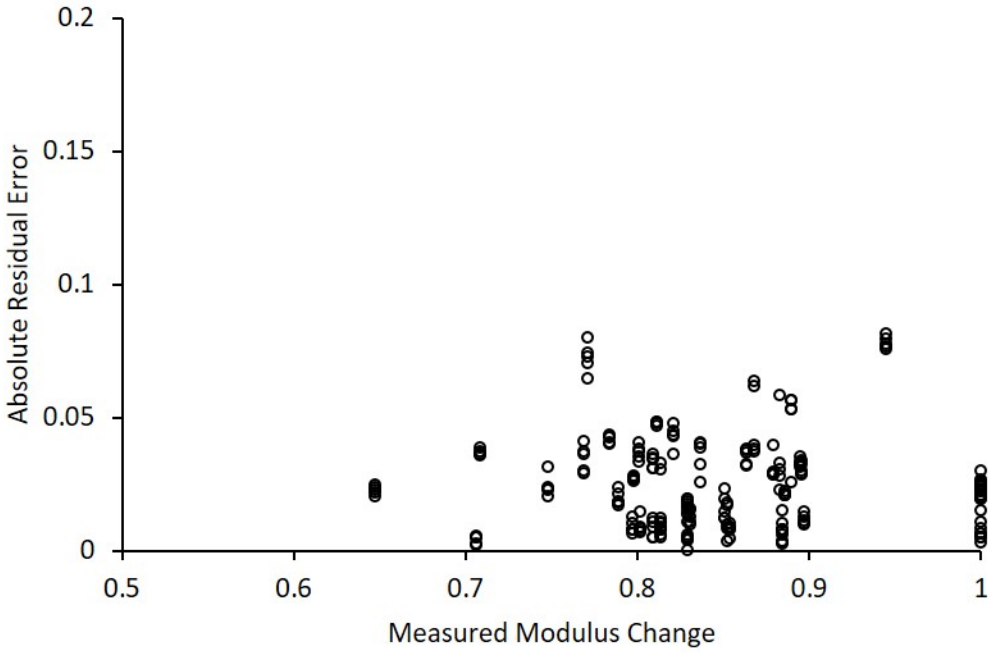


Figure 133: An absolute residual error plot for the HOCV results of the $[0/90/\pm45]_S$ fatigue model.

Coefficient Comparisons

Table 32 shows a comparison of the model coefficients determined through the maximum likelihood estimation method for the fatigue models for each of the three layups. Variables that were removed from the datasets through the variable reduction procedure have been left blank.

Variable	$[0/90]_S$	$[90/0]_S$	$[0/90/\pm45]_S$
Rise Time	0.0317		
Counts	-0.0844	0.138	
MARSE Energy	0.0626	-0.056	0.125
Duration	0.264		-0.0880
Amplitude		-0.229	
Abs. Energy	0.0348	0.105	
P-Freq			
C-Freq			0.424
Cumulative Abs. Energy		4.04×10^{-9}	
Cumulative MARSE Energy	1.16×10^{-5}	-1.09×10^{-4}	-3.44×10^{-5}
Number of AE Events	-3.09×10^{-4}	3.44×10^{-3}	
Cumulative Counts		2.17×10^{-4}	1.12×10^{-5}
Constant	0.627	1.03	0.520

Table 32: A comparison of the regression model coefficients for the fatigue models, with removed variables left blank.

The first thing to note is that the previously explained collinearity effects are also present in these models. The "Collinearity and Principal Component Analysis" section of this chapter has already shown that these anomalies were not a big concern for these particular models, so no further collinearity analysis was conducted for the fatigue models.

GUW MARSE energy and AE cumulative MARSE energy were the only two variables selected for all three models. Peak frequency was not used for any of the models and centroid frequency was only used for the $[0/90/\pm45]_S$ model. Interestingly,

the $[90/0]_S$ model made use of all four AE variables, whereas the other two models only used two out of the four AE variables.

Generally, all three models made use of the variables with the highest coefficients of determination in relation to changes in modulus (see Table 30). Like the static models, some variables were selected which had shown little to no correlation at all with changes in modulus, such as GUW rise time and centroid frequency. This may be indicative of underlying interactions between variables, which cannot be accounted for using simple linear regression analysis techniques.

Static Testing for Fatigue Prediction

As a final test of the statistical modeling possibilities in this research, regression coefficients determined from the static predictive models were applied to the fatigue datasets to evaluate the quality of predictions. If accurate, this method could serve to save significant amounts of time and money through reducing the number of fatigue tests that have to be conducted in the future. It could also serve as a measure of quality of the acquired GUW and AE data. Static modeling showed close linear relationships between changes in moduli and various GUW and AE variables. It was suspected that this could hold true in fatigue loading, if accurate data was acquired.

Figures 134-136 show plots of the measured moduli changes against the predictions made using this method. Figures 137-139 show the respective residual error plots associated with the results. Note that these residual plots are not absolute values, to differentiate between under and over predictions. Positive values are over predictions and negative values are under predictions

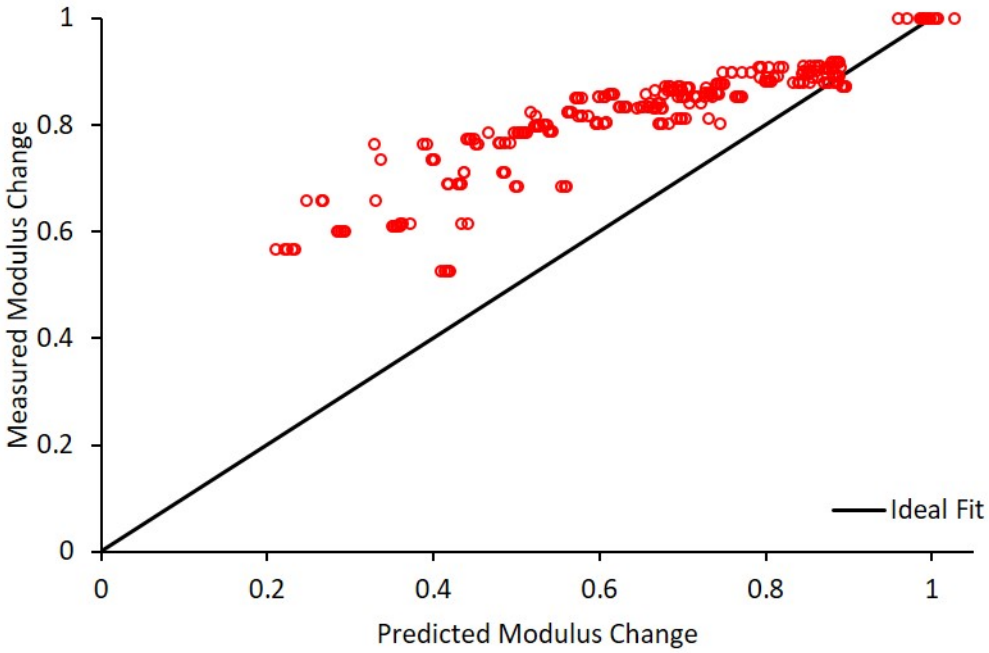


Figure 134: Measured modulus change against predicted modulus change when the $[0/90]_S$ static model regression coefficients were applied to the $[0/90]_S$ fatigue testing dataset.

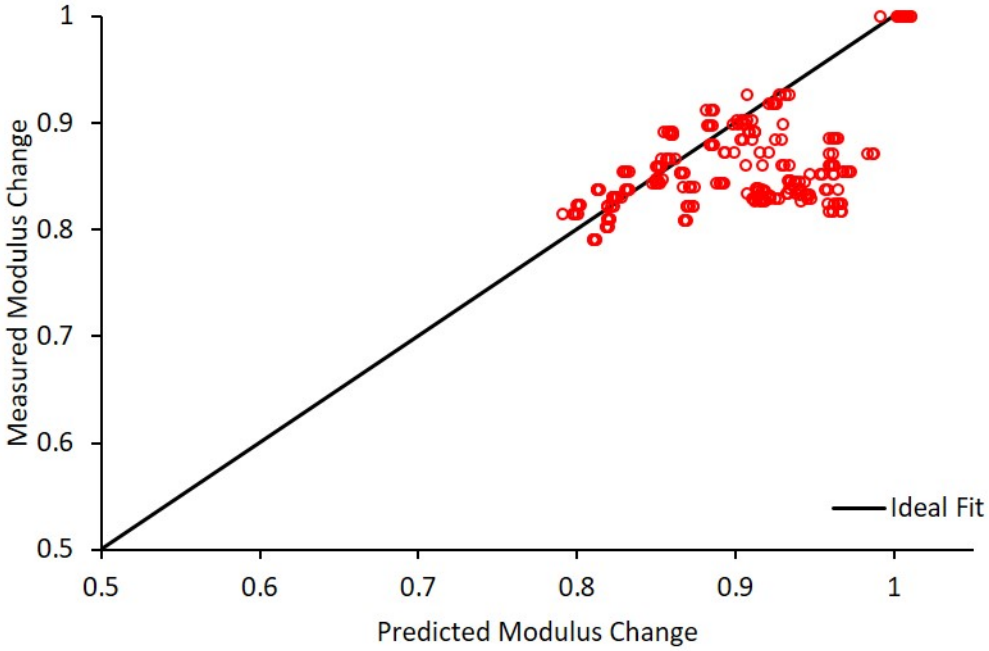


Figure 135: Measured modulus change against predicted modulus change when the $[90/0]_S$ static model regression coefficients were applied to the $[90/0]_S$ fatigue testing dataset.

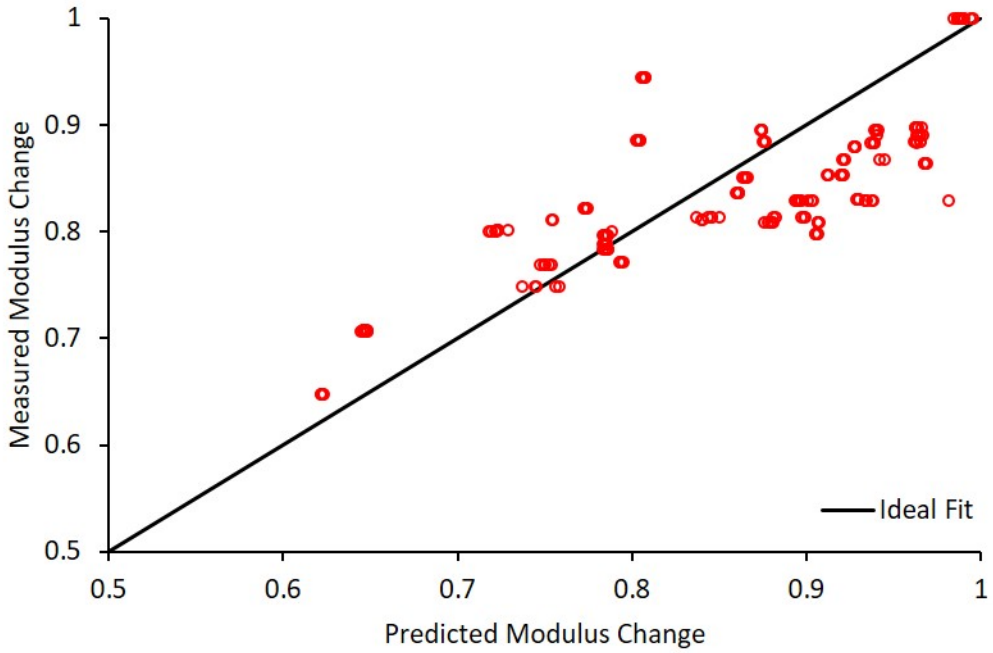


Figure 136: Measured modulus change against predicted modulus change when the $[0/90/\pm45]_S$ static model regression coefficients were applied to the $[0/90/\pm45]_S$ fatigue testing dataset.

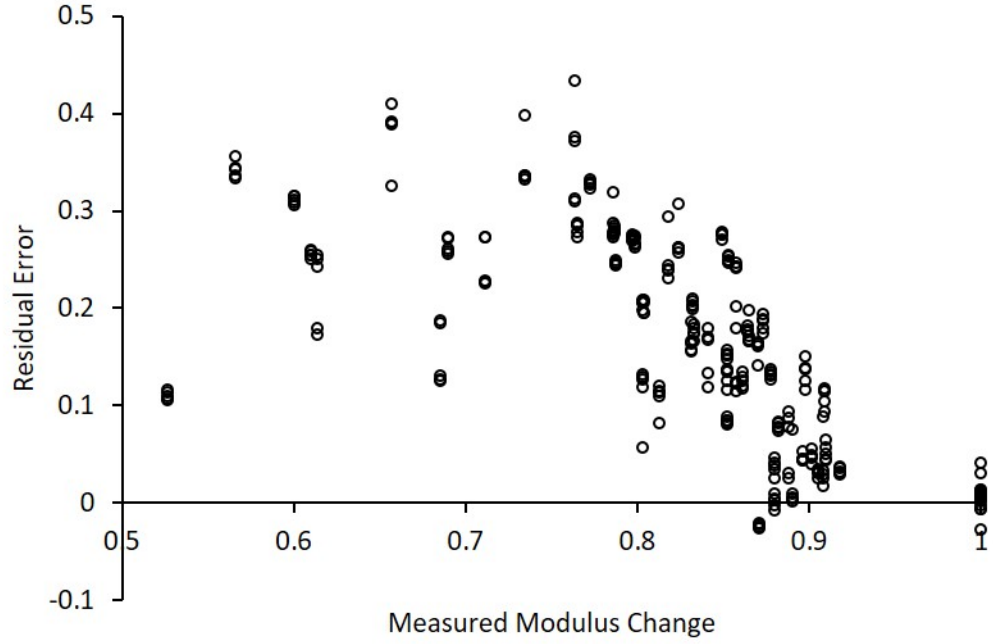


Figure 137: Residual errors when the $[0/90]_S$ static model regression coefficients were applied to the $[0/90]_S$ fatigue dataset.

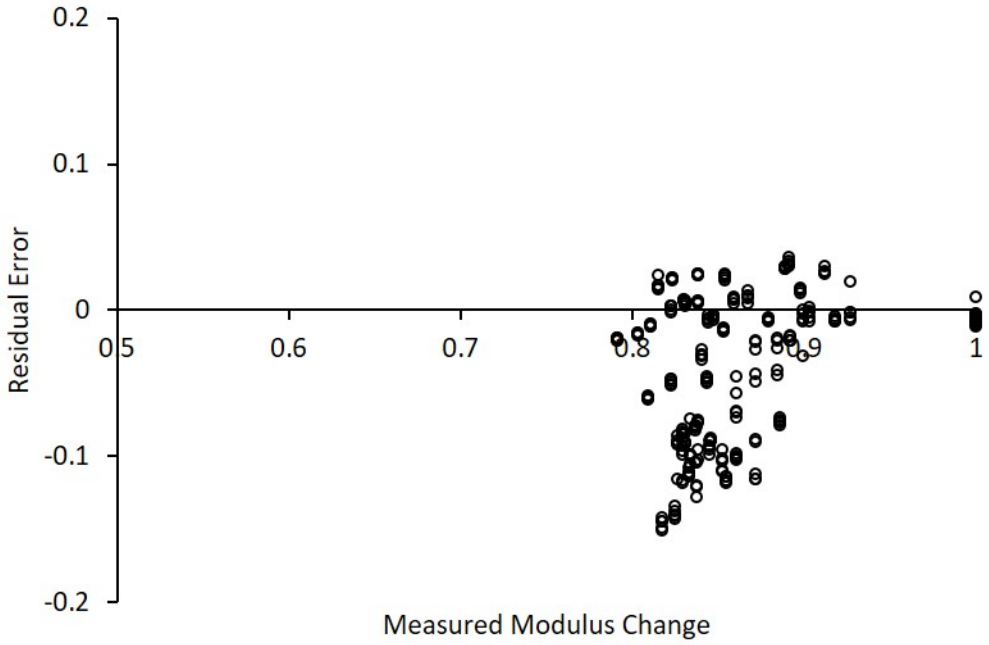


Figure 138: Residual errors when the $[90/0]_S$ static model regression coefficients were applied to the $[90/0]_S$ fatigue dataset.

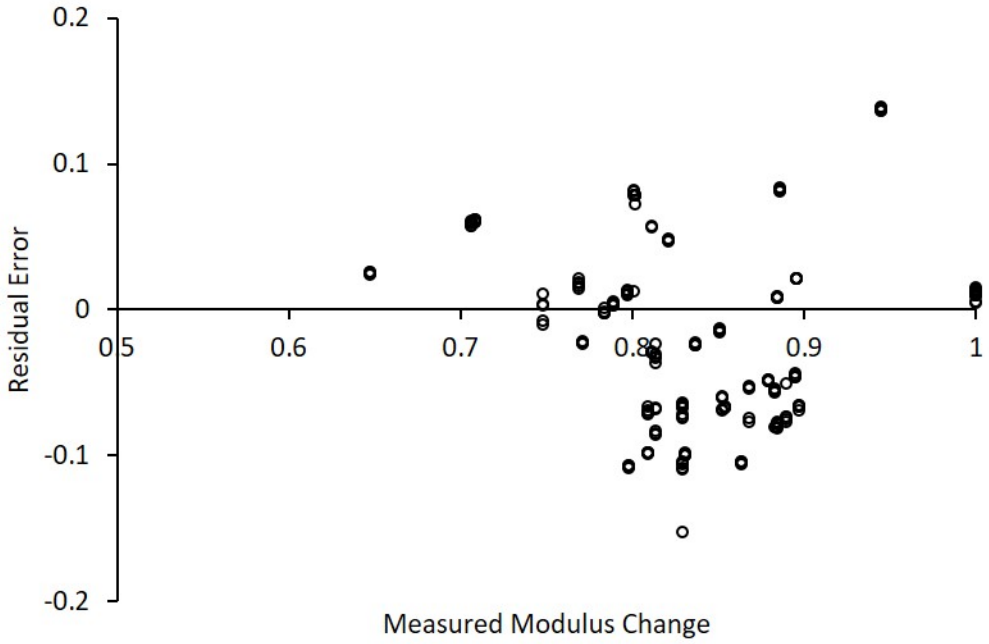


Figure 139: Residual errors when the $[0/90/\pm45]_S$ static model regression coefficients were applied to the $[0/90/\pm45]_S$ fatigue dataset.

The $[0/90]_S$ plots show relatively small errors for the initial drops in moduli after the first load cycle, but then begins to over predict by up to 45% as modulus degradation becomes more severe (see Figure 134 and Figure 137). Comparisons of the static and fatigue GUW coefficients shown in Table 18 and Table 32 suggest that the predictions were most influenced by differences in the GUW data. The fatigue coefficients were almost an order of magnitude smaller for the $[0/90]_S$ fatigue model. The cause of this may have been due to the previously mentioned outer 0° tows buckling on the surface of the coupon and dislodging the sensors, resulting in a poor coupling between them and the coupons and enhanced attenuation of the GUWs propagating from the GUW actuator to the coupons and from the coupons into the receiving sensors. In contrast, the AE coefficients were much more comparable for the static and fatigue $[0/90]_S$ models, but were still likely to have been influenced by this phenomenon.

The $[90/0]_S$ static coefficients applied to the fatigue dataset actually resulted in relatively accurate predictions for the most severe measured modulus degradations, but as a whole there were a large number of data points which were significantly under predicted, by up to 15% (see Figure 135 and Figure 138). On comparison of the regression coefficients presented in Table 18 and Table 32, the differences in static and fatigue GUW coefficients were much smaller than those for the $[0/90]_S$ models. No buckling of tows on the surface occurred, so the sensors stayed in place throughout the fatigue tests. It was the AE coefficients that exhibited the most significant differences. Those for the fatigue model were orders of magnitude greater than those calculated for the static model. This would explain the noticeable under predictions. Total accumulated

energies acquired during fatigue testing were up to an order of magnitude less than those obtained from static test data. This could be attributed to the damage-based attenuation of AE damage events after the first fatigue cycle.

Finally, using the $[0/90/\pm45]_S$ static model coefficients to make fatigue modulus predictions resulted in a wide range of under and over predictions of up to 15% (see Figure 136 and Figure 139). On comparing the coefficients presented in Table 18 and Table 32, it can be observed that the coefficients for both the GUW and AE variables were of the same magnitude, but there were still large differences, which could explain the prediction errors. As has been previously described, the $[0/90/\pm45]_S$ coupons did exhibit failure and buckling of the outer 0° tows during fatigue tests, but not to the same extent as the $[0/90]_S$ coupons, which could explain the smaller differences in the GUW coefficients. The maximum accumulated AE energies were also noticeably lower than those acquired during static testing, but not to the extent of the $[90/0]_S$ datasets. Both of these phenomena varied randomly from test to test, so could explain the combination of the large under and over predictions.

Overall, applying the regression coefficients from the static prediction models to the fatigue datasets led to significant under and over predictions of varying amounts. This is thought to have been caused by damage phenomena observed during experimental testing, which had a noticeable influence on the acquisition of accurate GUW and AE data. It is strongly suspected that accurate predictions could be made if the data could be corrected for these inaccuracies and modifications are made to the test method. A more reliable method of bonding the GUW and AE sensors to the coupons could be applied to

prevent the sensors from becoming dislodged when outer tows fail and buckle. Also, a suitable compensation strategy could be applied to correct for damage-based attenuation in the AE data.

Model Improvements

The results presented above for the modeling portion of this research have shown good potential for using AE and GUW data to predict residual laminate properties for SHM applications. The models using static test data yielded highly accurate modulus degradation predictions, but the models constructed from the fatigue test data were lacking. Some explanations have already been provided, but there were many other things that could have been done to improve the datasets and their respective models, from modifications to the test methods, to further post-processing of the datasets for additional input variables, to applying other modeling techniques to the datasets.

Test Setup Changes

With regards to the test setup used throughout the experimental side of this research, there were several changes which could have been made to allow for more accurate results, more in depth analysis and better prediction results. The sensor setup could have been better optimized for static and fatigue tensile loading. A three sensor setup was used, since a function generator had to be used to apply the GUWs and an AE system had to be used to detect the GUWs and acquire AE data. Ideally, the two techniques could have been combined into a standalone system, so that only two sensors would have been required. Each of the two AE sensors could be used to apply and detect

the GUWs, similar to the way automatic sensor tests (ASTs) operate on some AE systems. This would allow more space for the GUWs to propagate further along the length of the coupons. The GUWs would propagate along the same path, but in opposite directions, so better comparisons could be made between the waveforms. In a true standalone system, differences between the time of triggering and detecting the GUWs could also be determined, so that wave velocities could be calculated and even the differences in velocities between different wave modes which are excited.

The use of a viscous vacuum grease couplant also appeared to cause some issues with the AE and GUW data, especially in fatigue, since the sensors were not firmly bonded to the test coupons. Adhesive bonding may have led to better results by reducing the variability through movement of the sensors. Epoxy adhesive has been commonly used with larger scale AE testing, but would risk damage to the sensors when removing them. Also, an epoxy adhesive may be severely degraded in testing, since the matrix material of the coupons tested was epoxy. Other adhesives, such as silicon were tested, but resulted in severe attenuation to the ultrasonic signals. Ideally, a solid adhesive with minimal viscoelastic properties and a higher strain to failure than epoxy, which could easily be removed from the sensors, would be used to bond the sensors to test coupons.

Changes in the setup of the AE system could be applied for more efficient and accurate monitoring, during experimental testing. The effects of damage-based attenuation were suspected to have had severe effects on the AE data acquired during fatigue testing, causing skewed trends in cumulative AE parameters. It has been suggested that a suitable compensation strategy could be applied, based on the GUW

datasets. With the datasets in their current state, it would not be possible to account for attenuated damage events that were not detected, during the tests. If tests were to be repeated, it would be advisable to reduce the AE detection threshold, so that lower amplitude events could be corrected for, before reapplying the original threshold to the event data in post-processing. This would improve the results, but would also risk a low signal to noise ratio for the lower amplitude damage events, especially when they are corrected for in post-processing. Finally, the HDT should be reduced during fatigue testing to account for the increased loading rate, which may have limited event detection, but may increase the risk of detecting reflections as damage events during acquisition. These changes would have led to significant improvements in the AE datasets for more accurate predictive modeling in fatigue.

With regards to the GUW monitoring, the most important thing lacking in the test setup was an in-line signal amplifier for the piezoelectric actuator. Received signals were severely attenuated at the most severe stages of the coupons' damage states, towards the end of the static and fatigue tests. The AE system thresholds and other parameters had to be modified to account for this and reliably detect the GUWs. Amplifying the input signal to the GUW actuator would prevent the need for this and increase the signal to noise ratio, particularly in fatigue. As well as this, different waveforms could have also been applied, such as chirps [101] and frequency and amplitude sweeps. The application of different waveforms may have led to a greater insight into frequency based attenuation, due to damage. Also, in retrospect, GUWs could have been applied at the average fatigue stress for each interruption during fatigue testing. The differences could

have been incorporated into the models for more comprehensive evaluations, as well as working towards a more universal tool for real-life SHM applications.

Ideally, making these changes to the test setup and procedures should allow for more accurate and reliable measurements, more comprehensive analyses and, ultimately, better and more accurate predictive models in the future.

Additional Variables

The results presented at the beginning of this chapter have shown the benefits of combining the two on-line damage monitoring techniques for making accurate predictions. In this study, only eight GUW variables and four AE variables were applied to the initial predictive models, before the variable reduction techniques were applied. There are many other variables that could have been included to make even more accurate and robust predictions.

Wave velocity is an important material parameter that could not be determined from the test setup that was used. In theory, in-plane wave velocity is directly proportional to material stiffness, therefore it should decrease as damage is introduced and laminate stiffness degrades [102], although it is unlikely that it would be perfectly proportional to residual modulus. The theory of in-plane wave velocity is based on atomic stiffness, whereas modulus degradation of composite laminates is due to discontinuities from distributed cracks, but there should still be some quantifiable correlation between them. It may also be possible to extract out-of-plane wave velocity from the GUW waveforms, through appropriate filtering and short term Fourier transforms [95], as an additional variable. Out-of-plane waves are frequency dispersive,

so should show different trends to the in-plane waves, when compared with modulus degradation.

In this research, only Dirac delta functions were used as an input signal for the GUWs. It would be perfectly feasible to apply multiple waveform types at each interruption during testing and apply all the resulting waveforms' features as separate sets of variables to the statistical analyses. Some waveform types may work better under certain circumstances, such as specific laminate geometries and layups, which would lead to more robust predictions in different scenarios.

With regards to AE monitoring, only cumulative events parameters could be applied to summarize the data before each interruption, so it could be combined with the GUW data. No specific attempt was made to differentiate between damage modes in the event data. It was assumed that applying cumulative energies and counts would account for them in an indirect manner. A more direct approach could have been taken by applying currently accepted, unsupervised clustering methods to the data to cluster events into their respective damage modes [44, 57-61, 66]. Cumulative parameters for the different clusters could be determined for a whole new set of variables, which would have their own individual effects in relation to modulus degradation.

When attempts were made to produce a layup independent model for the static test data, analytical initial laminate properties (E_L and E_B) were included as interaction parameters in the regression model. This model was only tested in its simplest form. If more complex styles of statistical models were to be applied to the datasets to build a more universal tool, they would certainly benefit from more initial laminate properties, to

make accurate predictions for any laminate that is tested. These could be in the form of E_L and E_B, but also include laminate thickness and shear modulus, as well as terms from the ABD matrix, calculated through classical laminate theory [100]. If it was to be scaled up to include other materials, fabrics and geometries, then constitutive properties, fabric architecture properties and laminate dimensions could also be included in the model.

Overall, there are plenty of additional variables, which could be calculated from AE data, GUW data and other laminate properties, which could be added to the models to make more accurate and robust predictions of degrading laminate properties from simultaneously applying AE and GUW techniques for SHM. These variables would be applicable for the current multivariate linear regression models that were used and if the data were applied to more sophisticated forms of statistical predictive models.

Other Modeling Techniques

Multivariate linear regression modeling was the chosen technique to make predictions in this research. Although relatively simplistic, it was used because the static testing data variables showed significant linear correlations with respect to changes in modulus and because of its interpretability. The regression modeling technique allowed for much better comparisons between models, as well as gaining deeper understandings of the intricacies within the datasets. Despite this, there are other, more sophisticated modeling techniques available, which would have certainly resulted in more accurate predictions, but at the cost of interpretability.

Artificial neural networks (ANNs) are the most prominent in this form of research. Rather than adding interactions to multivariate regression models, an ANN

would be able to do it iteratively and obtain a superior fit to the data. The main problem being that it would be difficult to understand the variable interactions and relate them back to physical interactions, which produced the data in the first place. Although not particularly useful for understanding the data, ANNs would be very beneficial for constructing a more universal tool with the datasets. As has been described previously, an ANN could be the solution to a layup independent model. The same laminate and material parameters, E_L and E_B, as well as other laminate properties, could be added to the datasets and an ANN would be able to apply and scale them to the AE and GUW variables appropriately and make accurate predictions for all layups tested in a single, standalone model. There are plenty of commercially available ANN tools from various software, such as MATLAB, for constructing these types of models, but issues would arise when trying to tailor them specifically to the datasets that have been presented. Ideally, the same coupon-by-coupon HOCV procedure should be applied to make direct comparisons, or, in the case of a layup independent model, it would be more appropriate to apply a layup-by-layup validation procedure, to truly test the model's capabilities. This is certainly possible, but would require testing more layups and a much greater, in depth understanding of ANNs.

It has already been discussed that differentiating between AE damage modes could result in significant improvements to modulus degradation predictions. The background research has shown that there are many complex, multivariate analysis techniques available, typically in the form of unsupervised clustering techniques, such as k-means and fuzzy c-means [44, 57, 59-61, 65]. These methods may benefit the models

as another form of pre-processing the AE datasets by providing more variables, but caution must be taken by relating clusters back to original variables within the datasets. It would be easy to infer that natural statistical clusters in the AE event data are directly related to specific damage modes, but would be reckless to do so without an adequate form of inspection and validation of the damage modes that have actually occurred within the test coupons. These techniques would require extensive efforts to test for repeatability from coupon to coupon.

To conclude the modeling portion of this research, multivariate linear regression models were able to make accurate modulus predictions on an individual layup basis in static testing, when AE and GUW datasets were combined, but fell short when used for constructing a layup independent model. Residual fatigue modulus predictions also left a lot to be desired, due to several testing factors, causing large variations and non-linearities within the datasets, which has been discussed in detail. Despite this, they have paved the way for a much greater understanding of combining the datasets and making better, more accurate and more reliable predictions, with continued research. In the future, if larger structures with more complex sensor arrays are tested, then more sophisticated modeling techniques, such as ANNs, will need to be applied for the most accurate predictions. In conjunction with this, it would still be advisable to continue to apply the more simplistic regression modeling techniques for gaining deeper understandings of the fundamental interactions and intricacies of the datasets acquired during experimental testing.

FUTURE WORK

The research presented in this dissertation has taken a novel approach to combining multiple sensing technologies (AE and GUWs) and applied them to the mechanical testing of GFRP laminates. According to the background research that was reviewed, this approach had never been taken before. Because of this, the most basic, representative test methods were applied initially, as a proof of concept and with the idea of gradually increasing the complexity, while continuously improving the test setups, data processing techniques and predictive modeling techniques. The first step was taken by moving from static testing to fatigue testing; a more complex, but more realistic loading scenario. This means that there is a wide scope for continuing this research and moving towards real-life monitoring of large composite structures. To do this, testing techniques will have to be scaled-up to be more representative, while also refining AE and GUW setups and methodologies, continuously improving signal processing techniques and advancing predictive modeling strategies, to accompany larger scale testing.

Test Methodologies

With regards to testing methodologies, the application of the AE and GUW monitoring techniques would benefit significantly from a user-built, automated, standalone system, rather than an AE system and a signal generator. This would allow for custom tuning of the monitoring setups, the application of multiple GUW waveforms, the ability to accurately measure the velocity of the GUWs and the use of more applicable

data analysis techniques. The Physical Acoustics 1283 USB-AE Nodes™ are compatible with LabView software, so a custom built LabView VI may be beneficial for continued research, to incorporate the GUWs into a standalone system. It may also be beneficial to incorporate electro-mechanical impedance testing into the system, to make full use of the piezoelectric sensors [88, 89].

Many of the other testing issues arose during fatigue testing. One of the main problems was sufficient, reliable bonding of the sensors to the test coupons. If fatigue testing with AE and GUWs is to be continued, it is recommended that a better sensor bonding method is investigated, ideally in the form of an adhesive. The adhesive would have to be strong enough to hold the sensors in place throughout tests, have negligible viscoelastic properties to minimize attenuation of the applied and received ultrasonic waves, have a higher strain to failure than the matrix properties of the laminates tested (epoxy in this case) and can be easily removed from the sensors without causing damage at the end of tests. In this research, fatigue tests were only conducted at one stress level to acquire the data that was applied to the statistical models. Ideally, data should be acquired for multiple stress levels, which would result in fatigue failures of up to 1 million cycles. This would require a more powerful servo-hydraulic load frame to test at higher cycle frequencies and significantly reduce testing times. During fatigue tests, final failures almost always originated in the gripping areas of the test coupons, which were almost impossible to detect with the AE system. This is the unfortunate reality of tension-tension fatigue testing with composite laminates. The alternating stresses are always going to be higher in the gripping areas than the gage section of coupons. Because of this, it might be

worth considering a different form of fatigue testing, such as three or four-point bending to reduce these gripping issues, or at least promote failures within the gage section of the test coupons, so that the AE monitoring can adequately detect it.

Residual strength was a fatigue property that was not tested in this research. Residual strength testing requires significantly more tests than residual modulus characterization at multiple stress levels and proportions of fatigue life. It would be a very important parameter to be able to measure and predict for real-life SHM applications. The fatigue life results acquired in this research could be used as a baseline to begin tests for residual fatigue strength. Also, since this research was primarily directed towards wind turbine blades, it would be beneficial to test layups which are representative of spar caps, such as $[0/\pm45]_{nS}$. These layups may not exhibit quite as much damage before failure as the others tested in this study, so it would be important to understand the effects on AE and GUW responses.

Previous research has shown that AE and GUW techniques have a lot of potential for detecting and measuring delamination growth in composite laminates [52, 64, 79, 103-106]. Wind turbine blades have shown to be very susceptible to shear web bond line failures when in service, often originating from manufacturing defects. The use of combined AE and GUW monitoring could be applied to these phenomena for more accurate, reliable and robust monitoring of delamination initiation and growth in composite structures. Similarly, the same techniques could be applied to evaluate impact damage. Both techniques have shown promise in detecting, locating and evaluating

barely visible impact damage, but little has been done to combine the data to make more accurate assessments of the severity of impact damage [38, 41, 42, 64, 78, 105].

Ideally, the next stages of this research, with regards to testing methodologies, would be scaling up to testing sub-structures, such as sandwich beams, I-beams or box beams. These tests would require larger, more complex sensor arrays which are capable of detecting and locating damage events across the structure as well as applying the GUWs throughout the sensor network, while the structures are being tested to failure and degrading laminate properties are monitored. This would allow for data from sensor to sensor to be processed based on their location and the location of detected damage events to effectively form a damage map across the structure, which could then be used to pinpoint areas of severe degradation for repair. Sensors could then be used to monitor any repairs that are made when testing is resumed.

Acoustic Emission and Guided Ultrasonic Wave Monitoring

Fatigue testing highlighted some other issues with the AE and GUW monitoring that have seldom been mentioned in previous research. First of all, the AE system timing parameters would benefit from some fine tuning before further testing is conducted, to account for the higher strain rates than those applied in static testing. The main phenomenon that came to light during fatigue testing was damage-based attenuation of AE damage events. The GUWs underwent significant attenuation when propagating through damaged coupons when compared to them propagating through undamaged coupons. It is logical to assume that ultrasonic waves originating from damage events are experiencing the same phenomenon. This issue only manifested itself in fatigue testing

because damage events were occurring at similar stress levels with every fatigue cycle. This would suggest that there would be a significant benefit to applying a damage-based compensation strategy to AE data using changes in GUW signal parameters. This appears to be an area which has been completely overlooked by AE researchers. Ideally, fatigue tests could be conducted using a lower threshold for the AE system, so that the heavily attenuated events can be detected. Then the changes in propagation of GUWs could be used to correct for important event parameters, such as amplitude, energies, duration and wave velocities. Then a filter could be applied in post-processing to eliminate events that are still below the desired threshold. Ultimately, these changes and strategies would make notable steps forward in producing AE data that is more comparable, or even shows similar linear trends, to static testing AE results.

With regards to GUW monitoring, different waveforms should be explored to investigate more signal processing methods associated with current research, to gain deeper understandings of frequency-based characteristics of ultrasonic waves propagating through damaged composite laminates. As has been described previously, it would also be beneficial to apply amplification to the GUW signals for a better signal to noise ratio at higher levels of wave attenuation. It would also be beneficial to be able to set up the sensors so that they can apply the pitch-catch methodology in both directions for better, more robust evaluation of changes in propagation of the waves. Finally, combined load and damage based attenuation models do not appear to have been explored in current research for GUWs. Some researchers have explored load-based compensation strategies, but these models quickly fell apart when damage was introduced to the laminates tested

[42, 84-86]. This could be aided by the use of finite element wave propagation models to evaluate the propagation of waves through damage sites under different applied loads.

Modeling Strategies

As a continuation of the modeling portion of this research, the most important thing to address would be an effective layup independent model to apply the combined AE and GUW datasets to and make accurate predictions. This would require testing one or two additional layups to properly validate a model. The previous chapter outlined the possibility of applying the data to train an ANN with sufficient additional laminate properties, which could be considered as interaction parameters in the model. Validating the model would require removing the all the data from one layup for validation and training the model with data from the other layups tested. This validation procedure could be repeated, similar to the HOCV procedure applied in this research, to truly test the layup independent characteristics of the ANN. This would lead to a more universal tool for making predictions using the combined monitoring techniques. It should also aid in scaling up these techniques to substructures, where the piezoelectric sensors are not always going to be oriented in the loading direction of the test samples.

Also, other modeling techniques from current AE and GUW research could be applied to the datasets, in conjunction with other modeling strategies, which would likely aid in more accurate laminate property predictions. For example, AE damage classification clustering methods could be used as a form of pre-processing for the AE data to be applied to current and future predictive models. Finally, GUW time-frequency analyses for common blade failure modes, such as those applied to evaluate barely visible

impact damage and delamination length, could be used in conjunction with AE data for more effective evaluations and a more global SHM tool.

Ultimately, if all of the aspects described above, from testing techniques, to AE and GUW monitoring and modeling procedures can be explored in an effective manner, this research could pave the way for a new form of smart structural health monitoring system, which is capable of detecting, locating and evaluating specific damage areas and common wind turbine blade failure modes, while also assessing degrading laminate properties across the structure. A system built in such a way would truly allow for cost-based maintenance and repair strategies for owners and operators of wind farms. If done correctly, it could all be implemented into a cost-effective, standalone system, with minimal chances of false readings and errors.

FINAL CONCLUSIONS

Referring back to the original goals of this dissertation, the research presented has been able to gain a deeper understanding of current research and its limitations, with regards to applying novel sensing technologies, particularly AE and GUW techniques, for the SHM of large GFRP composite structures, such as wind turbine blades. AE and GUW on-line damage monitoring techniques were successfully applied simultaneously to the mechanical testing of GFRP composite laminates, which background research showed to be an area which has never been explored previously. For this research, the mechanical testing was in the form of increasing LUR static tensile and tension-tension fatigue testing, while measuring modulus changes of multiple GFRP laminates. Using data from the two techniques, changing laminate damage states were effectively assessed, particularly for static testing, using multiple analysis techniques. Analysis of the fatigue data revealed several unexpected testing errors, which previous AE and fatigue research appears to have overlooked. These issues and how they can be remedied and improved upon have been discussed in detail.

Furthermore, as well as applying AE and GUW techniques simultaneously, datasets from the two techniques have never been combined to make more accurate and effective laminate health predictions for SHM applications. By applying the static test datasets to multivariate linear regression models, results showed the power of combining the two techniques over using each one individually for predicting modulus degradation in GFRP laminates. When compared with separate AE and GUW predictive models, the combined models resulted in much improved modulus degradation predictions for all

four layups tested, with absolutely no knowledge of the test coupons' loading histories. Overall, the predictions from the validation procedures were excellent in all four cases tested.

Using the static datasets, other methods were applied in attempts to build the regression models into more universal and robust tools. Layup independent predictive models were constructed with limited success, but the prediction results were lacking when compared to constructing models on a layup-by-layup basis. This highlighted some of the limitations of the multivariate linear regression modeling techniques. PCA was applied to evaluate possible areas of instability within the original models and explore sources of variance within the datasets. Techniques were also applied in the form of PCRs in attempts to correct possible instabilities in the models and as an alternative, unbiased data reduction method. Despite what the underlying theory of the method suggested, these models did not result in improved predictions when compared to the original models, but would still be worth considering if more complex statistical models are to be applied to the data in the future. The presented PCR model results will certainly be useful if or when instability issues do arise in the predictive models.

Finally, modulus prediction models were constructed from the fatigue testing datasets. The three chosen layups were tested at a maximum stress level of 310 MPa and $R = 0.1$. Analysis of the acquired datasets had already revealed large amounts of statistical variation between tests, so the resulting models were unable to make accurate modulus degradation predictions in all cases. Despite this, they were able to make good predictions for the most severe modulus degradations and certainly showed potential for

making accurate predictions in the future. The fatigue datasets were also applied to the models constructed from the static test data. This method resulted in consistent under and over predictions, depending on the layup that was tested. These prediction errors were evaluated through comparison of the regression coefficients for the respective static and fatigue models. The differences in magnitude of the coefficients further verified the errors that had been observed during fatigue testing and the subsequent inspection of the datasets. It is firmly believed that if the fatigue testing and AE and GUW monitoring setups are refined and the appropriate procedures are taken to correct the acquired data, then the static models will be able to effectively and accurately predict modulus degradation in fatigue, with no prior knowledge of the laminate's loading history.

Overall, the concepts, techniques and results presented in this research have shown great promise and potential for combining AE and GUW on-line damage monitoring techniques for making more effective damage state evaluations and degrading property predictions for GFRP laminates. It has shown that the techniques can be easily combined into a single, standalone system with minimal additional complexity and cost.

As a final conclusion, this research has provided a solid baseline for combining multiple novel monitoring techniques into a single, cost-effective SHM system. This research can be continued with guidance from the future work presented in the previous chapter to develop a monitoring system that would be capable of making a notable shift towards cost-based maintenance strategies for wind turbine blades, which would reduce the probability of catastrophic failures and operational down time. Ultimately, this

research had aimed to provide steps towards making wind energy a greener and more economically viable for of renewable energy for future generations.

REFERENCES CITED

[1] T. Bosma. (2018). *Third Generation Wind Power*. Available: https://www.dnvgl.com/technology-innovation/broader-view/electrifying-the-future/third-generation-wind-power.html

[2] M. Hofmann and I. B. Sperstad, "Will 10 MW wind turbines bring down the operation and maintenance cost of offshore wind farms?," (in English), *Eera Deepwind' 2014, 11th Deep Sea Offshore Wind R&D Conference,* Proceedings Paper vol. 53, pp. 231-238, 2014.

[3] D. Chan and J. Mo, "Life cycle reliability and maintenance analyses of wind turbines," (in English), *1st International Conference on Energy and Power, Icep2016,* Proceedings Paper vol. 110, pp. 328-333, 2017.

[4] J. Nilsson, L. Bertling, and Ieee, "Maintenance management of wind power systems using Condition Monitoring Systems," (in English), *2007 Ieee Power Engineering Society General Meeting, Vols 1-10,* Proceedings Paper pp. 124-124, 2007.

[5] Z. G. Tian, T. D. Jin, and Ieee, "Maintenance of Wind Turbine Systems under Continuous Monitoring," (in English), *Annual Reliability and Maintainability Symposium (Rams), 2011 Proceedings,* Proceedings Paper p. 6, 2011.

[6] A. H. Nithin and P. Omenzetter, "Optimization of Monitoring and Inspections in the Life-cycle of Wind Turbines," in *Conference on Smart Materials and Nondestructive Evaluation for Energy Systems 2016*, Las Vegas, NV, 2016, vol. 9806, BELLINGHAM: Spie-Int Soc Optical Engineering, 2016.

[7] B. Griffiths. (2005). *Boeing sets pace for composite usage in large civil aircraft*. Available: https://www.compositesworld.com/articles/boeing-sets-pace-for-composite-usage-in-large-civil-aircraft

[8] U. S. D. o. Defense, *Polymer Matrix Composites - Guidelines for Characterization of Structural Materials* (Composite Materials Handbook). 2002.

[9] T. L. Anderson, *Fracture Mechanics: Fundamentals and Applications*, Third Edition ed. CRC Press, 2005.

[10] K. Reifsnider, "Fatigue behavior of composite materials," *International Journal of Fracture,* journal article vol. 16, no. 6, pp. 563-583, December 01 1980.

[11] T. P. Philippidis and A. P. Vassilopoulos, "Fatigue design allowables for GRP laminates based on stiffness degradation requirements," *Composites Science and Technology,* vol. 60, 2000.

[12] J. F. Mandell, D. D. Samborsky, D. A. Miller, P. Agastra, and A. T. Sears, "Analysis of SNL/MSU/DOE Fatigue Database Trends for Wind Turbine Blade Materials, 2010-2015," Sandia National Labs2016.

[13] V. A. Passipoularidis and T. P. Philippidis, "A study of factors affecting life prediction of composites under spectrum loading," *International Journal of Fatigue,* vol. 31, no. 3, pp. 408-417, Mar 2009.

[14] O. Krause, C. W. Kensche, R. P. L. Nijssen, T. P. Philippidis, and A. P. Vassilopoulos, "A benchmark on lifetime prediction of composite materials under fatigue," Stuttgart, 2003.

[15] T. P. Philippidis and A. P. Vassilopoulos, "Fatigue of composite laminates under off-axis loading," *International Journal of Fatigue,* vol. 21, 1991.

[16] T. P. Philippidis and A. P. Vassilopoulos, "Fatigue strength prediction under multiaxial stress," *Journal of Composite Materials,* vol. 33, no. 17, pp. 1578-1599, 1999.

[17] X. S. Sun, A. Haris, V. B. C. Tan, T. E. Tay, S. Narasimalu, and C. N. Della, "A multi-axial fatigue model for fiber-reinforced composite laminates based on Puck's criterion," *Journal of Composite Materials,* vol. 46, no. 4, 2011.

[18] T. P. Philippidis and A. P. Vassilopoulos, "Complex stress state effect on fatigue life of GRP laminates. Part I, experimental," *International Journal of Fatigue,* vol. 24, 2002.

[19] T. P. Philippidis and A. P. Vassilopoulos, "Complex stress state effect on fatigue life of GRP laminates. Part II, theoretical formulation," *International Journal of Fatigue,* vol. 24, 2002.

[20] E. N. Eliopoulos and T. P. Philippidis, "A progressive damage simulation algorithm for GFRP composites under cyclic loading. Part I: Material constitutive model," *Composites Science and Technology,* vol. 2011, no. 5, 2011.

[21] E. N. Eliopoulos and T. P. Philippidis, "A progressive damage simulation algorithm for GFRP composites under cyclic loading. Part II: FE implementation and model validation," *Composites Science and Technology,* vol. 71, no. 5, 2011.

[22] M. M. Shokrieh and L. B. Lessard, "Progressive fatigue damage modeling of composite materials, part I: Modeling," *Journal of Composite Materials,* vol. 34, no. 13, 2000.

[23] M. M. Shokrieh and L. B. Lessard, "Progressive fatigue damage modeling of composite materials, part II: Material characterization and model verification," *Journal of Composite Materials,* vol. 34, no. 13, 2000.

[24] M. M. Shokrieh and F. Taheri-Behrooz, "Progressive fatigue damage modeling of cross-ply laminates, part I: Modeling strategy," *Journal of Composite Materials,* vol. 44, 2009.

[25] F. Taheri-Behrooz, M. M. Shokrieh, and L. B. Lessard, "Progressive fatigue damage modeling of cross-ply laminates, part II: Experimental evaluation," *Journal of Composite Materials,* vol. 44, 2010.

[26] S. Sihn and S. W. Tsai, "Prediction of fatigue S-N curves of composite laminates by Super Mic-Mac," *Composites: Part A,* vol. 36, 2005.

[27] S. Sihn and J. W. Park, "MAE: An integrated design tool for failure and life prediction of composites," *Journal of Composite Materials,* vol. 42, 2008.

[28] M. Naderi and A. R. Maligno, "Finite element simulation of fatigue life prediction in carbon/epoxy laminates," *Journal of Composite Materials,* vol. 47, no. 4, 2012.

[29] C. Stens and P. Middendorf, "Computationally efficient modelling of the fatigue behaviour of composite materials," *International Journal of Fatigue,* vol. 80, 2015.

[30] M. M. Shokrieh and F. Taheri-Behrooz, "A unified fatigue life model based on energy method," *Composite Structures,* vol. 75, 2006.

[31] D. Vasiukov, S. Panier, and A. Hachemi, "Direct method for life prediction of fibre reinforced polymer composites based on kinematic of damage potential," *International Journal of Fatigue,* vol. 70, 2015.

[32] K. Momenkhani and S. Sarkani, "A new method for predicting the fatigue life of fiber-reinforced plastic laminates," *Journal of Composite Materials,* vol. 40, 2006.

[33] C. J. Keulen *et al.*, "Prediction of fatigue response of composite structures by monitoring the strain energy release rate with embedded fiber Bragg gratings," *Journal of Intelligent Material Systems and Structures,* vol. 27, no. 1, pp. 17-27, Jan 2016.

[34] C. R. Farrar and K. Worden, "An introduction to structural health monitoring," *Philosophical Transactions of the Royal Society a-Mathematical Physical and Engineering Sciences,* vol. 365, no. 1851, pp. 303-315, Feb 2007.

[35] N. K. Tsopelas, D. G. Papasalouros, A. A. Anastasopoulos, D. A. Kourousis, and J. W. Dong, "Acoustic Emission for Structural Integrity Assessment of Wind Turbine Blades," in *2nd World Conference on Acoustic Emission (WCAE)*, Shanghai, PEOPLES R CHINA, 2013, vol. 158, pp. 369-382, BERLIN: Springer-Verlag Berlin, 2015.

[36] T. Arsenault *et al.*, "Integrated Sensor System for Structural Integrity and Load Monitoring of Wind Turbines," *Structural Health Monitoring 2011: Condition-Based Maintenance and Intelligent Structures, Vol 2,* pp. 2647-2654, 2013.

[37] X. H. Lu and H. F. Zuo, "A New Technology of Aircraft Structural Health Monitoring," in *Advanced Manufacturing Technologies and Material Properties*, vol. 764, D. Zuo, H. Guo, J. Xu, T. Wang, G. Tang, and Z. Chen, Eds. (Advanced Materials Research, Stafa-Zurich: Trans Tech Publications Ltd, 2013, pp. 71-74.

[38] W. J. Staszewski, S. Mahzan, and R. Traynor, "Health monitoring of aerospace composite structures - Active and passive approach," (in English), *Composites Science and Technology,* Article; Proceedings Paper vol. 69, no. 11-12, pp. 1678-1685, Sep 2009.

[39] A. G. Beattie, "Acoustic emission non-destructive testing of structures using source location techniques," in "Sandia Report," Sandia National Laboratories, Albuquerque, NMSeptember 2013 2013.

[40] J. L. Tang, S. Soua, C. Mares, and T. H. Gan, "An experimental study of acoustic emission methodology for in service condition monitoring of wind turbine blades," (in English), *Renewable Energy,* Article vol. 99, pp. 170-179, Dec 2016.

[41] J. B. Ihn and F. K. Chang, "Pitch-catch active sensing methods in structural health monitoring for aircraft structures," (in English), *Structural Health Monitoring-an International Journal,* Article vol. 7, no. 1, pp. 5-19, Mar 2008.

[42] B. Eckstein, M. Bach, and M. M. Bonet, "Analysis of Loading Effects on Guided Ultrasonic Waves and Damage Assessment in a Full-scale CFRP Fuselage Structure," *Structural Health Monitoring 2015: System Reliability for Verification and Implementation, Vols. 1 and 2,* pp. 19-25, 2015.

[43] J. Martinez-Jequier, A. Gallego, E. Suarez, F. J. Juanes, and A. Valea, "Real-time damage mechanisms assessment in CFRP samples via acoustic emission Lamb wave modal analysis," (in English), *Composites Part B-Engineering,* Article vol. 68, pp. 317-326, Jan 2015.

[44] S. K. Al-Jumaili, K. M. Holford, M. J. Eaton, J. P. McCrory, M. R. Pearson, and R. Pullin, "Classification of acoustic emission data from buckling test of carbon fibre panel using unsupervised clustering techniques," *Structural Health Monitoring-an International Journal,* vol. 14, no. 3, pp. 241-251, May 2015.

[45] D. Tsamtsakis, M. Wevers, and P. De Meester, "Acoustic emission from CFRP laminates during fatigue loading," (in English), *Journal of Reinforced Plastics and Composites,* Article vol. 17, no. 13, pp. 1185-1201, 1998.

[46] R. Hill, R. Brooks, and D. Kaloedes, "Characterization of transverse failure in composites using acoustic emission," *Ultrasonics,* vol. 36, no. 1-5, pp. 517-523, Feb 1998.

[47] T. P. Philippidis and T. T. Assimakopoulou, "Strength degradation due to fatigue induced matrix cracking in FRP composites: An acoustic emission predictive model," *Composites Science and Technology,* vol. 68, 2008.

[48] T. P. Philippidis and T. T. Assimakopoulou, "Using acoustic emission to assess shear strength degradation in FRP composites due to constant and variable amplitude fatigue loading," *Composites Science and Technology,* vol. 68, 2007.

[49] S. Barre and M. L. Benzeggagh, "On the use of acoustic-emission to investigate damage mechanisms in glass-fiber-reinforced polypropylene," *Composites Science and Technology,* vol. 52, no. 3, pp. 369-376, 1994.

[50] R. P. Reed and J. C. Berg, "Measuring effective interfacial shear strength in carbon fiber bundle polymeric composites," *Journal of Adhesion Science and Technology,* vol. 20, no. 16, pp. 1929-1936, 2006.

[51] M. Bourchak, I. R. Farrow, I. P. Bond, C. W. Rowland, and F. Menan, "Acoustic emission energy as a fatigue damage parameter for CFRP composites," *International Journal of Fatigue,* vol. 29, 2007.

[52] P. F. Liu, J. Yang, and X. Q. Peng, "Delamination analysis of carbon fiber composites under hygrothermal environment using acoustic emission," (in English), *Journal of Composite Materials,* vol. 51, no. 11, pp. 1557-1571, May 2017.

[53] F. Nkrumah, M. J. Sundaresan, and L. Uitenham, "Life prediction and life extension of composite specimens using acoustic emission technique," *Smart Structures and Integrated Systems,* vol. 603, 2005.

[54] C. R. Ramirez-Jimenez, N. Papadakis, N. Reynolds, T. H. Gan, P. Purnell, and M. Pharaoh, "Identification of failure modes in glass/polypropylene composites by means of the primary frequency content of the acoustic emission event," *Composites Science and Technology,* vol. 64, no. 12, pp. 1819-1827, Sep 2004.

[55] Q. Q. Ni, K. Kurashiki, and M. Iwamoto, "AE technique for identification of micro failure modes in CFRP composites," *Materials Science Research International,* vol. 7, no. 1, pp. 67-71, Mar 2001.

[56] M. F. Schuster, "Characterization and energy analysis of fiber reinforced polymer composites by acoustic emission analysis," Masters, Mechanical and Industrial Engineering, Montana State University, Bozeman, MT, 2014.

[57] M. Diakhate, N. Tual, N. Carrere, and P. Davies, "Cracking and Durability of Composites in a Marine Environment," in *SEM Annual Conference and Exposition on Experimental and Applied Mechanics*, Orlando, FL, 2016, pp. 1-8, NEW YORK: Springer, 2017.

[58] J. P. McCrory *et al.*, "Damage classification in carbon fibre composites using acoustic emission: A comparison of three techniques," *Composites Part B-Engineering,* vol. 68, pp. 424-430, Jan 2015.

[59] V. Arumugam, C. S. Kumar, C. Santulli, E. Sarasini, and A. J. Stanley, "A Global Method for the Identification of Failure Modes in Fiberglass Using Acoustic Emission," *Journal of Testing and Evaluation,* vol. 39, no. 5, pp. 954-966, Sep 2011.

[60] M. Assarar, M. Bentahar, A. El Mahi, and R. El Guerjouma, "Monitoring of damage mechanisms in sandwich composite materials using acoustic emission," *International Journal of Damage Mechanics,* vol. 24, no. 6, pp. 787-804, Aug 2015.

[61] M. G. R. Sause, A. Gribov, A. R. Unwin, and S. Horn, "Pattern recognition approach to identify natural clusters of acoustic emission signals," *Pattern Recognition Letters,* vol. 33, no. 1, pp. 17-23, Jan 1 2012.

[62] C. S. Kumar, V. Arumugam, R. Sengottuvelusamy, S. Srinivasan, and H. N. Dhakal, "Failure strength prediction of glass/epoxy composite laminates from acoustic emission parameters using artificial neural network," *Applied Acoustics,* vol. 115, pp. 32-41, Jan 2017.

[63] C. Leone, G. Caprino, and I. de Iorio, "Interpreting acoustic emission signals by artificial neural networks to predict the residual strength of pre-fatigued GFRP laminates," *Composites Science and Technology,* vol. 66, 2006.

[64] D. Crivelli *et al.*, "Localisation and identification of fatigue matrix cracking and delamination in a carbon fibre panel by acoustic emission," *Composites Part B-Engineering,* vol. 74, pp. 1-12, Jun 1 2015.

[65] R. Gutkin, C. J. Green, S. Vangrattanachai, S. T. Pinho, P. Robinson, and P. T. Curtis, "On acoustic emission for failure investigation in CFRP: Pattern recognition and peak frequency analyses," (in English), *Mechanical Systems and Signal Processing,* Article vol. 25, no. 4, pp. 1393-1407, May 2011.

[66] N. F. Ince, C. S. Kao, M. Kaveh, A. Tewfik, J. F. Labuz, and Ieee, "Averaged acoustic emission events for accurate damage localization," in *IEEE International Conference on Acoustics, Speech and Signal Processing*, Taipei, TAIWAN, 2009, pp. 2201-+, NEW YORK: Ieee, 2009.

[67] M. A. Torres-Arredondo *et al.*, "Multivariate data-driven modelling and pattern recognition for damage detection and identification for acoustic emission and acousto-ultrasonics," (in English), *Smart Materials and Structures,* Article vol. 22, no. 10, p. 20, Oct 2013, Art. no. 105023.

[68] S. Huguet, N. Godin, R. Gaertner, L. Salmon, and D. Villard, "Use of acoustic emission to identify damage modes in glass fibre reinforced polyester," *Composites Science and Technology,* vol. 62, no. 10-11, pp. 1433-1444, 2002, Art. no. Pii s0266-3538(02)00087-8.

[69] A. R. Oskouei, M. Ahmadi, and M. Hajikhani, "Wavelet-based acoustic emission characterization of damage mechanism in composite materials under mode I delamination at different interfaces," *Express Polymer Letters,* vol. 3, no. 12, pp. 804-813, Dec 2009.

[70] M. Eaton, M. May, C. Featherston, K. Holford, S. Hallet, and R. Pullin, "Characterisation of Damage in Composite Structures using Acoustic Emission," in *9th International Conference on Damage Assessment of Structures (DAMAS)*, Univ Oxford, St Annes Coll, Oxford, ENGLAND, 2011, vol. 305, BRISTOL: Iop Publishing Ltd, 2011.

[71] D. D. Doan, E. Ramasso, V. Placet, S. Zhang, L. Boubakar, and N. Zerhouni, "An unsupervised pattern recognition approach for AE data originating from fatigue tests on polymer-composite materials," *Mechanical Systems and Signal Processing,* vol. 64-65, pp. 465-478, Dec 2015.

[72] G. Caprino, R. Teti, and I. de Iorio, "Predicting residual strength of pre-fatigued glass fibre-reinforced plastic laminates through acoustic emission monitoriing," *Composites: Part B,* vol. 36, 2005.

[73] M. R. Bhat, M. A. Majeed, and C. R. L. Murthy, "Characterization of fatigue damage in unidirectional GFRP composites through acoustic emission signal analysis," *NDT & E International,* vol. 27, no. 1, 1994.

[74] J. L. Rose, "A baseline and vision of ultrasonic guided wave inspection potential," (in English), *Journal of Pressure Vessel Technology-Transactions of the Asme,* Review vol. 124, no. 3, pp. 273-282, Aug 2002.

[75] Z. Q. Su, L. Ye, and Y. Lu, "Guided Lamb waves for identification of damage in composite structures: A review," *Journal of Sound and Vibration,* vol. 295, no. 3-5, pp. 753-780, Aug 2006.

[76] K. Worden, "Rayleigh and Lamb Waves - Basic Principles," *Strain,* vol. 37, no. 4, pp. 167-172, Nov 2001.

[77] W. B. Williams, T. E. Michaels, and J. E. Michaels, "Characterization of Guided Wave Velocity and Attenuation in Anisotropic Materials from Wavefield Measurements," in *42nd Annual Review of Progress in Quantitative Nondestructive Evaluation (QNDE)*, Minneapolis, MN, 2015, vol. 1706, 2016.

[78] B. Zhang *et al.*, "An integrated numerical model for investigating guided waves in impact-damaged composite laminates," (in English), *Composite Structures,* Article vol. 176, pp. 945-960, Sep 2017.

[79] F. Ricci, E. Monaco, L. Maio, N. D. Boffa, and A. K. Mal, "Guided waves in a stiffened composite laminate with a delamination," (in English), *Structural Health Monitoring-an International Journal,* Article vol. 15, no. 3, pp. 351-358, May 2016.

[80] D. Wang, L. Ye, Y. H. Tang, and Y. Lu, "Monitoring of delamination onset and growth during Mode I and Mode II interlaminar fracture tests using guided waves," (in English), *Composites Science and Technology,* Article vol. 72, no. 2, pp. 145-151, Jan 2012.

[81] M. He and T. Yang, "Non-Destructive Evaluation of the Bending-Fatigue Damage in Carbon-Fiber-Composite Laminates Based on Ultrasonic Wave Propagation," *Journal of Testing and Evaluation,* vol. 46, no. 2, pp. 647-655, Mar 2018.

[82] C. L. Wilson and F. K. Chang, "Monitoring fatigue-induced transverse matrix cracks in laminated composites using built-in acousto-ultrasonic techniques," *Structural Health Monitoring-an International Journal,* vol. 15, no. 3, pp. 335-350, May 2016.

[83] G. T. Mase, T. E. Wong, and G. C. Johnson, "ACOUSTOELASTICITY IN LAYERED COMPOSITES," *Journal of Engineering Materials and Technology-Transactions of the Asme,* vol. 112, no. 3, pp. 266-270, Jul 1990.

[84] C. L. Rosania, N. C. Bradley, M. A. Haile, and F.-K. Chang, "Effects of applied load on guided waves based structural health monitoring of CFRP composites," in *SAMPE*, Seattle, WA, 2017: SAMPE.

[85] S. Roy, P. Ladpli, and F. K. Chang, "Load monitoring and compensation strategies for guided-waves based structural health monitoring using piezoelectric transducers," *Journal of Sound and Vibration,* vol. 351, pp. 206-220, Sep 2015.

[86] S. Roy, P. Ladpli, K. Lonkar, and F. K. Chang, "Structural Damage Detection Using Ultrasonic Guided Waves Under Varying Ambient Temperature and Loading Environments," *Structural Health Monitoring 2013, Vols 1 and 2,* pp. 1284-1293, 2013.

[87] S. Chaki, W. Harizi, G. Bourse, and M. Ourak, "Multi-technique approach for non destructive diagnostic of structural composite materials using bulk ultrasonic waves, guided waves, acoustic emission and infrared thermography," (in English), *Composites Part a-Applied Science and Manufacturing,* Article vol. 78, pp. 358-361, Nov 2015.

[88] A. Nasrollahi, W. Deng, Z. Y. Ma, and P. Rizzo, "Multimodal structural health monitoring based on active and passive sensing," (in English), *Structural Health Monitoring-an International Journal,* Article vol. 17, no. 2, pp. 395-409, Mar 2018.

[89] W. Deng, A. Nasrollahi, P. Rizzo, and T. S. Li, "Merging Three NDT Techniques into a Single Structural Health Monitoring System," (in English), *Materials Evaluation,* Article vol. 75, no. 10, pp. 1299-1307, Oct 2017.

[90] G. James, D. Witten, T. Hastie, and R. Tibshirani, *An Introduction to Statistical Learning with Applications in R*, 6th ed. New York, NY: Springer, 2015.

[91] P. Murdy, D. A. Miller, M. M. Voth, D. D. Samborsky, and M. Q. Edens, "Comparing acoustic emission and guided ultrasonic wave data to evaluate damage states in glass fiber reinforced epoxy," presented at the CAMX, Dallas, TX, 2018.

[92] K. Pearson, "On Lines and Planes of Closest Fit to Systems of Points in Space," *Philosophical Magazine,* vol. 2, no. 11, pp. 559-572, 1901.

[93] Statsoft. *How to Reduce Number of variables and Detect Relationships, Principal Components and Factor Analysis*.

[94] L. V. Perez, "Principal Component Analysis to Address Multicollinearity," 2017.

[95] M. M. Voth, D. A. Miller, J. D. Nunemaker, P. Murdy, D. D. Samborsky, and D. S. Cairns, "Exploring frequency based analysis methods for damage identification in fiberglass-epoxy composite systems," in *SAMPE*, Seattle, WA, 2017, pp. 865-879.

[96] A. El-Sabbagh, L. Steuernagel, and G. Ziegmann, "Ultrasonic testing of natural fibre polymer composites: effect of fibre content, humidity, stress on sound speed and comparison to glass fibre polymer composites," (in English), *Polymer Bulletin,* Article vol. 70, no. 2, pp. 371-390, Feb 2013.

[97] W. H. Presser, M. D. Seale, and B. T. Smith, "Time-frequency analysis of the dispersion of Lamb modes," (in English), *Journal of the Acoustical Society of America,* Article vol. 105, no. 5, pp. 2669-2676, May 1999.

[98] K. Asamene, L. Hudson, and M. Sundaresan, "Influence of attenuation on acoustic emission signals in carbon fiber reinforced polymer panels," (in English), *Ultrasonics,* Article vol. 59, pp. 86-93, May 2015.

[99] K. Ono, "Review on Structural Health Evaluation with Acoustic Emission," (in English), *Applied Sciences-Basel,* Review vol. 8, no. 6, p. 33, Jun 2018, Art. no. 958.

[100] E. J. Babero, *Introduction to Composite Materials Design*. Boca Raton, FL: CRC Press, 2011.

[101] S. Mann and S. Haykin, "The chirplet transform: A generalization of Gabor's logon transform," in *Vision Interface '91*, 1991.

[102] M. R. Gorman, "Plate wave acoustic emission," *The Journal of the Acoustical Society of America,* vol. 90, no. 1, pp. 358-364, 1991.

[103] D. Aljets *et al.*, "CLASSIFICATION OF DELAMINATION AND MATRIX CRACKING IN CARBON FIBRE COMPOSITE PLATES USING ACOUSTIC EMISSION (AE)," *Proceedings of the Asme International Design Engineering Technical Conferences and Computers and Information in Engineering Conference, Vol 1, Pts a and B,* pp. 29-36, 2010 2010.

[104] L. Li, S. V. Lomov, and X. Yan, "Correlation of acoustic emission with optically observed damage in a glass/epoxy woven laminate under tensile loading," *Composite Structures,* vol. 123, pp. 45-53, May 2015.

[105] A. Katunin, K. Dragan, and M. Dziendzikowski, "Damage identification in aircraft composite structures: A case study using various non-destructive testing techniques," (in English), *Composite Structures,* Article vol. 127, pp. 1-9, Sep 2015.

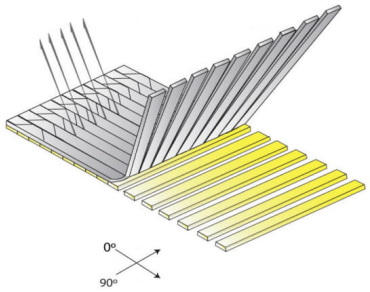
[106] T. Priess, M. G. R. Sause, D. Fischer, and P. Middendorf, "Detection of delamination onset in laser-cut carbon fiber transverse crack tension specimens using acoustic emission," *Journal of Composite Materials,* vol. 49, no. 21, pp. 2639-2647, Sep 2015.

APPENDICES

APPENDIX A

MATERIALS

VECTORPLY®
Performance Composite Reinforcements



E-LT 3800-10

Fiber Type: E-Glass
Architecture: 0º/90º Biaxial

Total Weight: 37.26 oz/sq.yd / 1263 g/sq.m

Roll Specifications			**Fiber Architecture Data**	
Roll Width:	Roll Weight:	Roll Length:	0 ° :	33.55 oz/sq.yd / 1138 g/sq.m
50 in. / 1270 mm	220 lbs / 100 kg	68 yd / 62 m	90 ° :	3.36 oz/sq.yd / 114 g/sq.m
			Chopped Mat:	N/A
			Polyester Stitching:	0.35 oz/sq.yd / 12 g/sq.m

* Packaging: Bag

Vectorply Corporation
3500 Lakewood Drive Phenix City, AL 36867
tel. 334-291-7704 fax. 334-291-7743

Disclaimer:

The customer is solely responsible for determining the performance and fitness for a particular use of any product produced by customer utilizing a reinforcement fabric or material produced or manufactured by Vectorply Corp. Specifications of reinforcements may change without notice.

REV: 3/13/2015

SPECIFICATION

561-18

Product: DB 810-E05

Rev.data:

Layers

Layer	Material 1								Area Weight [g/m²]
	Tex	Material Type							
+45°	600	E-Glass							401
0°	68	E-Glass							2
-45°	600	E-Glass							401
Stitch	7.6	Polyester/							5

Nominal area weight:	809
Theoretical width [mm]:	2540 mm
Average area weight:	809

Resin Compatibility *
UP, EP, VE

Processing and Controll

Binding/ Stitch Information	
Stitch type:	Chain
Stitch length:	3mm / Stitch
Space between needles:	5mm
Pilot yarn colour:	

Quality Assurance / Test		
Weight:	ISO 4605	
Loss of ignition:	ISO 1887	
Moisture content:	ISO 3344	

Logistics

Roll length:	65m
Roll width:	1270mm, ±10mm
Roll weight:	66.8kg
Roll direction:	Topp layer facing roll
Max fringe length:	= 10mm

Tube size:	76mm
Pallet size:	120x130
Rolls per pallet:	19
Stacking:	Pyramide

Devold AMT Acceptance Criteria

1. Area weight should be within ±3% of average value
2. Fibre orientation should be within ±2° of nominal value
3. There should be no dirt or oil spots
4. Gap wider than 5mm will be considered as a defect (measured 90° on roving)
5. No damage on outer roving or stitch yarn due to cutting edges

** UP:Polyester; EP: Epoxy; VE: Vinylester; ac: Anhydride cure*
*** CpE: Counts per ends, yarns/cm*

Comment

HEXION

Technical Data Sheet

Issued: August 2006

EPIKOTE™ Resin MGS™ RIMR 135 and EPIKURE™ Curing Agent MGS™ RIMH 134–RIMH 137

CHARACTERISTICS

Approval	German Lloyd
Application	Specially designed for infusion processes (RMT, SCRIMP/VARI); rotor blades for wind turbines, boat and shipbuilding, sports equipment
Operational Temperature	-60 °C up to +50 °C (-76 °F up to 122 °F) without heat treatment -60 °C bis +80 °C (-76 °F up to 176 °F) after heat treatment
Processing	At temperatures between 10 °C and 50 °C (50-122 °F) due to the very low mixing viscosity especially suited for infusion, injection and pultrusion
Features	Very low viscosity, excellent initial curing properties at room temperature, pot life from approx. 0,5 hours to approx. 4 hours, short curing times at high temperatures
Storage	Shelf life of 24 months in originally sealed containers

APPLICATION

Very low viscosity laminating resin system with different pot lives for processing of glass, carbon and aramide fibers. Due to its good mechanical properties, this system is suitable for the production of components featuring high static and dynamic loadability.

The range of pot lives is between approx. 0,5 hour and 3-4 hours. The parts can be worked and demoulded after curing at room temperature. Curing at higher temperatures (up to approx. 80-100 °C, 176-212 °F) is possible, depending on layer thickness and geometry of the parts to be manufactured. The curing times can be reduced to a few minutes by this.

Adding internal parting agents, such as zinc stearate, etc., has proven useful for pultrusion processes. Profiles with good surface qualities are obtained. Depending on profile geometry, mould temperatures in the range of 180-230 °C (356-446 °F) are possible, thus permitting high drawing speeds.

The mixing viscosity is very low, which is especially advantageous for infusion and injection processes. It may be lowered to approx. 150 mPas by heating the resin mass (see diagram). This means that even complicated molded parts with long flow paths can be easily infused. The temperature rise with hardener RIMH 137 remains very low up to a mold temperature of approx. 30 °C, so that even parts of greater thickness can be produced at elevated temperatures.

The infusion resin system does not contain any unreactive components. The raw materials used feature a

very low vapor pressure. This permits processing of the material under vacuum even at elevated temperatures (VARIM process). Compatibility problems are not to be expected in combination with UP gelcoats, various paints (e.g. PUR-based), etc. However, comprehensive tests are indispensable.

The relevant industrial safety regulations for the handling of epoxy resins and hardeners and our instructions for safe processing are to be observed.

The resin and hardeners can be stored for at least 24 months in their carefully sealed original containers. The resin and hardeners may crystallise at temperatures below +15 °C (59 °F). The crystallisation is visible as a clouding or solidification of the contents of the container. Before processing, the crystallisation must be removed by warming up. Slow warming up to approx. 50-60 °C (122-140 °F) in a water bath or oven and stirring or shaking will clarify the contents of the container without any loss of quality. Use only completely transparent products. Before warming up, open containers slightly to permit equalization of pressure. Caution during warm-up! Do not warm up over an open flame! While stirring up, use safety equipment (gloves, eyeglasses, respirator).

SPECIFICATIONS

		Infusion Resin RIM 135
Density	[g/cm³]	1,13 - 1,17
Viscosity	[mPas]	700 - 1.100
Epoxy equivalent	[g/equivalent]	166 - 185
Epoxy value	[equivalent/100g]	0,54 - 0,60
Refractory index		1,548- 1,552

		Hardener RIMH 134	Hardener RIMH 137
Density	[g/cm³]	0,93 - 1,00	0,93 - 0,98
Viscosity	[mPas]	10 - 80	10 - 50
Amine Value	[mg KOH/g]	550 - 700	400 - 600
Refractory index		1,4900 - 1,5000	1,460 - 1,463

Measuring conditions: measured at 25 °C / 77 °F

PROCESSING DETAILS

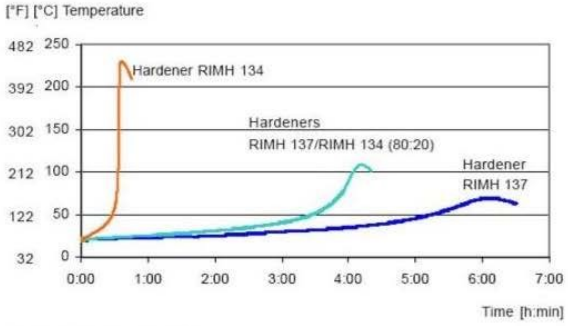
	Infusion Resin RIMR 135	Hardeners RIMH 134-137
Average EP - Value	0,56	-
Average amine equivalent	-	52

MIXING RATIOS

	Infusion Resin RIMR 135 : Hardener RIMH 134 – RIMH 137
Parts by weight	100 : 30 ± 2
Parts by volume	100 : 36 ± 2

The specified mixing ratios must be observed as exactly as possible. Adding more or less hardener will not effect a faster or slower reaction - but in incomplete curing which cannot be corrected in any way. Resin and hardener must be mixed very thoroughly. Mix until no clouding is visible in the mixing container. Pay special attention to the walls and the bottom of the mixing container.

TEMPERATURE DEVELOPMENT



Quantity: 100 g / 20 °C (77 °F)

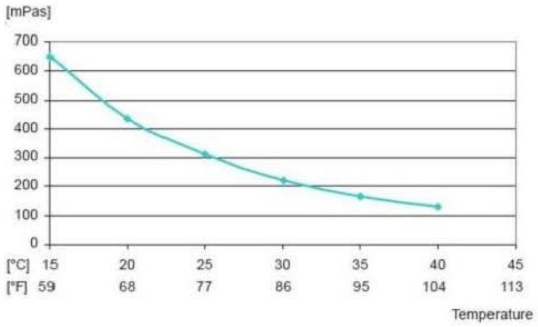
The optimum processing temperature is in the range between 20 °C and 25 °C (68-77 °F). Higher processing temperatures are possible, but will shorten pot life. A rise in temperature of 10 °C (50 °F) will halve the pot life. Water (for example very high humidity or contained in fillers) causes an acceleration of the resin/hardener reaction. Different temperatures and humidities during processing have no significant effect on the strength of the hardened product.

Do not mix large quantities - particularly of highly reactive systems - at elevated processing temperatures. The heat flow from the mixing container is very low, so the contents will heat up fast because of the dissipating reaction heat (exothermic resin-hardener reaction). This can result in temperatures of more than 200 °C (392 °F) in the mixing container, which may cause smoke-intensive burning of the resin mass.

VISCOSITY

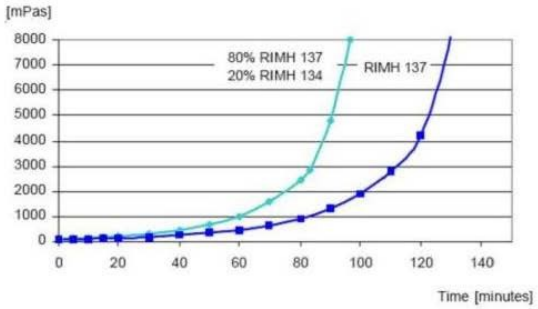
Viscosity of mixture at different temperatures

Infusion resin RIM 135 with mixture of Hardeners RIMH 137 (80 %) /RIMH 134 (20 %)



Viscosity development

Infusion resin RIM 135 with mixture of Hardeners RIMH 137 (80 %) /RIMH 134 (20 %) and Hardener RIMH 137



Measuring conditions:
Temperature: 40°C (104 °F); measuring gap 0,2 mm

MECHANICAL DATA

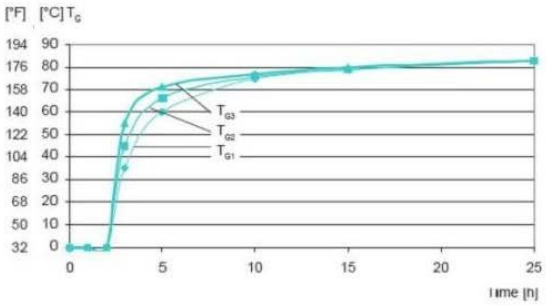
Mechanical Data of Neat Resin		
Density	[g/cm³]	1,18 - 1,20
Flexural strength	[N/mm²]	90 - 120
Modulus of elasticity	[kN/mm²]	2,7 - 3,2
Tensile strength	[N/mm²]	60 - 75
Compressive strength	[N/mm²]	80 - 90
Elongation of break	[%]	8 - 16
Impact strength	[KJ/m²]	70 - 80
Water absorption at 23 °C	24 h [%] 7 d [%]	0,10 - 0,20 0,20 - 0,50
Fatigue strength under reversed bending stresses acc. to DLR Brunsw.	10% 90%	exp. > 1 x 10^6 exp. > 2 x 10^6
Curing: 24 h at 23° C (74° F) + 15 h at 60° C (140° F), partly cured/full cure Typical data according to WL 5.3203 Parts 1 and 2 of the GERMAN AVIATION MATERIALS MANUAL		

Advice: Mechanical data are typical for the combination of laminating resin RIMR 135 with hardener RIMH 137. Data can differ in other applications.

T_G DEVELOPMENT

Development of glass transition temperature (T_G) at 60 °C

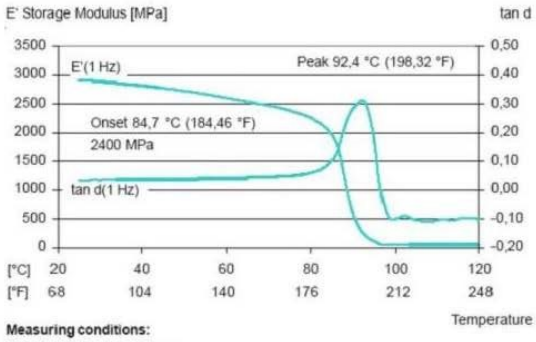
Infusion resin RIM 135 with mixture of Hardeners RIMH 137 (80 %) /RIMH 134 (20 %)



DMA

DMA Measuring after heat treatment

DMA-T_g (peak) tan delta
Infusion resin RIM 135 with mixture of Hardeners RIMH 137 (80 %) /RIMH 134 (20 %)



Measuring conditions:
Sample thickness: 2 mm
Heat rate: 2 K/min

APPENDIX B

TEST COUPONS

Plate Number	Coupon Number	Thickness (mm)	Width (mm)	Cross-Sectional Area (mm^2)	Test
4103	01	3.10	29.58	91.63	LUR w/ AE & GUWs
	02		29.06	90.04	LUR w/ AE & GUWs
	03		29.50	91.39	LUR w/ AE & GUWs
	04		29.63	91.80	LUR w/ AE & GUWs
	05		29.73	92.11	LUR w/ AE & GUWs
	06		29.47	91.31	LUR w/ AE & GUWs
	07		29.66	91.90	LUR w/ AE & GUWs
	08		29.37	91.00	LUR w/ AE & GUWs
	09		29.63	91.79	LUR w/ AE & GUWs
	10		29.76	92.20	LUR w/ AE & GUWs
	11		29.70	92.02	LUR w/ AE & GUWs
	12		29.63	91.80	Static w/ AE
	13		29.41	91.10	Static w/ AE
	14		29.45	91.23	LUR w/ AE & GUWs
	15		29.56	91.59	LUR w/ AE & GUWs
	16		29.42	91.14	Fatigue w/ AE
	17		29.68	91.95	Fatigue w/ AE
	18		29.41	91.11	Fatigue w/ AE
	19		29.54	91.51	Fatigue w/ AE
	20		29.31	90.81	Fatigue w/ AE
	21		29.56	91.59	Fatigue w/ AE
	22		29.71	92.04	Fatigue w/ AE
	23		29.70	92.00	Fatigue w/ AE
	24		29.14	90.28	Fatigue w/ AE
4107	01	3.11	29.92	93.00	Fatigue w/ AE
	02		29.66	92.20	Fatigue w/ AE & GUWs
	03		29.79	92.58	Fatigue w/ AE & GUWs
	04		29.63	92.10	Fatigue w/ AE & GUWs
	05		29.66	92.17	Fatigue w/ AE & GUWs
	06		29.70	92.31	Fatigue w/ AE & GUWs
	07		29.82	92.68	Fatigue w/ AE & GUWs
	08		29.75	92.46	Fatigue w/ AE & GUWs
	09		29.48	92.64	Fatigue w/ AE & GUWs
	10		29.47	91.60	Fatigue w/ AE & GUWs
	11		29.64	92.13	Static w/ AE
	12		29.65	92.16	Static w/ AE
4108	15	3.25	29.42	95.72	Static w/ AE
	16		29.52	96.04	Static w/ AE
	17		29.69	96.61	Static w/ AE
	18		29.71	96.66	Static w/ AE

Plate Number	Coupon Number	Thickness (mm)	Width (mm)	Cross-Sectional Area (mm^2)	Test
4109	01	3.18	29.69	94.48	LUR w/ AE & GUWs
	02		29.78	94.77	LUR w/ AE & GUWs
	03		29.67	94.42	LUR w/ AE & GUWs
	04		29.82	94.90	LUR w/ AE & GUWs
	05		29.75	94.67	LUR w/ AE & GUWs
	06		29.56	94.06	LUR w/ AE & GUWs
	07		29.77	94.74	LUR w/ AE & GUWs
	08		29.66	94.38	LUR w/ AE & GUWs
	09		29.73	94.61	LUR w/ AE & GUWs
	10		29.83	94.92	LUR w/ AE & GUWs
	11		29.77	94.73	LUR w/ AE & GUWs
	12		29.85	95.00	Static w/ AE
	13		29.83	94.94	Static w/ AE
	14		29.67	94.43	Static w/ AE
4110	01	3.21	29.94	96.07	LUR w/ AE & GUWs
	02		29.97	96.15	LUR w/ AE & GUWs
	03		29.76	95.49	LUR w/ AE & GUWs
	04		29.86	95.80	LUR w/ AE & GUWs
	05		30.01	96.29	Static w/ AE
	06		29.90	95.93	Static w/ AE
	07		29.99	96.22	Fatigue w/ AE
	08		30.05	96.41	Fatigue w/ AE
	09		29.83	95.70	Fatigue w/ AE
	10		30.04	96.40	Fatigue w/ AE
	11		30.03	96.35	Fatigue w/ AE
	12		29.97	96.15	Fatigue w/ AE & GUWs
	13		29.90	95.93	Fatigue w/ AE
	14		30.00	96.25	Fatigue w/ AE & GUWs
	15		29.94	96.07	Fatigue w/ AE & GUWs
	17		29.97	96.17	Fatigue w/ AE & GUWs
	19		30.00	96.27	Fatigue w/ AE & GUWs
4111	01	3.20	29.52	94.37	Static w/ AE
	02		29.49	94.30	Static w/ AE

Plate Number	Coupon Number	Thickness (mm)	Width (mm)	Cross-Sectional Area (mm^2)	Test
4113	01	3.18	29.79	94.84	LUR w/ AE & GUWs
	02		29.80	94.87	LUR w/ AE & GUWs
	03		29.79	94.84	LUR w/ AE & GUWs
	04		29.75	94.96	LUR w/ AE & GUWs
	05		29.77	94.75	LUR w/ AE & GUWs
	06		29.79	94.82	LUR w/ AE & GUWs
	07		29.81	94.89	LUR w/ AE & GUWs
	08		29.84	95.00	LUR w/ AE & GUWs
	09		29.88	95.10	LUR w/ AE & GUWs
	10		29.96	95.36	LUR w/ AE & GUWs
	11		29.97	95.41	LUR w/ AE & GUWs
	12		29.92	95.23	LUR w/ AE & GUWs
	13		29.88	95.10	Static w/ AE
	14		29.96	95.36	Static w/ AE
	15		29.84	95.00	LUR w/ AE & GUWs
	16		29.83	94.97	LUR w/ AE & GUWs
	17		29.91	95.20	Static w/ AE
	18		29.74	94.68	Static w/ AE
4114	25	3.24	30.49	98.91	Static w/ AE
	26		30.40	98.62	Static w/ AE
	27		30.47	98.86	Static w/ AE
	28		30.43	98.74	Static w/ AE

Plate Number	Coupon Number	Thickness (mm)	Width (mm)	Cross-Sectional Area (mm^2)	Test
4115	01	3.26	29.19	95.11	Static w/ AE
	02		29.31	95.51	Static w/ AE
	04		29.37	95.72	Static w/ AE
	05		29.45	95.96	Static w/ AE
4116	05	3.37	29.25	98.71	Static w/ AE
	06		29.24	98.65	Static w/ AE
	07		29.21	98.56	Static w/ AE
	14		29.05	98.03	Static w/ AE

Plate Number	Coupon Number	Thickness (mm)	Width (mm)	Cross-Sectional Area (mm^2)	Test
4120	01	4.29	29.98	128.57	Static w/ AE
	02		29.94	128.39	Static w/ AE
	03		29.95	128.45	Static w/ AE
	04		29.99	128.62	Static w/ AE
	05		29.90	128.22	Static w/ AE
	06		30.00	128.68	Static w/ AE
	07		30.04	128.82	Static w/ AE
	08		29.98	128.59	Static w/ AE
	09		29.94	128.41	Static w/ AE
	10		30.05	128.88	LUR w/ AE & GUWs
	11		29.99	128.62	LUR w/ AE & GUWs
	12		29.88	128.14	LUR w/ AE & GUWs
	13		29.96	128.49	LUR w/ AE & GUWs
	14		30.10	129.11	LUR w/ AE & GUWs
	15		29.93	128.38	LUR w/ AE & GUWs
	16		30.04	128.82	LUR w/ AE & GUWs
	17		30.01	128.72	LUR w/ AE & GUWs
	18		29.99	128.61	LUR w/ AE & GUWs
	19		29.94	128.42	LUR w/ AE & GUWs
	20		30.03	128.79	Static w/ AE
	21		29.93	128.38	Fatigue w/ AE
	22		29.98	128.59	Fatigue w/ AE
	23		29.93	128.37	Fatigue w/ AE
	24		29.94	128.39	Fatigue w/ AE
	25		29.98	128.59	Fatigue w/ AE
	26		30.02	128.74	Fatigue w/ AE
4121	01	4.37	32.50	142.16	Fatigue w/ AE & GUWs
	02		32.35	141.49	Fatigue w/ AE & GUWs
	03		32.41	141.74	Fatigue w/ AE & GUWs
	04		32.29	141.24	Fatigue w/ AE & GUWs
	05		32.28	141.20	Fatigue w/ AE & GUWs
	06		32.33	141.42	Fatigue w/ AE
	07		32.34	141.43	Static w/ AE
	08		32.30	141.27	Static w/ AE

APPENDIX C

AE SYSTEM INFORMATION

MISTRAS A World of NDT Solutions | Products & Systems Division

Product Bulletin

USB Acoustic Emission (AE) Node

Easy Laptop & PC Connection and Low Cost Acoustic Emission System

USB AE Node

The USB AE Node is a single channel Acoustic Emission (AE) Digital Signal Processor with full AE hit and time based features, including waveforms. Through the USB Connector, the AE Node is easily interfaced to a Notebook or PC running Windows XP™ or Vista™ and Physical Acoustics Corporation (PAC) well known AEwin™ or AEwin Lite™. Up to 4 AE Nodes can be controlled by one Notebook or PC.

The AE Node can accept single ended or differential sensors amplified by an internal low noise preamplifier. Additionally, PK Series low power integral preamp sensors can be used for long distance connections.



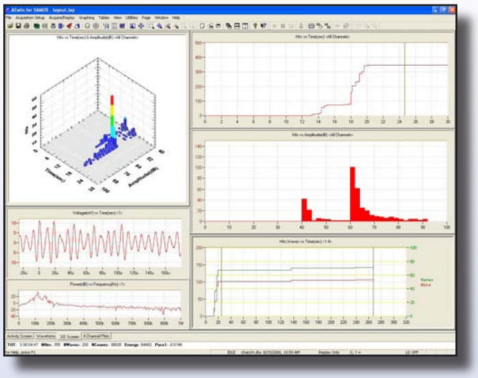
"AEwin for USB" AE NODE Software

Extracted Hit Features:

Time of 1st Threshold Crossing
Time to Peak, Peak Amplitude, Envelope Strength,
Duration Rise Time, Counts, True Energy
RMS, ASL
Parametrics (1-2)

Time Based Features

ASL, RMS, Parametrics (1-4)
Peak Amplitude, Crest Factor, Energy rate



Features & Benefits

- Powered and operated through USB Port
- Rugged surface mount (SMT) construction
- High performance AE at a low cost
- 1kHz to 1MHz bandwidth
- Selectable analog filters and programmable digital filter
- Waveform and Location Options

Specifications

AE Input:	1 Channel per USB node (4 nodes per system)
Frequency Response:	1.0 kHz to 1.0 MHz
AE Digitizing:	16 bit, 20 MSPS ADCs
Parametric Inputs:	CH 1, +/- 10V, 16 bits CH 2-4, 0-10V, 16 bits
OS:	Windows XP or Vista
Case Size:	L5.25" x W3.25" x H1.25" (133 x 83 x 32mm)
Weight:	0.5 lbs. (0.23kg)
Power Requirements:	USB Powered (5V) < 100 mA when running
Power Consumption:	< 0.5 watt

For additional information, please contact:
Physical Acoustics at 609-716-4000 or
email: sales.systems@mistrasgroup.com

195 Clarksville Road, Princeton Junction, NJ 08550 USA
Phone: (609) 716-4000 • Fax: (609) 716-0706
Email: sales.systems@mistrasgroup.com • www.mistrasgroup.com

CE ISO 9001

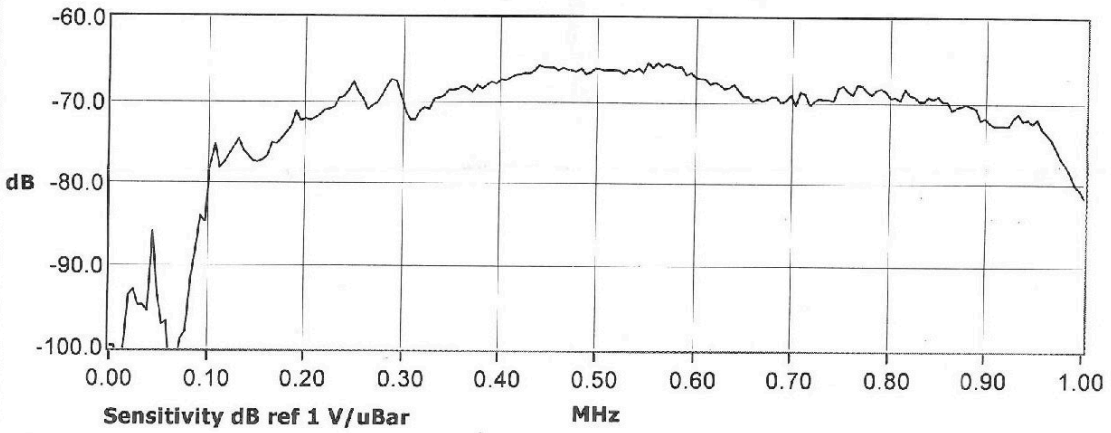
Copyright © 2009 MISTRAS Group Inc. #325-08 Specifications subject to change without notice.

PHYSICAL ACOUSTICS CORPORATION
A MISTRAS Holdings Company

AE SENSOR CALIBRATION CERTIFICATE

Sensor Name: WSA
Sensor S/N: AF85
Comment:

Max. Value (dB): -65.32
Peak Freq.(kHz): 561.52
Test Date: 7/27/2015
Tested By: J.G



PAC Certifies that this sensor meets all performance, environmental and physical standards established in applicable PAC specifications. Calibration methodology based on ASTM standard E976- "Guide for Determining the Reproducibility of AE Sensor Response."

PHYSICAL ACOUSTICS CORPORATION

A MISTRAS Holdings Company

AE SENSOR CALIBRATION CERTIFICATE

Sensor Name: WD

Sensor S/N: FV83

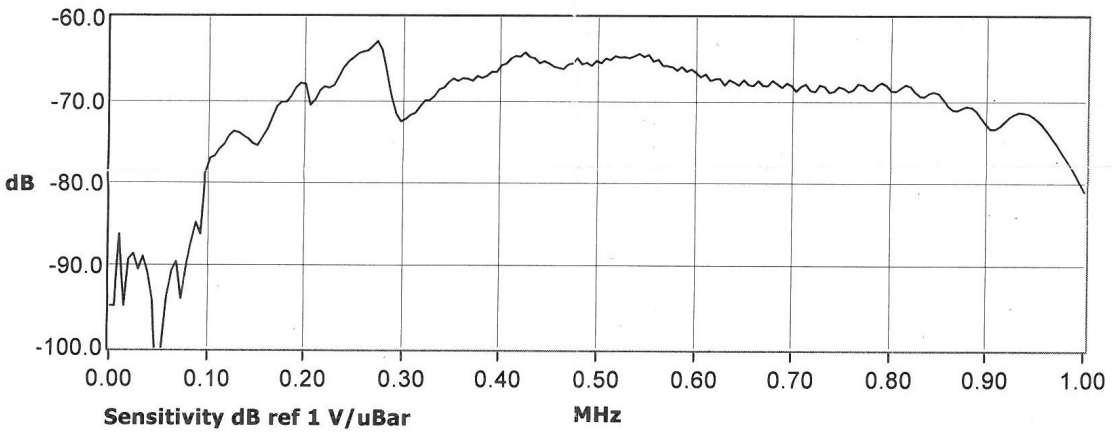
Comment: 1 METER CABLE

Max. Value (dB): -62.87

Peak Freq.(kHz): 273.44

Test Date: 1/18/2016

Tested By: N.M.

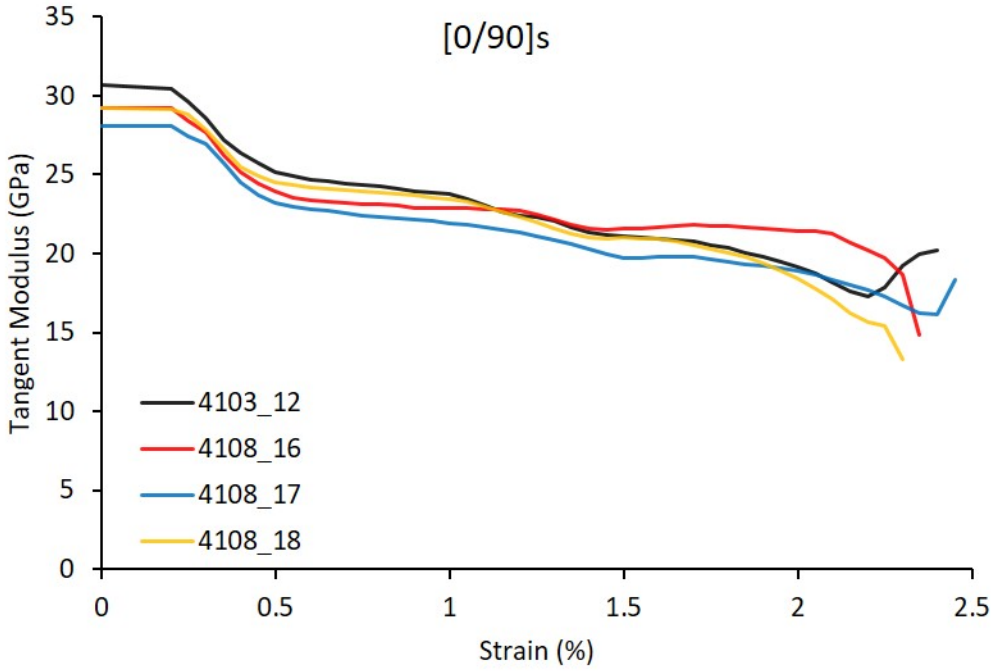


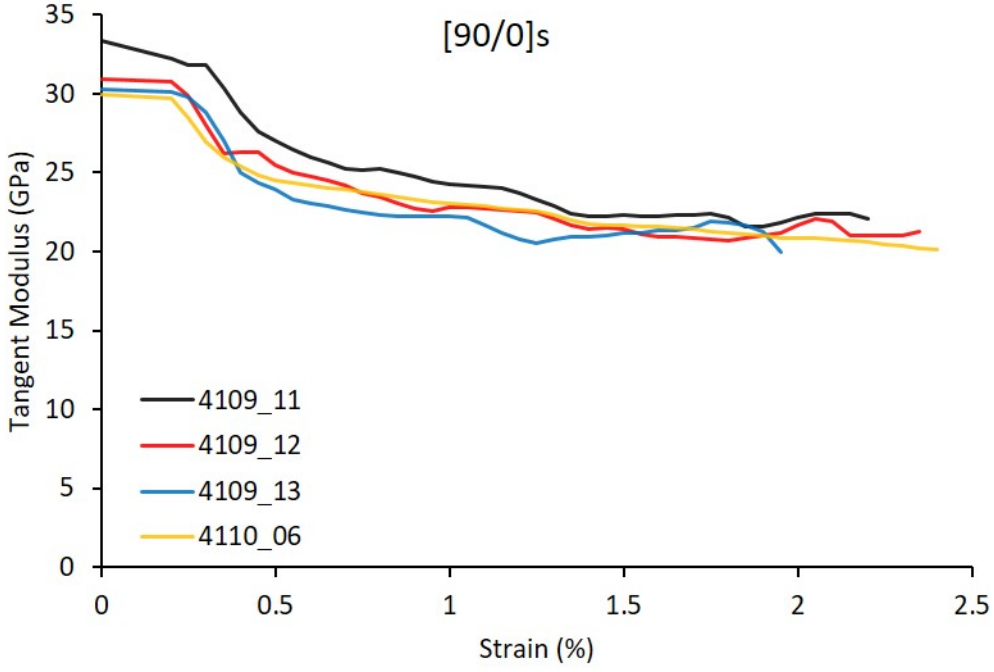
PAC Certifies that this sensor meets all performance, environmental and physical standards established in applicable PAC specifications. Calibration methodology based on ASTM standard E976- "Guide for Determining the Reproducibility of AE Sensor Response."

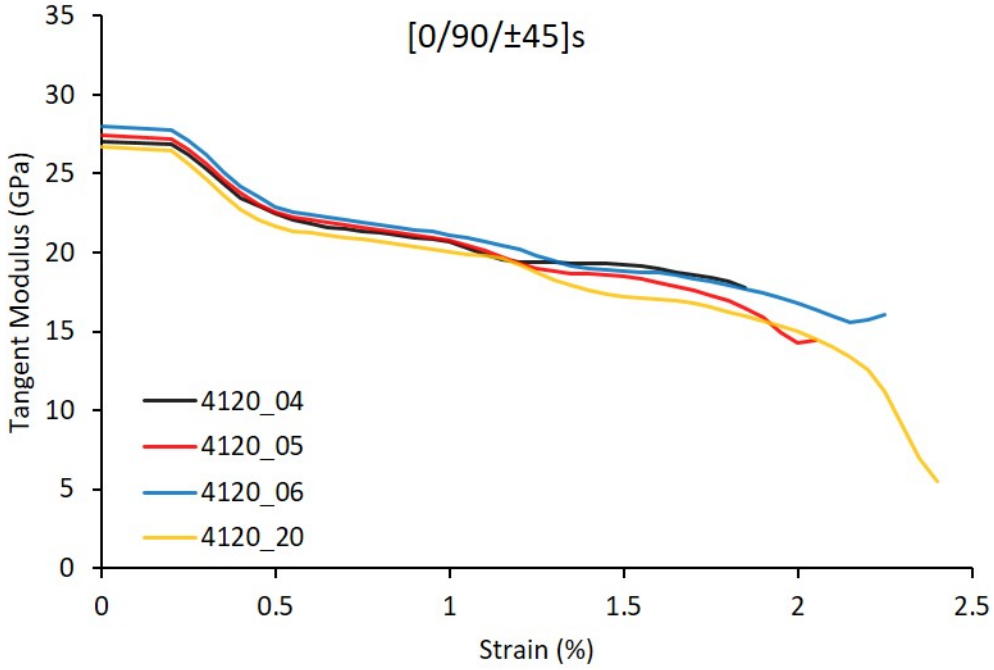
APPENDIX D

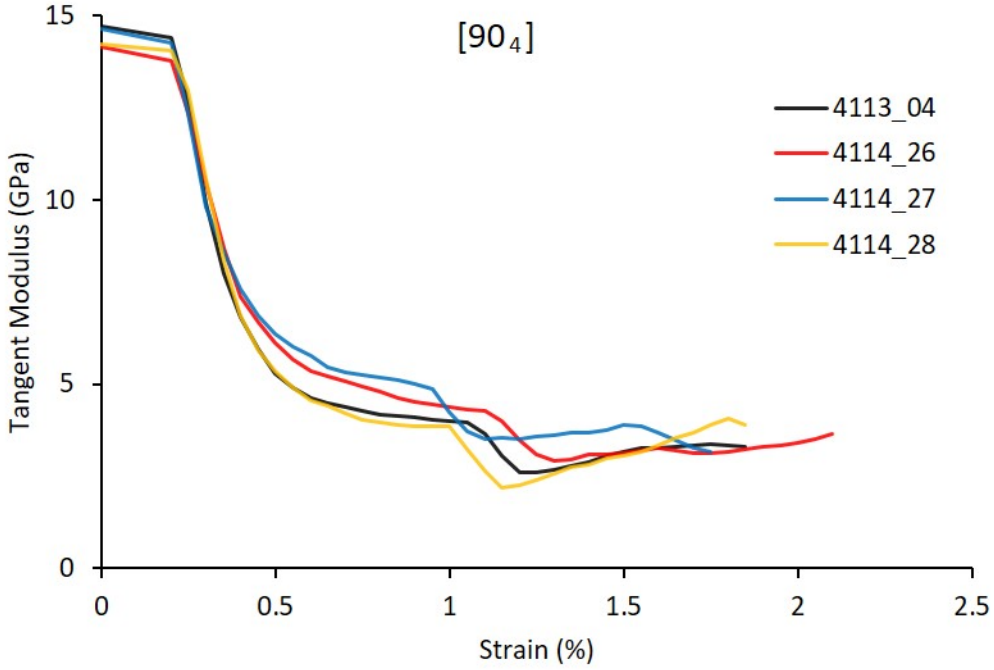
ADDITIONAL STATIC TEST DATA

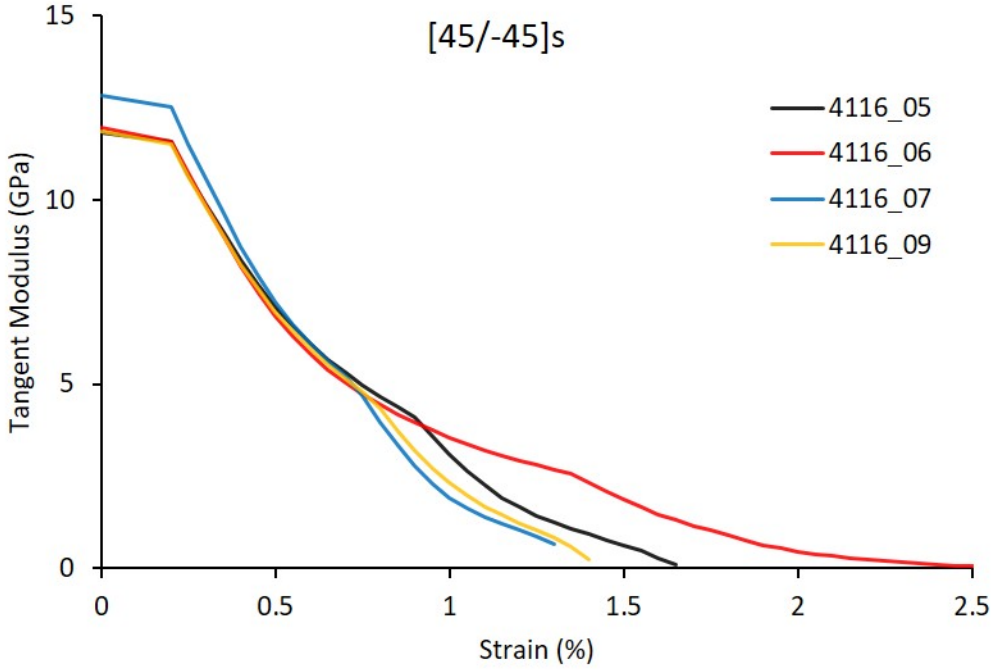
Tangent Modulus Plots



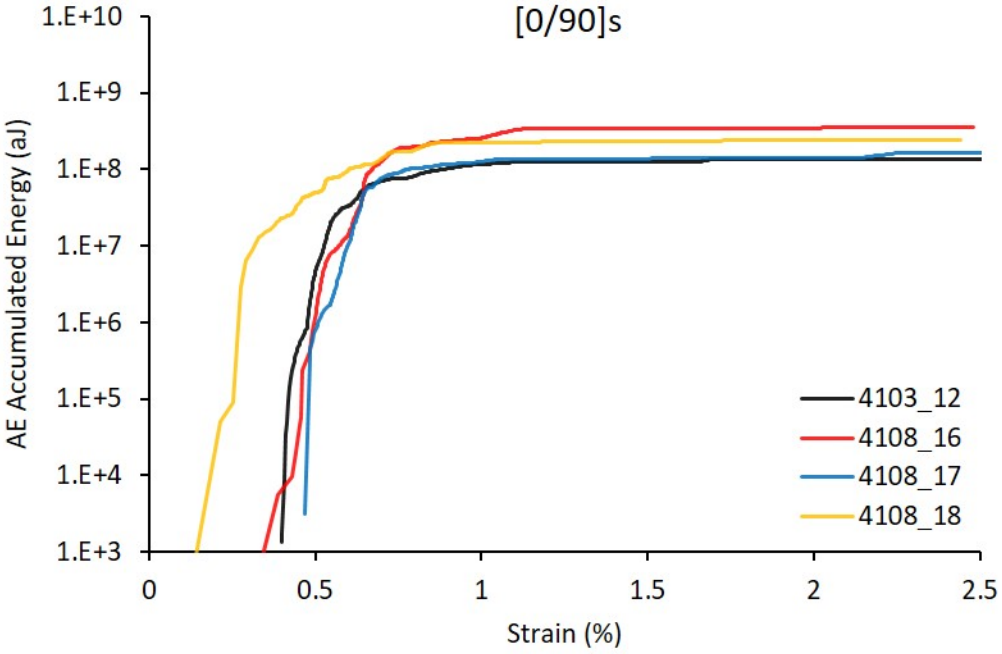


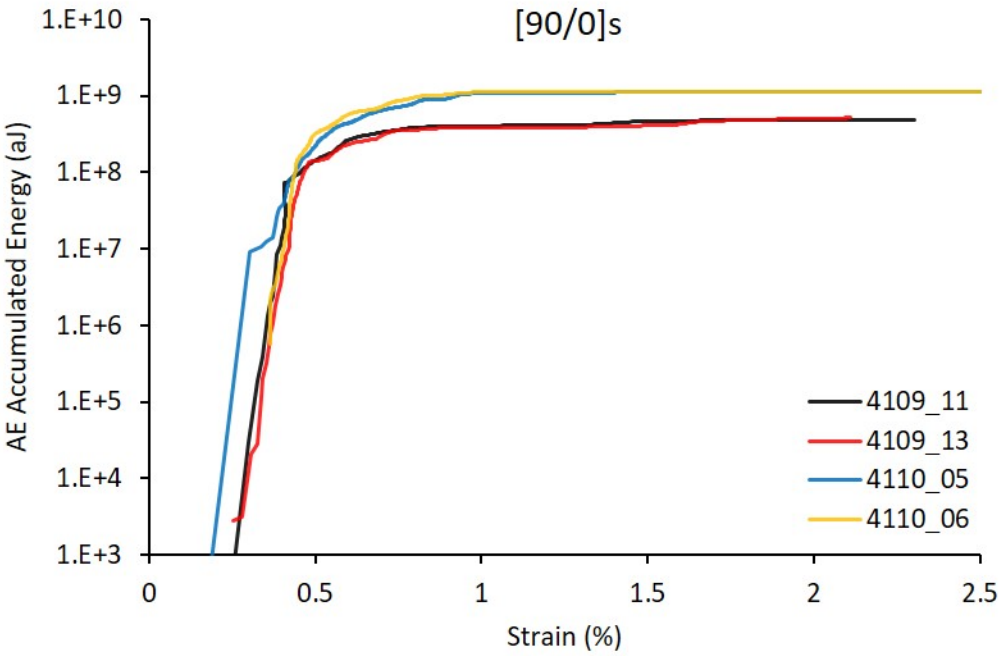

[0/90/±45]s
Tangent Modulus (GPa)
Strain (%)
4120_04
4120_05
4120_06
4120_20
0
5
10
15
20
25
30
35
0
0.5
1
1.5
2
2.5

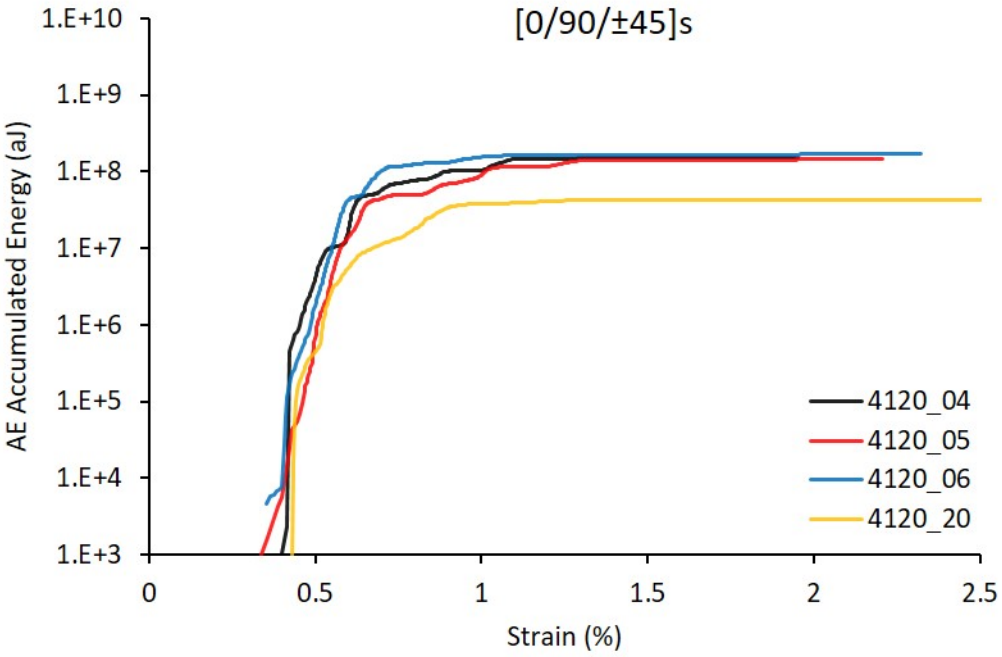

[90 4]
Tangent Modulus (GPa)
Strain (%)
4113_04
4114_26
4114_27
4114_28
0
5
10
15
0
0.5
1
1.5
2
2.5

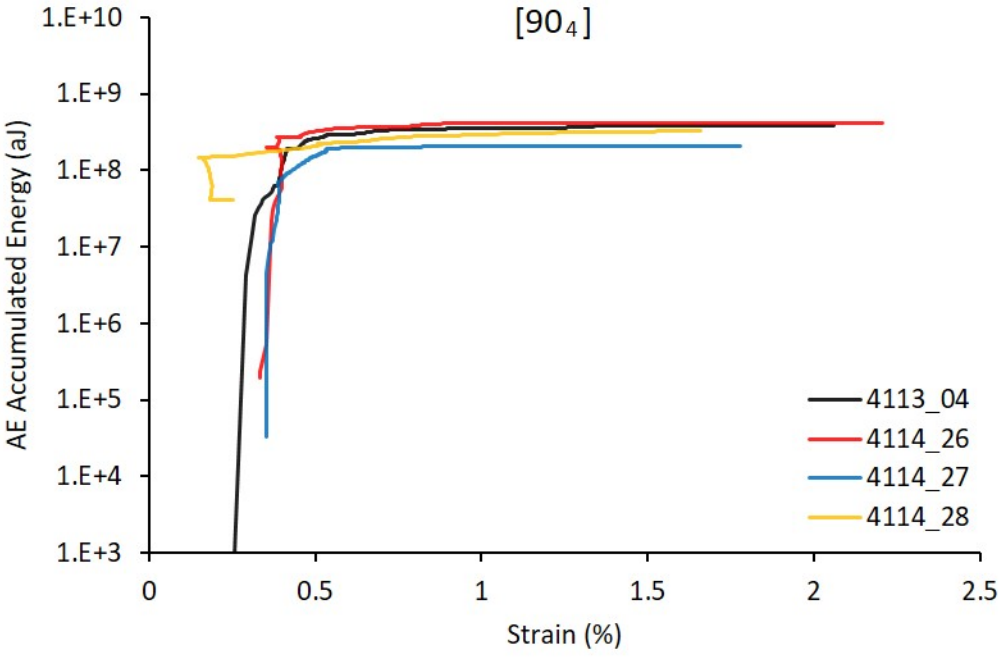

[45/-45]s
Tangent Modulus (GPa)
Strain (%)
0
5
10
15
0
0.5
1
1.5
2
2.5
4116_05
4116_06
4116_07
4116_09

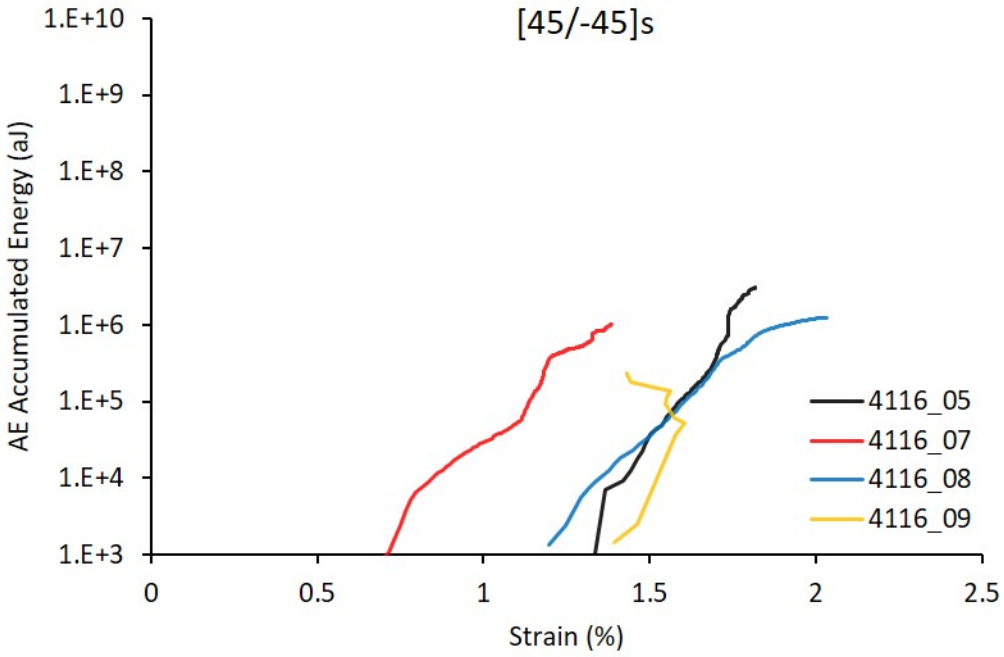
AE Accumulated Energy Plots



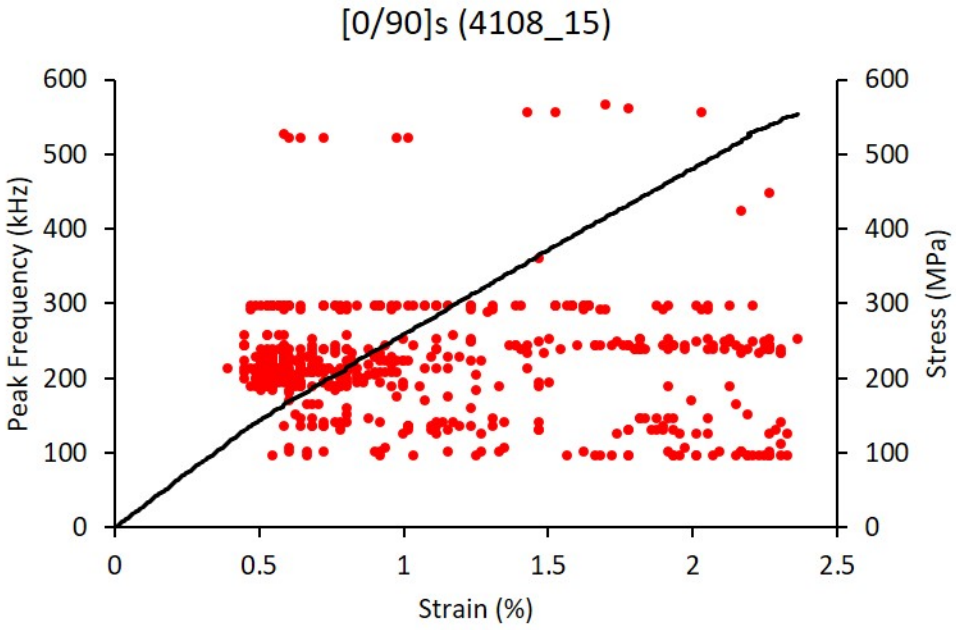


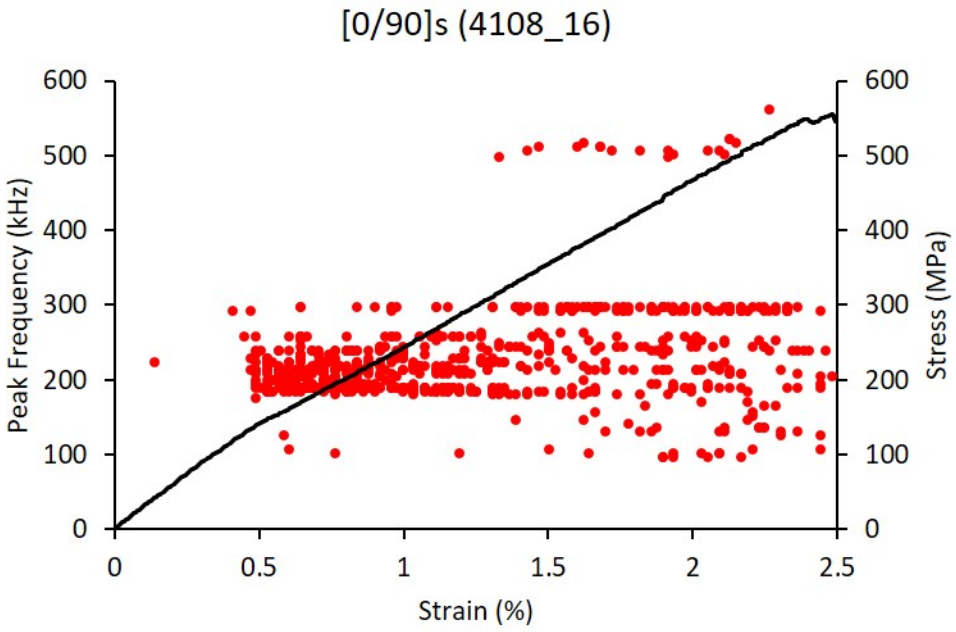

[0/90/±45]s
AE Accumulated Energy (aJ)
1.E+10
1.E+9
1.E+8
1.E+7
1.E+6
1.E+5
1.E+4
1.E+3
0
0.5
1
1.5
2
2.5
Strain (%)
4120_04
4120_05
4120_06
4120_20

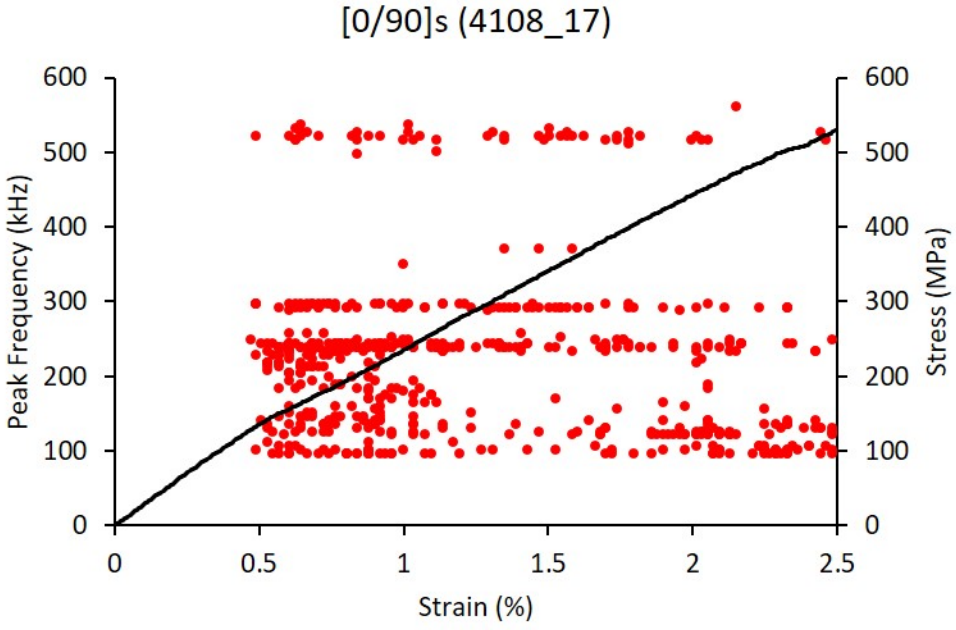

[90$_4$]
AE Accumulated Energy (aJ)
1.E+10
1.E+9
1.E+8
1.E+7
1.E+6
1.E+5
1.E+4
1.E+3
0
0.5
1
1.5
2
2.5
Strain (%)
4113_04
4114_26
4114_27
4114_28

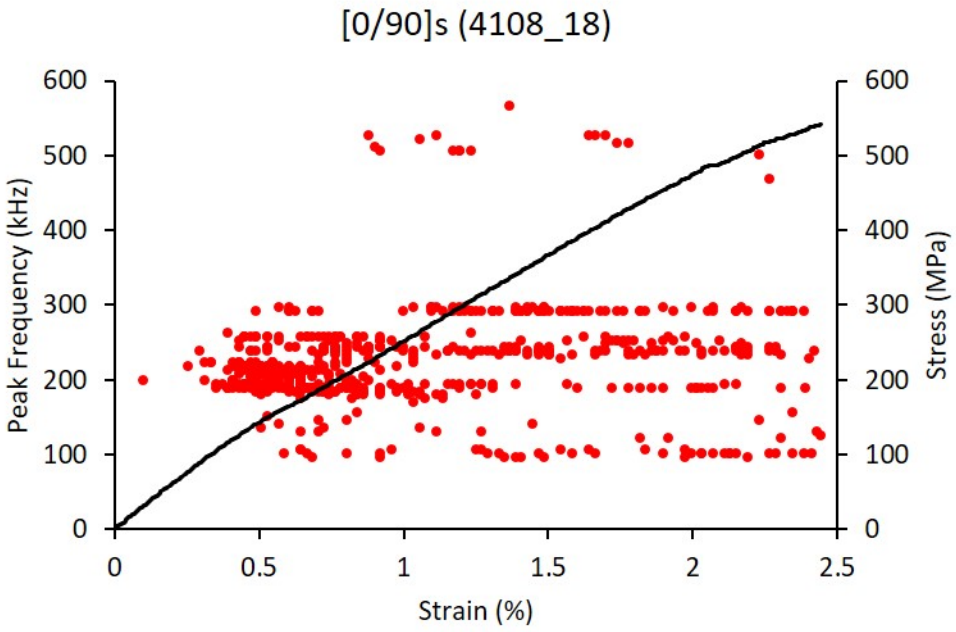


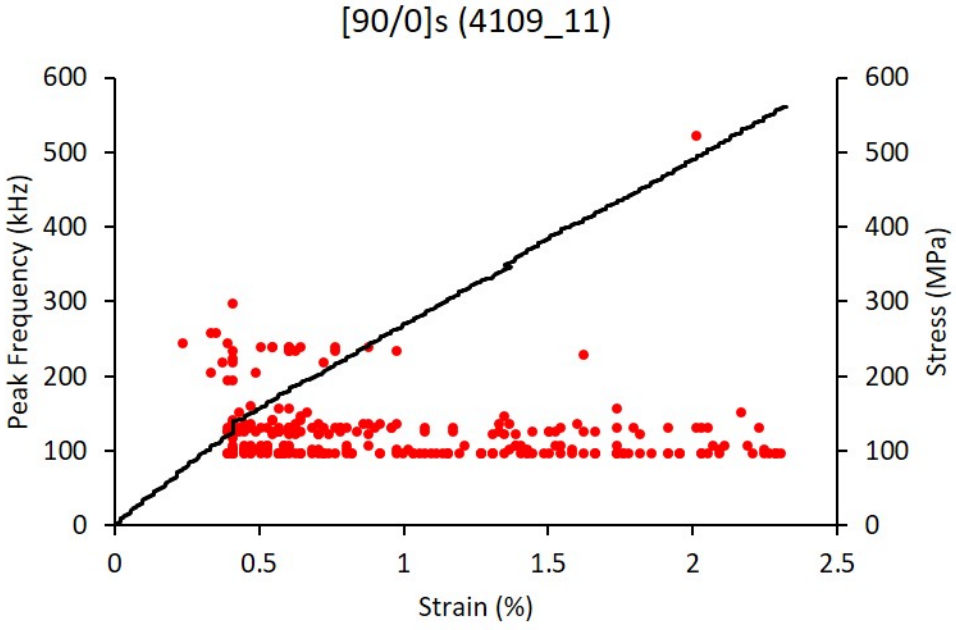
AE Peak Frequency Plots

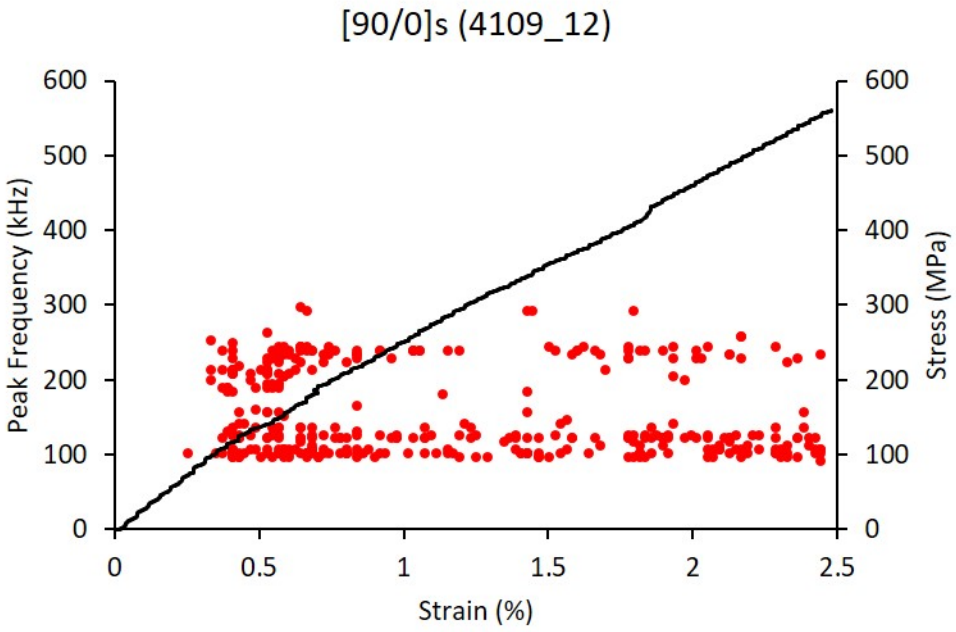


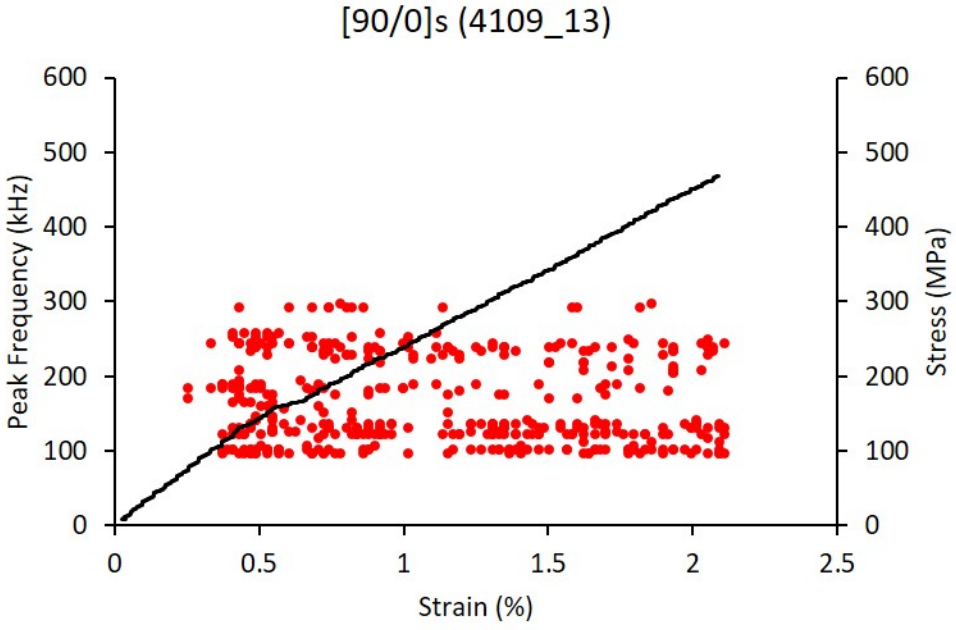

[0/90]s (4108_16)
Peak Frequency (kHz)
Stress (MPa)
Strain (%)
0
100
200
300
400
500
600
0
0.5
1
1.5
2
2.5

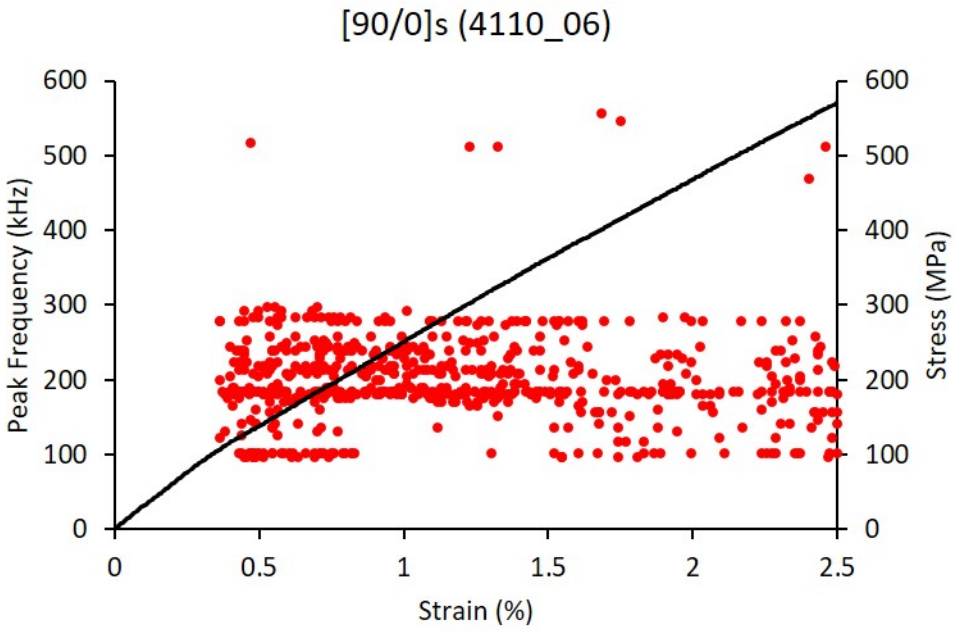

[0/90]s (4108_17)
Peak Frequency (kHz)
Stress (MPa)
Strain (%)
0
100
200
300
400
500
600
0
0.5
1
1.5
2
2.5

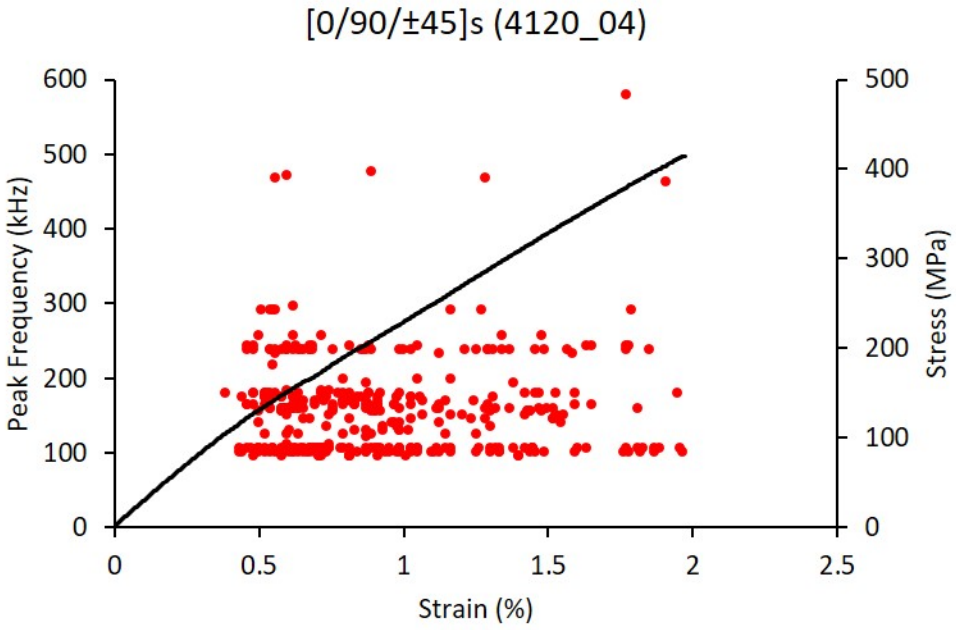

[0/90]s (4108_18)
Peak Frequency (kHz)
Stress (MPa)
Strain (%)
0
100
200
300
400
500
600
0
0.5
1
1.5
2
2.5

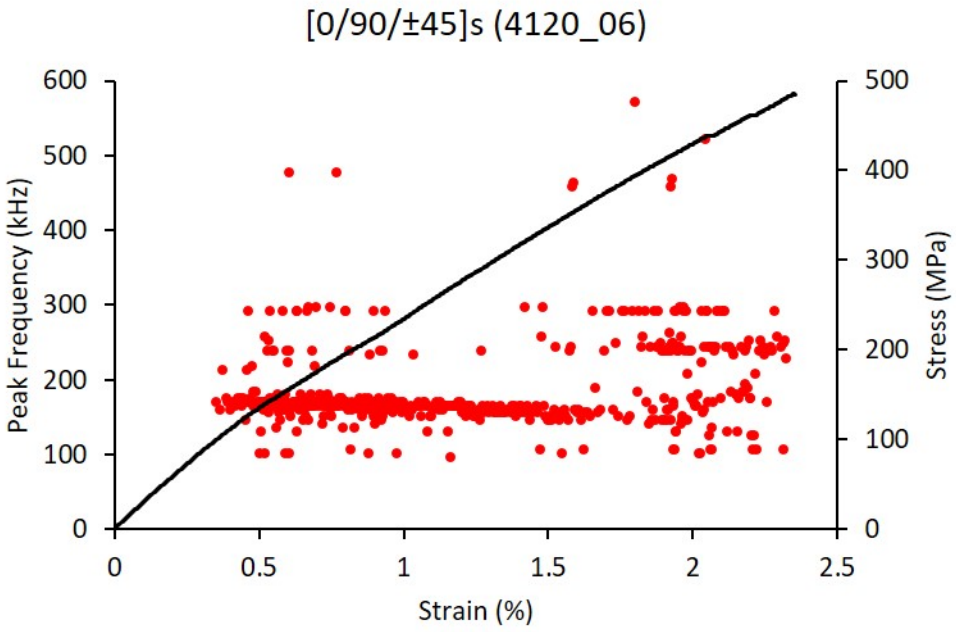

[90/0]s (4109_11)
Peak Frequency (kHz)
Stress (MPa)
Strain (%)
0
100
200
300
400
500
600
0
0.5
1
1.5
2
2.5

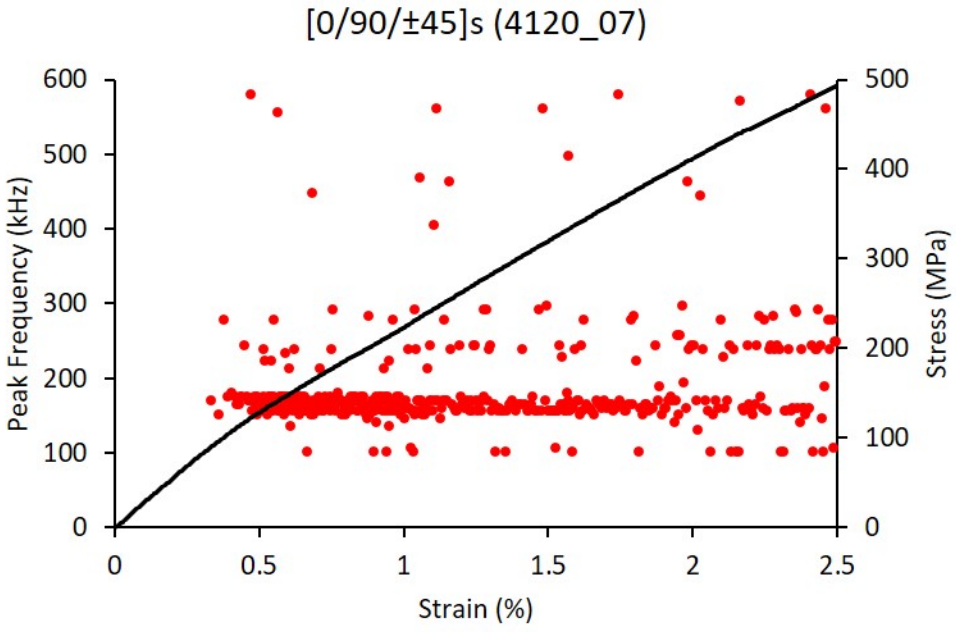

[90/0]s (4109_12)
Peak Frequency (kHz)
Stress (MPa)
Strain (%)
0
100
200
300
400
500
600
0
0.5
1
1.5
2
2.5

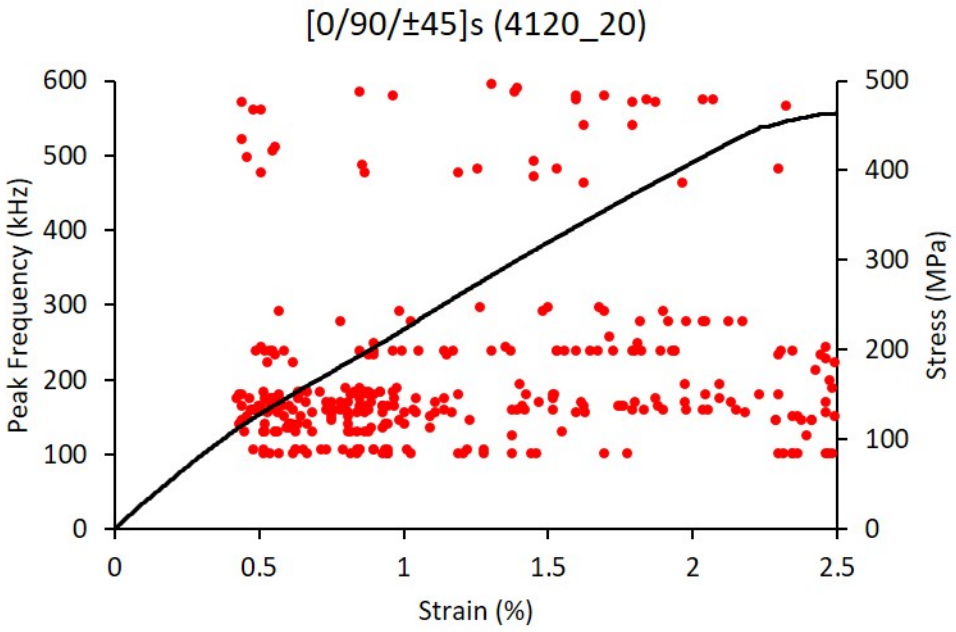

[90/0]s (4109_13)
Peak Frequency (kHz)
Stress (MPa)
Strain (%)
0
100
200
300
400
500
600
0
0.5
1
1.5
2
2.5

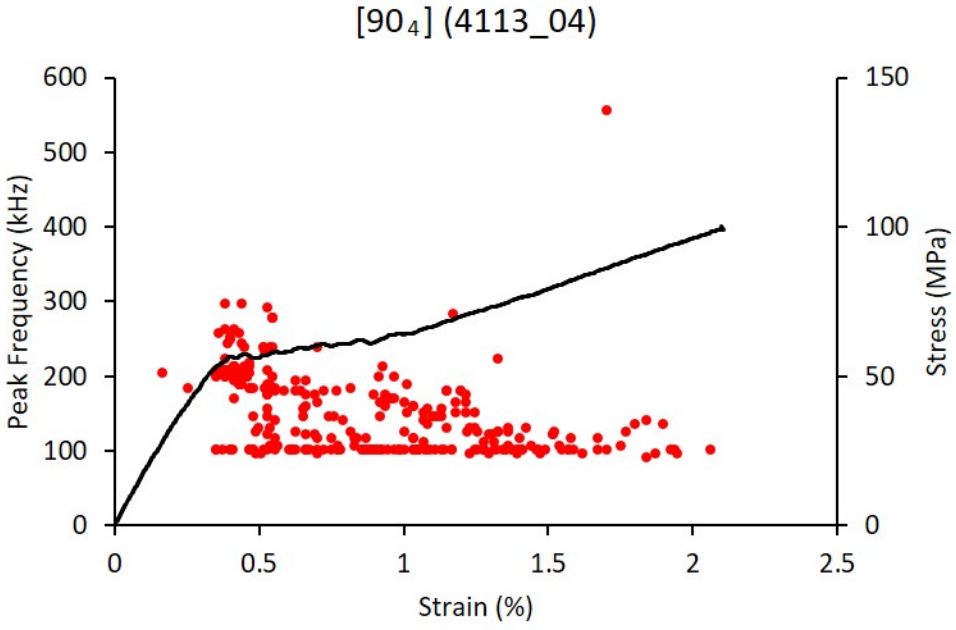

[90/0]s (4110_06)
Peak Frequency (kHz)
Stress (MPa)
Strain (%)
0
100
200
300
400
500
600
0
0.5
1
1.5
2
2.5

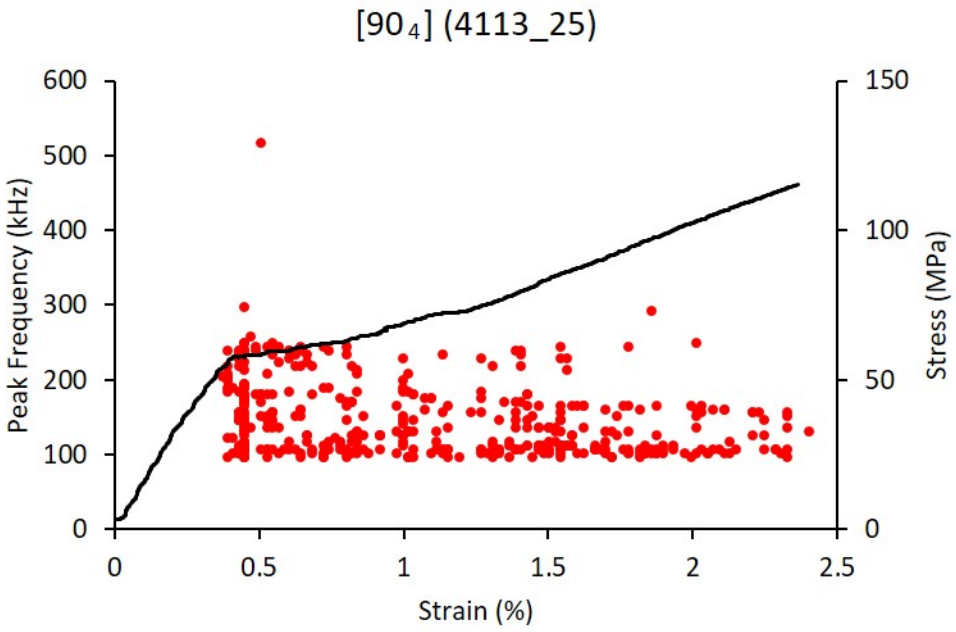

[0/90/±45]s (4120_04)
Peak Frequency (kHz)
Stress (MPa)
Strain (%)
0
100
200
300
400
500
600
0
0.5
1
1.5
2
2.5

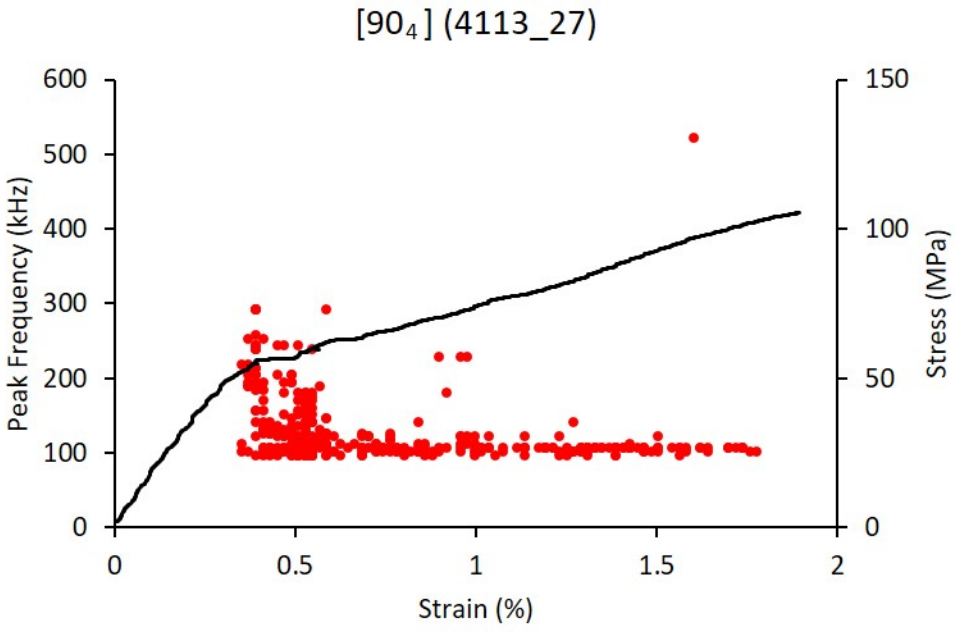

[0/90/±45]s (4120_06)
Peak Frequency (kHz)
Stress (MPa)
Strain (%)
0
100
200
300
400
500
600
0
0.5
1
1.5
2
2.5

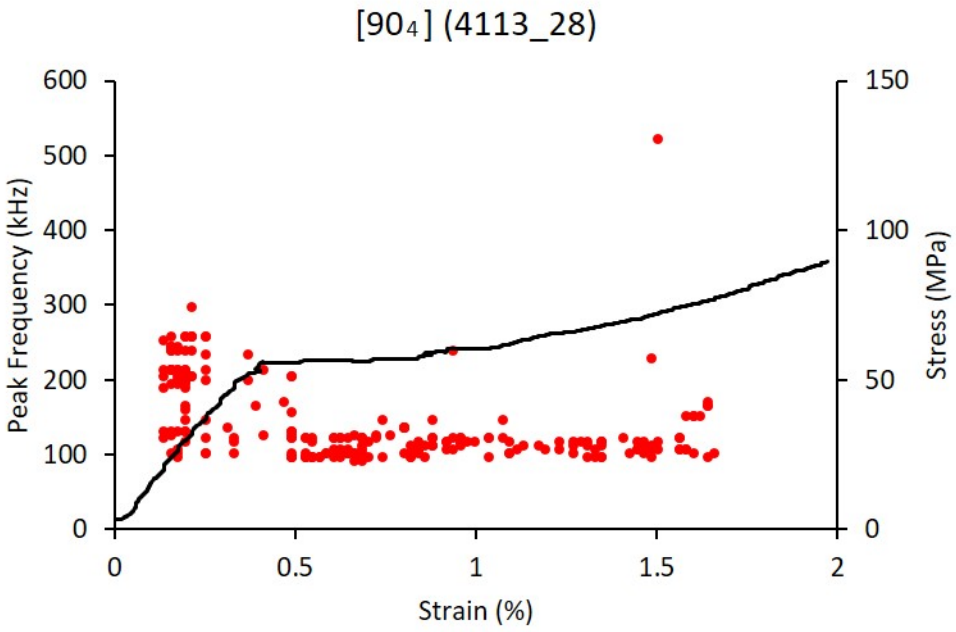

[0/90/±45]s (4120_07)
Peak Frequency (kHz)
Stress (MPa)
Strain (%)
0
100
200
300
400
500
600
0
0.5
1
1.5
2
2.5

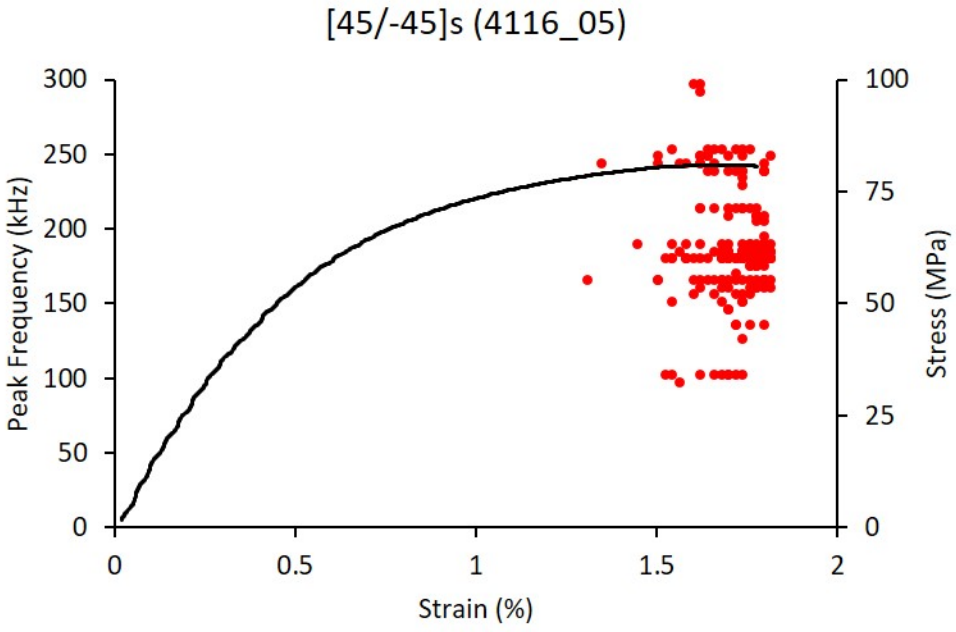

[0/90/±45]s (4120_20)
Peak Frequency (kHz)
Stress (MPa)
Strain (%)
0
100
200
300
400
500
600
0
100
200
300
400
500
0
0.5
1
1.5
2
2.5

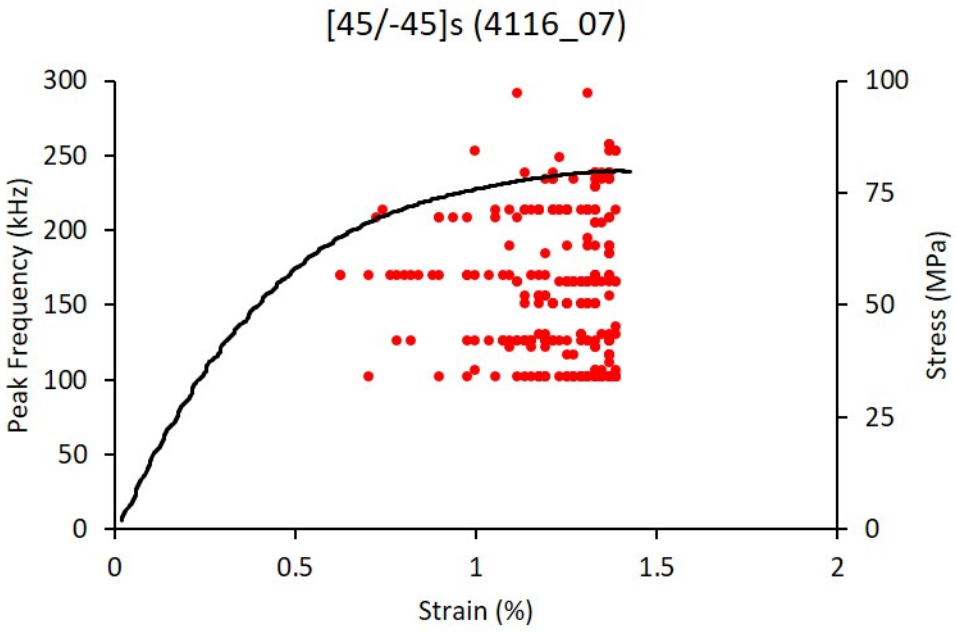

[90$_4$] (4113_04)
Peak Frequency (kHz)
Stress (MPa)
Strain (%)
0
100
200
300
400
500
600
0
50
100
150
0
0.5
1
1.5
2
2.5

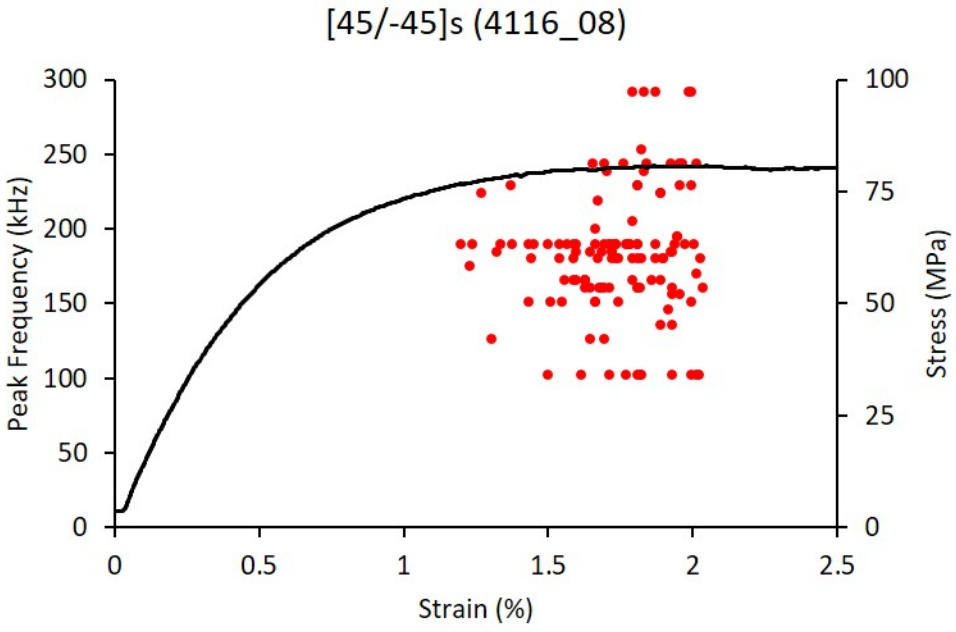

[90$_4$] (4113_25)
Peak Frequency (kHz)
Stress (MPa)
Strain (%)
0
100
200
300
400
500
600
0
50
100
150
0
0.5
1
1.5
2
2.5

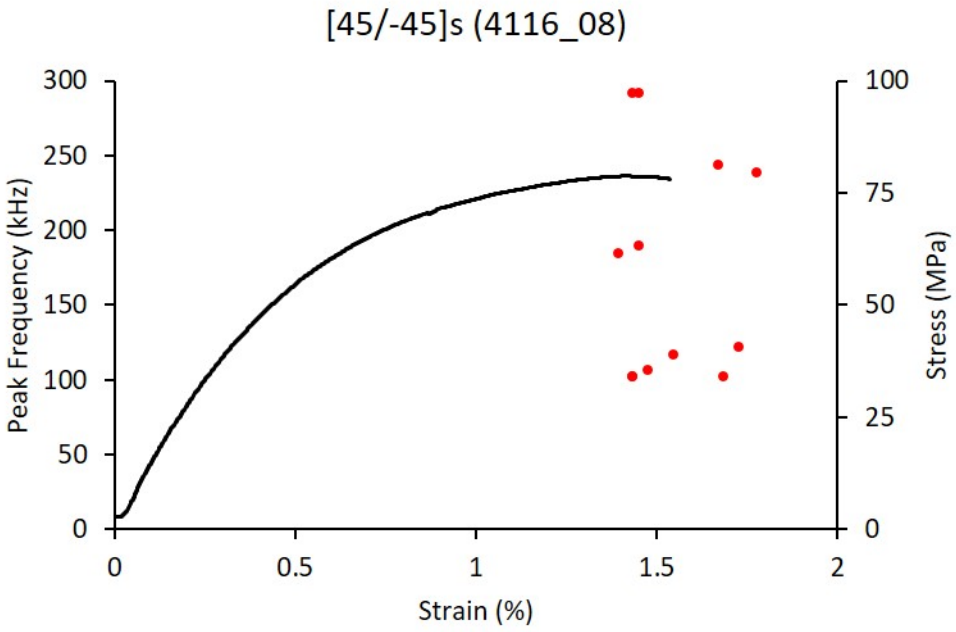

[90$_4$] (4113_27)
Peak Frequency (kHz)
Stress (MPa)
Strain (%)
0
100
200
300
400
500
600
0
50
100
150
0
0.5
1
1.5
2


[90₄] (4113_28)
Peak Frequency (kHz)
Stress (MPa)
Strain (%)
600
500
400
300
200
100
0
150
100
50
0
0
0.5
1
1.5
2

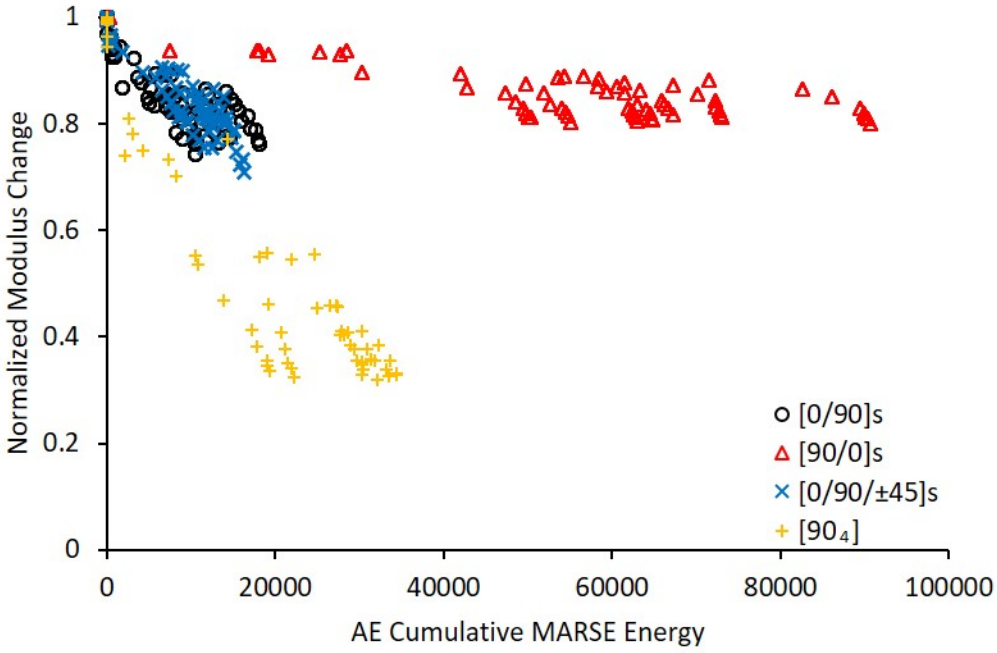

[45/-45]s (4116_05)
Peak Frequency (kHz)
Stress (MPa)
Strain (%)
300
250
200
150
100
50
0
100
75
50
25
0
0
0.5
1
1.5
2

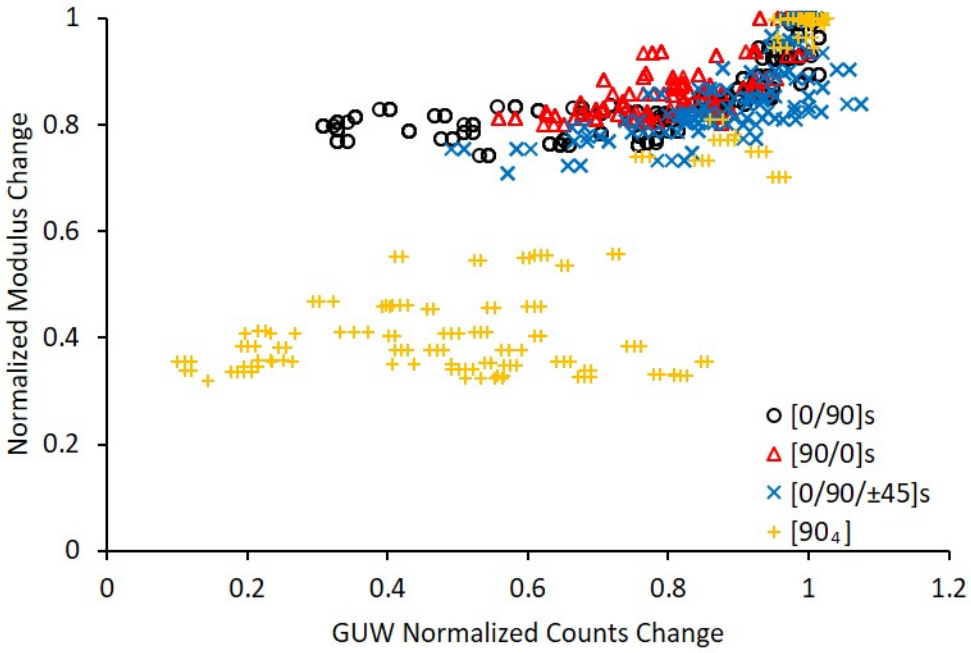

[45/-45]s (4116_07)
Peak Frequency (kHz)
Stress (MPa)
Strain (%)
0
50
100
150
200
250
300
0
25
50
75
100
0
0.5
1
1.5
2

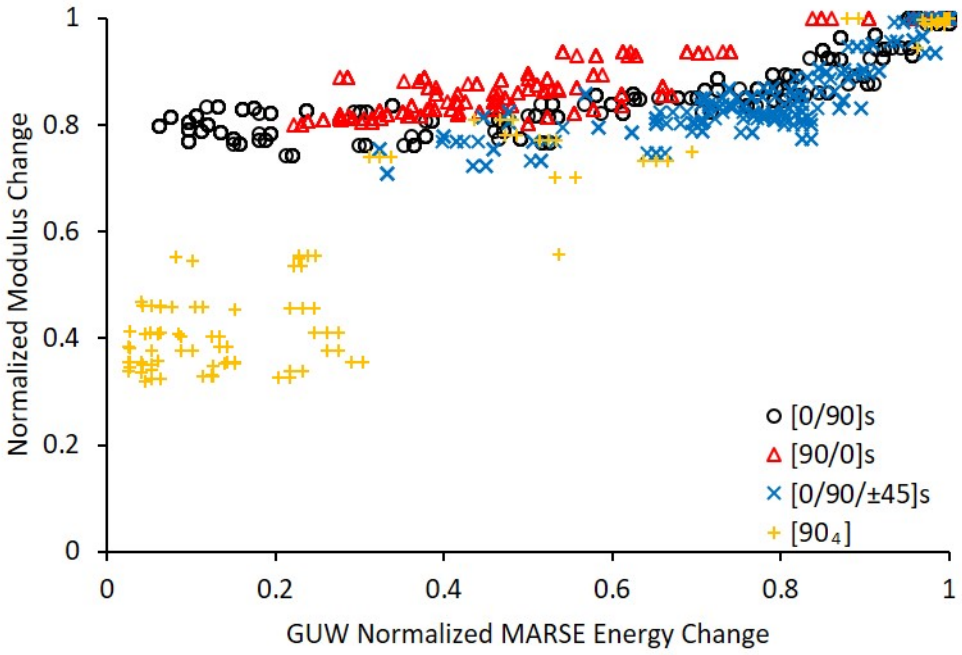

[45/-45]s (4116_08)
Peak Frequency (kHz)
Stress (MPa)
Strain (%)
0
50
100
150
200
250
300
0
25
50
75
100
0
0.5
1
1.5
2
2.5

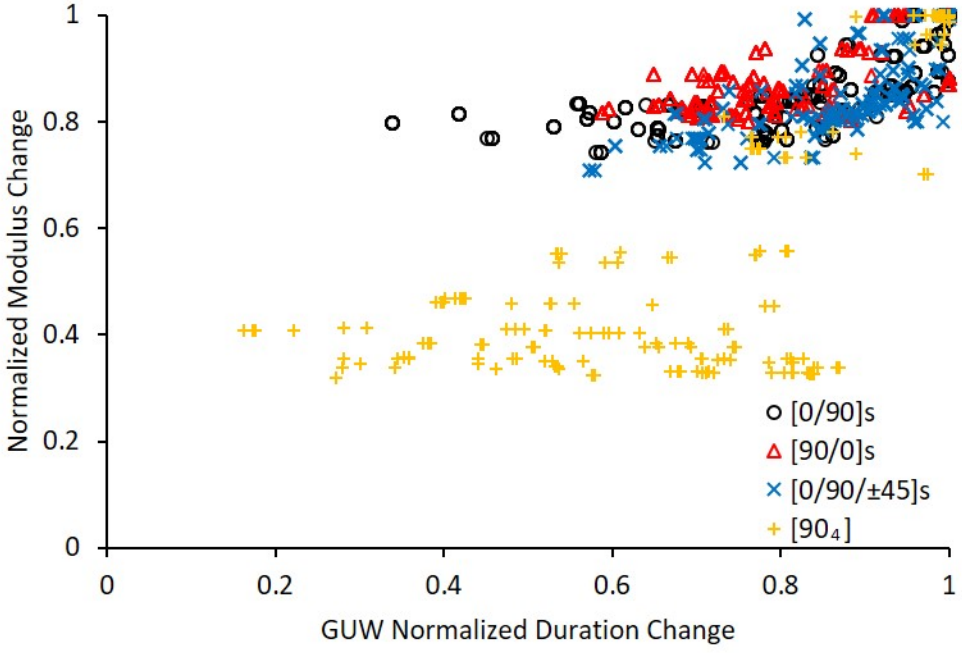

[45/-45]s (4116_08)
Peak Frequency (kHz)
Stress (MPa)
Strain (%)
300
250
200
150
100
50
0
100
75
50
25
0
0
0.5
1
1.5
2

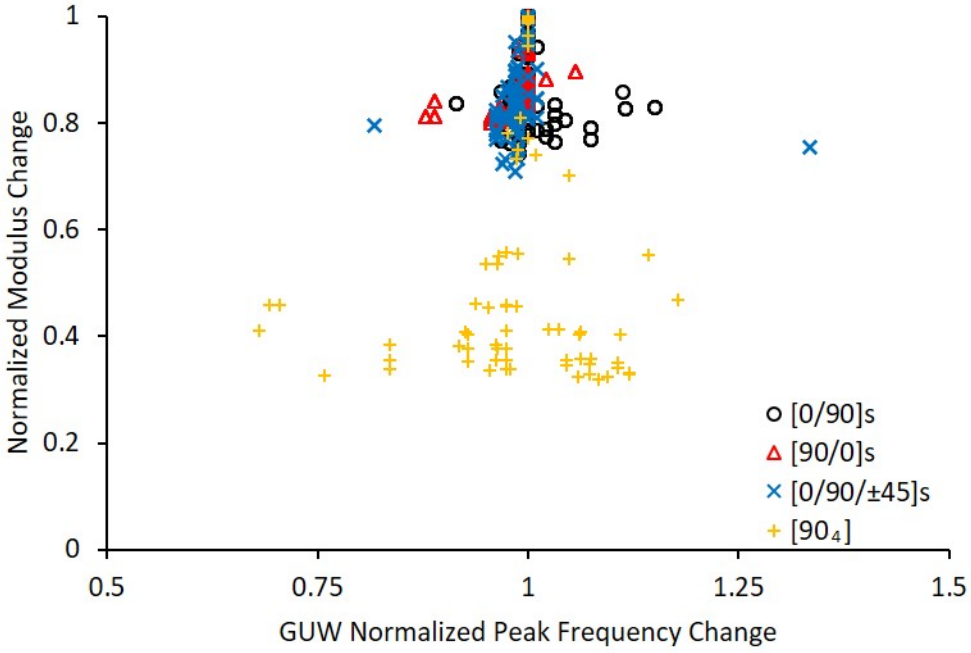
GUW and AE Data vs. Modulus Change






Normalized Modulus Change
GUW Normalized MARSE Energy Change
0
0.2
0.4
0.6
0.8
1
[0/90]s
[90/0]s
[0/90/±45]s
[90$_4$]

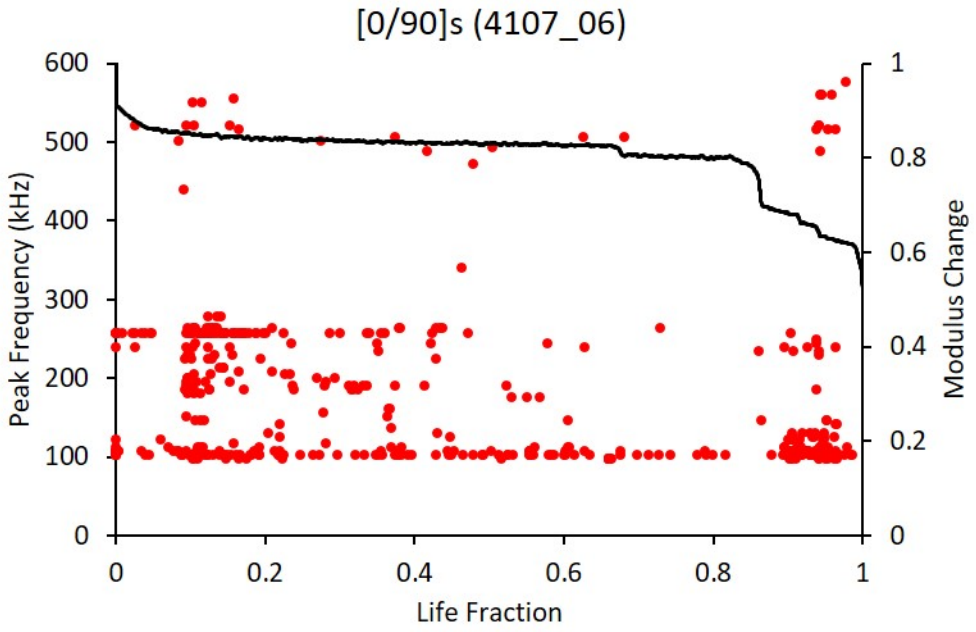

Normalized Modulus Change
GUW Normalized Duration Change
0
0.2
0.4
0.6
0.8
1
[0/90]s
[90/0]s
[0/90/±45]s
[90$_4$]

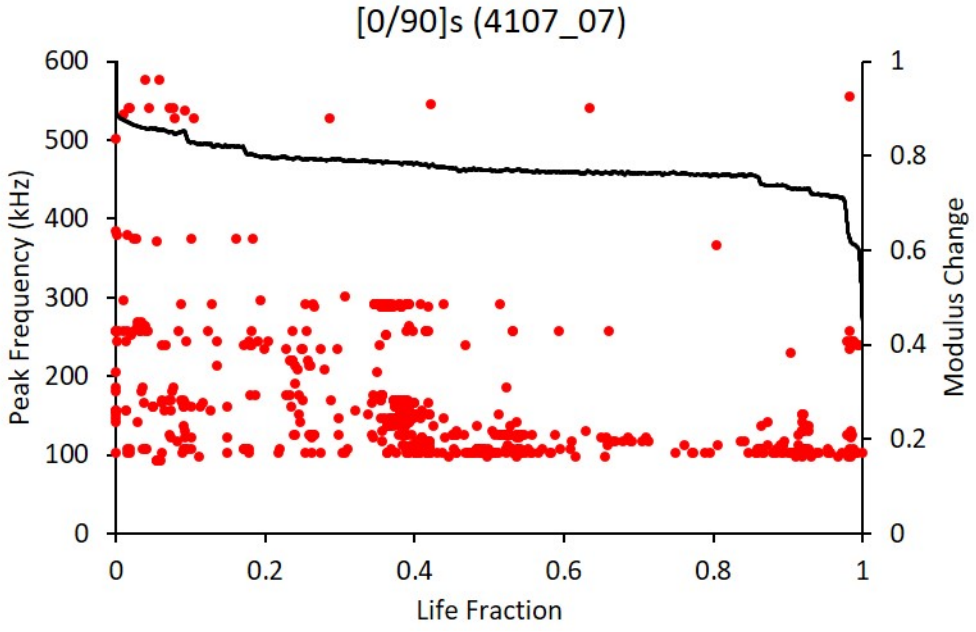

Normalized Modulus Change
1
0.8
0.6
0.4
0.2
0
0.5
0.75
1
1.25
1.5
GUW Normalized Peak Frequency Change
[0/90]s
[90/0]s
[0/90/±45]s
[90$_4$]

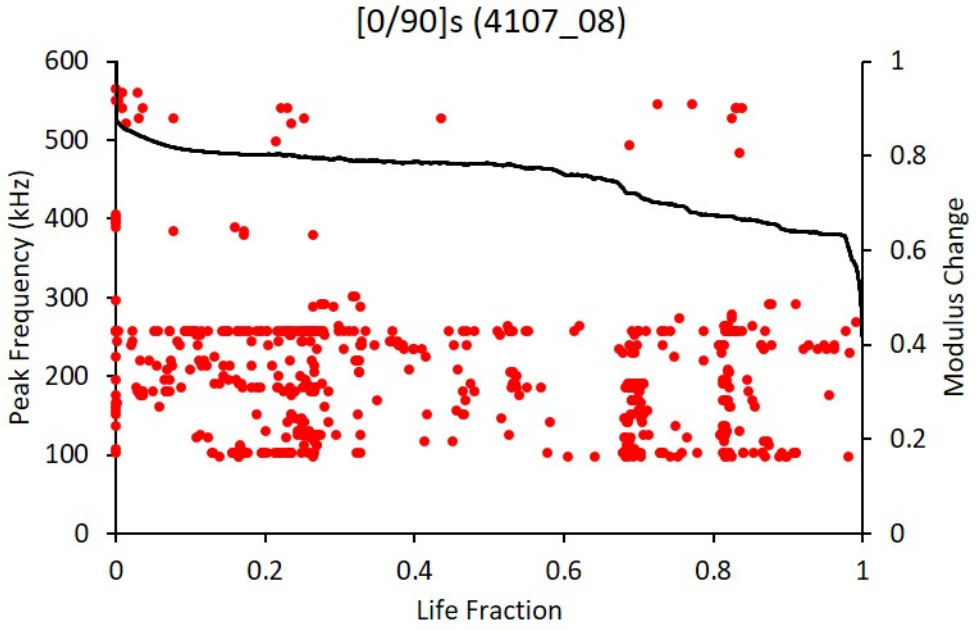
APPENDIX E

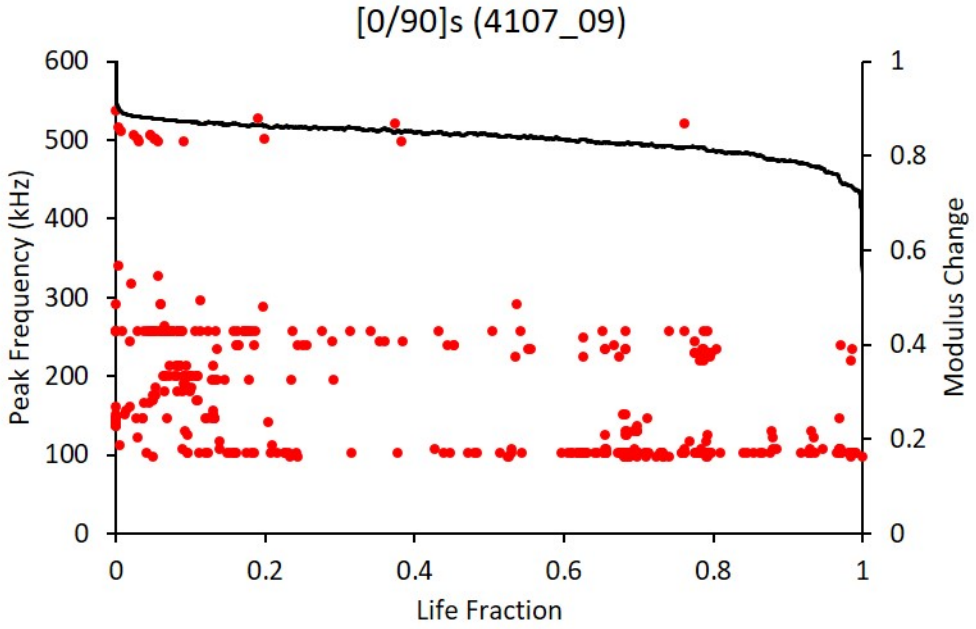
ADDITIONAL FATIGUE TEST DATA

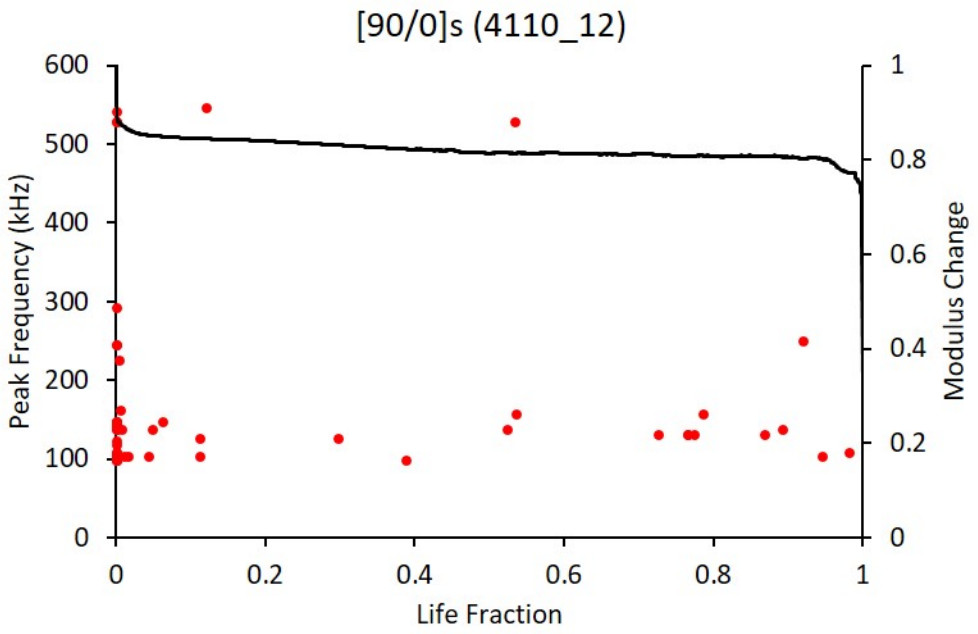
AE Peak Frequency Plots

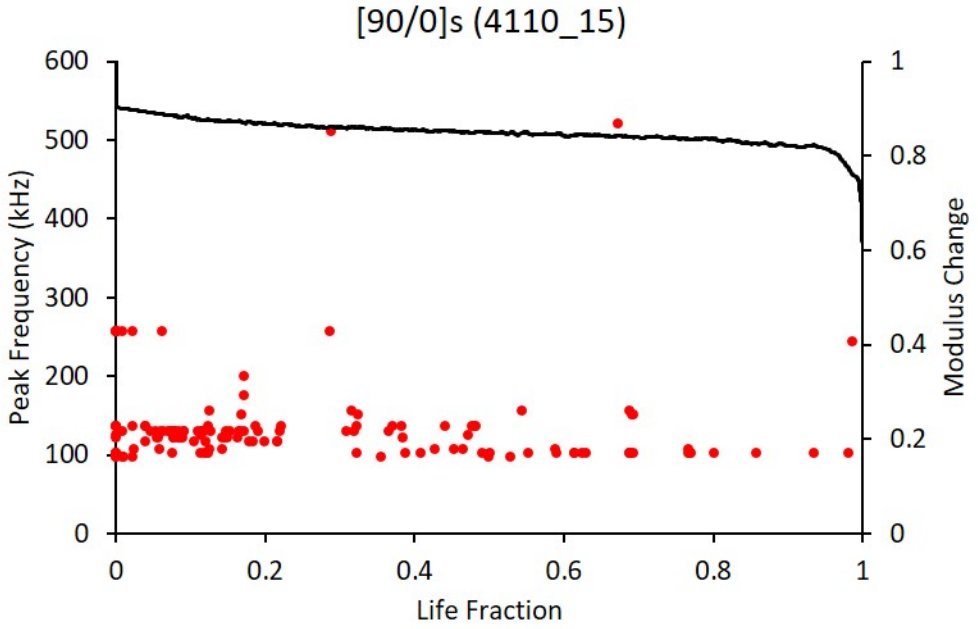


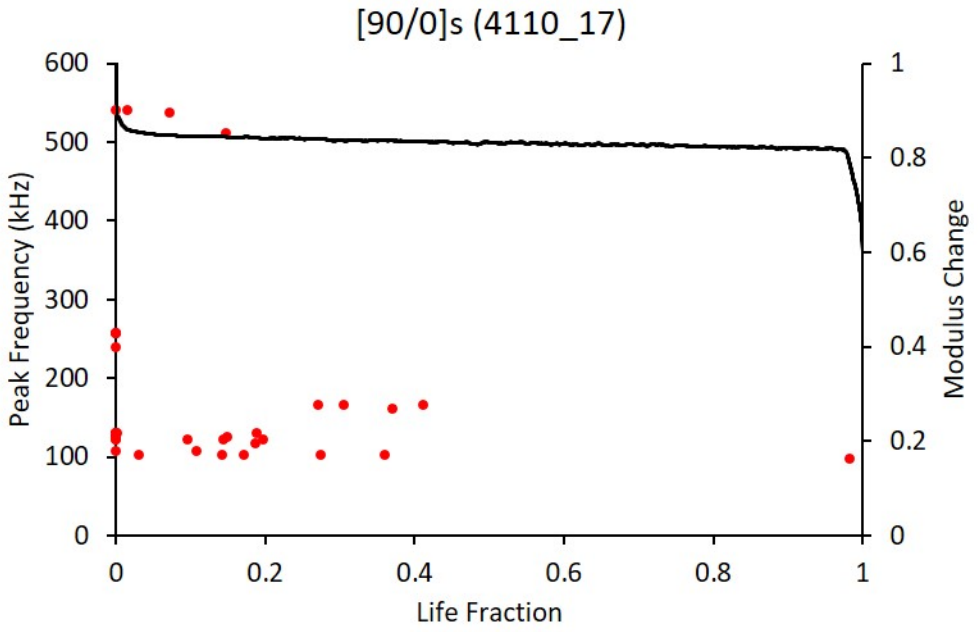


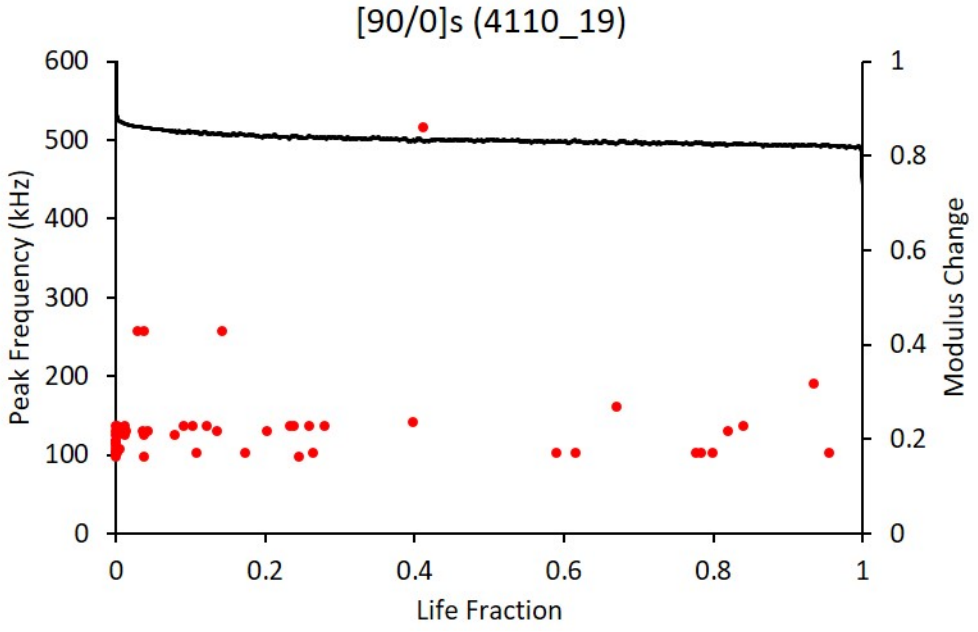

[0/90]s (4107_08)
Peak Frequency (kHz)
Modulus Change
Life Fraction
0
100
200
300
400
500
600
0
0.2
0.4
0.6
0.8
1

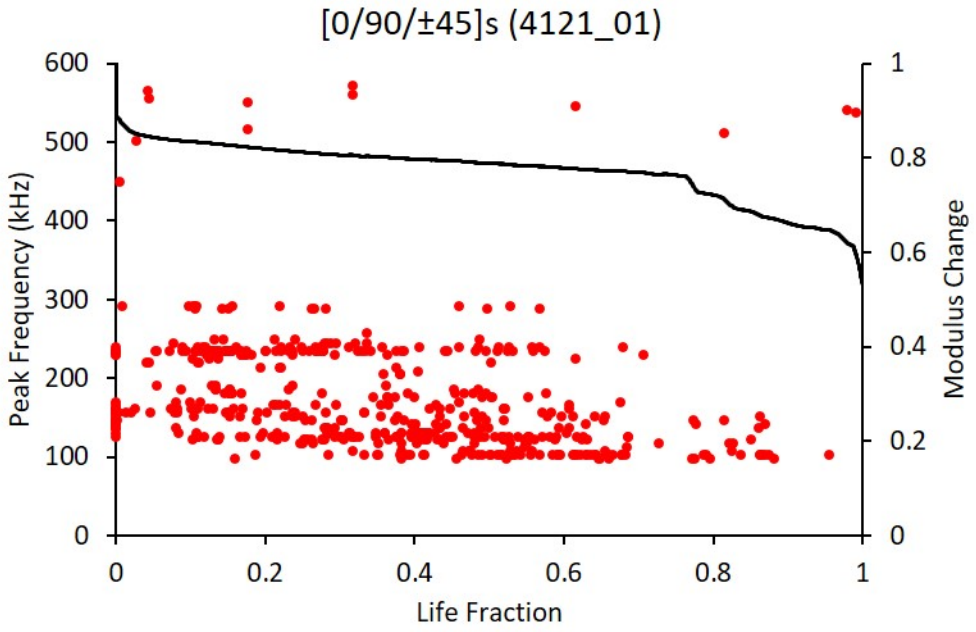

[0/90]s (4107_09)
Peak Frequency (kHz)
Modulus Change
Life Fraction
0
100
200
300
400
500
600
0
0.2
0.4
0.6
0.8
1

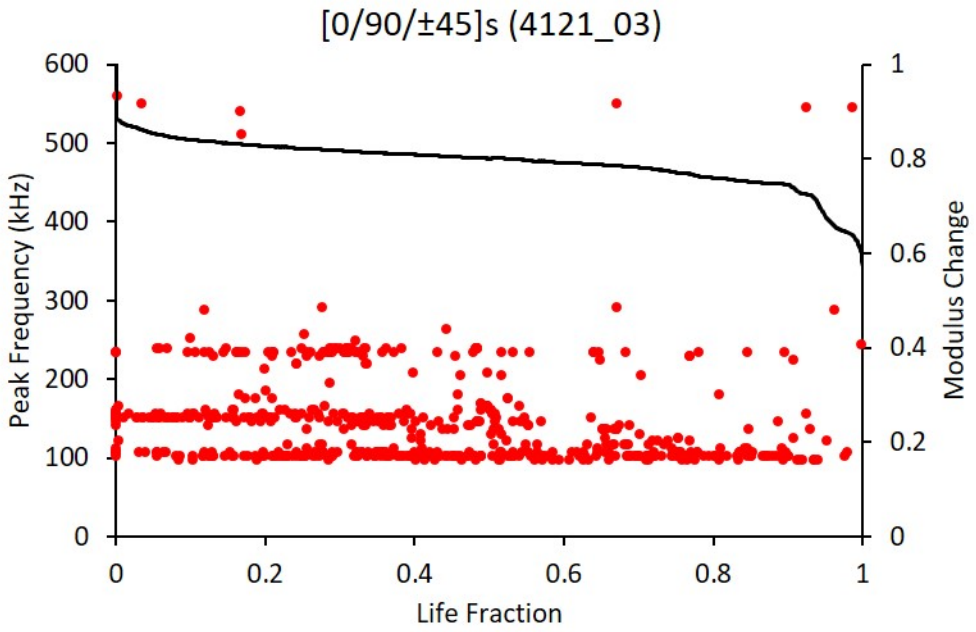

[90/0]s (4110_12)
Peak Frequency (kHz)
Modulus Change
Life Fraction
0
100
200
300
400
500
600
0
0.2
0.4
0.6
0.8
1

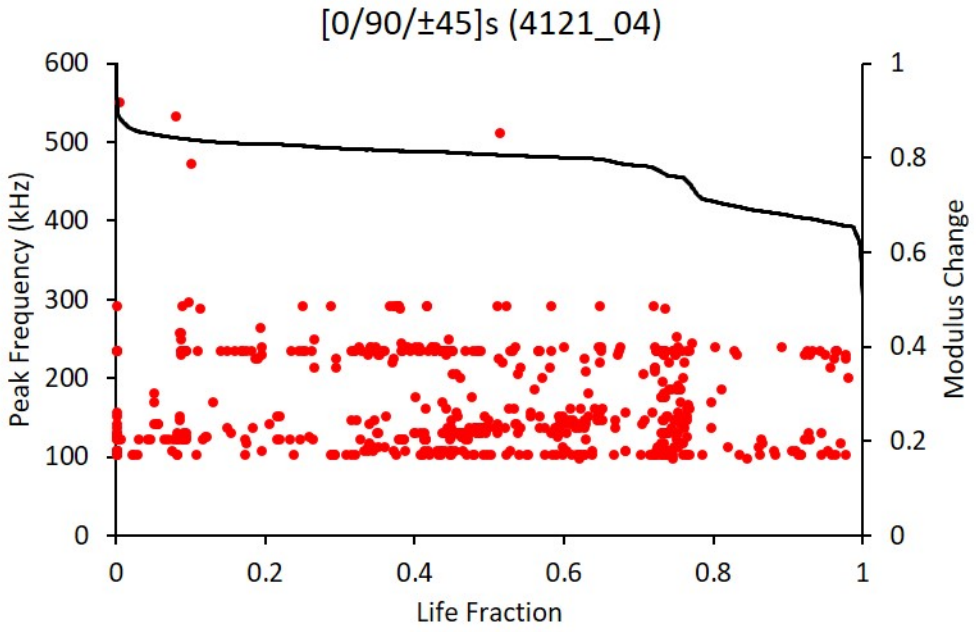

[90/0]s (4110_15)
Peak Frequency (kHz)
Modulus Change
Life Fraction
0
100
200
300
400
500
600
0
0.2
0.4
0.6
0.8
1

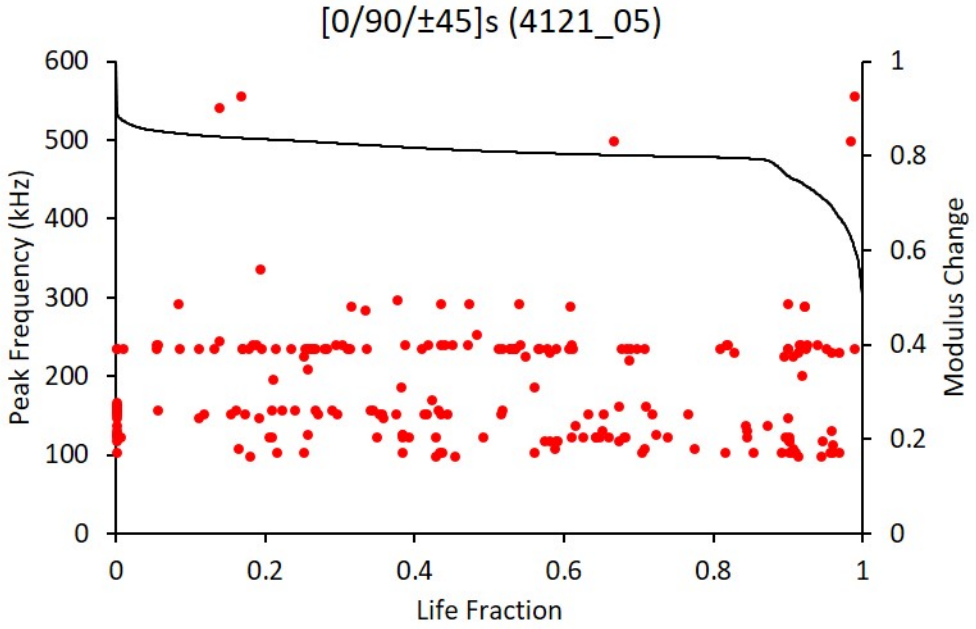

[90/0]s (4110_17)
Peak Frequency (kHz)
Modulus Change
Life Fraction
0
100
200
300
400
500
600
0
0.2
0.4
0.6
0.8
1


[90/0]s (4110_19)
Peak Frequency (kHz)
Modulus Change
Life Fraction
0
100
200
300
400
500
600
0
0.2
0.4
0.6
0.8
1

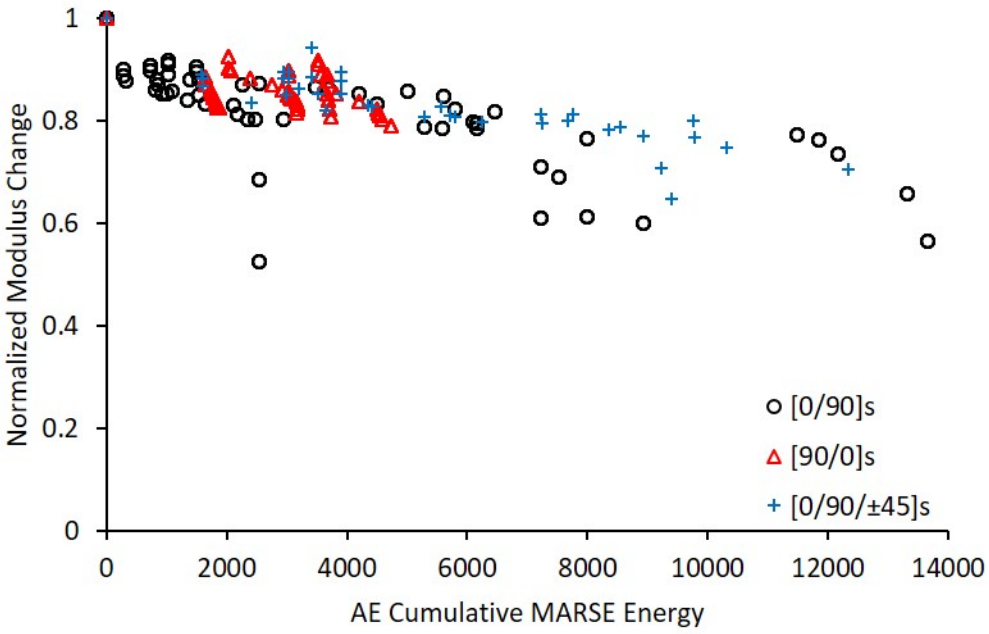

[0/90/±45]s (4121_01)
Peak Frequency (kHz)
Modulus Change
Life Fraction
0
100
200
300
400
500
600
0.2
0.4
0.6
0.8
1

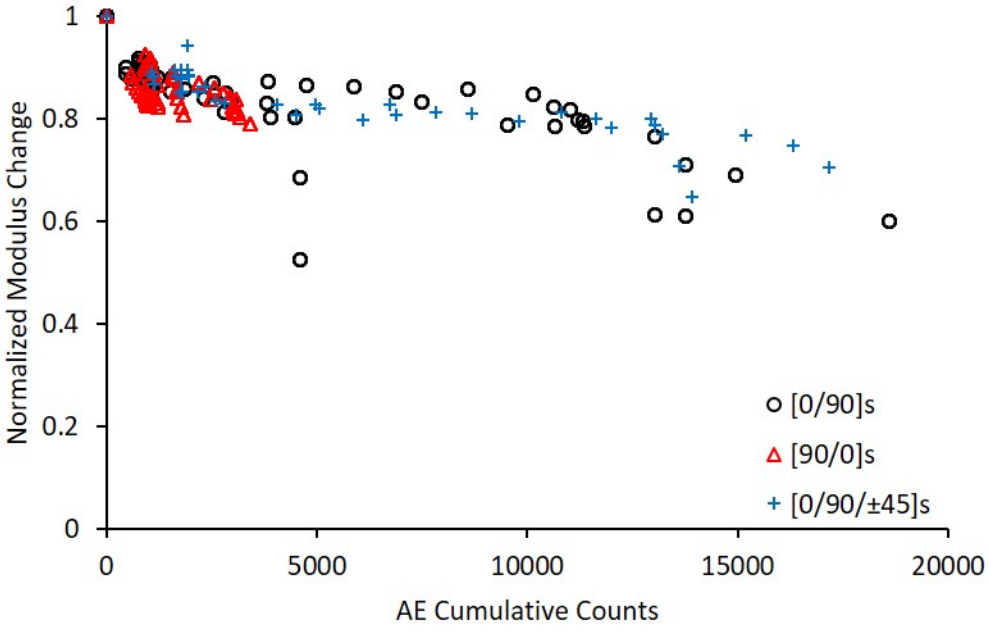

[0/90/±45]s (4121_03)
Peak Frequency (kHz)
Modulus Change
Life Fraction
0
100
200
300
400
500
600
0.2
0.4
0.6
0.8
1

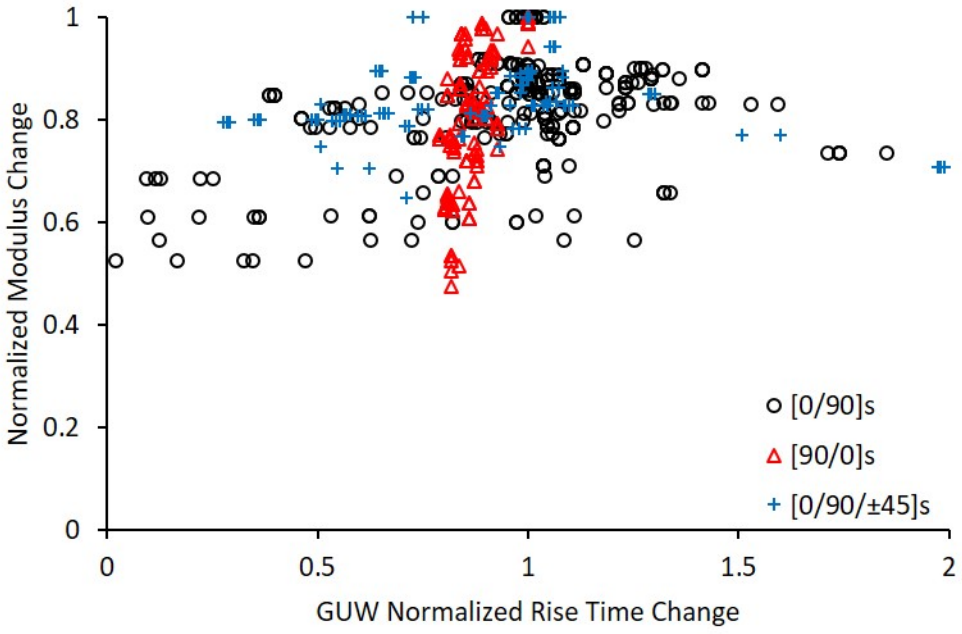

[0/90/±45]s (4121_04)
Peak Frequency (kHz)
Modulus Change
Life Fraction
0
100
200
300
400
500
600
0
0.2
0.4
0.6
0.8
1

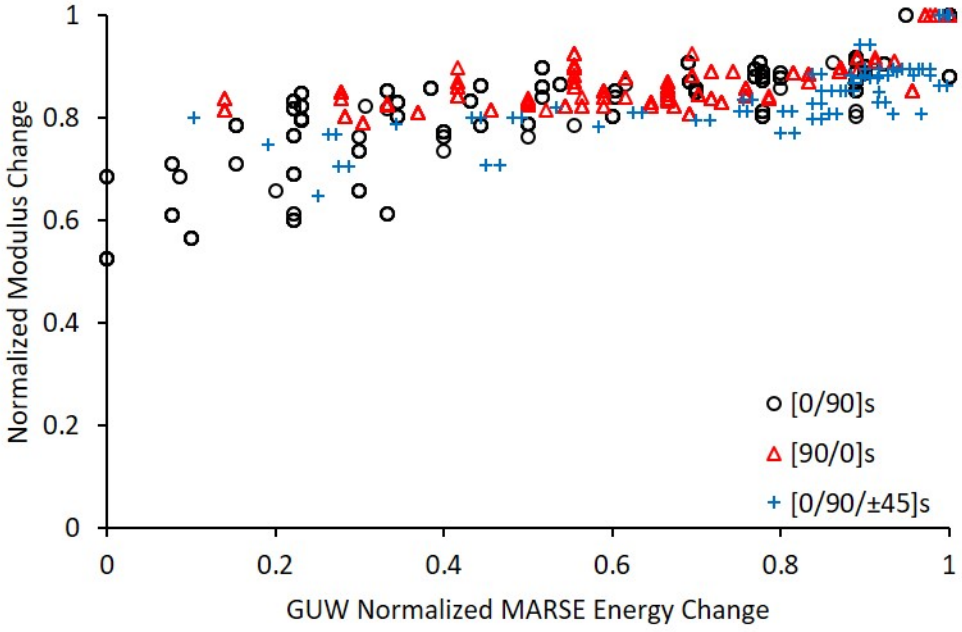

[0/90/±45]s (4121_05)
Peak Frequency (kHz)
Modulus Change
Life Fraction
0
100
200
300
400
500
600
0
0.2
0.4
0.6
0.8
1

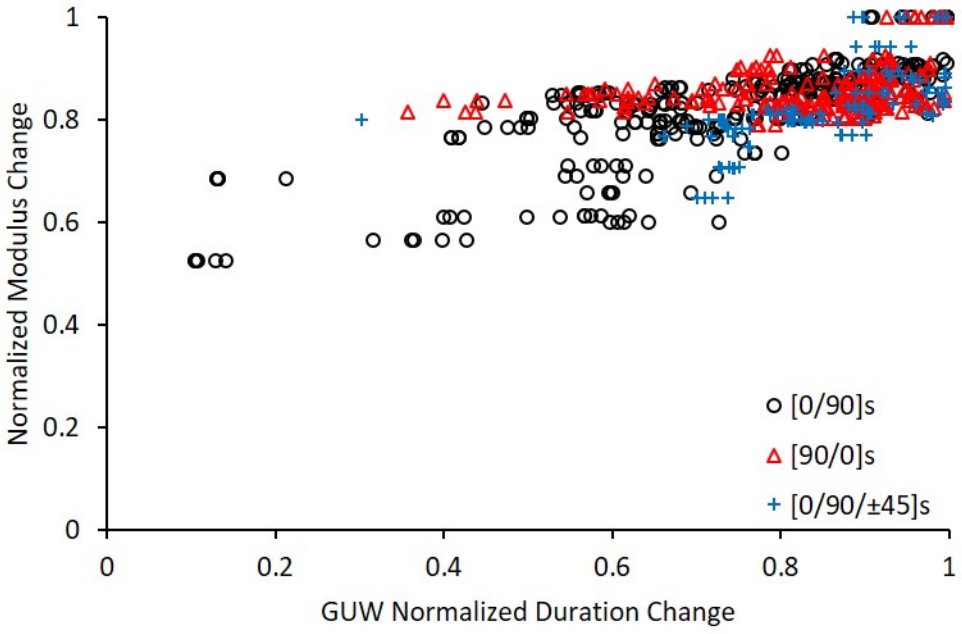
GUW and AE Data vs. Modulus Change

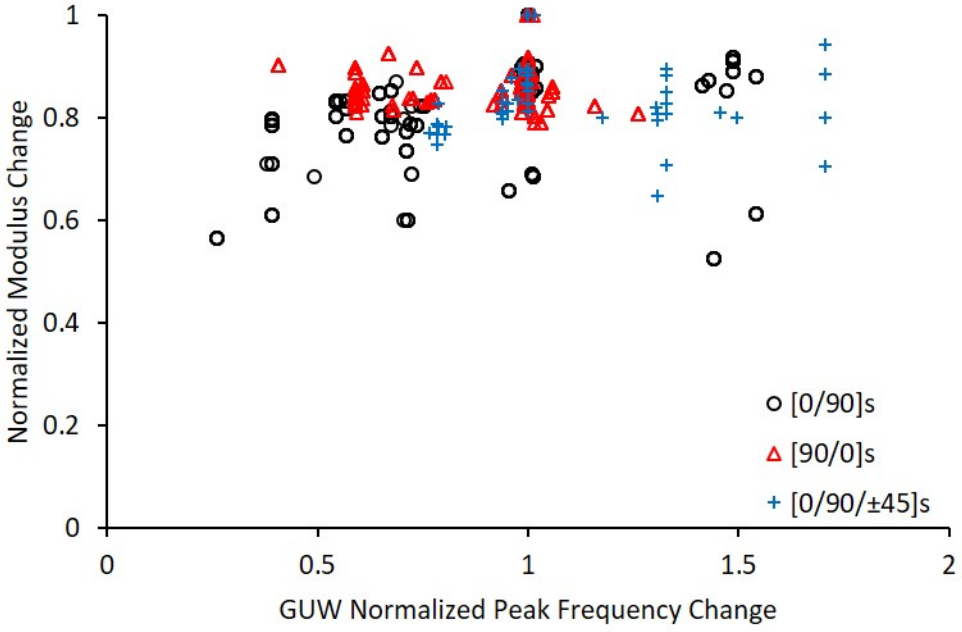


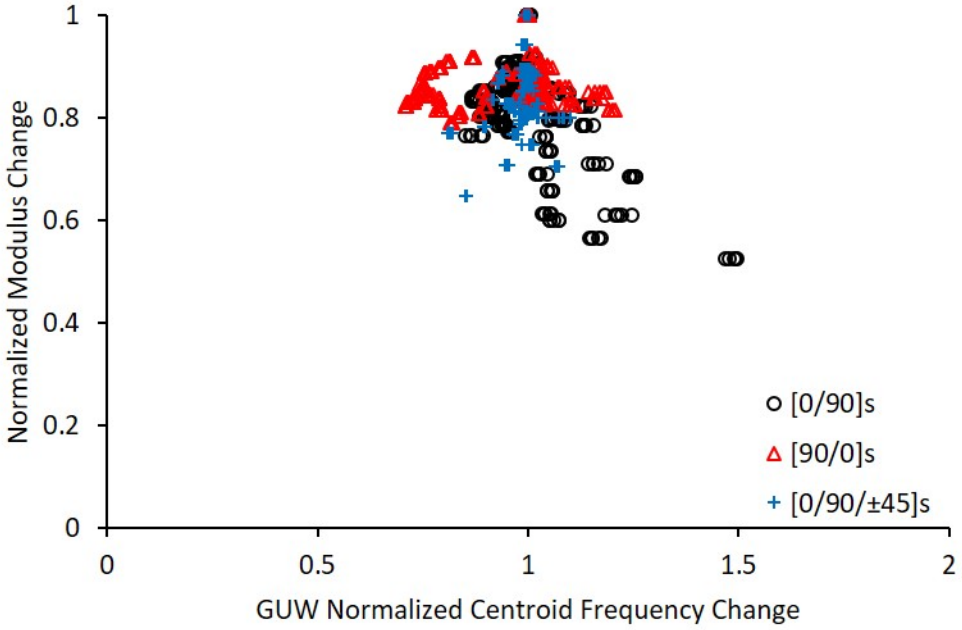



Normalized Modulus Change
GUW Normalized Rise Time Change
[0/90]s
[90/0]s
[0/90/±45]s
0
0.2
0.4
0.6
0.8
1
0
0.5
1
1.5
2


Normalized Modulus Change
GUW Normalized MARSE Energy Change
[0/90]s
[90/0]s
[0/90/±45]s
0
0.2
0.4
0.6
0.8
1
0
0.2
0.4
0.6
0.8
1


Normalized Modulus Change
GUW Normalized Duration Change
0
0.2
0.4
0.6
0.8
1
[0/90]s
[90/0]s
[0/90/±45]s


Normalized Modulus Change
GUW Normalized Peak Frequency Change
0
0.2
0.4
0.6
0.8
1
0.5
1.5
2
[0/90]s
[90/0]s
[0/90/±45]s


Normalized Modulus Change
1
0.8
0.6
0.4
0.2
0
0
0.5
1
1.5
2
GUW Normalized Centroid Frequency Change
[0/90]s
[90/0]s
[0/90/±45]s